Chair of Resource Mineralogy

Master's Thesis

The epithermal Chah-Mesi Cu-Pb-Zn-(Ag-Au) deposit, SE Iran: Petrography, ore mineralogy and fluid inclusions

Florian Peter Altenberger, BSc

September 2019

Lehrstuhl für Rohstoffmineralogie

Masterarbeit

Die polymetallische Cu-Pb-Zn-(Ag-Au) Epithermallagerstätte Chah-Mesi, Südostiran: Petrographie, Erzmineralogie und Fluideinschlüsse

Florian Peter Altenberger, BSc

September 2019

AFFIDAVIT

I declare on oath that I wrote this thesis independently, did not use other than the specified sources and aids, and did not otherwise use any unauthorized aids.

I declare that I have read, understood, and complied with the guidelines of the senate of the Montanuniversität Leoben for "Good Scientific Practice".

Furthermore, I declare that the electronic and printed version of the submitted thesis are identical, both, formally and with regard to content.

Date 05.08.2019

Altenberger, F.

Signature Author
Florian Peter, Altenberger
Matriculation Number: 01321795

چاه مسی

آنچه شما را آزار می دهد ، شما را برکت می دهد. تاریکی شمع شماست

“What hurts you, blesses you. Darkness is your candle.” - Rūmī

ACKNOWLEDGMENTS

I am very grateful for this opportunity to work on the Chah-Mesi project and for the considerable logistical support I received from Montanuniversität Leoben and the Shahid Chamran University Ahvaz. Alireza Zarasvandi is thanked for shaping this joint project, organizing the field trip, obtaining permissions for visiting the mines and core shed and for sharing his expertise with me in the field. I am especially thankful to my Iranian friends Mohsen Rezai and Majid Tashi for providing reports and analytical data as well as accompanying me during field work and for fruitful discussions. Moreover, they ensured that I was well looked after during my field visit and they showed me the best spots for pizza and ice cream in Ahvaz.

To my supervisor, Johann Raith, thank you for your guidance and particularly your patience. Also, for several hours-long discussions and mutual sessions on the microscope. I have learned so much from you. Your trust means a lot to me and I am so glad that you have given me the chance to see so many amazing places and stunning deposits during our field trip to Iran. Working on this wonderful project with you and traveling to this beautiful country was really a dream come true.

This work also benefited from several conversations over some beers with the godfather of ore microscopy, Werner Paar. Several parts of this thesis were completed thanks to your wisdom on ore mineralogy and microscopy. Thanks for giving me inspiration and sharing your passion for the world of ore minerals with me.

Thank you also, Ronald Bakker, for awakening my interest in the stunning field of Fluid Inclusions and your precious words of advice. I appreciated your help during seemingly endless Raman and microthermometry sessions.

To Gerhard Feitzinger, my workmate and very good friend, you introduced me to the great world of mining and ore deposits. I am glad that I eventually followed your advice in starting my education in Leoben, where I learned more than I could have ever imagined. Thank you for your generous support and continued encouragement during my studies. This would have never been possible without you and it is great to have you as my mentor.

I am so grateful for my friends at the Chair of Resource Mineralogy. Kristina Stocker, Monika Feichter, Daniela Wallner and Maik Zimmermann, thank you for endless discussions during coffee breaks and for helping me out whenever I was clueless. Especially, I want to thank Maik for giving me advice on the microprobe and for the preparation of all of my samples.

Love and thanks to my parents, Monika and Peter. You encouraged me during hard times of my studies and never lost faith in me. Moreover, all of this would not have been possible without your financial help for my excessive student life.

Last but not least, I cannot properly put into words how grateful I am for my girl. Eva, you are the best. Thank you for your patience and support to fulfill my dreams during my days in Leoben. You always help me with my English whenever I need your advice, such as in this moment. Moreover, thank you for occasionally kicking me outside for some needed fresh air. I could not have done all of this without you!

Abstract

The epithermal Chah-Mesi Cu-Pb-Zn-(Ag-Au) deposit, SE Iran: Petrography, ore mineralogy and fluid inclusions

In the southeastern part of the Cenozoic Urumieh-Dokhtar Magmatic Belt of Iran the NW-trending Kerman Porphyry Copper Belt hosts major porphyry Cu-(Mo-Au) deposits (PCD) of Miocene age; e.g. the diorite-type Cu-Au Meiduk and granodiorite-type Cu-Mo Sar Cheshmeh deposits. The polymetallic vein type deposit Chah-Mesi is located ~ 1.5 km south of the Meiduk porphyry stock. Its genetic relation to the porphyry system is unclear. At Chah-Mesi, Paleocene to Eocene calc-alkaline volcanic and pyroclastic rocks of mainly basaltic-andesitic composition were intruded by Miocene microdioritic dykes. The host rocks were affected by intense hydrothermal alteration exhibiting a central zone of strong silicification that grades into sericitization and propylitic alteration towards the peripheral parts. Argillic alteration is restricted to superficial areas and in direction to the Meiduk PCD propylitic alteration changes into potassic alteration. Six different vein types are distinguished: including two porphyry-related vein types, three alteration-related types of veinlets as well as mineralized veins showing massive, banded, crustiform and brecciated textures. Mineralization occurs as open space fillings and minor replacement and breccia bodies. The paragenetic sequence encompasses four mineralization stages starting with the early high-sulfidation assemblage pyrite + chalcopyrite + enargite-luzonite ± bornite with a continuous transition into intermediate-sulfidation state assemblages comprising pyrite + chalcopyrite + tennantite-tetrahedrite ± electrum ± Ag-bearing sulfosalts. The late paragentic stage with sphalerite + galena + pyrite ± electrum overprints the earlier ones. Supergene mineralization with chalcocite + covellite + Fe-oxyhydroxides + Cu-carbonate hydroxides is restricted to the shallow weathered part of the deposit. A regional zoning of ore minerals is apparent; central parts of the deposit are dominated by Cu-Fe-rich sulfides showing a transition to Pb-Zn-dominated zones mainly in the deeper and distal sections. Variations in the chemical composition of fahlores range from Fe-bearing tennantite to Zn-rich tetrahedrite with a strong positive correlation between Sb and Ag contents. The fahlores are complexly zoned and display a progressive increase of Sb concentration with increasing distance to the nearby Meiduk deposit. Primary fluid inclusions in mineralized O-type veins are low saline aqueous H_2O-salt inclusions. They yield homogenization temperatures ($T_{h\ LV\rightarrow L}$) between 115 to 295 °C for sphalerite and 145 to 397 °C for quartz. Salinity values range between 1.2 to 9.9 and 2.1 to 9.2 wt% NaCl equiv., respectively. Raman spectroscopy confirms low CO_2 concentrations of the vapor phase of the fluid inclusions. The fluids are interpreted to be of magmatic origin as indicated by previously published stable isotope studies. We propose that ascending cooling magmatic fluids were responsible for the transport of metals and mineral precipitation occurred in the epithermal regime upon dilution of magmatic fluids with meteoric water. Similar low-salinity, CO_2-bearing fluids were reported from the nearby Meiduk deposit. Conclusively, Chah-Mesi is classified as an intermediate-sulfidation epithermal deposit with a genetic link to the Meiduk porphyry (Cu-Au) deposit. Mineralization is inferred to hydrothermal fluids with an initial high-sulfidation state, which changed into intermediate-sulfidation state during cooling, dilution and fluid-wallrock interaction.

Zusammenfassung

Die polymetallische Cu-Pb-Zn-(Ag-Au) Epithermallagerstätte Chah-Mesi, Südostiran: Petrographie, Erzmineralogie und Fluideinschlüsse

Im Südosten des iranischen Urumieh-Dokhtar Magmatic Belts befindet sich der NW streichende Kerman Porphyry Copper Belt mit bedeutenden, miozänen porphyrischen Kupferlagerstätten (PCD); z.B. die Cu-Au bzw. Cu-Mo Tagbaue Meiduk und Sar Cheshmeh. Die polymetallische Ganglangerstätte Chah-Mesi befindet sich ca. 1,5 km südlich von Meiduk. Der genetische Zusammenhang war bisher unklar. In Chah-Mesi bilden paläozäne bis eozäne Andesite und dazitische Pyroklastite sowie miozäne Intrusionen von Mikrodioriten das Nebengestein. Dieses wurde hydrothermal stark alteriert und weist im Lagerstättenzentrum intensive Silizifizierung auf. Zur Peripherie findet zunächst ein Übergang in serizitische und schließlich in propylitische Alteration statt. Argillitisch alterierte Gesteine finden sich an der Oberfläche und nächst der Meiduk Lagerstätte tritt die äußerste potassische Zone auf. Unterschieden werden sechs Gangtypen: zwei Porphyry-assoziierte und drei Alteration-assoziierte Gangtypen sowie Erzgänge mit massiven, gebänderten, krustiformen und brekziierten Texturen. Die Vererzung tritt versprengt in Gängen, sowie in metasomatischen Erzkörpern und Erzbrekzien auf. Die paragenetische Abfolge umfasst vier Vererzungsphasen. Die frühe, hoch sulfidierte Vergesellschaftung von Pyrit + Chalcopyrit + Enargit-Luzonit ± Bornit geht kontinuierlich in eine intermediär sulfidierte Vergesellschaftung mit Pyrit + Chalcopyrit + Tennantit-Tetraedrit ± Electrum ± Ag-reiche Sulfosalze über. Die Spätphase mit Sphalerit + Galenit + Pyrit ± Electrum überprägt frühere Vererzungen. Die supergene Vererzung umfasst Chalkosin + Covellin + Fe-Oxyhydroxide + Cu-Carbonate und ist auf den oberflächennahen, verwitterten Lagerstättenbereich begrenzt. Die regionale Erzzonierung zeigt im Lagerstättenzentrum Cu-Fe bzw. zur Teufe und lateral Pb-Zn dominierte Sulfiderze. Die Fahlerzchemie reicht von Fe-Tennantit bis Zn-Tetraedrit und zeigt häufig eine positive Korrelation zwischen den Sb- und Ag-Gehalten. Komplex zonierte Fahlerzkristalle weisen einen progressiven Anstieg der Sb Konzentration mit steigender Distanz zur Meiduk Lagerstätte auf. Primäre Fluideinschlüsse in Quarz und Sphalerit der Erzgänge bestehen aus gering salzhaltigen, wässrigen H_2O-Salz Lösungen. Die Homogenisierungstemperatur ($T_{h\ LV\rightarrow L}$) liegt zwischen 115 und 295 °C in Sphaleriteinschlüssen und reicht von 145 bis 397 °C in Quarzeinschlüssen. Die Salinität erreicht zwischen 1,2 und 9,9 bzw. 2,1 und 9,2 Gew% NaCl equiv. Mittels Raman Spektroskopie wurden in der Gasphase von Einschlüssen geringe Konzentrationen an CO_2 nachgewiesen. Publizierte stabile Isotopendaten deuten auf einen magmatischen Ursprung der Fluide hin. Der Metalltransport wird auf aszendente Fluide magmatischer Abstammung zurückgeführt. Die epithermale Erzausfällung erfolgte, als die magmatischen Lösungen mit Grundwasser ausreichend verdünnt waren. Ähnliche CO_2 führende Fluide mit geringem Salzgehalt wurden auch in Meiduk dokumentiert. Chah-Mesi wird als eine intermediär sulfidierte Epithermallagerstätte klassifiziert, die eine genetische Verbindung zur porphyrischen Kupferlagerstätte Meiduk aufweist. Die hydrothermale Vererzung bildete sich anfänglich noch durch hoch sulfidierte Fluide, die kontinuierlich durch Abkühlung, Verdünnung und Reaktionen mit dem Nebengestein in einen intermediär sulfidierten Zustand übergingen.

Contents

1 Introduction

Chah-Mesi (چاه مسی) is a Farsi expression and has the meaning of 'well copper' in the Persian language. Based on the omnipresence of superficial Cu mineralization in this area it is obviously a suitable name for the Chah-Mesi deposit, which is located about 40 km northeast of Shahr-e-Babak city and only 1.5 km south of the Meiduk porphyry copper mine. Geologically, the mineralization occurs within the Kerman Porphyry Copper Belt in the southeastern part of the Urumieh-Dokhtar Magmatic Belt (UDMB), extending from Shahr-e-Babak to Bazman. In this 600 km northwest-southeast trending belt more than 300 copper deposits and showings are known, including 20 major porphyry copper deposits (PCDs) (Ghorbani, 2013). Vein type, base metal deposits with varying amounts of precious metals are also common and some of them are spatially associated with porphyry copper deposits (Padyar et al., 2017).

In 2018 Shahid Chamran University Ahvaz, Iran, invited Montanuniversität Leoben, Austria, for a joint project including a field trip to investigate and sample the Chah-Mesi deposit and the nearby Meiduk porphyry deposit. This study arises from a joint project of the two universities on "Transitional porphyry to epithermal systems in Iran" that started in 2018. During the visit of the open pits several samples of host rocks and different vein types were collected. Moreover, drill cores of five exploration drillings from an earlier exploration project by the National Iranian Copper Industries Company (NICICO) were extensively sampled and drill core samples were brought back to Austria for further investigation.

The present thesis attempts to understand the origin and evolution of mineralization at Chah-Mesi and to confirm or rebut any genetic relationship to the nearby Meiduk porphyry system. Polymetallic Cu-Zn-Pb-(Ag-Au) vein type mineralization at Chah-Mesi is linked with strong hydrothermal alteration and the deposit is spatially located close to the Meiduk porphyry deposit suggesting a genetic link.

To establish a correct ore deposit model for Chah-Mesi and to find out whether there is a genetic link between the hydrothermal vein type and the porphyry style mineralization are the main aims. The hypothesis to be tested is: Chah-Mesi could represent an epithermal deposit formed at the periphery or on top of the nearby Meiduk porphyry system.

The first aspect to be defined is a relative chronology of the vein formation to receive an estimation of hydrothermal development. This is done by studying crosscutting vein relationships of field observations and drill cores. Hydrothermal alteration is an ubiquitous characteristic of the deposit. Its distribution and type of alteration were investigated by optical microscopy, electron probe micro analysis (EPMA) and Laser Raman micro-spectroscopy (LRMS). To answer the questions regarding mineralization type and the mineral chemical composition of the ore minerals, a detailed mineralogical study of the ore and gangue mineral assemblages of the different veins demands the use of optical microscopy and EPMA. These methods were also used to check whether the deposit contains any precious metals (Au, Ag) and to identify the carriers. By studying the textural relationship between the ore minerals, a possible paragenetic sequence for the mineralization and the distinction of several mineralization stages has been established. Mineral chemistry data were also correlated with the position and depths of the sampled drill cores in order to find out if there is a spatial distribution of certain elements or minerals that could eventually be used for vectoring. Fluid inclusion studies provided important evidence for the ore deposit model and allowed to constrain the development of mineralizing fluids and PT-X conditions of ore formation.

Data of ore mineralogy and fluid inclusion investigations are compared with published data for the Meiduk deposit. The purpose is to see if there is any relation to the proximal porphyry stock of Meiduk and therefore a genetic link with PCD. Additionally, comparisons are drawn of the studied ore mineralization, alteration and fluid inclusions of the hydrothermal veins in Chah-Mesi with similar epithermal vein style mineralization elsewhere. On that basis, epithermal mineralization at Chah-Mesi is classified with respect to high- (HS), intermediate- (IS) and low- (LS) sulfidation state deposits. Conclusively, a synthesis of all obtained data and information is used to construct a correct genetic model for the Chah-Mesi deposit.

2 Geology and metallogeny

2.1 Geodynamic evolution of the Tethyan orogenic belt

The Alpine-Himalayan Tethyan orogenic belt extends over 12000 km from the Alps, along southeastern Europe, Turkey, Iran, Pakistan, Tibet to Indochina. The Neotethyan orogenic belt comprises sections where oceanic lithosphere is still being subducted, such as in the eastern Mediterranean and the Makran Trench, and other segments with advanced continental collision as in the Alps or Himalayas. Tectonic, magmatic and metallogenic processes provided a variety of valuable mineral deposits. The formation of porphyry Cu ± Mo ± Au deposits related to subduction of the Neotethys and subsequent collisional processes is seen as being the most important mineral deposit type. Several sections comprising world class porphyry deposits can be distinguished (Figure 1), including the collided arcs of the Carpathians and Balkans, the incipient Afro-Arabian collision zone (Turkey-Iran-Western Pakistan) and the advanced Indian collision zone (Pamir-Himalayas-Indochina). The Alpine section of the orogen lacks significant porphyry deposits, likely due to deeper levels of erosion and smaller total volumes of subduction in the western Tethys (Richards, 2015).

During the Paleozoic and Mesozoic, the Paleotethys and Neotethys ocean basins, respectively, were formed between the continental masses of Laurasia (Eurasia) to the north and the southern supercontinent Gondwana (Richards, 2015). Concerning the subduction polarity and the locations of individual continental fragments plate tectonic reconstructions (Scotese, 2007; Stampfli and Borel, 2004) disagree in many details, however, there is general agreement that the opening of the Paleotethys began in the mid-Paleozoic. This is related to the Early Paleozoic drifting away from Gondwana of an array of microcontinents, grouped under the label of Hun superterrane (von Raumer et al., 2002), which were later accreted to Laurussia in Devonian times (Stampfli and Borel, 2002). The subsequent convergence between Laurentia and Gondwana started the northward subduction of the newly formed ocean, creating the Variscan cordillera system. Crete, Turkey, Iran and Afghanistan were in a fore-arc-type position of the northward subduction of Paleotethys. These microcontinents were affected by the Eo-Cimmerian tectonic event that marked the final episode of the diachronous closure in the western Tethyan region with only small remnants of Paleotethys remaining by the Late Triassic (Stampfli and Borel, 2004).

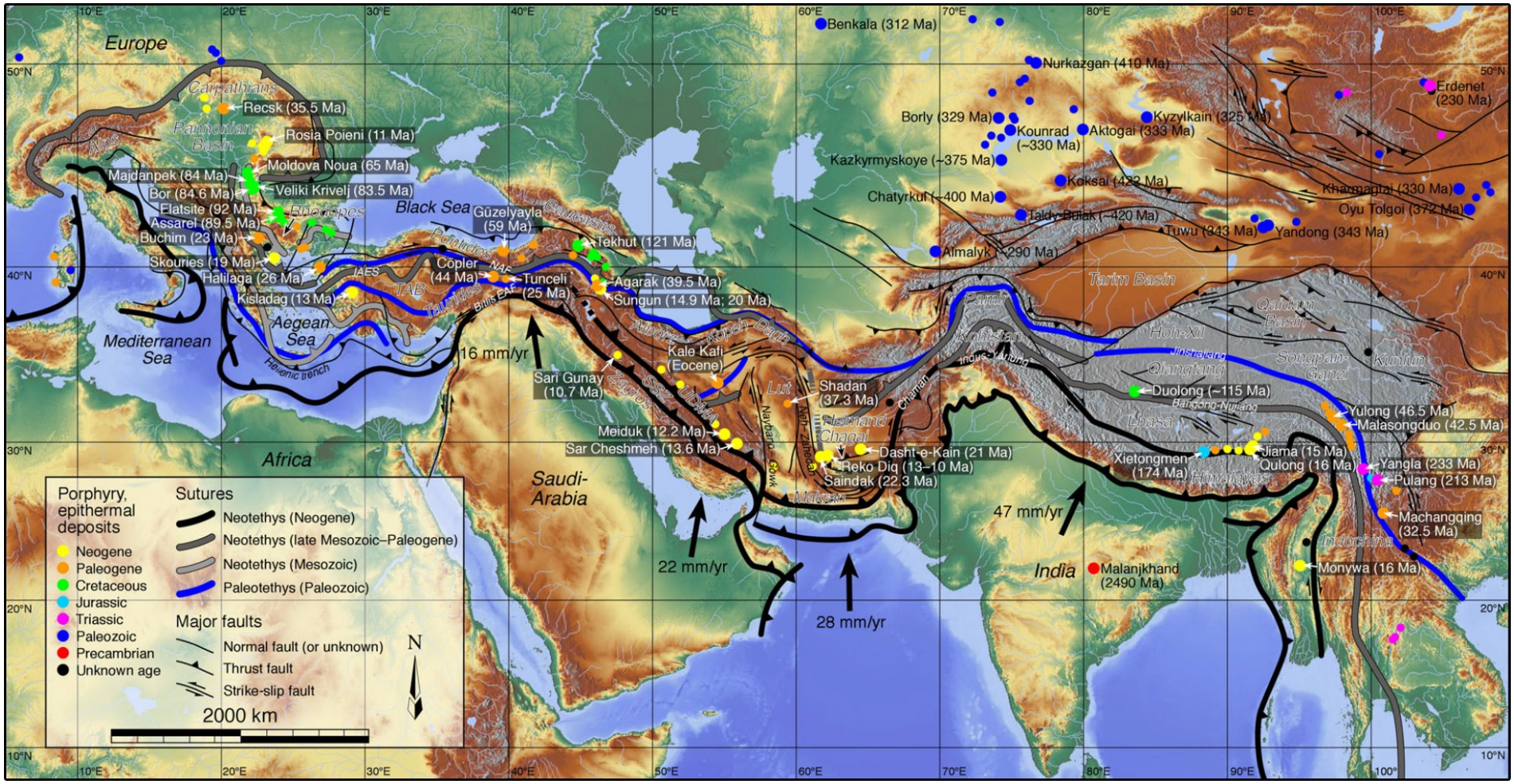

Figure 1: Topographic relief map of the Alpine-Himalayan Tethyan orogenic belt, showing major structures, Tethyan sutures and porphyry Cu ± Au deposits grouped by age. Larger deposits (generally >100 Mt resource) are identified by names and larger symbol sizes. Locations and ages of porphyry deposits are derived principally from Singer et al. (2008) with included updates collected by Richards (2015), e.g. Perelló et al. (2008) and Taghipour et al. (2008). Tethyan sutures and structures are derived primarily from Stampfli and Kozur (2006) with additional information collected by Richards (2015). Plate velocities relative to Eurasia are from Calais and Amarjargal (2000) and (Regard et al., 2005). The map is from Richards (2015) and for further information see therein. Abbreviations: EAF – East Anatolian Fault, IAES – Izmir-Ankara-Erzincan suture zone, NAF – North Anatolian Fault, SSZ – Sanandaj-Sirjan Zone, UDMA – Urumieh-Dokhtar magmatic arc.

The final welding of Gondwana and Laurasia culminated in the creation of the Permo-Triassic supercontinent Pangea (Stampfli and Borel, 2004). The Neotethyan ocean basin began to form in the southwest of Paleotethys also during the Permian-Early Triassic (Richards, 2015). In the Middle Permian the margin in southeastern Europe was a transform-type plate boundary and due to locking of the Gondwana-Laurasia suture little subduction occurred. In Late Permian roll-back of the Paleotethys slab generated quite active back-arc rifting along the entire Paleotethys northern margin and progressed to sea-floor spreading and opening of a series of marginal oceanic basins together with a general collapse of the Variscan cordillera from Italy to Iran (Stampfli and Borel, 2004). In Iran, the development of a large molassic basin (Shemshak basin) was generated by the closing of the Paleotethyan ocean and also caused subduction progradation to the northern side of Neotethys (Stampfli and Borel, 2004).

The subduction-related Mesozoic volcanics are preserved in the central Iranian NW-SE striking Sanandaj-Sirjan Zone, the eastern Alborz-Kopeh Dagh and the Central Iranian microcontinent. The detailed history of Neotethyan basin opening and closure in Iran is still under debate, but several ophiolite belts across the country indicate the formation of several (back-arc?) basins in addition to the main Neotethys ocean basin (Desmons and Beccaluva, 1983; Takin, 1972). The opening of the main Neotethys ocean basin was initiated by rifting of a collage of island arcs and continental fragments, the Cimmerian continents, from the northeastern margin of Gondwana in the Early Triassic (Hooper et al., 1994). The Cimmerian continents included the cores of present-day Turkey, Tibet and Indochina, as well as the Iranian Sanandaj-Sirjan Zone and the Central Iranian microcontinent (Lut, Tabas and Yazd blocks). These drifted northwards and eventually accreted to the southern margin of Eurasia in the Late Triassic-Early Jurassic along the Paleotethys suture, followed by northward-directed subduction of the Neotethys beneath this accreted margin (Horton et al., 2008; Richards, 2015). Related to this period of subduction Late Triassic-Cretaceous I-type arc plutons intruded the Iraqi Zagros Suture Zone, the Sanandaj-Sirjan Zone and the Makran (Agard et al., 2005; Ali et al., 2013). Further, several small ocean basins such as the Sabzevar and Sistan oceans (Figure 2 a, b) in northeast and eastern Iran, respectively, formed along the accreted margin due to back-arc rifting, whereas the closure of these basins gave rise to calc-alkaline arc magmatism in the Arghash Massif and Lut Block during the Late Cretaceous-Oligocene (Alaminia et al., 2013). Concerning the collision between the Sanandaj-Sirjan Zone, Central Iran and Arabia paleogeographic reconstructions indicate that in the Mesozoic the Sanandaj-Sirjan Zone docked with Eurasia (Figure 2 a). This is associated with formation of a small back-arc basin between these blocks in the Middle Cretaceous (Ghasemi and Talbot, 2006). For the final phase of Neotethyan closure, Alavi (1980, 1994) assumed a Cretaceous age for the collision of the Sanandaj-Sirjan Zone with Arabia, whereas Hooper et al. (1994) suggested an Oligocene age, followed by the Late Cenozoic collision with Central Iran (Ghalamghash et al., 2009).

During the Late Cretaceous/Paleogene the Mesozoic arc magmatism shifted from the Sanandaj-Sirjan Zone about 100 km to the northeast to the Urumieh-Dokhtar Magmatic Belt. The reasons of this shift are still under debate. The simplest explanation would be that the angle of subduction flattened, so the NW-SE axis of magmatism moved further to the northeast to form the Urumieh-Dokhtar arc (Mohajjel and Fergusson, 2014). Glennie (2000) postulates the closure of two separate Neotethyan basins to the south and north of the Sanandaj-Sirjan Zone. Verdel et al. (2011) prefer the alternative explanation that the angle of Neotethyan subduction shallowed in the Cretaceous and forced a northeastern shift of the axis of arc magmatism from the Sanandaj-Sirjan Zone to the parallel extending Urumieh-Dokhtar Magmatic Belt. Then the flat-subducting slab rolled back prior to Miocene collision and exposed hydrated lithosphere to an influx of hot asthenospheric material in the re-opened mantle wedge. Initially, the Eocene magmatism was of calc-alkalic character, but developed to more potassic (shoshonitic) compositions during the Oligocene to Early-Middle Miocene, and finally changed to even more alkaline composition in the Late Neogene (Hassanzadeh, 1993). The transition reflects the onset of diachronous collision between the irregular shaped Arabian indenter and the accreted Eurasian margin. A Miocene age is generally preferred for the final collision along the Bitlis-Zagros subduction zone (Agard et al., 2005). Initialized in the Late Eocene (35 Ma), the collision was followed by crustal thickening in the Oligocene and uplift of the central Iranian plateau in the Middle Miocene (15-12 Ma) prior to slab breakoff (Mouthereau et al., 2012). Eocene volcanism also occurred behind the main Neotethyan destructive margin, such as in the Alborz in north and northeastern Iran, as well as in the Lut Block in eastern Iran and it appears to have involved the formation and destruction of several small back-arc basins, such as the Sabzevar and Sistan oceans (Richards, 2015). The Oligocene magmatism in northeastern Iran was of collisional character and coincided with the onset of oroclinal bending and the uplift in the Kopeh Dagh (Hollingsworth et al., 2010). Similar magmatic development is recognized in northwestern Iran, where normal calc-alkaline magmatism in the early Oligocene changed to shoshonitic plutonism in the late Oligocene (Aghazadeh et al., 2011).

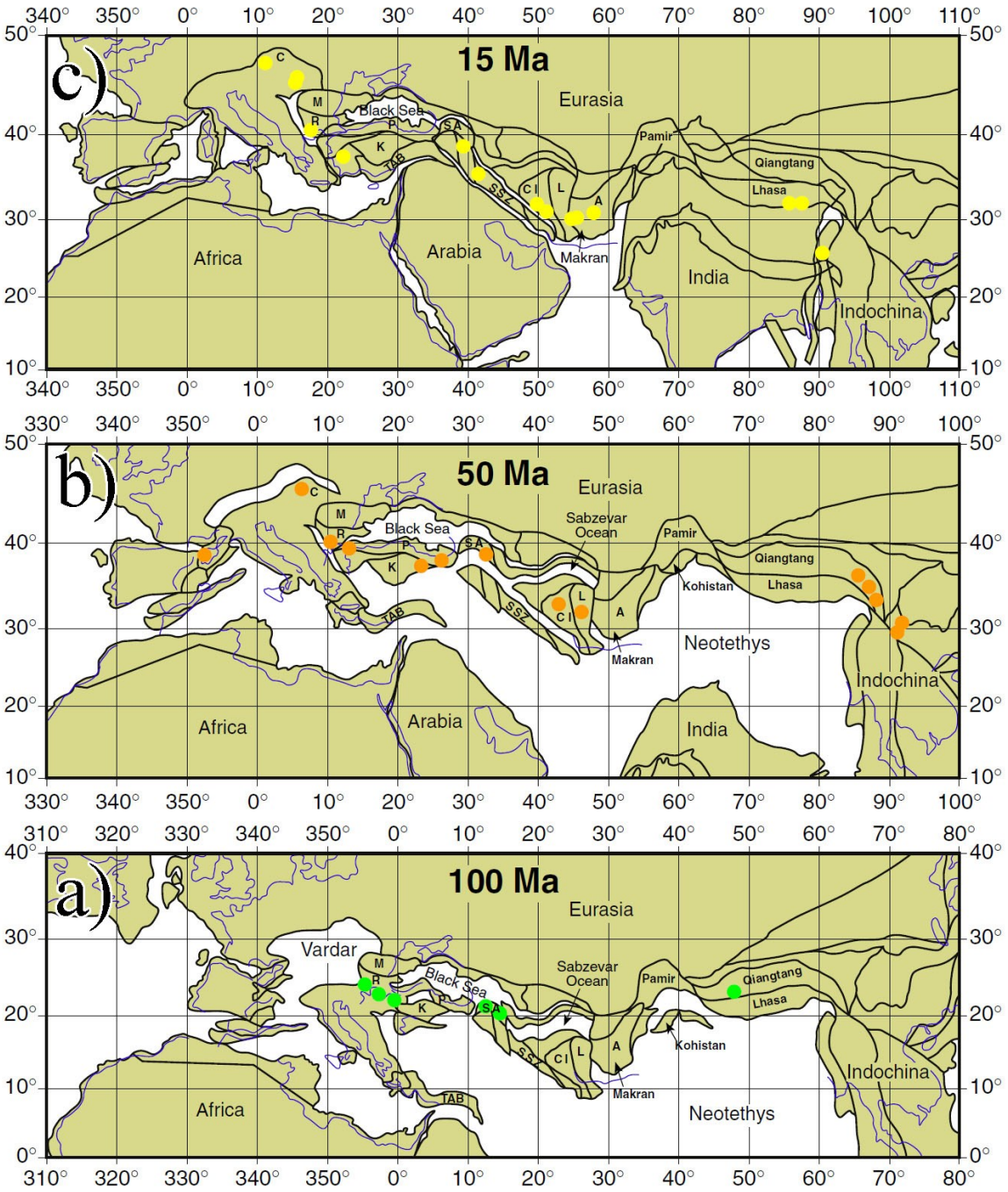

Figure 2: Paleogeographic reconstructions of the Neotethyan region at a) 100 Ma, b) 50 Ma and c) 15 Ma. These reconstructions are from Richards (2015) and were redrawn from maps generated using the Ocean Drilling Stratigraphic Network's Plate Tectonic Reconstruction Service (www.odsn.de/odsn/services/paleomap/paleomap.html). Plate motions are modeled relative to a magnetic reference frame using a Mercator projection and the blue lines represent the present-day coastlines for reference. Locations of major porphyry deposits forming around the time of each image are approximate and for more precise locations, deposit names and ages see Figure 1. Abbreviations: A – Afghan block, C – Carpathians, CI – Central Iranian block, K – Kirşehir block, L – Lut block, M – Moesian Platform, P – Pontides, R – Rhodopes, SA – South Armenian block, SSZ – Sanandaj-Sirjan Zone, TAB – Tauride-Anatolide block.

The orogen was lengthened by Neogene dextral strike-slip faulting (Figure 2 c) as the eastward extension was blocked by the collision of the Afghan plate with India (Allen et al., 2011) and the shortening of about 68 km across the Zagros and 120 km across the Arabian plate caused crustal thickening (Allen et al., 2013). Further, the subsequent slab breakoff in the Mid-Late Miocene (Allen et al., 2011) or Plio-Pleistocene (Molinaro et al., 2005) caused uplift and post-collisional magmatism throughout Iran. The Neogene-Quaternary mafic post-collisional volcanism expanded from the northwest to the Lut Block and showed potassic to ultrapotassic character with subduction-modified mantle lithosphere origin (Ahmadzadeh et al., 2010). Concerning the isolated Damavand stratovolcano, Davidson et al. (2004) assumed that perhaps an asthenospheric component was also included. Usually, volcanism is localized along trans-tensional structures (Ahmadzadeh et al., 2010). Alkali basaltic rocks are associated with N-S oriented strike-slip faults in eastern Iran that formed in response to extension following delamination of thickened subcontinental lithospheric mantle as a delayed response to Late Cretaceous collision between the Lut and Afghan blocks (Pang et al., 2012). The magmatic arc of Urumieh-Dokhtar is characterized by Eocene calc-alkaline, followed by Oligocene shoshonitic magmatism and finally developed to bimodal felsic and mafic alkalic composition during the Miocene (Hassanzadeh, 1993). Adakite-like Pliocene-Quaternary magmatism is associated with slab breakoff (Omrani et al., 2008) and the Miocene formation of post-collisional calc-alkaline magmas involved a significant fraction of remobilized subduction-modified lower crust (Shafiei et al., 2009).

2.2 Geological and structural units of Iran

Magmatic activities, metamorphism and tectonics related to orogenic events created several structural units, each representing an exclusive component in a geological mosaic that builds up todays Iran. The first subdivision into structural zones was done by Stöcklin and Nabavi (1973) and remained as a reference for later models with separation into several microcontinental blocks (Aghanabati, 2004; Alavi, 1994; Berberian and King, 1981; Ghorbani, 2013). The continental blocks are separated from each other by fold and thrust belts that are related to the opening and closure of ocean basins in the former Tethys realm (Stampfli and Borel, 2002).

Berberian and King (1981) distinguished three major structural units based on geological features and fold-thrust belts. These major units comprise the Southern Unit represented by the Zagros Fold and Thrust Belt, the Cimmerian Blocks as the Central Unit and the Northern Unit. In western Iran the very distinctive mountain range of the NW-SE striking Zagros Orogen consists of three subparallel tectonic zones. These are from northeast to southwest: the Urumieh-Dokhtar Magmatic Belt, the Sanandaj-Sirjan Zone and the Zagros Fold and Thrust Belt (Alavi, 2007). Each zone records its individual geological development and belongs to a different major structural unit.

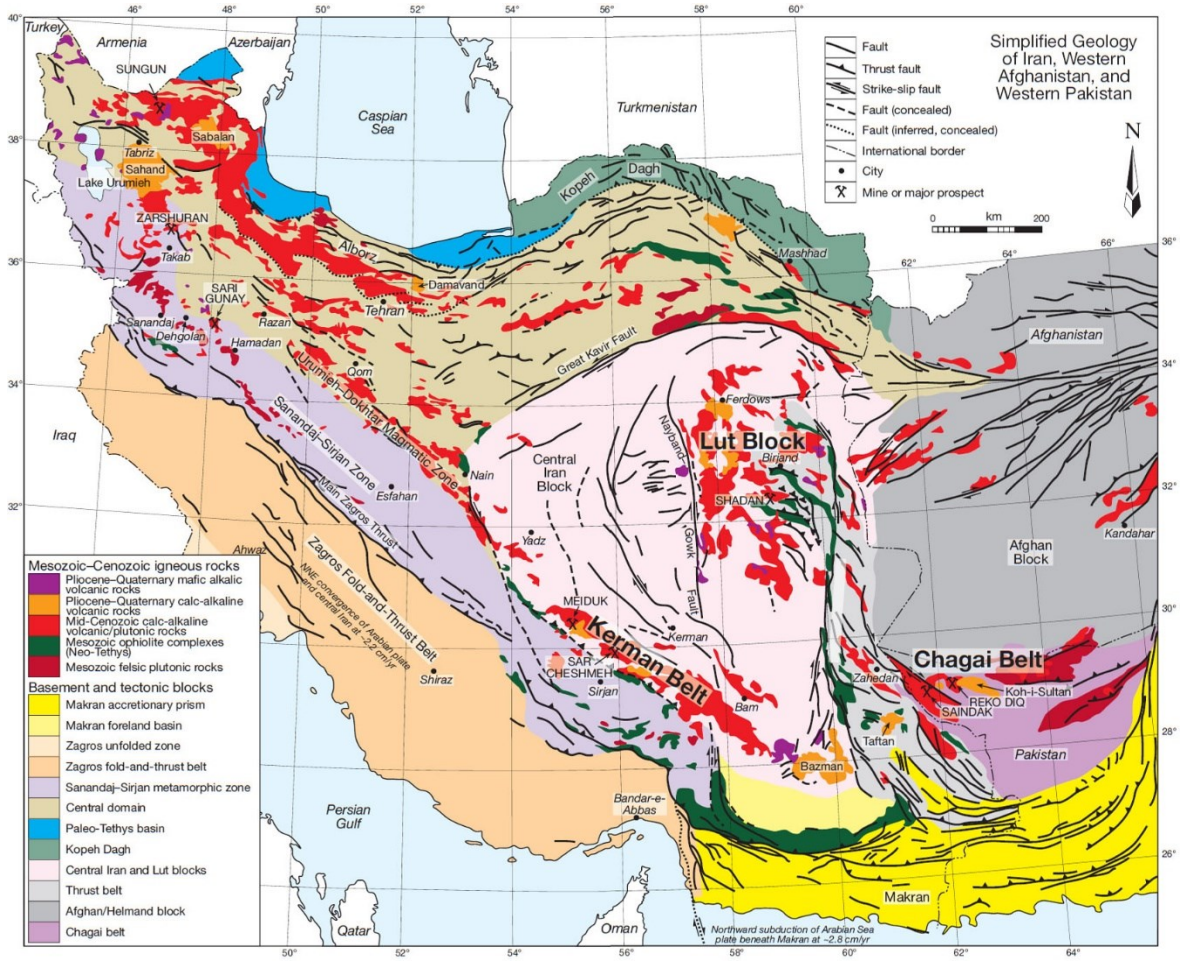

Figure 3: Simplified geology of Iran with parts of western Afghanistan and western Pakistan, highlighting Mesozoic-Cenozoic igneous rocks and ophiolites. Quaternary sediments cover large areas of the region, beneath which basement and other tectonic blocks are inferred. This geological map from Richards et al. (2012) is based on maps from the Geological Survey of Iran (1989, 2009) with additional information from Berberian and King (1981), Mohajjel et al. (2003) and Regard et al. (2005).

2.2.1 Zagros Fold and Thrust Belt (the Southern Unit)

The Zagros Orogen exposed in the Zagros Mountains represents the northeastern edge of the Arabian plate and extends from Bandar Abbas in the south to Kermanshah in the northwest, where its elevation reaches a maximum of 4548 m in the Khuzestan province (Mouthereau et al., 2012). The Zagros Fold and Thrust Belt is built up by Pan-African metamorphic basement overlain by a thick Phanerozoic succession together with remnants of the Neotethys (Berberian and King, 1981). It can be further subdivided into the Zagros Fold Belt, the Zagros Thrust Zone and the Makran, Zabol-Baluch Zone, including the Eastern Iranian Ranges (Mouthereau et al., 2012; Rahmati-Ilkhchi, 2009).

The *Zagros Fold Belt* is characterized by orogen-parallel NW-SE trending regional-scale structures - folds, anticlines and synclines - covering a 200 to 300 km wide zone. It occurs in southwestern Iran and forms the northern margin of the Arabian platform. Caused by flexural slip mechanism the Zagros Fold Belt formed from an up to 12 km thick pile of sedimentary rocks including Paleozoic, Mesozoic and Cenozoic strata (Colman-Sadd, 1978). The sediments were deposited in an extensional and passive margin setting during the Paleozoic and most of the Mesozoic periods. Compression and flexural basin development were induced by the protracted subduction of the Neotethys beneath the Alborz continental

margin in Late Cretaceous times. Consumption of oceanic crust lasted until Early Eocene when the Urumieh-Dokhtar Magmatic Arc started to collide with the magmatic assemblage of the Alborz Mountains (Alavi, 2007; Homke et al., 2009).

The *Zagros Thrust Zone and Zagros Suture,* also known as the High Zagros, represent a narrow zone that occurs along the northeastern margin of the Zagros Fold Belt separated by the High Zagros Fault. The belt consists of an imbricate fault system that comprises a more deeply eroded level exposing Paleozoic rocks close to the Dezful Embayment as well as less deeply eroded mainly Mesozoic rocks around Kermanshah. Structurally, it constitutes the more deformed, internal part of the Zagros Fold and Thrust Belt. The NE-dipping imbricate stack of Early Paleozoic to Early Cenozoic rocks shows a duplex style tectonics controlled by detachments along locally intruded Cambrian salt diapirs. For the High Zagros and part of the adjoining Zagros Fold Belt a minimum shortening of 37 % during the Mesozoic and Cenozoic convergence between the Arabian and Eurasian plate was calculated (Mohajjel and Fergusson, 2014).

The Zagros Suture shows imbrications of thrust units of different tectonic origins including rifted continental blocks, ophiolites and tectonic mélanges. To the north, the High Zagros is bounded by the Main Zagros Thrust, a north steeply-dipping thrust with a southward connection to the hanging wall carrying ultramafic suites of the Kermanshah and Neyriz obducted complexes (Mouthereau et al., 2012). Berberian and King (1981) interpret this as the plate boundary between the folded cover of the Arabian margin to the SW and the upper magmatic-metamorphic belt of central Iran to the NE.

The southeastern continuation of the Zagros Mountains is to be found in the *Makran accretionary wedge*, which stretches from eastern Iran to central Pakistan. It is located to the south of the Jazmourian depression and the Minab fault in the west confines the structural unit together with the Oman sea in the south (Nabavi, 1976). Formed by still ongoing subduction of the Arabian plate underneath Eurasia the Makran accretionary wedge consists largely of sediments scraped off the Arabian plate (Berberian and King, 1981). The accretionary prism still propagates seaward at a rate of approximately 10 mm per year (White, 1982) with an extremely low subduction angle of about 5° (Byrne et al., 1992). Large sections of ophiolite series can be found along the east-west trending faults that dominate the northern part of Makran. Cretaceous to Paleocene ophiolites are the oldest rocks in the Makran area which are overlain by a 5 km thick sequence of sandstone, shale and marl deformed prior to Early Miocene. This series is covered by a sequence of Neogene rock units with a thickness in excess of 5 km (Nabavi, 1976).

The east of Iran comprises flysch and mélange sediments of the *Zabol-Baluch Zone* to the east of the Lut Block. Rock units can be grouped into flyschoid sediments, a series of volcanic, volcano-sedimentary and intrusive rocks, as well as an ophiolitic series (Ghorbani, 2013). These post-Cretaceous flysch to molasse type sediments (Falcon, 1974) were deposited on a basement of oceanic crust and show intense deformation and tectonization. A succession of thick deep-sea sediments, such as argillaceous and silicic shales, radiolarite and pelagic limestone overlay the flyschoid sediments. Volcanic rocks are also present and include, basalt, spilitic basalt, diabase, andesite, dacite, rhyolite and subordinate serpentinized ultramafic rocks.

2.2.2 Cimmerian Blocks (the Central Unit)

This assemblage of several tectonic units represents detached marginal fragments from northern Gondwana (Brunet, 2009) that drifted northward across the Paleotethys during Early Permian to Late Early Triassic (Muttoni et al., 2009). The opening of the Neotethys accreted these Cimmerian Blocks to southern Eurasia in Triassic times (Horton et al., 2008) and caused the Eo-Cimmerian orogeny with the final closure of the Paleozoic Paleotethys ocean (Berberian & King, 1981). The northeast-directed subduction of the Neotethys ocean induced the Middle Cimmerian orogenic event of the Middle Jurassic (Fürsich et al., 2009). The Central Unit comprises major parts of the Zagros Orogen, such as the Sanandaj-Sirjan Zone and the UDMB as well as parts of the Central Iranian Zone and the Alborz Mountains (Rahmati-Ilkhchi, 2009).

2.2.2.1 Sanandaj-Sirjan Zone

Located to the northeast of the Main Zagros Thrust the Sanandaj-Sirjan Zone represents the tectono-magmatic and metamorphic part of the Zagros Mountains with a length of about 1500 km (Rahmati-Ilkhchi, 2009). The zone consists of sedimentary and metamorphic rocks of Paleozoic to Cretaceous age formed at the former active margin of an Iranian microcontinent which collided with the Arabian plate during the Miocene (Berberian and Berberian, 1981). Mohajjel et al. (2003) subdivide the zone into an outer belt of imbricate thrust slices comprising radiolarite, ophiolite and marginal sub-zones consisting of Mesozoic deep-marine sediments, shallow-marine carbonates, oceanic crust and volcanic arcs. The inner complexly deformed sub-zone represents a Late Paleozoic-Mesozoic passive margin succession. In the Late Jurassic to Cretaceous the subduction of the Neotethys resulted in deformation, metamorphism and development of unconformities in the marginal and complexly deformed sub-zones. The Late Cretaceous deformation climax created a major southwest-vergent fold belt associated with greenschist facies metamorphism post-dated by emplacement of abundant Paleogene granitic plutons. Ophiolite emplacement onto the northern Arabian margin occurred in the southwestern Sanandaj-Sirjan Zone due to a Late Cretaceous island arc – passive margin collision. The Zagros suture is located along this discontinuous ophiolite bearing zone at the southwestern margin of the Sanandaj-Sirjan Zone (Mohajjel et al., 2003).

2.2.2.2 Urumieh-Dokhtar Magmatic Belt

Positioned between the Sanandaj-Sirjan Zone and continental blocks of the Central Iranian Zone the Urumieh-Dokhtar Magmatic Belt (UDMB) extends over 2000 km from the NW to the SE of Iran extending parallel to the Zagros Mountains (Alavi, 2007). Voluminous tholeiitic, calc-alkaline, and K-rich magmatic rocks form the magmatic arc of UDMB. Magmatic activity shows migration from the SE to NW and magmatism was mainly active in the Eocene associated with the subduction and closure of the Neotethys followed by the Paleogene to Neogene continent-continent collision (Mohajjel et al., 2003). Episodes of slab retreat or slab rollback forced an extensional magmatic flare-up from 55 to 37 Ma which generated vast amounts of Paleocene-Eocene volcanic rocks (Verdel et al., 2011). The Paleogene volcanics together with the sedimentary rocks reach 3-8 km in thickness indicating subsidence due to back-arc extension (Ballato et al., 2011). In the Oligocene OIB-like magmatism reflects asthenospheric-derived melting (Verdel et al., 2011). The youngest rocks in the UDMB formed

due to breakoff of the Neotethyan slab beneath the Iranian Plateau (Omrani et al., 2008). They mostly consist of alkaline lava flows and pyroclastics of Pliocene and Quaternary age.

The southern segment of the Urumieh-Dokhtar Magmatic Belt is known as Kerman Porphyry Copper Belt (or Kerman Belt, Figure 3) and constitutes the main Cu-bearing region of Iran. The Cenozoic magmatic assemblage forms a 40 to 50 km wide, northwest-southeast trending arc segment extending over 400 km along the southern margin of the central Iranian micro-continent (Mirzaie et al., 2015). The southern structural boundary between the Kerman belt and its ophiolite suture zone is formed by the Nain-Baft thrust, whereas the Rafsanjan strike-slip fault represents the northern separation of the Kerman arc and Central Iran. Geophysical and structural field constraints indicate a collisional northeast-verging fold and thrust belt traversed by cross-cutting dextral strike slip faults (Shafiei et al., 2009). The distinct magmatic history of the Kerman porphyry copper belt and the main Urumieh-Dokhtar Magmatic Belt shows differences that may be related to regional changes in the collisional tectonic setting (Shafiei, 2008). Igneous rock formation of the Kerman Belt happened during the early Eocene when the steep and oblique subduction of the Neotethyan oceanic lithosphere beneath the rotating micro-continent of central Iran initiated the onset of volcanic activity. Mid to Late Eocene basaltic-rhyolitic volcaniclastic sequences followed as well as intrusions of barren granitoids (Dimitrijević, 1973) both showing calc-alkaline and locally tholeiitic affinity, typical for subduction-related island arc settings (Shahabpour, 2007). During the Oligocene, magmatic activity was characterized by mainly high-K calc-alkaline and shoshonitic volcanic complexes and plutonic rocks (Hassanzadeh, 1993). A short interruption of magmatic activity is reflected by Oligocene to Miocene red beds and limestones that overly volcaniclastics and intrusive rocks unconformably (Dimitrijević, 1973). However, magmatism resumed during the Mid-Late Miocene with a second episode of intrusive activity associated with porphyritic ore-hosting granitoids (McInnes et al., 2005) and continued into the Pliocene. The concentration of more felsic rocks in the northwestern and central part of the Kerman Belt indicate a northwestern shift of Neogene magmatism and the production of Pliocene to Quaternary alkali basalts and foidites represent the youngest magmatic activity (Dimitrijević, 1973; Hassanzadeh, 1993).

2.2.2.3 Central Iranian Zone

The Central Iranian Zone comprises a microcontinent consisting of several crustal fragments and is located between the Alborz and Kopeh Dagh ranges in the north and the ranges of Zagros and Makran in the west and south, respectively. The Central Iranian Zone consists of the Central Iran Block in the northeast and three north to south oriented crustal domains, namely from east to west the Lut Block, the Tabas Block and Yazd Block (Masoodi et al., 2013). Upper Cretaceous to Lower Eocene ophiolites partly confine the structural components (Takin, 1972).

The Central Iran Block is situated in the middle of Iran with a triangular shape and borders the Alborz Mountains in the north, the Yazd, Tabas and Lut Blocks in the east and the Sanandaj-Sirjan Zone in the south-southwest (Stöcklin and Nabavi, 1973). Alavi (1991) subdivides the Central Iran Block into the eastern Sabzevar Block and the western Tabriz Qom Belt. The Lut Block extends over 900 km in north-south direction restricted by the Dorooneh fault in the north and the Jazmourian depression in the south. The Nehbandan fault separates the Lut Block from Eastern Iran and the Zabol-Baluch Zone, whereas the western boundary to the Tabas Block is the north-trending Nayband fault and the Shotori Mountains. Between the Tabas and Yazd Blocks the 600 km long and narrow Kashmar-Kerman Tectonic Zone is a

distinct fault bounded zone of Upper Neoproterozoic to Lower Paleozoic metamorphic rock units intruded by Upper Triassic granite-tonalite plutons and overlain by Cenozoic strata series (Masoodi et al., 2013). The Lut Block is covered by Neogene volcanic and continental deposits with widely scattered outcrops of Mesozoic to Paleozoic rocks overlying the metamorphic basement. The succession of the Lut Block is characterized by a low degree of Alpine deformation and shows different lithologies than the Precambrian to Quaternary succession of Central Iran. The Yazd and Tabas Blocks in the west of the Nayband fault show a succession of fault-bounded, graben-like structures. There, horsts expose the metamorphic basement and its Paleozoic cover and the grabens are filled with thick and strongly folded Jurassic to Cretaceous sediments (Stöcklin, 1974b).

2.2.2.4 Alborz Belt

As a 1500 km long mountain system, the Alborz Belt, extends from Azerbaijan to the Caspian Sea in its central part and further to Afghanistan forming a gently sinuous east-west range in the north of Iran (Stöcklin, 1974a). Several successive tectonic events affected this northernmost geological unit of Iran, such as the Eo-Cimmerian orogeny causing Pliocene-Quaternary intracontinental transpression (Allen et al., 2003). The Alborz Belt comprises stratigraphic successions with more than 12 km in thickness, spanning from the Late Precambrian to the Holocene (Alavi, 1991).

2.2.3 The Northern Unit

The Northern Unit is composed of remnants of the Paleotethys and crustal rocks formed at the margins of the Variscan orogen in Central Asia that were overprinted by the Alpine orogeny. A suture separates the Northern Unit from the Cimmerian Blocks. The continental crust includes fragments of Paleozoic oceanic crust and was deformed and consolidated during the early Cimmerian and late Alpine orogenic events (Stöcklin, 1977). According to Rahmati-Ilkhchi (2009) the Northern Unit also includes the South Caspian depression, the northern part of the Iranian suture zone, the Paropamisus, the Western Hindu Kush ranges and the Kopeh Dagh range.

The fold and thrust belt of Kopeh Dagh is an intra continental range that marks the northern limit of the Alpine-Himalayan orogeny in northeastern Iran. The stratigraphic succession of the Kopeh Dagh was deposited in a former basin that developed after the Cimmerian orogeny (Garzanti and Gaetani, 2002) and was covered with a vast continental shelf sea from Middle Jurassic to Oligocene when the onset of uplift within the Kopeh Dagh begun about 30 Ma ago (Berberian and King, 1981; Robert et al., 2014). Overlying the Variscan metamorphosed basement a sequence of continuous marine and continental sediments reaches about 10 km in thickness with no major sedimentary gap or volcanic activities during Jurassic to Oligocene. The sedimentary pile was affected by final Alpine tectonics during Plio- to Pleistocene and therefore provides suitable conditions for accumulation of hydrocarbons (Ghorbani, 2013; Rahmati-Ilkhchi, 2009).

2.3 Metallogeny of Iran

Iran, as a part of the Alpine-Himalayan belt, was affected by several orogenic phases from the Precambrian to the Cenozoic, but especially the Alpine orogeny constitutes an essential period during the metallogenic evolution of the country. Hence, all the major Mesozoic and Cenozoic tectonic units evolved in response to the Alpine-Himalayan orogeny as a result of the Neotethyan subduction. The metallogenetic record of Iran provides a good correlation between the mineralization phases and tectono-magmatic events, which include Pan-African, Hercynian, Early and Late Cimmerian, Laramide, and Middle to Late Alpine. All events played an essential role in the formation of mineral resources (Ghorbani and Momenzadeh, 1995; Momenzadeh and Walther, 1984). A generally accepted metallogenic classification of Iran has not been established yet, but Ghorbani (1999) introduced the following geographic metallogenic provinces: Central Iran, Urumieh-Dokhtar, Sanandaj-Sirjan, Northeast metallogenic province (Taknar, Kavir, Sabzevar Belts), Alborz, Southeast and east of Iran metallogenic province, Zagros oil and gas province and Kopet Dagh oil and gas province (Figure 3).

When considering mining of the various commodities several belts are distinguished in Iran: Malayer-Isfahan lead and zinc belt, Kerman copper belt, Esfandagheh-Faryab chromite ophiolitic belt, Khash-Nehbandan belt (with chromium, copper and magnesium deposits), Qom-Naein belt (with manganese, barite and copper deposits), Kavir-Sabzevar belt (with copper, chromium, gold and iron deposits) and Taknar belt (with copper, gold and arsenic deposits).

These metallogenic provinces and belts of Iran are the result of the above-mentioned orogenic phases and tectono-magmatic events. Based on timing of magmatism, stratigraphy, structural geology as well as the geological evolution of Iran, Ghorbani (2013) classifies the mineralization phases of Iran as follows:

A first mineralization phase during Late Proterozoic to Early Cambrian (800 to 530 Ma) coincided with the Pan-African tectono-magmatic event. During this phase, mineralization included mainly sedimentary and volcano-sedimentary iron deposits (Jafarzadeh et al., 1995), large deposits of lead-zinc associated with submarine volcanic activities, mesothermal gold deposits, high-grade magmatic iron ores of Kiruna-type (Nabatian et al., 2015) and nonmetallic deposits such as salt or sedimentary phosphate (Ghorbani and Momenzadeh, 1994; Ghorbani et al., 2000).

The Lower Paleozoic phase corresponds to the Caledonian tectono-magmatic event and is poor in metallic mineralizations. During the Early Paleozoic mainly deposits of silica and phosphate formed in different regions of Iran, but also smaller copper deposits in the Zagros region are related to this phase. In contrast, the Late Paleozoic to Triassic phase associated with the Hercynian and Early Cimmerian tectono-magmatic events induced the deposition of metallic and nonmetallic ores during the Devonian, Carboniferous, Permian and Early to Middle Triassic in all places of Iran. Mineralization during this phase includes massive sulfide deposits with copper-lead-zinc, volcano-sedimentary iron and iron-manganese deposits, magmatic-hydrothermal lead-zinc-silver occurrences, but also deposits of fireclay, bauxite, phosphate, barite and fluorite (Ghorbani and Momenzadeh, 1994).

During the Jurassic to Early Cretaceous, in the late Cimmerian orogenic phase, extensive magmatism and metamorphism occurred in vast areas of Central and Eastern Iran, particularly in the Sanandaj-Sirjan Zone. This phase was associated with the formation of MVT-type lead-zinc and barite deposits in Lower Cretaceous carbonate rocks (Ghorbani et al., 2000), volcano-sedimentary Mn-bearing iron deposits (Nabatian et al., 2015), granite-related tungsten, gold and tin in east and northwest of Iran as well as the Sanandaj-Sirjan Zone (Ghorbani, 2013). Associated with the Laramide orogeny in the Late Cretaceous to Paleogene, significant ore deposits formed in ophiolite complexes, predominantly chromite deposits in northwest (Gheshlagh, Khoy), northeast (Sabzavar Region) and southeast (Neyriz, Fanouj) Iran, but also deposits of magnesite, manganese as well as massive sulfide deposits of copper, gold and silver. Moreover, occurrences of phosphate and bauxite have been reported from Zagros (Ghorbani and Momenzadeh, 1994).

In the Middle to Late Alpine tectono-magmatic phase during the Neogene to Quaternary the largest and economically most important Iranian ore deposits were formed. These include the porphyry Cu - (± Mo ± Au) deposits hosted in the Urumieh-Dokhtar Magmatic Belt (UDMB), but also those at the southern margin of central Alborz and in northeastern Iran. About 95 % of the known copper deposits of Iran are assigned to this phase. Most of them are found in the southeastern part of UDMB, particularly in the Kerman Porphyry Copper Belt and include some of the largest porphyry Cu deposits of Iran (Ghorbani, 2013). Ore formation related to these phase also includes volcano-sedimentary manganese, magmatic-hydrothermal lead-zinc, magmatic and volcano-sedimentary iron, but also epithermal gold deposits with arsenic, antimony and mercury (Ghorbani, 2009).

Iran, as a geological bridge between Gondwana and Eurasia, and its mineral wealth are to a large extent associated with the formation and closure of the Neotethys. The Neotethyan subduction- and collision-related magmatism along the Laurasian continental margin produced vast amounts of economic valuable deposits including porphyry Cu ± Mo ± Au and related epithermal Au ± Cu deposits representing the predominant mineral deposit type (Richards, 2015). Thus, in the Alpine-Himalayan metallogenic belt, Iran is one of the major copper provinces and the mining of copper is believed to have commenced in the 6th millennium BC (Samani, 1998). During the past 10 years, the National Iranian Copper Industries Company has carried out extensive exploration efforts, especially for porphyry copper deposits. The regional focus was set particularly on the northwestern Arasbaran and the southeastern Kerman regions of the country from where the three largest porphyry copper mines in the country are known, Sar Cheshmeh and Meiduk in Kerman Province and Sungun in eastern Azerbaijan Province (Zuercher et al., 2015). More recently, several other porphyry deposits are in development or have begun operations, including Haft Cheshmeh (Adeli et al., 2014) and Masjed Daghi (Atalou et al., 2017) in the northwestern part as well as Darrehzar (Alizadeh Sevari and Hezarkhani, 2014), Chah-Firuzeh (Hezarkhani, 2009), Taft (Zarasvandi et al., 2005) and Dar Alu in the southeastern part of the country (National Iranian Copper Industries Company, 2012). Limited information regarding exploration is available for the northern Alborz, western Sanandaj-Sirjan, Central Iran and Makran regions and it is concluded that these regions are comparatively underexplored for porphyry copper deposits (Zuercher et al., 2015).

2.4 Major ore deposits in the Kerman Belt

The study area is part of the Kerman Porphyry Copper Belt that hosts some of the world's largest copper deposits. Economic copper mineralization is focused in several major porphyry Cu deposits located along this NW-SE trending belt. Most pre-collisional late Eocene to Oligocene intrusions lack Cu mineralization, but economic porphyry Cu deposits formed coeval with or after the emplacement of collisional Mid to Late Miocene granitoids (Shafiei, 2008). The size of Cu porphyry deposits in the Kerman arc increases from southeast to northwest. The majority of these deposits occurs in a segment characterized by orogenic thickened arc crust with Moho depths of 45 to 55 km (McInnes et al., 2005) and they are concentrated at fault intersections (Förster, 1978).

The two major porphyry deposits in the Kerman region are Sar Cheshmeh (29º 56' 55" N, 55º 52' 28" E) and Meiduk (30°10' 27" N, 55º 10' 8" E). Vein type, base and precious metal deposits are also known in the surroundings of Meiduk. Mineralized quartz veins are not restricted to the investigated Chah-Mesi deposit but are also known from the Latala vein type deposit which is located about 8 km to the north of Meiduk (Padyar et al., 2017). These three deposits are briefly described in the following.

2.4.1 Sar Cheshmeh porphyry deposit

Sar Cheshmeh is a porphyry Cu-Mo-(Au-Ag) deposit (Zuercher et al., 2015) emplaced in several pulses forming a composite Miocene stock of dioritic through granodioritic to quartz-monzonitic composition. The mineralized granodiorites provide K/Ar (fresh biotite) and Rb/Sr (biotite-whole rock pairs) ages of 12.5 ± 0.5 Ma and 12.2 ± 1.2 Ma, respectively (Shahabpour and Kramers, 1987). Hence, Sar Cheshmeh has been referred to as granodiorite-type porphyry deposit (Waterman and Hamilton, 1975). Zuercher et al. (2015) report proven and probable reserve estimates of 1538 Mt at 0.58 wt% Cu, 0.03 wt% Mo, 0.06 g/t Au and 1.14 g/t Ag at a cutoff of 0.25 wt% Cu (Singer et al., 2008). Hydrothermal activity started mainly with molybdenum mineralization and was followed by copper. Mineralization is associated with four main vein types characterized by different mineral associations: (I) quartz + molybdenite + anhydrite ± K-feldspar with minor pyrite, chalcopyrite and bornite; (II) quartz + chalcopyrite + pyrite ± molybdenite ± calcite; (III) quartz + pyrite + calcite ± chalcopyrite ± anhydrite (gypsum) ± molybdenite; (IV) quartz ± calcite ± gypsum ± pyrite ± dolomite. Orthomagmatic fluids of high temperature (350-520 °C) and high salinity (up to 61 wt% NaCl equivalent) produced potassic alteration assemblages (orthoclase-biotite) in the central and deeper parts of the deposit. Contemporaneous propylitic alteration in the peripheral parts is attributed to lower temperature (220-310 °C), Ca-rich, evolved meteoric fluids. Subsequent phyllic alteration resulted from influx of meteoric water into the central part of the system followed by mixing with magmatic fluid and eventually overprinted earlier high-temperature alteration (Hezarkhani, 2006a).

2.4.2 Meiduk porphyry deposit

The Meiduk porphyry Cu-Mo-(Au-Ag) deposit (Zuercher et al., 2015) is associated with a porphyry stock composed of quartz-diorite and granodiorite (Meiduk porphyry) that intruded Eocene volcano-sedimentary rocks in several pulses. Aliani et al. (2009) conclude an emplacement within a tectonic framework of a continental arc during a late orogenic stage of the post-collisional event between the Arabian and Iranian plates. The pluton forms a semi-circular body about 300 m in diameter and is slightly elongated into north-south direction (Hezarkhani, 2008). The supergene and hypogene mineralization has reported proven and probable reserves of 176 Mt with 0.61 wt% Cu, 0.007 wt% Mo, 0.08 g/t Au and 1.80 g/t Ag at a 0.15 wt% cutoff (National Iranian Copper Industries Company, 2012; Zuercher et al., 2015). Two calc-alkaline intrusive phases are associated with porphyry-type mineralization and in contrast to Sar-Cheshmeh, alkali metasomatism at Meiduk produced five distinct hypogene alteration zones in the Meiduk deposit. These include magnetite-rich potassic, potassic, potassic-phyllic, phyllic and propylitic alteration. Ore minerals occur as stockwork and dissemination as well as in nine different generations of veinlets and veins. After Taghipour et al. (2008) veins are classified into (I) M_1-type: magnetite; (II) M_2-type: quartz + magnetite ± chalcopyrite; (III) B_1-type: quartz + anhydrite ± chalcopyrite; (IV) A_1-type: quartz + magnetite + chalcopyrite + anhydrite ± K-feldspar ± pyrite; (V) A_2-type: chalcopyrite + anhydrite; (VI) C-type: quartz + chalcopyrite + anhydrite + pyrite; (VII) B_2-type: quartz + molybdenite ± chalcopyrite ± magnetite ± anhydrite; (VIII) D_1-type: pyrite ± quartz and (IX) D_2-type: quartz + pyrite + anhydrite ± sericite. The timing of sulfide mineralization, determined by Re-Os molybdenite dating, is 12.23 ± 0.07 Ma (Taghipour et al., 2008) and is within error identical with U/Pb zircon ages (McInnes et al., 2005) of the second intrusive phase at Meiduk. High-temperature (380 to 550 °C) and high-salinity (up to 60 wt% NaCl equiv.), liquid-rich fluid inclusions as well as high-temperature (320 to 550 °C), low-salinity, vapor-rich inclusions give evidence of early magmatically derived fluid that boiled episodically (Hezarkhani, 2008). Potassic alteration of the central stock is related to early-stage hydrothermal fluids and peripheral propylitic alteration is the product of liquid-rich, lower temperature (200 to 350 °C), low- to moderate-salinity (1 to 20 wt% NaCl equiv.), Ca-rich, evolved meteoric fluids. Phyllic alteration and copper leaching coincide with the inflow of oxidized, acidic meteoric waters during cooling of the magmatic-hydrothermal system. In the upper part of the phyllic zone, late boiling caused significant copper deposition (Hezarkhani, 2008).

2.4.3 Latala deposit

Similar to Chah-Mesi, the Latala deposit is a vein-type deposit, which is located about 9.5 km north of Chah-Mesi. It consists of quartz veins with sulfide mineralization occurring as open space fillings, minor replacement bodies and hydrothermal breccias. The veins include quartz, carbonate, pyrite, chalcopyrite, sphalerite, galena, bornite and minor sulfosalts, particularly enargite. For the Latala deposit homogenization temperatures of FI ranging from 380 to 131 °C and salinities corresponding to 10.6 to 0.17 wt% NaCl equiv. were reported (Padyar et al., 2017). Fluid inclusion studies determined that the liquid phase belongs to the H_2O-NaCl system, whereas the gas phase is dominated by CO_2 with minor amounts of CO and H_2, indicating reducing conditions associated with ore deposition and a magmatic-hydrothermal fluid source. Base and precious metals deposited at pressures between 200 and 100 bars, corresponding to a depth of less than 1 km. Investigation of sulfur isotopic composition of sulfide

minerals showed variations between -9.8 and -1.0 ‰, and were explained with a magmatic sulfur source. In comparison to Meiduk, the Latala deposit shows similar evolution in respect to P-T paths and fluid composition. Sulfur isotopic ($\delta^{34}S$) analysis of sulfides suggests that magmatic fluid was modified by mixing with circulating meteoric water. The ore-bearing magmatic fluid transported metals from deeper levels through structural pathways to shallow environments. In this context the formation of brittle tectonic structures, such as large-scale ring structures and NE-SW as well as NW-SE striking fault systems as fluid conduits is important (Sadeghi et al., 2008). Thus, Padyar et al. (2017) assumed a direct link between the Latala base metal deposit and the porphyry system of Meiduk, which is further supported by elevated assays of Cu-Au-Mo in Latala.

2.5 Chah-Mesi deposit

Chah-Mesi is situated about 40 km to the northeast of Shahr-e-Babak city in the Kerman region of central Iran and only 1.5 km to the south of the Meiduk porphyry copper mine (Figure 4). In the following chapters a short summary of the previous studies on the Chah-Mesi deposit and its regional geology is given.

2.5.1 Previous studies on Chah-Mesi

Chah-Mesi is characterized as polymetallic Cu-Au vein deposit (Tangestani and Moore, 2002) hosted by rocks of the Middle-Upper Eocene Razak volcanic complex and shallow Oligocene intrusions of intermediate composition. Hosseinkhani (2009) identified an enrichment in LREE relative to HREE in the REE patterns of these rocks and a weak Eu anomaly, features consistent with an arc-related continental margin setting. Both volcanics and porphyritic intrusives are highly faulted and fractured and structural analysis of Shafiei and Ghiyasi (2014) indicates that formation of the NNE-SSW trending main ore veins in the deposit is related to extensional faulting. Minor veins are related to extensional-shear faults postdating the phase of main faulting. Hydrothermal fluid transport along the NNE-SSW and NW-SE trending major fracture system in the area caused the formation of mainly NNE-SSW trending Cu-Pb-Zn bearing quartz veins containing gold. Several smaller quartz veins and four distinct ore-bearing silica veins with 100 to 300 m length and several centimeters to 12 m thickness were determined to constitute the main host to mineralization (Ebadi Rajoli et al., 2015).

Pyrite, chalcopyrite, galena and sphalerite represent the main ore minerals within the mineralized veins. Gold is mainly hosted by pyrite and associated sulfosalt minerals, such as enargite and tetrahedrite-tennantite. Sulfosalts may contain up to 950 ppm Au and 1520 ppm Ag, respectively (Hosseinkhani, 2009). The average ore grade is 1.27 wt% copper, 1.01 wt% lead and 2.12 wt% zinc with minor amounts of silver (10-150 ppm) and gold up to 7 ppm (Ebadi Rajoli et al., 2015; Omaljev, 1972). Ebadi Rajoli et al. (2015) distinguished different populations of mineralized veins and reported up to 2.24 wt% Cu for the highly mineralized veins. Au values range from 0.08 to 3.54 ppm. Hosseinkhani (2009) reported $\delta^{18}O$ values of fluid in equilibrium with quartz ranging between +1.9 and +6.04 ‰ suggesting a magmatic fluid source that was mixed with meteoric waters. The $\delta^{18}O$ and δD values of fluid in equilibrium with sericite range from -5.2 to -9.6 ‰, and from -95.5 to -108.5 ‰, respectively. Hence, the oxygen and hydrogen isotope composition indicate meteoric water as the source of fluids that caused sericitic alteration.

2.5.2 Geology of the Chah-Mesi deposit

The regional geology of Chah-Mesi comprises faulted and gently folded country rocks with Cenomanian-Turonian calcareous flysch as the oldest rock formation (Figure 4 and Figure 5). Cretaceous flysch sediments are unconformably overlain by Paleocene Kerman conglomerate and covered by Eocene flysch (Dimitrijević, 1973; Saric et al., 1971). These units are exposed in the core zone of a NW-trending anticline and were cross-cut by three Paleogene volcanic complexes occurring mostly in the western limb of the fold (Hezarkhani, 2006a). In the area of Chah-Mesi the oldest complex, the *Bahraseman volcanic complex*, has a thickness of 400-500 m and was formed during the Lower Eocene by an initially explosive phase of acidic volcanism producing pyroclastic rocks (tuffs and volcanic breccias) and rhyolite lava flows. The overlying Middle-Upper Eocene *Razak volcanic complex* hosts the Meiduk porphyry deposit and is subdivided into three units. The lower subcomplex consists of trachybasalt, andesite and trachyandesite, the middle subcomplex is built up mainly by acidic tuffs. The upper subcomplex includes a succession of trachyandesite and andesite-basalt (Dimitrijević, 1973). $^{40}Ar/^{39}Ar$ dating of albite from the lower subcomplex yielded an age of 37.5 ± 1.4 Ma (Hassanzadeh, 1993). The third and highest complex, the *Hezar volcanic complex* is of Oligocene age and was dated at 32.7 ± 6.3 Ma (Hassanzadeh, 1993). It covers large parts of the western area and mainly consists of trachyandesite and trachybasalt (Saric et al., 1971).

Neogene intrusions close to Chah-Mesi were emplaced in several phases during the Miocene to Pliocene. Miocene intrusions which are associated with porphyry copper mineralization at Meiduk intruded these Eocene to Oligocene volcanic complexes. These shallowly emplaced stocks of granodiorite-tonalite to diorite and quartz-diorite are partly covered by Late Miocene-Pliocene volcanic and subvolcanic rocks that are located southeast of the Masahim stratovolcano. The youngest subvolcanic and volcanic activity started during the Pliocene and created dacitic domes, lava plugs and the Masahim stratovolcano at around 6.8 ± 0.4 to 7.5 ± 0.1 Ma (Hassanzadeh, 1993; McInnes et al., 2005). The Chah-Mesi and Meiduk deposits are located in a basin that is confined within the curved, north-facing U-shaped ridge of Kuh e La Chah (La Chah Mountain) the latter reaching elevations of 2700-2850 m a.s.l. La Chah Mountain is built up by extrusive rocks of the Razak volcanogenic complex. This area has been in focus of mineral exploration since ancient time. However, porphyry mineralization was recognized only after discovery of Sar-Cheshmeh in the 1970s (Hezarkhani, 2008).

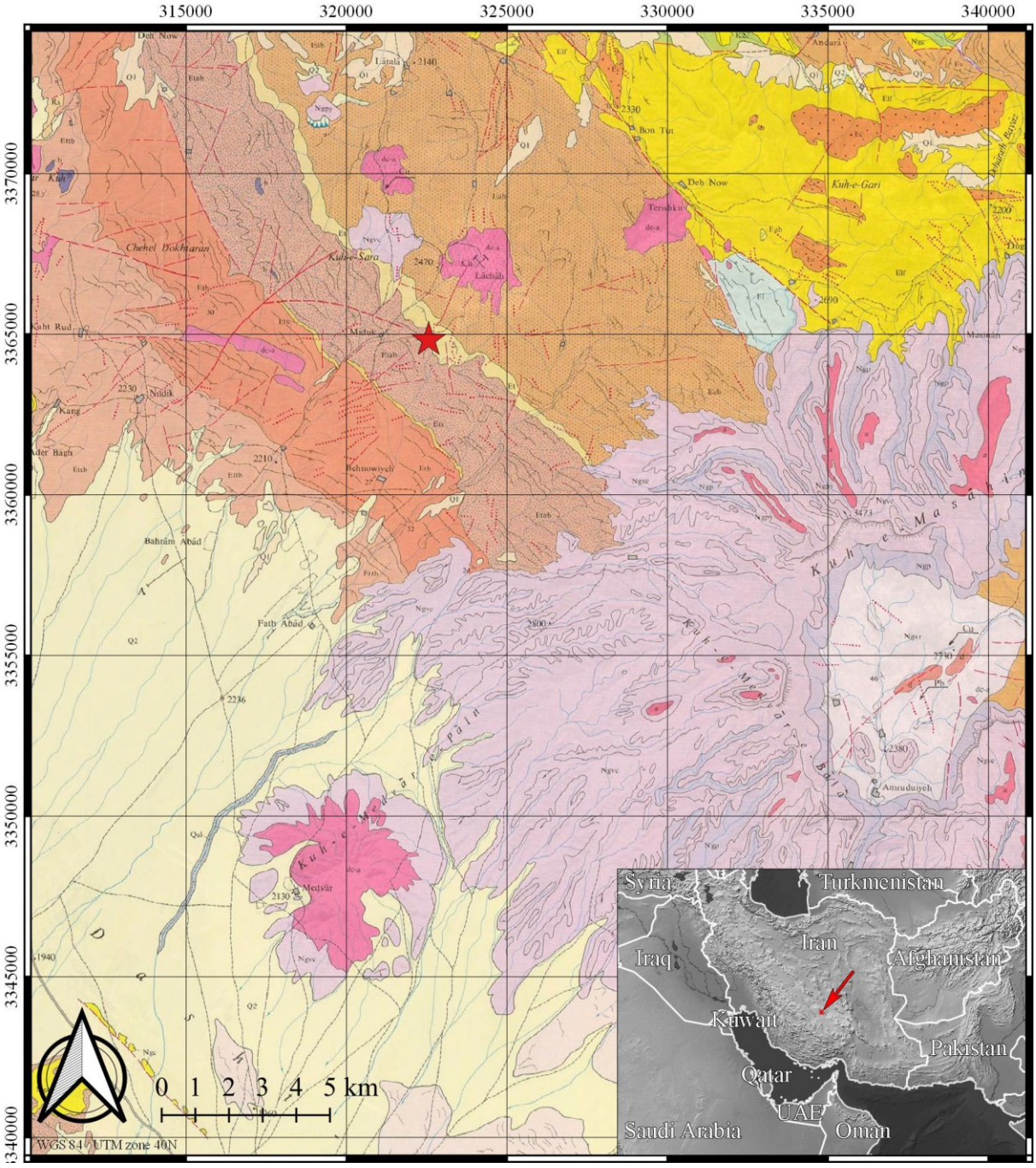

Figure 4: Geological map of Shahr-e-Babak area after Saric et al. (1971). The location of Chah-Mesi is marked with a red star. Inset shows topography and location of the study area (red arrow); made with Natural Earth. Free vector and raster map data @ naturalearthdata.com. For legend see Figure 5.

Figure 5: Legend of the geological map of Shahr-e-Babak shown in Figure 4; after Saric et al. (1971).

2.5.3 Field observations

The Chah-Mesi open pit extends from north to south over a length of 280 m with a width of approximately 110 m (Figure 7) and was mined to a lowest level of 2488/2487 m a.s.l. The northern part consists of three mining benches each about 8 m in height and slope inclinations between 60 to 70° (Figure 6). Andesites are the dominating lithology and show 10 to 20 cm thick layering that dips steeply to the southeast to southwest (145/70 – 245/40, Figure 8 a), respectively. In the northeastern section of the open pit, a NNE-SSW trending 5 m thick microdiorite dyke was documented, which intruded the layered andesites almost vertically (Figure 9 c). The whole area of Chah-Mesi is characterized by several meters thick fault zones with strike directions of NNE-SSW and lengths of more than 100 m. Along the eastern slope, the open pit is dissected by two prominent fault zones with intense silicification of up to 10 m thickness (Figure 8 c, d). These structures are associated with mineralized silica veins and veinlets (Figure 8 b). The host rocks adjacent to the fault zones are strongly leached and largely replaced by silica with typical vuggy silica textures. Commonly, outcropping quartz veins are coated by colorful crusts of secondary minerals including Cu-carbonate hydroxides and Fe-oxyhydroxides (Figure 8 e).

On the small hill to the south of the Chah-Mesi mine, thin veinlets of whiteish to slightly greenish color were observed with steep dip directions towards the north (Figure 9 a). These veinlets were found again in the western outside area of the open pit. There, they were crosscut by calcite-rich veinlets with almost vertical inclination and N-S strike direction (Figure 9 b).

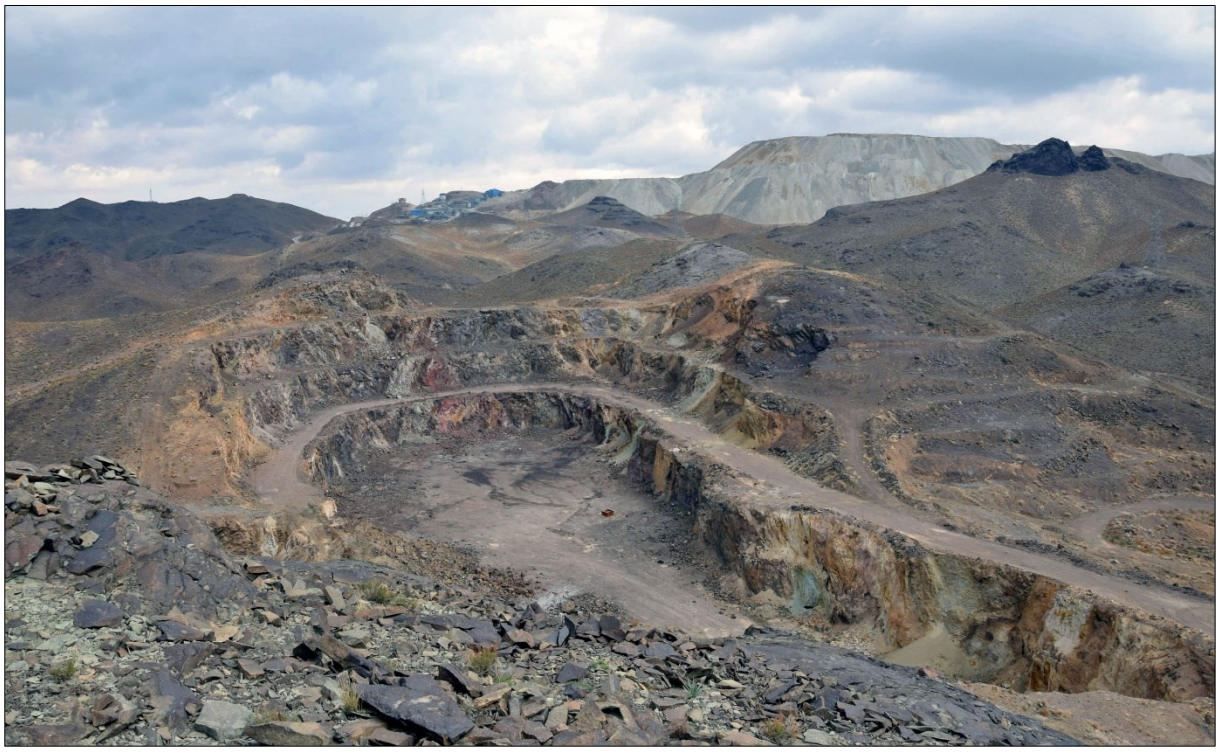

Figure 6: Overview of the Chah-Mesi open pit with the Meiduk mine dump (background) at a distance of 1.5 km to the north. The northern slope of the open pit consists of three mining levels with about 8 m bench height and 60 to 70° face angles. The lowest level is situated at around 2488/2487 m a.s.l. and the eastern slope partly follows a mineralized fault zone (Photo: J.G Raith, 2018).

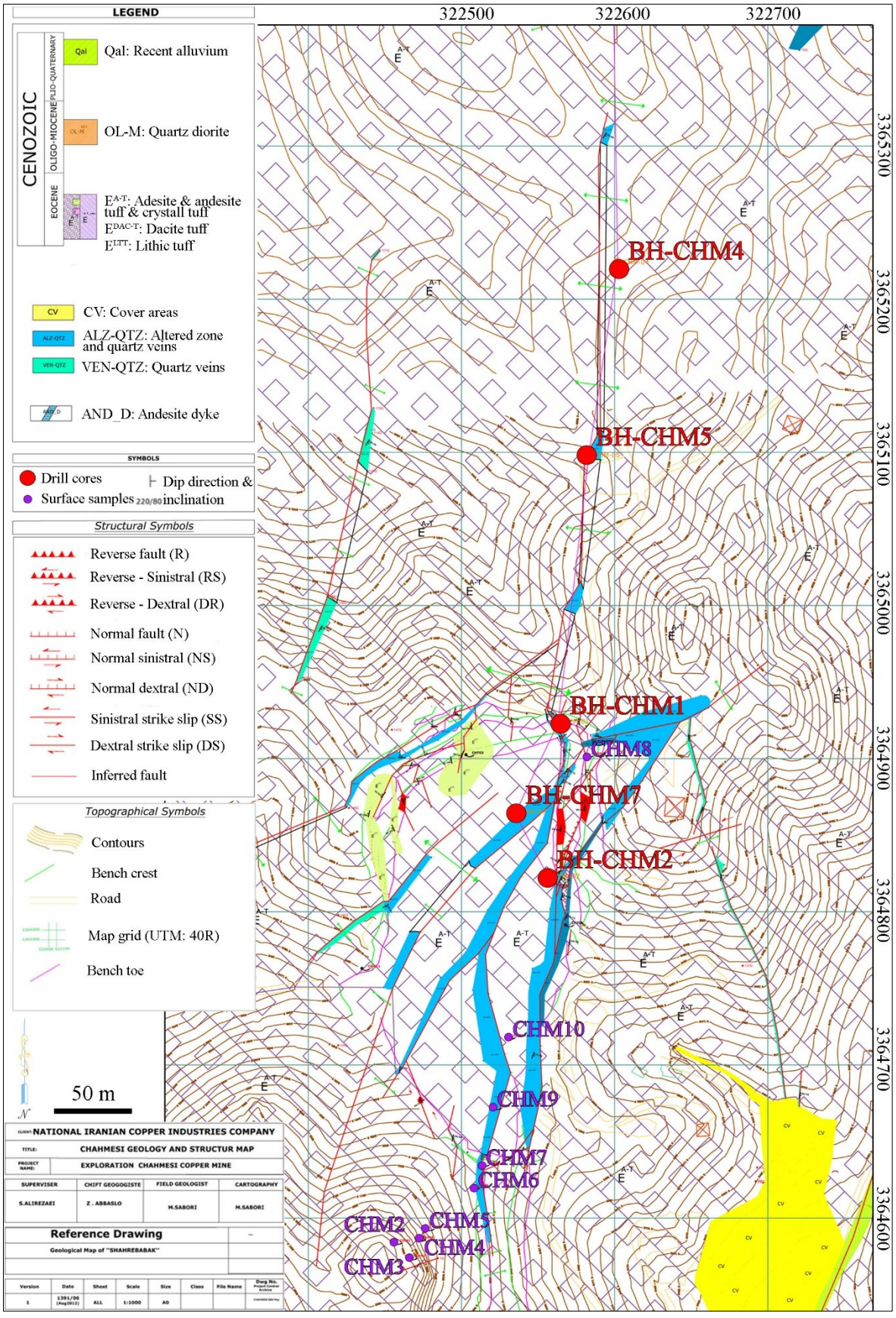

Figure 7: Location map of the study area at Chah-Mesi open pit showing sample and drill core (prefix BH-) locations (see Table 1 and Table 2). Modified after the geological and structural map of the Iranian National Copper Industries Company, 2012.

Superficial alteration is dominated by argillic alteration and extends over wide areas even beyond the open pit of Chah-Mesi. Argillic alteration is characterized by intense decomposition of the country rocks into clay minerals and limonitic aggregates. Colors of weathered rocks are typically white and tan with a dark brown to orange oxidized outer surface (Figure 9 d). Towards the peripheral parts of the mining area, argillic alteration turns into propylitic alteration, which is indicated by a color change of country rocks into a greenish-grey (Figure 9 a).

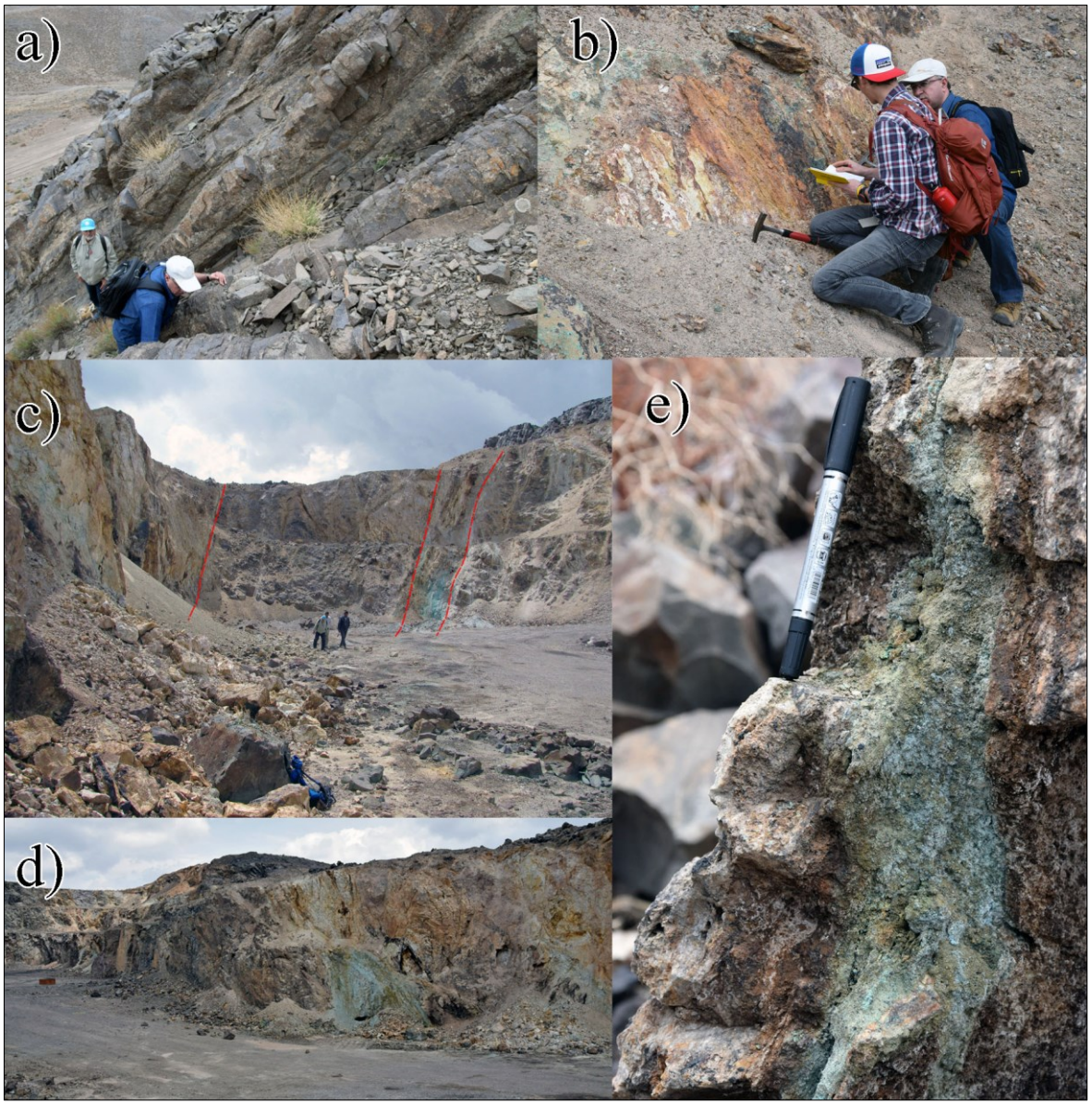

Figure 8: Photographs from the Chah-Mesi field area. a) Layers of andesite dipping into southeastern direction; b) Outcrop of a NNE-SSW trending, about 2 m thick mineralized stained quartz vein; c) Two steeply ESE dipping (248/74 – 251/84) massive mineralized quartz veins (outlined in red) in the southern part of the open pit; d) the almost subvertical eastern slope of the open pit following the mineralized (green staining) big vein structure; e) Detail of replaced wallrock showing strong silicification with vuggy texture. The adjacent altered host rock contains secondary minerals formed due to supergene weathering: Cu-carbonate hydroxides (greenish-blue) and Fe-oxyhydroxides (reddish-brown).

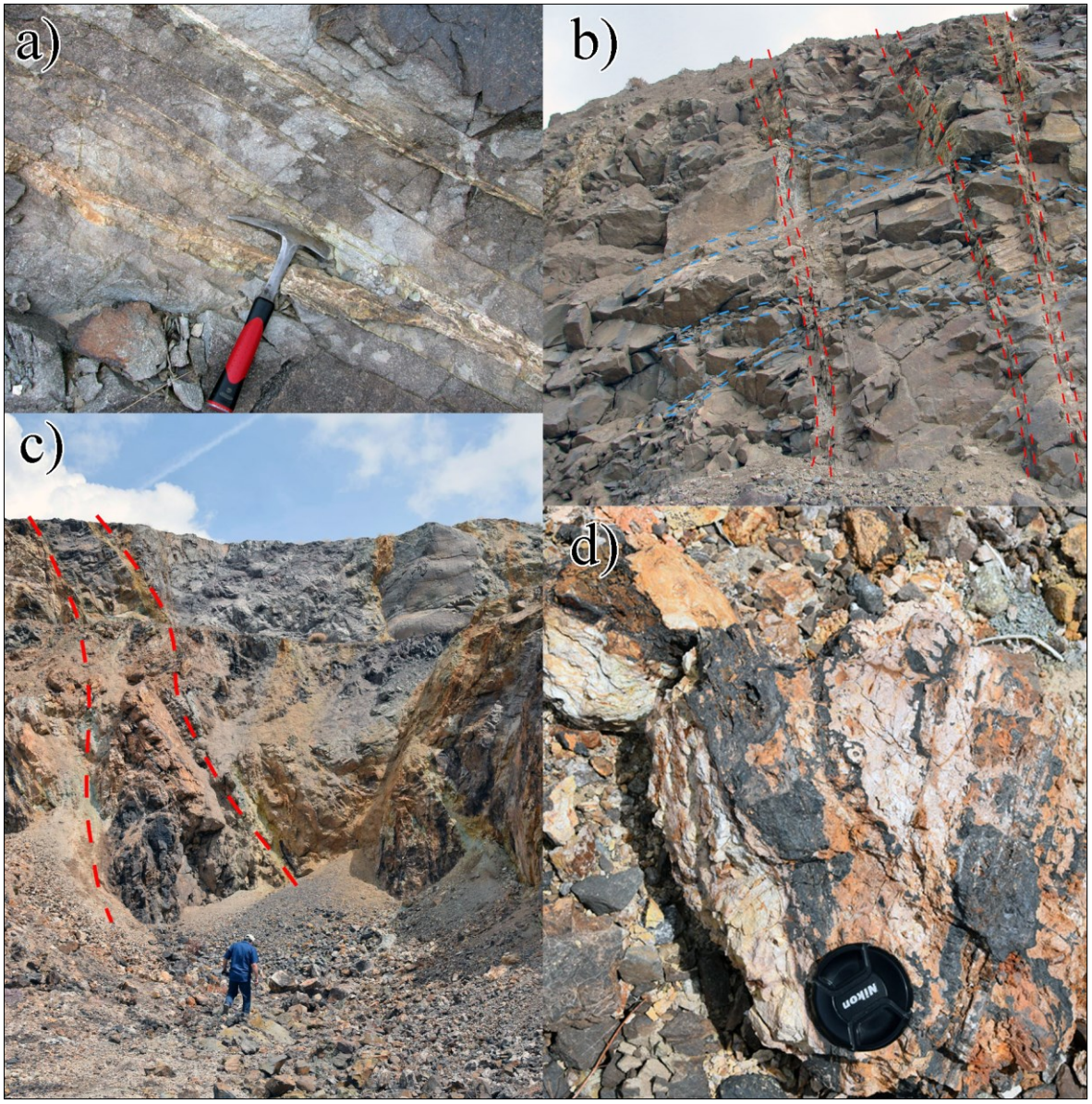

Figure 9: Photographs from the Chah-Mesi field area. a) Sheeted PCE-type veins dipping to the north (357/56) exposed at the small hill south to the Chah-Mesi open pit; b) Subvertical CC-type veins with ±N-S strike direction crosscutting PCE-type veinlets in the western part of the deposit; c) An approximately 5 m thick microdiorite dyke (outlined in red) crosscutting andesitic host rocks in the northeastern part of the open pit; d) Intense decomposition of the host rocks due to argillic alteration on the surface. For vein terminology see text.

3 Methods

In order to answer the scientific questions of this project outlined in chapter 1, the focus of sampling and analysis was mainly on mineralized veins and adjacent wallrocks. A detailed mineralogical investigation was done on samples taken from outcrops in the Chah-Mesi open pit mine and from drill cores. Methods included transmitted and reflected light microscopy of thin and polished sections combined with mineral chemical analysis by electron microprobe techniques focusing on the ore minerals particularly the sulfosalts. Mineralogical investigations were complemented by a preliminary fluid inclusion study.

3.1 Sampling

In total, eighty-seven samples of altered wallrock and different vein types from the polymetallic Chah-Mesi deposit were collected from surface outcrops and drill cores. The cores are from exploration drillings made by National Iranian Copper Industries Company in the period of January to April 2007. The cores are stored at the NICICO drill core stock in Rafsanjan about 80 km to the east of Meiduk Copper Mine. Seventy-five samples were gathered from five drill cores (Table 1). Selective sampling focused mainly on vein core intercepts and adjacent wallrocks. Representative material was collected for detailed investigation of the ore mineralogy as well as the alteration. Several samples were also taken from non-mineralized core to study the petrography of the host rock and the alteration. Regarding the location of the drill cores, the original bore holes were aligned north to south and encompass an about 400 m long profile extending from the small hill to the south of Chah-Mesi to the northernmost borehole with a distance of 1100 m to the Meiduk open pit (Figure 4 and Figure 7). Information about the geographic position of the drill holes is summarized in Table 1.

Table 1: Data of drill holes at Chah-Mesi sampled for this project (National Iranian Copper Ind. Co.)

Hole id	Coordinates (WGS84 – UTM:40R)			Depth (m)	Inclination
	x	y	m a.s.l.		
BH-CHM1	3364923	322563	2487	195.05	70° - NW
BH-CHM2	3364822	322558	2488	200.00	70° - NW
BH-CHM4	3365223	322602	2506	188.35	70° - NW
BH-CHM5	3365097	322584	2511	135.45	75° - NW
BH-CHM7	3364864	322535	2492	150.25	75° - SW

Samples were also gathered during the mine visit from eleven different locations to sample those parts of Chah-Mesi exposed at the surface. Large samples of several kilograms were collected in the field, but much of this material was processed in the laboratories at Shahid Chamran University of Ahvaz. There, it was cut and for easier transportation representative smaller samples (slabs) were taken; the remaining material was archived at SCU. At Montanuniversität Leoben polished sections and polished thin sections were prepared of 59 samples including two sections for fluid inclusion investigation.

Table 2: Data of surface samples at Chah-Mesi sampled for this project

Location	Coordinates (WGS84 – UTM:40R)		
	x	y	m a.s.l.
1	322580	3364486	2474
2	322456	3364584	2532
3	322466	3364574	2529
4	322471	3364586	2521
5	322477	3364593	2516
6	322507	3364620	2501
7	322513	3364635	2500
8	3364902	322581	2499
9	3364672	322521	2488
10	3364718	322530	2488

The spatial spectrum of samples collected along the north to south extending profile of boreholes and from the open pit represents different distances and depths from the porphyry intrusion. This sample set allows the characterization of lateral compositional variations of ore minerals from North to South at Chah-Mesi and the identification of the chemical zoning from the surface down to the bottom of the deposit along the sampled drill cores.

Specimen-designation consists of a combination of the sampled drill core number (Table 1) and is followed by the depth from where it was collected; i.e. from drill core BH-CHM1 in 52 m depth sample CHM1-52 was taken. Surface samples have a chronological numbering starting with CHM1 for sampling location 1 (Table 2) and so on. If several samples were taken the designation has an additional numbering, which is separated by a dot; i.e. the first sample of location 8 was named CHM8.1.

3.2 Optical microscopy

After the macroscopic description of the hand specimens, the ore mineralogy as well as the petrographic characterization of the host lithologies was examined with a standard polarization microscope under reflected and transmitted light, respectively. The microscopes used were Olympus BX 40, Zeiss Axio Scope.A1, Zeiss Photomicroscope III. Photomicrographs were taken using a Canon EOS 450D digital camera and digital processing of the RAW pictures was done in Adobe Photoshop CS3. Opaque ore minerals and ore textures were identified and studied in reflected light. For the petrographic study of the igneous host rocks and alteration transmitted light microscopy was used.

3.3 Electron probe micro analysis (EPMA)

The chemical composition of the ore minerals was analyzed by EPMA focusing on the sulfides and sulfosalts and the distribution of precious metals in these phases. In addition to fahlore-group minerals, enargite/luzonite-famatinite, chalcocite and covellite were analyzed regarding precious metal distribution. Minor amounts of gold and submicroscopic Ag-bearing sulfides enclosed in pyrite and sulfosalts were also analyzed. Analyses were done with a JEOL JXA-8200 SuperProbe Electron Probe Microanalyzer at the Eugen F. Stumpfl Microprobe Laboratory at Montanuniversität Leoben, Austria. The electron microprobe operated at acceleration voltage 15 kV and 20 kV, current intensity 10 nA, and the beam diameter was set in focused mode to around 1 µm. Quantitative measurements were performed using a wavelength-dispersive system (WDS). The exact measurement conditions are summarized in Table 3 and Table 4. Analysis data was corrected for matrix effects by the ZAF-method.

Table 3: EPMA measurement conditions and standards for Sulfosalt2 analyses (02.10.2018 – 04.10.2018 and 13.11.2018 – 15.10.2018)

Sulfosalt2		**Acceleration voltage: 20 kV**			**Beam current: 10 nA**	
Element	Crystal	Line	Counting time peak [s]	Counting time background [s]	Standard	Detection limit [ppm]
As	TAP	*Lα*	20	10	$CoAs_3$	29.5±2.2
S	PETJ	*Kα*	20	10	CuS	7.4±0.8
Sb	PETJ	*Lα*	20	10	Sb_2S_3	20.5±3.5
Zn	LIFH	*Kα*	20	10	ZnS	85.4±3.5
Cu	LIFH	*Kα*	20	10	CuS	62.3±5.7
Ag	PETJ	*Lα*	60	30	100 % Ag	9.6±1.3
Fe	LIFH	*Kα*	20	10	$CuFeS_2$	30.8±2.7

Table 4: EPMA measurement conditions and standards for gold analyses (15.11.2018)

Gold		**Acceleration voltage: 20 kV**			**Beam current: 10 nA**	
Element	Crystal	Line	Counting time peak [s]	Counting time background [s]	Standard	Detection limit [ppm]
Au	PETJ	*Mα*	20	10	$AuTe_2$	8.8±0.6
Ag	PETJ	*Lα*	20	10	$AgBiSe_2$	16.9±0.9
Cu	LIFH	*Kα*	20	10	CuS	144.0±4.6

3.4 Fluid inclusion measurements

The fluid inclusion study focused on mineralized quartz-carbonate veins. Samples containing fluid inclusions that were trapped during ore formation were found in several sections providing ore-gangue assemblages with transparent sphalerite and euhedral cogenetic quartz grains. After careful fluid inclusion petrography few samples were selected for further measurements. Microthermometric measurements of the fluid inclusion assemblages were performed using a Linkam MDS 600 heating and freezing stage mounted on an Olympus BX 60 microscope adapted for the use with infra-red and transmitted-visible light. Chemical species within fluid inclusions were identified using a HORIBA LabRAM HR Evolution confocal-Raman spectrometer equipped with a frequency-doubled Nd-YAG laser (100 mW, 532 nm) and diffraction gratings of 1800 grooves mm^{-1}. Detection is with a Peltier-cooled, slow-scan, CCD matrix detector. Laser focusing and sample viewing are performed through an Olympus BX 40 microscope fitted with a 100x objective lens. The spot size has a diameter of about 1 µm, the resolution of the spectroscope is 0.2 cm^{-1}. The power of the laser can be reduced by density filters to about 1, 0.1 and 0.01 mW.

Fluid inclusion investigation allowed determination of the physical state of the fluid (single- vs. two-phase), the type of fluid system (H_2O-NaCl, presence or absence of condensed gases such as CO_2), fluid salinity and fluid density. In case of fluid entrapment in the two-phase field, the study provided information about pressure and temperature of entrapment. In order to determine the temperature of homogenization (T_h), the temperature of ice melting ($T_{m(ice)}$) as well as the temperature of ice nucleation during freezing ($T_{n(ice)}$) (Bakker, 2011), microthermometric studies were carried out on several grains of quartz and sphalerite. The investigation focused on different type of veins to compare the individual information of hydrothermal fluids and find out possible differences in the conditions of formation. The heating rate was approximately 3 °C/min near the temperatures of phase transitions. Data processing was done with the program AqSo_NaCl (Bakker, 2018). The software allows to calculate pressure – molar volume – temperature – composition (p-V-T-x) properties, enthalpy and heat capacity of the binary H_2O-NaCl system. The obtained microthermometric data (i.e. T_h and $T_{m(ice)}$) were used to calculate bulk fluid properties of fluid inclusions, such as salinity (NaCl wt% equivalent), density (g/cm^3) and pressure at homogenization (MPa).

4 Petrography

Polished and petrographic thin sections of selected samples were studied to determine the mineralogy and texture of the occurring lithologies. Several volcanic and intrusive rocks were distinguished petrographically and it was tried to correlate these lithologies in the drill cores studied. Due to presence of fluids of multiple mineralization events the host rocks display a distinct alteration overprint. For simplification, petrographic description of the country rocks is based on their primary mineralogy as far as possible. The vein types were classified based on textural features as well as ore and gangue mineralogy and described separately (Chapter 4.2). Also, alteration is described separately (Chapter 4.3). A summary of the studied samples with remarks on the observed host rocks and occurring vein types as well as hydrothermal alteration types is given in Table 5.

Table 5: List of samples used for petrographic and ore mineralogical studies; samples with prefix BH- are from drill cores; for vein terminology see Chapter 4.2; DP…petrographic (glass-covered) thin section, PD…polished thin section, A…polished section, FI…fluid inclusion section

Sample	Notes	Section	Veins	Alteration
		BH-CHM1		
CHM1-5	Andesite, porphyritic (large plag phenocrysts)	DP	D_1-type	argillic
CHM1-7	Andesite, porphyritic (large plag.-pheno.)	DP	D_1-type	argillic
CHM1-19.4	Andesite, porphyritic	DP	-	sericitic
CHM1-44	Cu-ore: py>ccp>enr>sp>gn>cv-chc	A	O-type (massive)	silicic
CHM1-45	Andesite	PD	QCS-, O-type (banded)	adv. argillic
CHM1-52	Cu-ore: py>ccp>enr>fh>cv-chc	A	O-type (massive)	silicic
CHM1-55.7	Cu-ore: py>ccp>enr>fh>cv-chc>bn	A	O-type (massive)	silicic
CHM1-59	Cu-Pb-Zn-ore: py>ccp>sp>gn>enr>goe	A	O-type (massive)	silicic
CHM1-62	Cu-ore: py>ccp, mainly py (incl.-rich)	A	O-type (massive)	silicic
CHM1-108	Basaltic andesite, vitrophyric-amygoidal	PD	CC-type	propylitic
CHM1-115	Basaltic andesite, porphyritic	PD	-	propylitic
CHM1-116.5	Andesite, trachytic-porphyritic	PD	-	propylitic
CHM1-157	Lithic pyroclastite, coarse comp. ~ 1 cm	PD	-	propylitic
CHM1-159	Pb-Zn-ore: sp>gn>ccp>enr	A	O-type (crustiform)	-
CHM1-160	Pb-Zn-ore: sp>gn>py>ccp>enr	A	O-type (crustiform)	-
CHM1-164	Lithic pyroclastite, dacitic? coarse comp.	PD	-	propylitic
CHM1-172	Lithic pyroclastite, fine comp.	PD	QCS-, CC-type	ser.-prop.?
CHM1-178	Ignimbrite? large pheno.	PD	-	propylitic
		BH-CHM2		
CHM2-16.5	Andesite, porphyritic	PD	-	sericitic
CHM2-21	Andesite, porphyritic	PD	-	sericitic
CHM2-32.5	Andesite, porphyritic	PD	O- (crustiform), CC-type	sericitic?
CHM2-39.5	Pb-Zn-ore: sp>gn>ccp>py>enr>fh, Sb-rich	A	O-type	adv. argillic
CHM2-60	Andesite, porphyritic	PD	-	propylitic
CHM2-67	Pb-Zn-ore: py>sp>gn>ccp>enr>fh	A	O-type (banded)	-
CHM2-68.5	Cu-Pb-Zn-ore: py>ccp>sp>gn>fh	PD, FI	O-type (banded)	adv. argillic
CHM2-69	Cu-ore: ccp>py>sp>gn>enr>fh>chc-cv	A	O-type (ginguro)	-
CHM2-72	Andesite, trachytic	PD	-	sericitic
CHM2-81	Andesite, breccia veinlet, Pb-Zn-ore:sp>gn	PD	O-type (breccia)	adv. argillic
CHM2-89	Cu-Pb-Zn-ore: py>sp>gn>ccp>enr>fh	A	O-type (banded)	-
CHM2-89.5	Andesite, porphyritic	PD	O- (banded), CC-type	sericitic
CHM2-92	Pb-Zn-ore: py>sp>ccp>gn>fh>enr>cc-cv	A	O-type (banded)	-
CHM2-119	Andesite, trachytic-porphyritic	PD	QCS-, CC-type	sericitic
CHM2-136	Breccia, pyroclastic components, Cu-Pb-Zn-ore	PD	O-type (breccia)	adv. argillic
CHM2-148	Pyroclastic rock, lapilli-tuff?	PD	CC-type	propylitic

BH-CHM4				
CHM4-20	Andesite, glomerophyric biotite alteration	PD	B_2, D_1-type	potassic
CHM4-36	basaltic Andesite	PD	CC-type	sericitic
CHM4-49	Pb-Zn-ore: goe>sp>py>gn, oxidized	A	O-type (banded)	adv. argillic
CHM4-50	Andesite, porphyritic, amygdaloidal	PD	CC-type	sericitic
CHM4-51	Andesite, (basaltic?)	PD	CC-type	sericitic
CHM4-59	Cu-Pb-Zn-ore: py>ccp>sp>gn>enr>fh	A	O-type (banded)	-
CHM4-117	Basaltic andesite, amygdaloidal, brecciated	PD	CC-type	sericitic
CHM4-122.5	Andesite (basaltic?), amygdaloidal	PD	CC-type	sericitic
CHM4-136	Andesite, porphyritic	PD	QCS-, CC-type	ser.-prop.?
CHM4-142	Lithic pyroclastics,	PD	QCS-, CC-type	propylitic
CHM4-146	Pyroclastics with tuff vein?	PD	CC-type	propylitic
BH-CHM7				
CHM7-23.7	Cu-Fe-(Pb-Zn)-ore: py>ccp>fh>sp>gn>cv, Au	A	O-type (ginguro)	adv. argillic?
CHM7-31.4	Cu-Fe-Pb-Zn-ore: py>ccp>fh>sp>gn	A	O-type (ginguro)	adv. argillic
CHM7-52	Pb-Zn-(Cu-Fe)-ore: sp-gn-py-ccp-enr-fh	FI	O-type (crustiform)	sericitic
CHM7-94	Pb-Zn-(Cu-Fe)-ore: sp>gn>py>ccp>enr>fh	PD	O-type (crustiform)	sericitic
Surface samples				
CHM1B	Pb-Zn-Cu-ore: sp>gn>ccp>py>fh>enr>cv	A	O-type (banded)	propylitic
CHM2A	Andesite, vitrophyric	PD	-	propylitic
CHM3B	Prehnite, epidote-zoisite, calcite, native Cu	PD	PCE-type	propylitic
CHM6C	Cu-Fe-ore: py>ccp>chc-cv	A	O-type (massive)	silicic
CHM8B	Microdiorite, porphyritc	PD	QCS-type	ser.-prop.
CHM8.1A	Pb-Zn-Fe-Cu-ore: sp>gn>py>ccp	A	O-type (banded)	-
CHM8.2C	Cu-Fe-ore: py>ccp>enr/luz>chc-cv	A	O-type (massive)	-
CHM9A	Cu-Fe-ore: py>ccp>enr/luz>chc-cv	A	O-type (massive)	silicic
CHM10A	Cu-Fe-(Zn)-ore: py>ccp>enr>fh>sp>chc-cv	A	O-type (massive)	-
CHM10D	Andesite (basaltic?), porphyritic-trachytic	PD	-	sericitic

4.1 Host rocks

The Chah-Mesi deposit is hosted by a succession of intermediate volcanic and pyroclastic rocks with minor intrusive rocks. The footwall constitutes lithic pyroclastic rocks, consisting mainly of volcanic rock components, with likely dacitic composition and minor intercalations of ignimbrites. A more than 100 m thick sequence of andesites represents the hanging wall of the deposit and it also occupies large areas on the surface. Andesites show different textures and modal mineralogical composition. Towards deeper levels, andesite grades into basaltic andesite. A younger magmatic event is indicated by a mainly fine-grained, porphyritic intrusion of microdiorite in the northern part of the deposit (Chapter 2.5.3). The microdiorite forms 3 to 4 m thick dykes which likely crosscut the whole volcanic succession. Mineralization is hosted mostly by andesites and to minor extent by pyroclastic rocks. The microdiorite is completely barren.

4.1.1 Microdiorite

The microdiorite is an intermediate, subvolcanic rock with a porphyritic fabric. This rock was observed on the surface as intrusive dyke in the northern part of the deposit and in drill core BH-CHM5 in about 38.5 m depth. The dyke likely cuts all other lithologies, therefore it is defined as the youngest magmatic phase in the investigated area although it still shows alteration. The hand specimen shows a massive, weakly weathered rock of dark grey color with a slight greenish discoloration (Figure 10 a). Macroscopically, the porphyritic texture comprises two distinct grain sizes; the fine-grained groundmass encloses homogeneously disseminated phenocrysts of burgundy to beige color mostly between 0.5 and 1 mm in size.

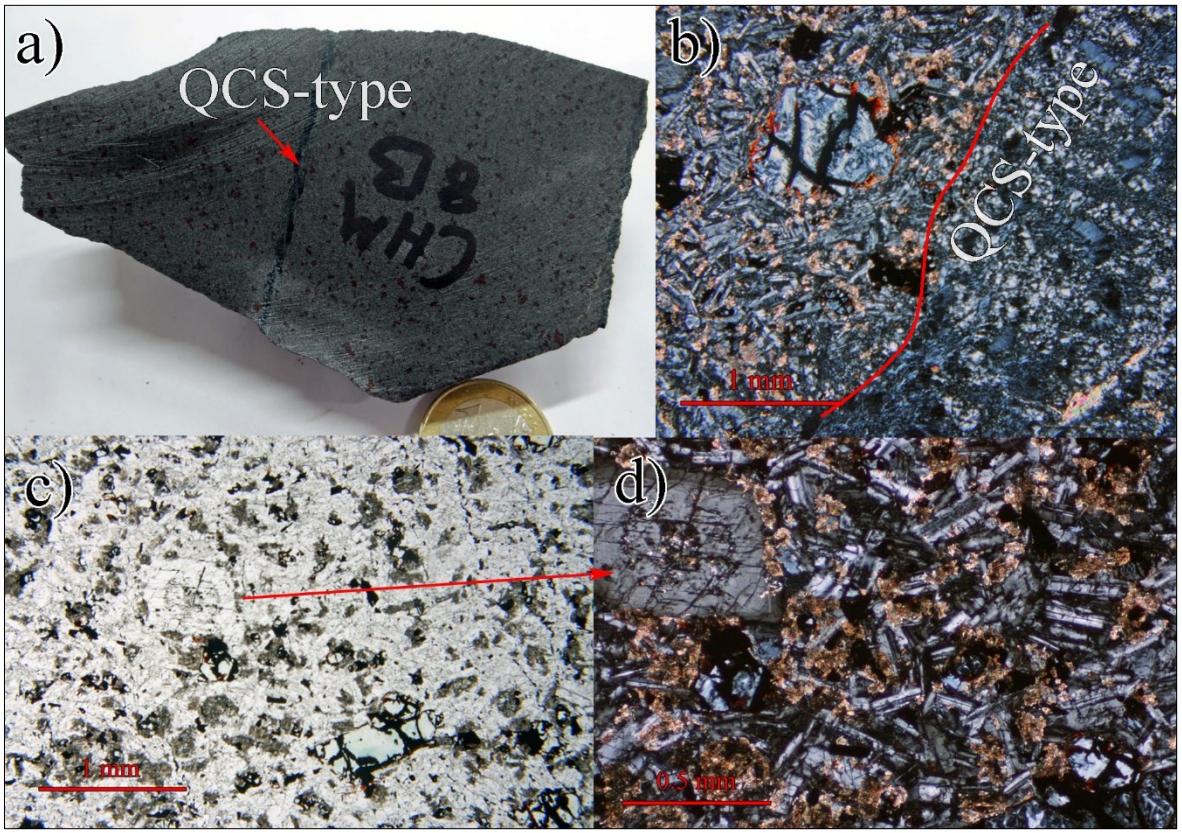

Figure 10: Photograph and microphotographs of microdiorite a) showing sample CHM8B taken from the microdiorite dyke. The rock is dissected by QCS-type veinlets. b) Intensely altered phenocryst (upper left) now consisting of opaque phases (black) and chlorite (light blue and whitish). The matrix consists of subhedral plagioclase laths (grey) and interstitial calcite (high birefringence); CHM8B, TL-XPL. c) Porphyritic texture of the microdiorite with (zoned?) phenocrysts of plagioclase (red arrow, low refraction) and altered Fe-Mg-silicates (light greenish color) embedded in plagioclase; CHM8B, TL-PPL. d) Enlargement of c) showing basal section of a plagioclase phenocryst with distinct cleavage embedded in matrix of euhedral plagioclase laths (grey, twinned) and interstitial calcite (high birefringence); CHM8B, TL-XPL.

Table 6: Petrographic composition of microdiorite.

Mineral	Description	Abundance
Plagioclase	medium- to fine-grained (0.5-1.5 mm), constituting phenocrysts and groundmass, mostly euhedral laths, albite law twinning with narrow-spaced polysynthetic twinning lamellae, partly altered (sericite)	70 %
Ca-Fe-Mg-silicate	fine-grained (0.5-1 mm) phenocrysts, subordinate abundance in matrix, comprising pyroxene, amphibole and phlogopite, constituting phenocrysts and groundmass, subhedral, intensely decomposed into hematite, chlorite, calcite and quartz, rare relicts, sometimes distinct cleavage visible	20 %
Accessory minerals	mostly magnetite, rare rutile, occur as very fine crystals (<0.5 mm) in the groundmass, sometimes martitization in highly altered rocks	10 %
Texture	porphyritic	

The groundmass is dominated by fine-grained, euhedral plagioclase laths showing a random orientation and disseminated subhedral crystals of magnetite (Figure 10 c). The rock is affected by strong alteration and shows vast amounts of interstitially formed calcite crystals (Figure 10 d). Euhedral to subhedral darker micro-phenocrysts comprise strongly altered Fe-Mg-silicates, without any relics of the primary minerals (Figure 10 b). They are characterized by prismatic crystal shapes and cleavage directions, typical for minerals such as pyroxenes or amphiboles. However, an adequate distinction was not possible. The alteration products are hematite and chlorite, which form opaque phases and small flakes of greenish color under plane polarized light, respectively. Subordinate medium-grained plagioclase laths up to 1.5 mm occur also as phenocrysts and show partly sericitized crystals. Raman spectroscopy revealed that plagioclase is labradorite.

4.1.2 Andesite

Andesites are intermediate, inequigranular rocks with a porphyritic fabric. They occur in the upper parts of the deposit forming most outcrops at Chah-Mesi open pit. The correlation of drill cores revealed that the footwall contact of the andesites is at around 2370 m a.s.l. and that their thickness is up to 136 m. Commonly these rocks have a dark gray to brownish-red color, but in deeper sections also a change into greenish colors was observed. Most andesites show porphyritic texture (Figure 11 a), but also vitrophyric and trachytic textures are present. At deeper sections, also amygdaloidal andesites were found with vesicles filled by dark blueish to white colored secondary minerals (Figure 11 b and Figure 12 b). Andesites at shallower depths mostly have a lot of larger phenocrysts, whereas towards depth their abundance decreases and also the size of phenocrysts becomes smaller.

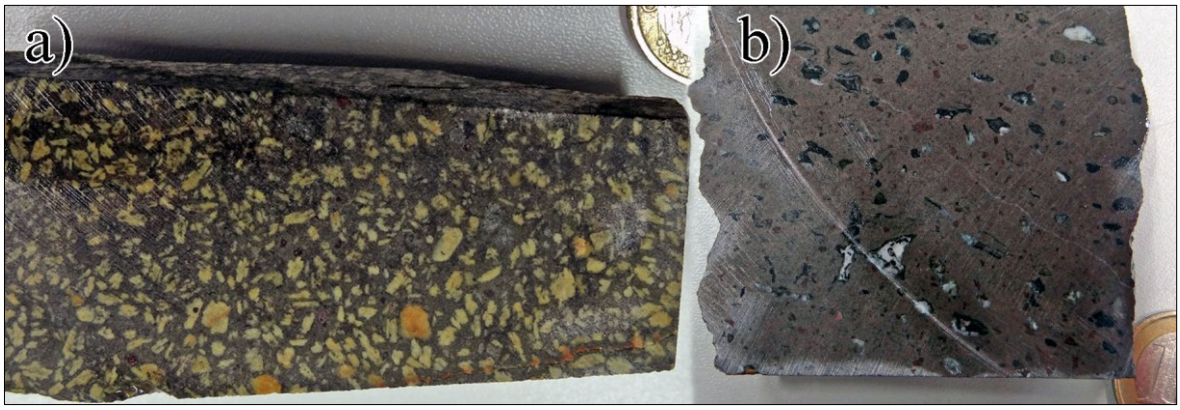

Figure 11: Photographs of andesite rock samples from drill core BH-CHM1. a) Andesite with porphyritic texture and large plagioclase phenocrysts from shallow levels of the deposit; CHM1-7. b) Porphyritic andesite with vast amounts of amygdales filled by chlorite (dark blue) and calcite (white) and intensely decomposed phenocrysts of Fe-Mg-silicate (dark red-brown); CHM1-108.

Phenocrysts mostly consist of 1 to 2 mm big laths of euhedral to subhedral plagioclase and reddish to brownish colored subhedral grains of (altered) Fe-Mg-silicates. Plagioclase dominates and commonly shows albite law twinning with narrow-spaced polysynthetic twinning lamellae (Figure 12 a). Phenocrysts of plagioclase show optical (and thus compositional) zoning, whereas the cores are more easily altered to sericite than the rims. Plagioclase is also a major constituent of the groundmass and mostly forms very fine-grained euhedral laths. These laths are either non-oriented in porphyritic textures or (sub)parallel oriented in trachytic textures.

Commonly, Fe-Mg-silicates are affected by intense alteration and were decomposed into hematite, chlorite, calcite and quartz. Alteromorphs (Delvigne, 1999) infer that the primary minerals were mostly amphibolite and pyroxene. However, neither microscopy nor Raman spectroscopy revealed unequivocal results allowing clear identification of the precursor minerals. Occasionally, cleavage planes were still visible and aided to distinguish between amphibolite and pyroxene and rare partial alteromorphs indicated the presence of orthopyroxene with rectangular cleavage planes and relatively low birefringence (Figure 12 c). These mineral phases also occur as very fine-grained constituents of the matrix. Accessory minerals are euhedral magnetite, apatite and rutile. In highly altered rocks oxidized magnetite often shows martitization.

At deeper levels, andesites grade into a transition of basaltic and andesitic composition with a higher abundance of mafic minerals (>35 %) and less amounts of plagioclase phenocrysts. Mostly basaltic-andesites include varying amounts of amygdales and might show an amygdaloidal texture.

Table 7: Petrography of andesite.

Mineral	Remarks	Abundance
Plagioclase	medium-grained (1-2 mm) phenocrysts, very fine-grained (<0.5 mm) in groundmass, mostly euhedral laths and rectangles, albite twinning with narrow-spaced polysynthetic twinning lamellae, often altered (sericite, calcite)	60-70 %
Ca-Fe-Mg-silicate	fine-grained (0.5-1 mm) phenocrysts, very fine-grained (<0.5 mm) in groundmass, comprising pyroxene, amphibolite, phlogopite?, subhedral, intensely decomposed into hematite, chlorite, calcite and quartz, rare relicts, sometimes distinct cleavage visible	30-40 %
Accessory minerals	mostly magnetite, apatite and rutile, occur as small crystals in the groundmass, sometimes martitization in highly altered rocks	5-10 %
Texture	mainly porphyritic, vitrophyric, trachytic; occasional amygdaloidal	

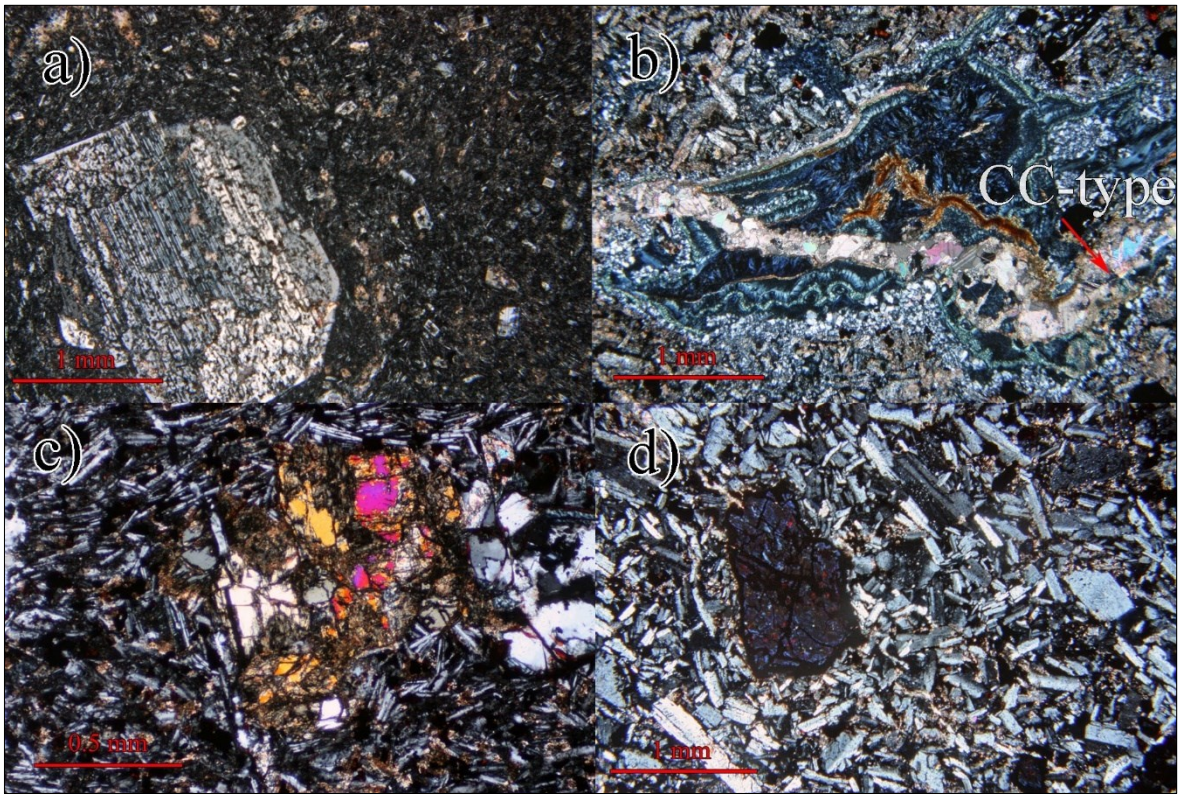

Figure 12: Photomicrographs of andesites; transmitted light with crossed nicols. a) Plagioclase phenocryst (partly altered or corroded) with albite law twinning embedded in a groundmass consisting of plagioclase, opaque phases etc.; CHM1-19.5. b) Amygdale filled with chlorite (light green to deep blue) and calcite (brownish red). Commonly, small quartz aggregates are found along the undulating boundaries of amygdales. Exterior parts are characterized by thin layers of light green chlorite fibers oriented perpendicular to the wall rock contact. Central parts of voids are mostly filled by Prussian blue chlorite exhibiting unoriented fibrous crystals. CC-type veinlet dissects amygdale filling; CHM1-108. c) Partial alteromorph of Fe-Mg-silicate in andesite showing trachytic texture with subparallel oriented plagioclase laths. The distinct rectangular cleavage and relatively low birefringence suggests orthopyroxene, CHM2-119. d) Strongly altered Fe-Mg-silicate in a porphyritic textured andesite; the matrix is mostly composed of unoriented laths of plagioclase; CHM1-115.

4.1.3 Pyroclastic rocks

Pyroclastic rocks consist of various volcanic rock fragments and crystals embedded in a finer-grained, sometimes even layered matrix (Figure 13 a, b). They were only observed in drill cores at depths below 2370 m a.s.l. Usually this rock type shows many different colors depending on the predominating components. Colors commonly range between greenish-grey and purple-red. The occurring pyroclastic rocks are predominated by rock fragments and therefore can be classified as lithic pyroclastic rocks in general. Depending on the grain size lithic pyroclastic rocks can be subdivided into fine and coarse tuffs (e.g., lapilli tuff; Figure 13 a). Minor amounts of ignimbrites were observed in the deepest parts of the drill cores. They show vitrophyric texture and welded fabrics with larger oriented rock fragments and crystals in a former glassy (?) groundmass (Figure 13 b). Microscopic investigation of the components revealed that plagioclase overweighs alkali feldspar. As quartz is also present the pyroclastic rocks are assumed to be mostly of dacitic composition.

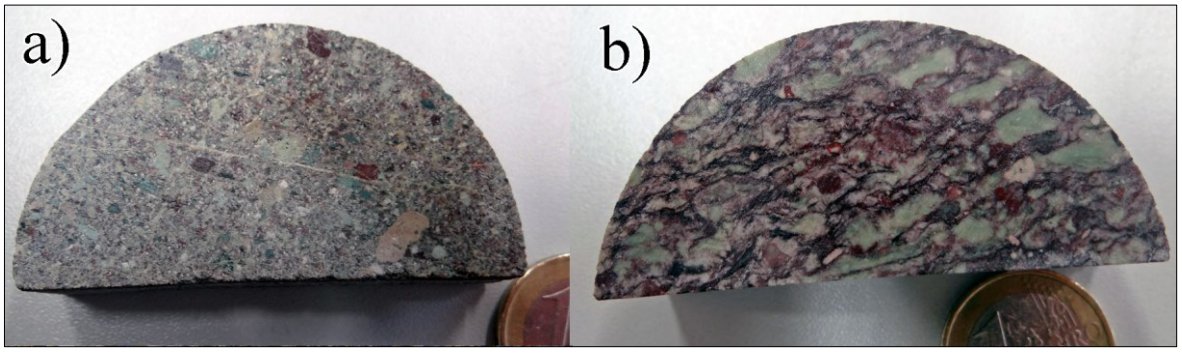

Figure 13: Photographs of pyroclastic rocks from drill cores showing different kind of textures. a) Lapilli tuff consisting of mainly rounded lithic components with grain sizes between 0.5 mm to 1 cm; CHM2-148. b) Ignimbrite exhibiting a welded fabric with elongated, highly altered, coarse-grained fiammae-like components (? alkalifeldspar); CHM1-164.

Rock fragments are angular to sub-rounded (Figure 14 a); often the larger components are better rounded. The average grain size of lithic components is below 2 mm, but in lapilli-tuffs grain sizes may reach up to 1 cm. Typically, the larger lithic components exhibit porphyritic texture with euhedral feldspar phenocrysts and micro-crystalline to (altered) glassy groundmass (Figure 14 b). Also, grains of pumice were observed. They occur as 1-2 mm large vesicle-rich grains with a black colored, glassy groundmass under plane polarized light (Figure 14 c). Crystalline components are usually alkali feldspar and plagioclase. Their distinction is not always easy, due to the high degree of alteration. However, plagioclase commonly can be recognized by its characteristic twinning. It seems that plagioclase is more affected by sericitization than alkali feldspar. In contrast, alkali feldspar is mostly totally decomposed into fine-crystalline aggregates of clay minerals and twinning is usually absent. Minor crystalline constituents are rounded quartz grains with sizes between 0.1 to 0.3 mm, which often exhibit corroded margins.

In tuffs the matrix consists mostly of microcrystalline to very fine-grained particles of ash or aggregates of clay (Figure 14 d). However, most tuffs are dominated by lithic and crystalline components and therefore show a component-supported fabric. In ignimbrites the matrix is mostly made up by glass and shows a vitrophyric texture with subparallel aligned feldspar phenocrysts and subrounded rock fragments.

Table 8: Petrography of pyroclastic rocks.

Component	Remarks	Abundance
Rock fragments	(very) coarse-grained up to 1 cm in lapilli-tuffites, mostly <2 mm, components often show porphyritic textures with feldspar phenocrysts or vesicle-rich pumice, mostly altered and decomposed into clay or sericite	65 %
Alkali feldspar	coarse- to medium grained, euhedral to subhedral, altered, often decomposed into clay or sericite (chlorite?)	15 %
Plagioclase	mostly medium-grained (0.5 to 1 mm), euhedral to subhedral, twinning lamellae, often sericitized	10 %
Matrix	mostly glass (partly devitrified?), fine-grained to microcrystalline ash, sometimes small rounded quartz crystals with corroded margins	10 %
Texture	volcanic rock fragments and crystals in fine-grained to layered matrix	

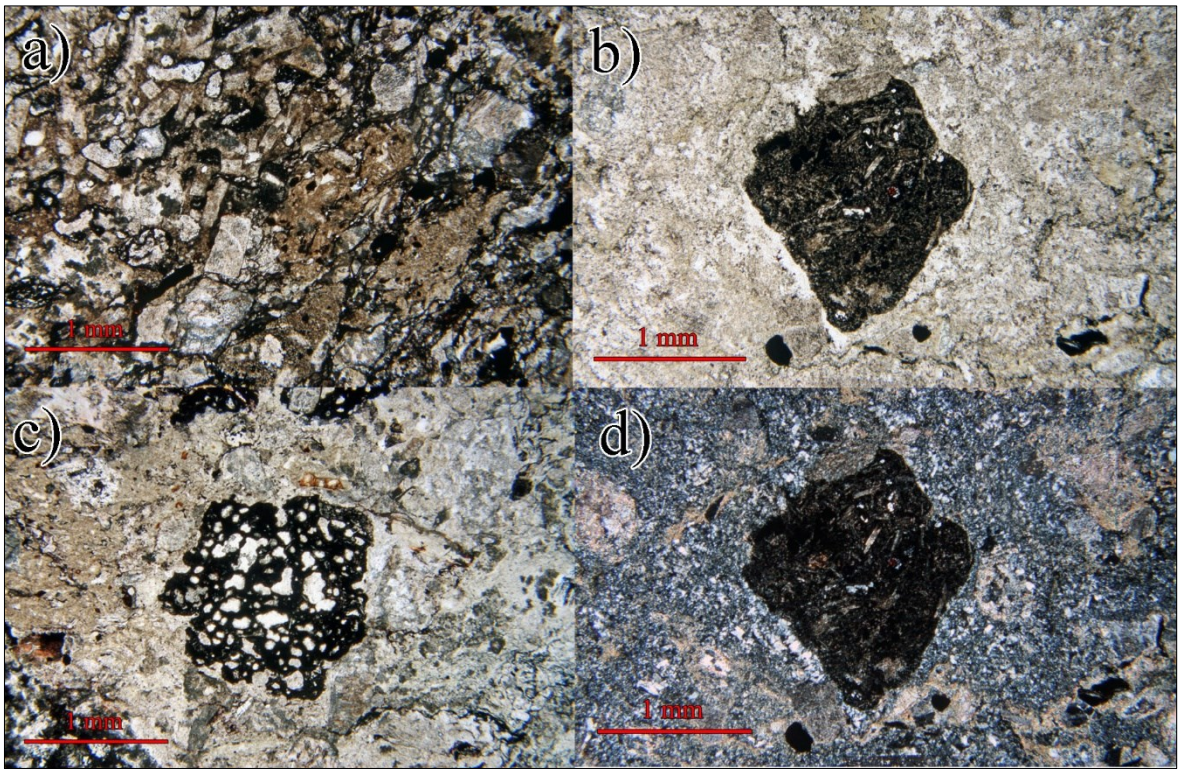

Figure 14: Photomicrographs of pyroclastic rocks. a) Medium- to coarse-grained crystals and subhedral feldspar crystals in a black colored glassy groundmass; CHM1-157, TL-PPL. b) Coarse-grained subrounded rock fragment in altered groundmass surrounded by feldspar phenocrysts; CHM1-178, TL-PPL. c) Pumice as a lithic component in lapilli-tuff showing a vesicle-rich microcrystalline groundmass; CHM1-157, TL-PPL. d) Same image as in b) under crossed nicols showing a large lithic component (center) embedded in an argillaceous matrix; CHM1-178, TL-XPL.

4.2 Vein classification

Successive hydrothermal activities produced six generations of veins and veinlets that can be distinguished in respect of vein mineralogy, wall rock alteration, mineralization and textural features. For general nomenclature, the studied veins and veinlets were compared to established vein types of Sillitoe (2010) and Gustafson and Hunt (1975). However, the used nomenclature is mainly applicable for PCDs and thus most vein types are named after the initial letters of the major vein filling minerals and are specific for Chah-Mesi. As Taghipour et al. (2008) distinguished several vein types at the nearby Meiduk deposit, their classification was also used for better comparison with Meiduk.

Two vein types associated with potassic alteration seem to be linked with porphyry-related activities and occur very close to Meiduk. These types include (1) B_2-type and (2) D_1-type veins and may represent the earliest formed veins in that area. Further, three vein types were distinguished and determined to be more or less barren, such as (3) QCS-type, (4) PCE-type and (5) CC-type veins. Mineralization is restricted to (6) O-type veins and textural as well as mineralogical features allowed to subdivide this type of vein into four subtypes.

These are: (1) Massive veins contain massive to disseminated sulfide mineralization and consist of mainly fine- to coarse-grained equigranular quartz associated with replacement and leaching textures. (2) Banded veins refer to a vein type characterized by banded or layered texture of mainly fine-grained ore and gangue minerals. (3) Crustiform veins are characterized by coarse ore and gangue minerals, typically comprising comb quartz textures and a high abundance of carbonates. Often banded and crustiform veins show transition states including diagnostic features of both subtypes. (4) Mineralized breccia zones consist of fragmented and altered wallrocks cemented by gangue minerals and sulfides.

Table 9: Summary of vein types distinguished in the Chah-Mesi deposit; for abbreviations see appendix I. Vein classification according to (Taghipour et al., 2008) established for Meiduk porphyry copper deposit.

Vein type	Texture	Thickness	Ore association	Gangue minerals	Alteration	Crosscutting relationships
B_2	thin veinlets, subrounded qz in carb matrix	1 – 5 mm	py, mo, ccp, bn	qz, carb	potassic	-
D_1	thin veinlets	1 – 2 mm	py, ±ccp, ±bn, ±Fe-oxyhyd.	qz, ±carb	potassic, argillic	cuts B_2
QCS	thin veinlets	0.5 – 4 mm	py	qz (chc), chl, ser, ±cal	sericitic, propylitic	-
O	massive: vein form and replacement with wavy shaped walls	10 – 20 cm	py, ccp, enr, luz-fm, ±sp, ±fh	qz, ±ser, ±Ca-Mg-Mn-Fe-carb	silicic	cut QCS ↓
	banded: vein form, regular – irregular walled, colloform to crystalline banding, massive sulfide (ginguro)	3 – 10 cm	exterior: ccp, py, enr, luz-fm, ±fh, ±Ag-Au interior: sp, gn, py, ±ccp, ±fh, ± enr	qz, Ca-Mg-Mn-Fe-carb, ±ser, ±rt	sericitic, adv. argillic	
	crustiform: straight walled veins, fine- to coarse-grained, comb quartz, mirror-plane symmetry	3 – 5 cm	ext.: ccp, py, enr, luz-fm, ±fh, ±Ag-Au int.: sp, gn, py, ±ccp ±fh, ±enr	qz, Ca-Mg-Mn-Fe-carb, ±ser	sericitic, adv. argillic	
	breccia: matrix in breccia, cockade quartz, comb quartz	3 – 30 cm, up to 1 m	sp, gn, py, ccp, ±enr, ±fh	qz, Ca-Mg-Mn-Fe-carb, ±ser, ±ba, ±fl, ±ap, ±rt	adv. argillic	
PCE	sheeted veins	4 – 10 cm	native copper	prh, cal, czo, ep, ±rt	propylitic	-
CC	sheeted veins, thin veinlets	4 to 10 cm, 1 – 5 mm	barren	cal, ±qz	propylitic	cuts QCS and PCE

4.2.1 B_2-type

B_2-type veins are composed of quartz + carbonate ± molybdenite ± pyrite ± chalcopyrite ± bornite and are associated with potassic hydrothermal alteration that is only found in the northernmost Chah-Mesi area. Despite some mineralogical deviation, these Mo-bearing veins are comparable to B_2-type veins of Meiduk according to the vein classification of Taghipour et al. (2008). At Meiduk, this vein type consists of quartz + molybdenite ± magnetite ± chalcopyrite ± anhydrite with <5 mm thick veinlets and occurs mainly in potassic alteration zones. Comparatively, B_2-type at Chah-Mesi includes higher amounts of carbonates and lacking magnetite. The only sample containing this assemblage was taken from the northernmost drill core studied, BH-CHM4 in 20 m depth. Thicker veinlets exhibit a banded texture with white to gray color (Figure 15 a). Maximum veinlet thickness is about 1 cm with undulating contact to the adjacent wall rock. Similar mineralized <1 mm thick microfractures are observed in the same sample. The mm thick veinlets form a stockwork-like network and contain sub- to anhedral quartz with an average size of <0.5 mm as well as interstitial carbonates; locally the veinlets show a breccia-like texture with subrounded anhedral quartz accompanied by sulfides occurring in a carbonate matrix. Quartz and carbonate account for more than 85 vol% of the veinlet. Pyrite, molybdenite and chalcopyrite constitute the major sulfide minerals. Pyrite and chalcopyrite occur as anhedral crystals. Pyrite includes small blebs of chalcopyrite, whereas chalcopyrite is framed by bornite along its margins. Molybdenite forms tiny flakes (<0.5 mm) (Figure 15 b) and is restricted to this vein type. It is very rare at Chah-Mesi reflecting the overall low Mo grade of this deposit.

4.2.2 D_1-type

These sulfide-bearing veinlets are very thin, usually between 1 to 2 mm, and contain mainly quartz + pyrite. This vein type is widespread at Chah-Mesi and can be found in zones of potassic, argillic and sericitic alteration, mainly near to the surface. Depending on the sulfide content, the color of the veinlets varies from silver-bronze in pyrite dominated veinlets to white translucent when they are barren. The gangue mineralogy is predominated by subhedral quartz mostly defining an inequigranular mosaic texture and minor carbonates. The main sulfide is anhedral pyrite sharing interpenetrating grain boundaries with quartz. Pyrite mostly forms polycrystalline aggregates but also develops individual crystals up to 2.4 mm in size. It is characterized by minor inclusions of bornite and chalcopyrite (Figure 15 d).

Drill cores from shallower depths (closer to the surface) in the southern part of the deposit are affected by supergene argillic alteration but contain quartz veinlets with a similar texture. However, there pyrite is mostly weathered to Fe-oxyhydroxides (Figure 15 e). Moreover, veinlets in argillaceous zones often have 0.5 to 1 mm thick selvages of sericite and minor chlorite along the wall contact. Trying to fit these veinlets into the vein classification scheme developed for Meiduk (Taghipour et al. (2008), they are best correlated with pyrite ± quartz (VIII, D_1-type) veins. Crosscutting relationships indicate that D_1-type veins postdate B_2-type veins as observed in sample CHM4-20 (Figure 15 a, c).

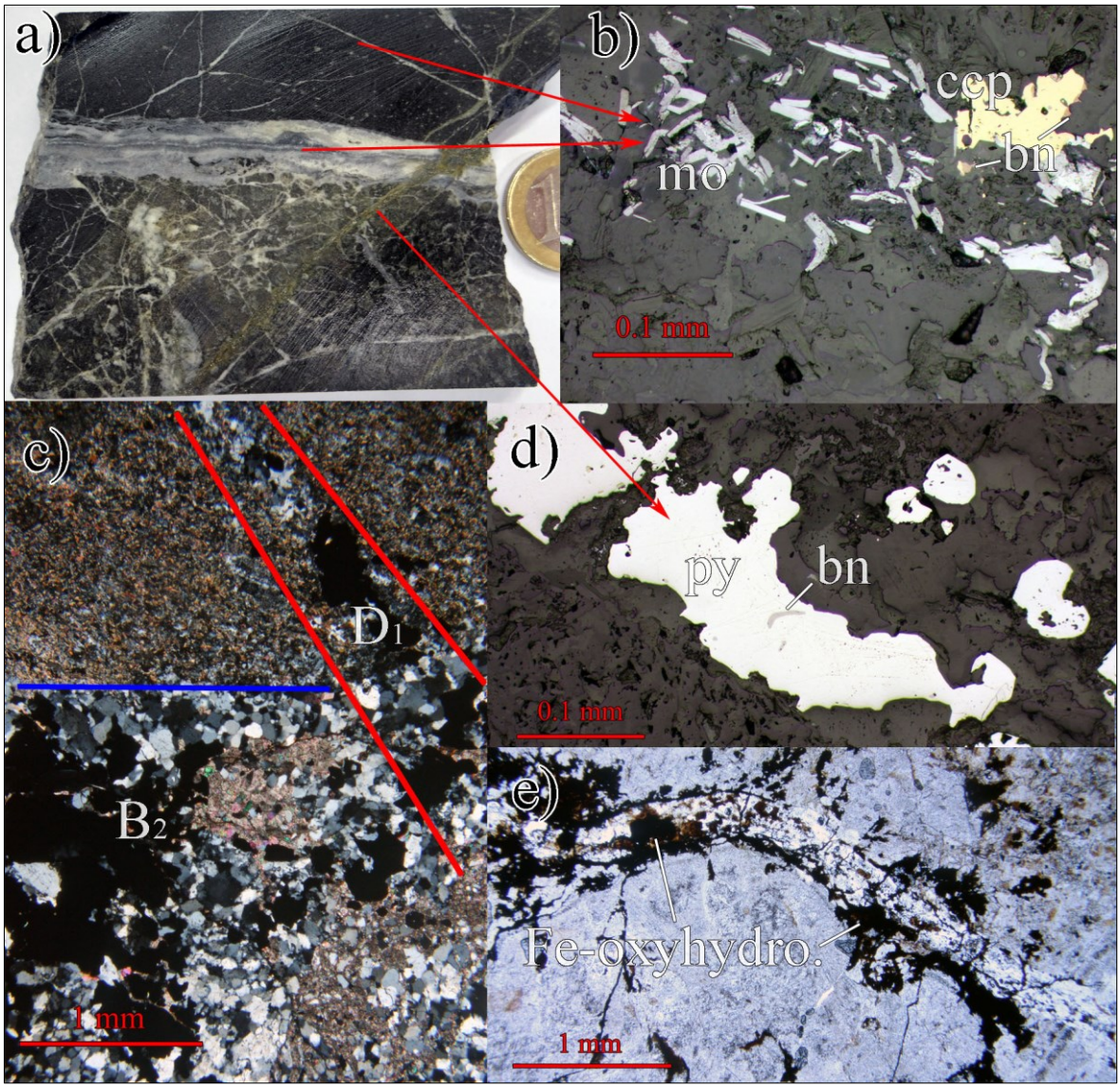

Figure 15: Photograph and microphotographs of Mo-bearing and pyrite-quartz veinlets; CHM4-20 (a-d) and CHM1-5 (e). a) Drill core illustrating the crosscutting relationship of grayish white stockwork-like veinlets (partly with breccia-texture), the horizontal cm-thick veinlet showing banded texture contains qz-carb-mo-py and is crosscut by a younger qz-py veinlet. b) Mo-bearing B_2-type vein with flaky irregular oriented molybdenite and anhedral chalcopyrite with fringing bornite; RL-PPL. c) Detail of D_1-type vein crosscutting B_2-type vein; TL-XPL. d) Anhedral pyrite in qz-py vein with small inclusions of bornite; RL-PPL. e) Supergene weathering of qz-py vein with anhedral Fe-oxyhydroxides and dendritic texture; TL-PPL.

4.2.3 Quartz-chlorite-sericite veinlets (QCS-type)

This vein type is characterized by quartz-chlorite-sericite (QCS) and lack of mineralization. It is present in many parts of Chah-Mesi deposit occurring in different lithologies. It was observed in pyroclastic rocks in the deepest sections of the deposit as well as in volcanic and intrusive rocks at shallower depths. Because QCS veins are crosscut by mineralized veins, this vein-type is regarded as pre-mineralization (Table 9).

QCS-type veins mostly form single individual veinlets with a thickness between 3 and 5 mm. In hand specimen the veinlets show varying colors from white to beige with irregular brownish bands or homogeneous white to bluish green. Wallrock contacts are sharp and straight and occasionally a distinctive selvage of calcite is developed along the margins. QCS veins are crosscut by crustiform textured mineralized veins and younger coarse- and fine-grained calcite veins (Figure 16 a). This vein type is common in zones of propylitic alteration; the wall rocks are mostly strongly altered with extensive formation of secondary calcite, chlorite, sericite and minor epidote. Vein mineralogy consists of SiO_2 minerals, commonly present as rhythmic chalcedony bands that form at the margins of the veinlets and show micro-fibrous habit (Figure 16 c, d). Besides chalcedony also fine grained to microcrystalline quartz may occur. The inner parts of the veinlets are dominated by chlorite with minor sericite. However, sericite and calcite can also be a major phase in the center of the veinlet (Figure 16 b). Microcrystalline to fine grained sericite and chlorite are oriented (sub)parallel to the vein walls. Chlorite shows anomalous interference colors (greenish Prussian blue) but the exact classification of these chlorite-group minerals was not possible even with Raman spectroscopy. Frequently, the veinlet cores contain coarse-grained calcite (Figure 16, e). QCS veins are completely barren; i.e. no sulfides or any other ore minerals were detected.

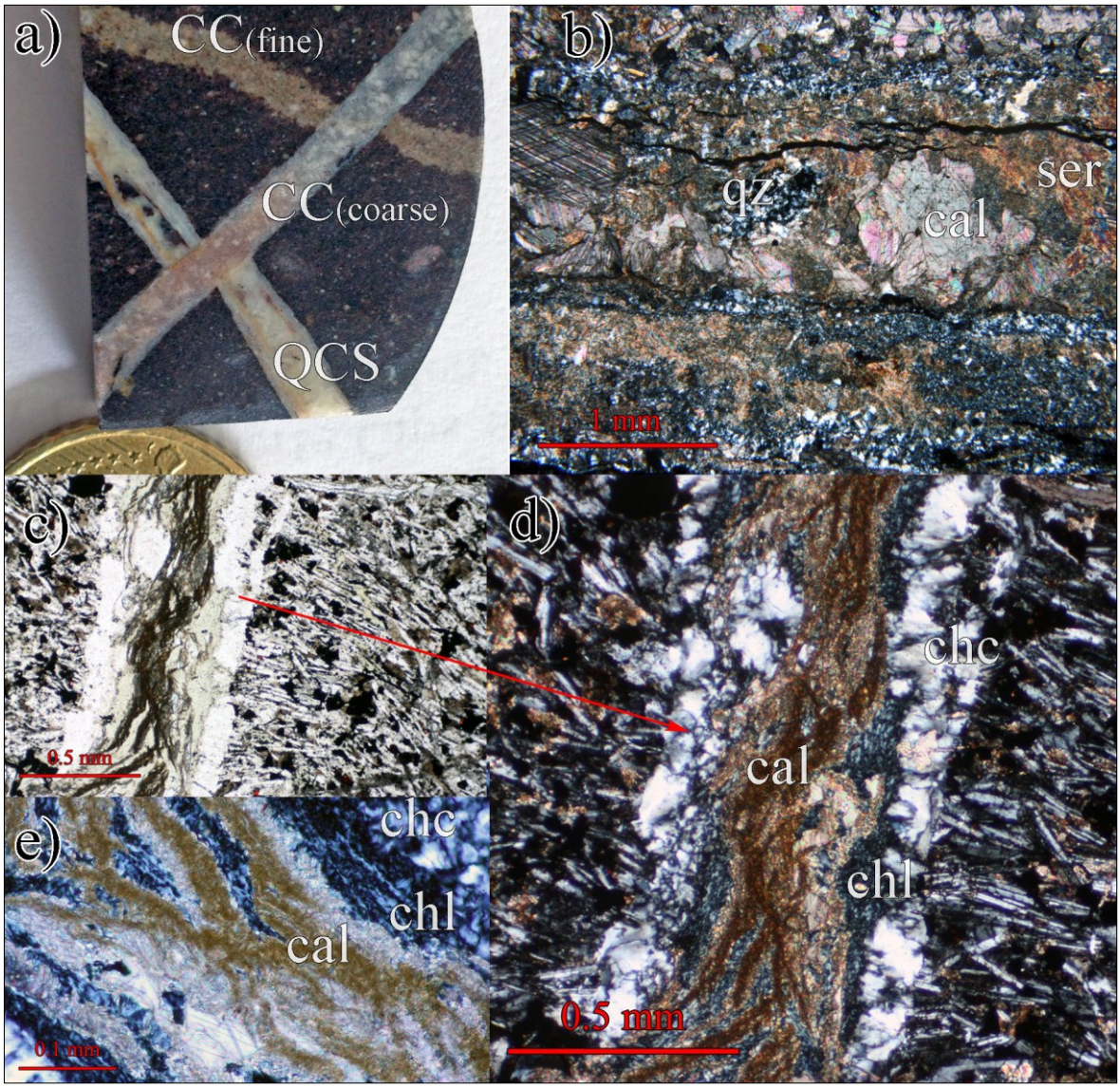

Figure 16: Photographs and photomicrographs of quartz-chlorite-sericite (QCS-type) veins showing crosscutting relationships and mineralogy; CHM1-172 (a, b) and CHM2-119 (c-e). a) QCS vein is crosscut and offset by a coarse-grained calcite veinlet, with carbonatization halo. b) QCS vein with fine grained quartz seams parallel to the vein margin and prevailing sericite among coarse anhedral calcite in the center; TL-XPL. c) Veinlet with sharp straight contacts dissecting andesitic country rock; transmitted light; TL-PPL. d) Same image as in c) under XPL showing microfibrous chalcedony at the margins enveloping a central core with chlorite and calcite. Alteration of the wall rock results in formation of dispersed microcrystalline calcite and sericitized plagioclase laths. e) Anastomosing veinlet core consisting of chlorite (anomalous interference colors) and microcrystalline partly brownish calcite; TL-XPL.

4.2.4 Ore veins (O-type)

Ore veins show a close relationship to the NNE-SSW trending fault zones (Figure 7 and Figure 8) with intense silicification. This vein type occurs mainly as open space fillings that formed along fault zones and caused distinct alteration and subordinate replacement of the adjacent wallrocks. Mineralization within veins formed mainly in unfilled voids or is intergrown with gangue minerals.

At Chah-Mesi, several subtypes of ore veins can be distinguished based on vein texture, wallrock alteration and mineralogy. In the following they are referred to as (1) massive veins, (2) banded veins, (3) crustiform veins and (4) mineralized breccia zones. The different veins record a sequence of several mineralizing pulses. It is to be noted that transitions do exist.

The gangue minerals in the central parts of the deposit consist mainly of quartz associated with replacement and leaching textures (vuggy quartz) and massive O-type veins. Vein textures comprise mainly fine- to coarse-grained equigranular quartz. Carbonates are almost absent in the central parts. However, they join the gangue assemblage towards the peripheral and deeper deposit sections where they become increasingly abundant. Banded and crustiform veins occur mainly in ore zones 2 and 3 (Chapter 5.1). These often show comb quartz textures, whereas cockade quartz is typical for mineralized breccias. Carbonates are very common in the banded and crustiform veins and in the breccia, though quartz is still the dominant gangue mineral. Only few crustiform veins consist mainly of coarse-grained carbonate which is associated with sphalerite and galena. Open spaces and vugs between quartz are often filled with rhombohedral carbonate crystals and therefore a relatively late formation is plausible. Carbonates often show a distinct growth zonation with cores of ankerite and rims of siderite. Often ankerite and siderite are manganiferous, but Mn-carbonates such as kutnohorite or rhodochrosite may be present as well. Other gangue minerals comprise minor barite, apatite, fluorite and anhydrite.

4.2.4.1 Massive veins

Mineralized massive quartz veins are most abundant in the Chah-Mesi open pit where they are 10 to 20 cm thick. They contain massive to disseminated sulfide mineralization. These veins are exposed on the surface particularly along the NNE-SSW striking vein system (Figure 8 c-d). Samples were studied from outcrops at sample locations CHM6, CHM8 and CHM9. Investigation of drill core BH-CHM1 confirmed that massive quartz veins are also present close to the northern border of the open pit at drill hole depths from 44 to 62 m (i.e. 2443 to 2425 m a.s.l.).

The host rocks adjacent to the veins show strong silicification. The silicified host rocks and the veins typically contain clusters of open vugs and voids (Figure 17 c). Also, irregular channel-like leaching textures were observed in wallrock samples adjacent to massive quartz veins. Occasionally euhedral crystal of quartz form in these cavities (Figure 17 d). In drill core BH-CHM1 massive quartz veins occur in a dense spacing at depths of 44, 52, 55.7 and 62 m forming a voluminous silicified ore body of up to 15 m thickness. This zone is characterized by strong fragmentation elucidated by low RQD (Rock-quality designation after Deere, 1964) values and core loss observed in drill cores (Figure 17 a, b).

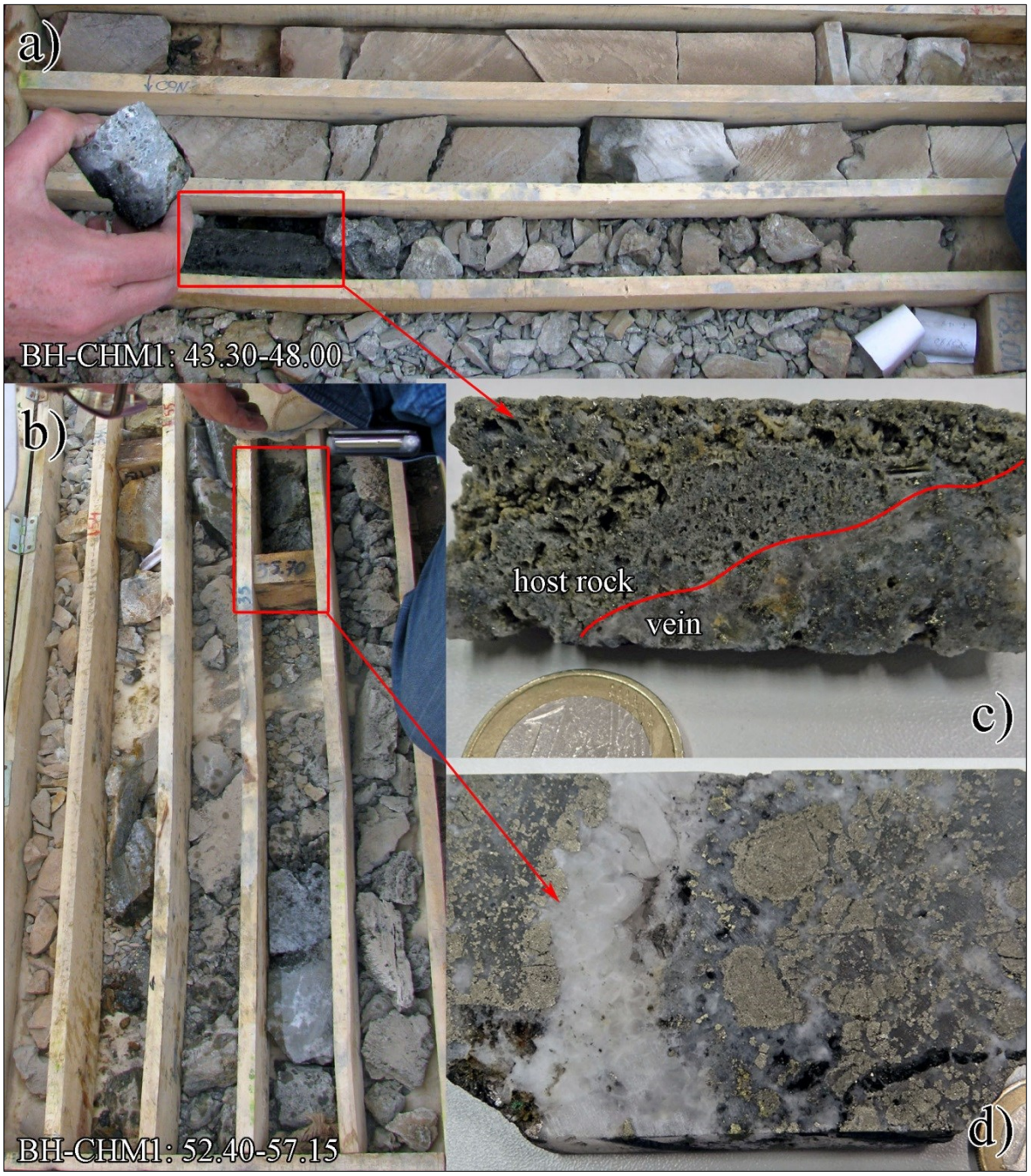

Figure 17: Massive quartz veins in drill core BH-CHM1. a) Section of drill core between 43.30-48.00 m of depth intersecting a massive 6-10 cm thick quartz vein that is surrounded by a symmetric 10-20 cm thick zone of strong silicification. Eventually, silicification grades into a zone of advanced argillic to sericitic alteration in the andesitic host rock. b) Section of drill core between 52.40-57.15 m showing strong fragmentation, which is characteristic for intersections with massive quartz veins. Several occasions of core loss are due to high decomposition of adjacent wall rocks. c) Sample CHM1-44 showing the undulating transition of a strongly silicified host rock and massive quartz vein. Voids and open spaces in the silicified host rock are due to extensive leaching of components. The dark gray part of the vein consists of disseminated sulfides in a fine-grained quartz matrix with minor amounts of carbonate. d) Massive quartz vein of sample CHM1-55.7 including nodular-shaped, polycrystalline sulfide aggregates consisting mainly of inequigranular pyrite and interstitial Cu-rich sulfides. A less mineralized band of euhedral prismatic quartz up to 1,5 cm thick is to be seen in the center.

Commonly, the gangue mineral is quartz occurring either as coarse-grained, milky-white crystals or as a dark-gray aggregate of fine-crystalline quartz with interstitial sulfides and vast amounts of small micro pores (Figure 18 b). Quartz may be microcrystalline (<25 µm), fine-grained (<1 mm) to coarse-grained (>1 mm) and individual crystals may even exceed 1 cm in size. The texture of quartz is more or less uniform; it is mostly an equigranular mosaic texture of anhedral to subhedral crystals with interlocking grain boundaries (Figure 18 c, d), also reported in the literature as “buck” quartz (John et al., 2018). Interstitial cavities are filled with sulfides or subordinate gangue minerals, such as carbonates or sheet silicates. Less common textures comprise comb quartz where crystallization of quartz crystals is perpendicular to the vein wall. Besides quartz, the gangue consists of minor microcrystalline carbonate and sheet silicates. Euhedral carbonate crystals show distinct growth zonation. Ankerite in the core grades into Mn-rich carbonates, Zn-rich kutnohorite and/or siderite (Chapter 5.3.3). Sheet silicates often form aggregates composed of non-oriented flakes 10 to 20 µm in length.

Mineralization is characterized by massive aggregates of sulfides within the veins or in the replaced host rock (Figure 17 c, d). Ore minerals may accumulate in massive nodules in the quartz, partly precipitating in open cavities, or occur as disseminated sulfides in the vein and leached host rock (Fig. 3 c, d). The size of individual sulfide grains is usually below 0.5 mm. In the massive quartz veins, ore minerals have an average abundance of about 10-20 vol% and are predominantly pyrite and chalcopyrite with varying minor amounts of enargite and/or luzonite-famatinite, tennantite-tetrahedrite, sphalerite, galena, bornite, chalcocite and covellite (Chapter 5.2.1).

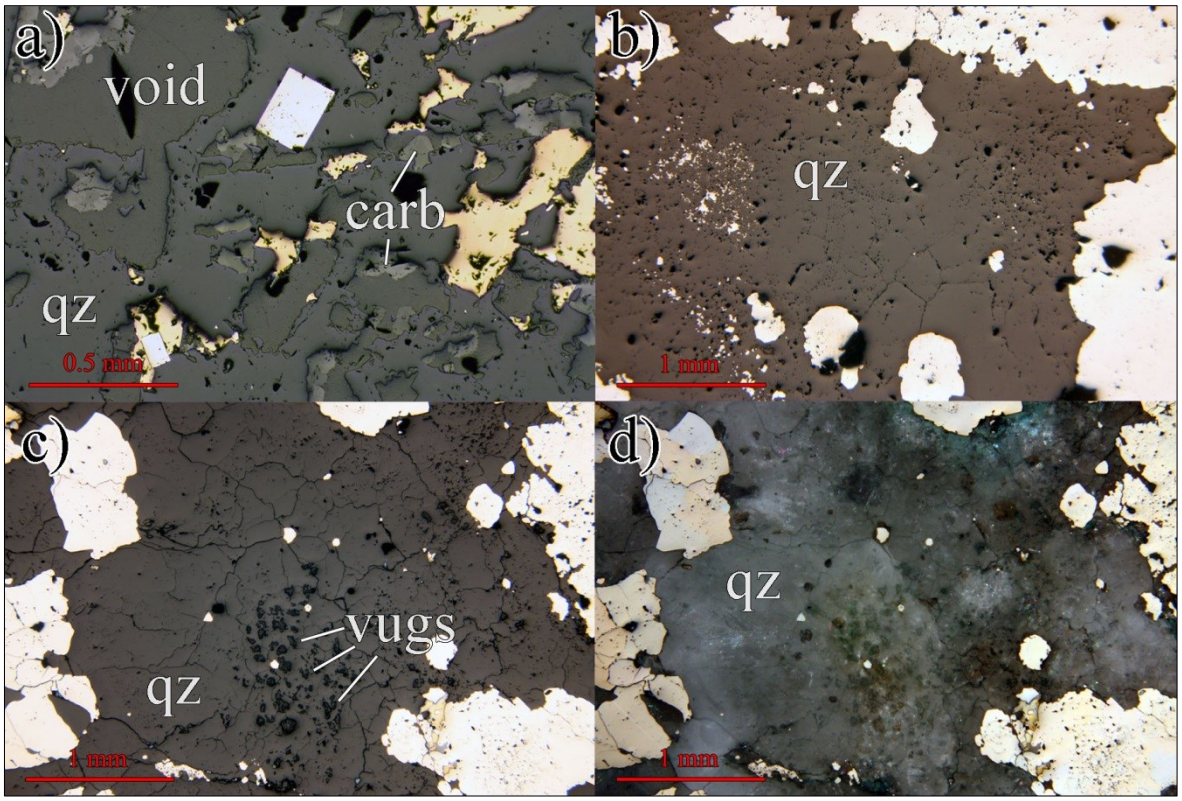

Figure 18↑: Photomicrographs of micro-textures in massive quartz veins and altered wallrock contacts. a) Silicified wallrock with vuggy quartz texture. Sulfides (chalcopyrite, pyrite) plus carbonate fill open spaces of leached minerals; CHM1-44, RL-PPL. b) Polycrystalline pyrite aggregates (of highly varying grain size) intergrown with quartz. The latter partly showing polygonal mosaic texture with interstitial vugs and finer sulfides; CHM1-52, RL-PPL. c) Equigranular "buck" quartz consisting of anhedral interlocking crystals (about 400-500 µm in size) with small vugs and intergrown with pyrite; CHM9A, RL-PPL. d) Same as in c) under crossed polarized light. Pyrite showing weak anisotropy; CHM9A, RL-XPL.

4.2.4.2 Banded veins

This vein type is characterized by banded to layered textures. These veins are 3 to 10 cm thick exhibiting undulating contacts to the adjacent wallrocks. Banded veins were observed mostly in drill cores BH-CHM2 (Figure 19 a), BH-CHM4 (Figure 19 b), BH-CHM5 and BH-CHM7 at depths between 2478 and 2399 m a.s.l. indicating widespread occurrence from north to south throughout the whole Chah-Mesi deposit. This vein type also crops out on the surface close to exposed massive vein structures. Surface samples were taken from locations CHM1 and CHM10. Spatially, banded veins tend to occur in proximity to massive quartz veins and thus, some samples may include characteristics of both the massive and banded texture type. Hence, they could represent a transitional type. Adjacent wallrocks were affected by strong advanced argillic alteration. Veins are composed of alternating laminar bands of gangue minerals and sulfides forming either elongated lenses or wavy layers of massive sulfide aggregates. Also disseminated ore texture may be present in some samples.

Generally, anhedral to subhedral quartz is the main gangue mineral showing colloform microcrystalline or coarse-crystalline grains up to 2 mm. Alternating bands within a single vein are generally subparallel, although slight deviation from parallelism has been observed. Individual bands are between 100 µm to 5 mm wide and thicker bands often contain several smaller bands of different thickness and crystallinity. Primarily, milky-white to slightly translucent colored layers consist of densely crystallized coarse quartz. Dark gray layers comprise cavity-rich anhedral mosaic quartz or jigsaw texture accompanied by interstitial fine-grained sulfides (Figure 21 b, d). Commonly, fine-grained (400 to 500 µm) quartz shows a homogeneous appearance within individual bands. Further, brownish to beige-white colored, microcrystalline and coarse-grained layers of carbonate are intercalated with quartz rich layers and tend to occur along vein margins (Figure 19 c). In comparison to massive quartz veins, carbonates are not only restricted to cavities, but represent a crucial part of the banded groundmass and are more abundant.

Euhedral carbonate crystals show well-developed rhombohedra, typically with growth zonation and may also occur in gaps of quartz layers (Figure 20 c, d). Microprobe analysis and Raman spectroscopy confirmed that carbonates consist of ankerite cores that grade into Mn-rich siderite and/or kutnohorite-rhodochrosite (Chapter 5.3.3). Moreover, accessory gangue minerals include barite, apatite and rutile, the latter with well-developed crystal faces embedded in the quartz matrix and interstitial to sulfides. Barite shows an elongated needlelike shape, whereas apatite often forms tiny prismatic crystals with characteristic hexagonal basal sections.

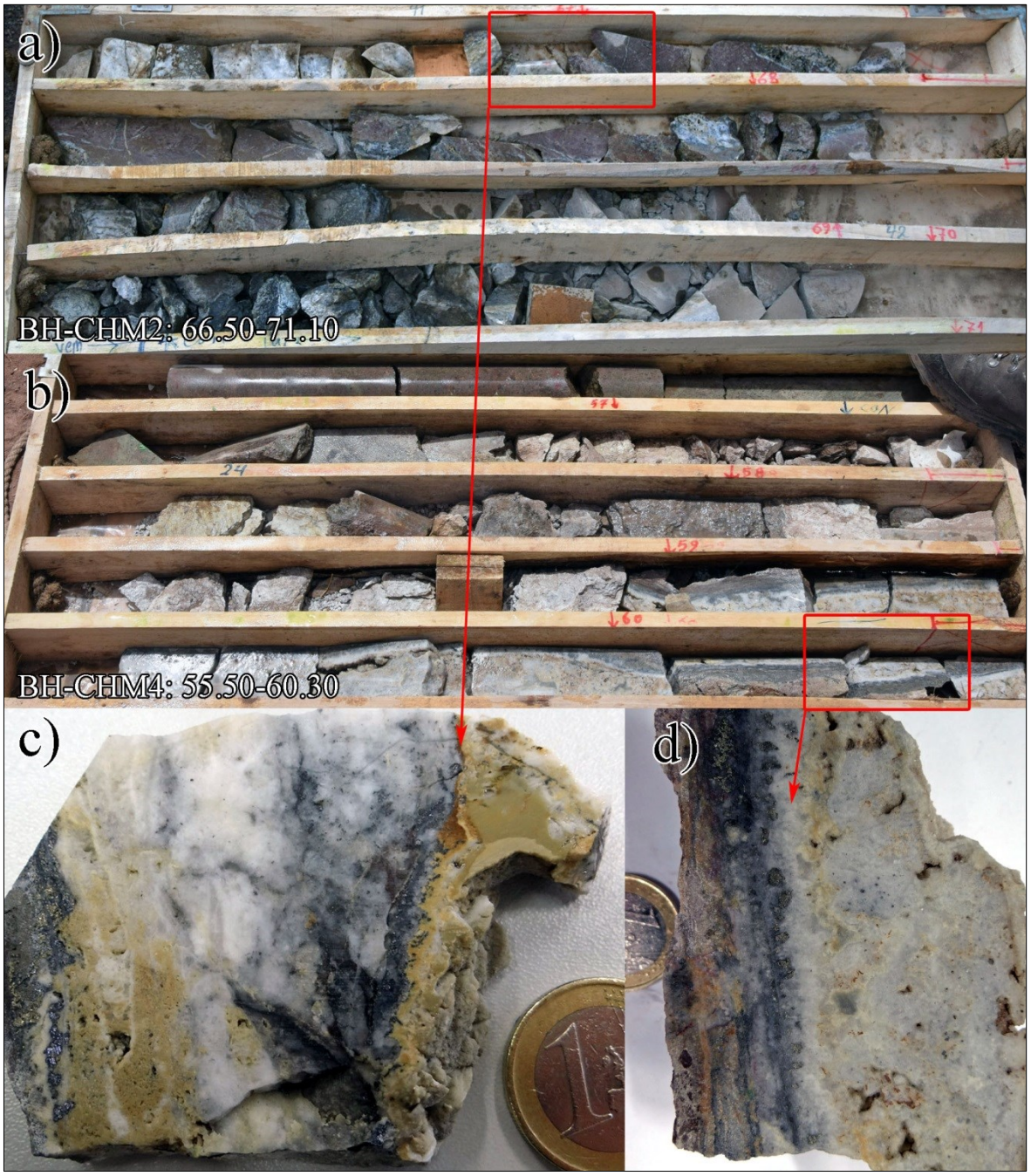

Figure 19: Banded quartz veins sampled from the northernmost (BH-CHM4) and southernmost (BH-CHM2) drill cores in the study area. a) Drill core BH-CHM2 consisting of argillic altered andesite with banded vein intersections. b) Drill core BH-CHM4 with banded veins oriented almost parallel to the drill axis outlining the steep inclination of the veins. c) Sample CHM2-67 representing a typical succession of banded texture with carbonate (brown) at the margins. The central part of the vein consists of quartz including several ore-bearing layers. Open space fillings with beige colored lattice-texture (or angel wing) calcite are seen on the right. d) Colloform silica with dark sulfide-rich bands occurring close to the carbonate vein-wallrock contact hosting fine-grained sulfides. These bands are followed by rather coarse-grained sulfides and gangue minerals and develop into massive quartz with voids towards the core.

The abundance of sulfides in this vein type is between 20-30 vol%. Mineralization occurs as mm to cm thick ore layers parallel to the wall contact and consists of fine- to coarse-grained sulfide assemblages revealing complex textures (Figure 21). Ore minerals include pyrite, chalcopyrite and minor sulfosalts (Figure 21 c) as well as Pb-Zn-dominated assemblages with sphalerite, galena and pyrite (Figure 21 e) interpreted as transition from high- to intermediate-sulfidation assemblages (see chapter 7). Temporal zonation of ore minerals is obvious where fine-grained Cu-Fe-sulfides occur disseminated or as laminar bands along vein margins and develop into sulfide bands consisting mainly of bigger subhedral crystals of sphalerite, galena and pyrite towards the vein cores. Moreover, sulfide contents may locally increase up to 50-60 vol% forming banded high-grade ores that are called ginguro (John et al., 2018). These massive ore bands are 3 to 20 cm thick and contain comparatively low amounts of fine-grained gangue minerals. About 10 to 20 cm thick halos of advanced argillic alteration are developed around these veins (Figure 22 a, d). However, colloform quartz bands along the vein margins (Figure 22 b) indicate their relationship to the banded veins. Typically, these bands are dark gray to silver-black and contain abundant sulfide minerals. A characteristic ore texture is brittle fractured pyrite enclosed in a chalcopyrite matrix. Moreover, sulfosalts and precious metals are more abundant. Voids are also common and partly they are still filled with anhydrite or carbonate (Figure 22 c).

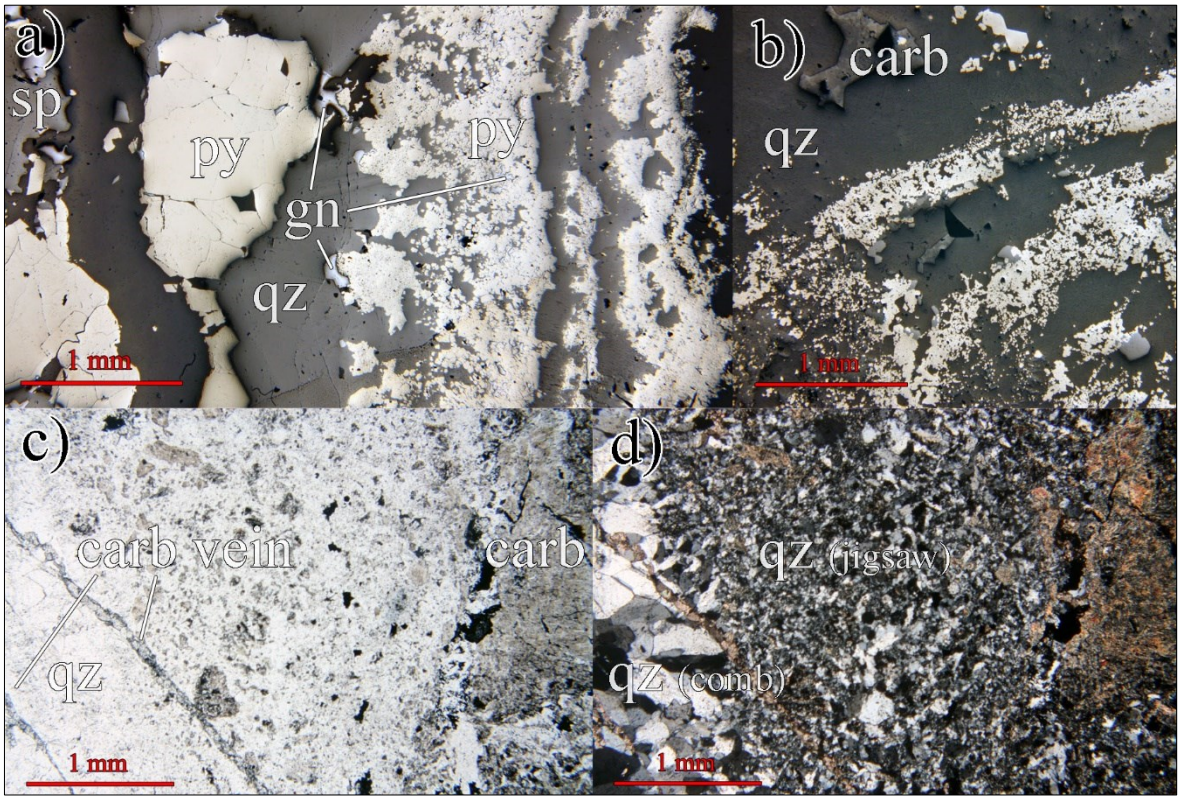

Figure 20: Photomicrographs of vein textures in banded veins. a) Bands of fine-grained pyrite and interstitial galena alternating with layers of fine crystalline quartz close to the vein margin (right). Towards the vein center (to left) the sulfides become coarser grained and mineralogy develops into a Pb-Zn rich assemblage; CHM2-67, RL-PPL. b) Bands of fine-grained pyrite alternating with quartz bands; interstitial space is filled with Ca-Mg-Fe-Mn carbonates; CHM2-92, RL-PPL. c) Alternating bands of coarse comb quartz (left, long axis of crystals oriented about perpendicular to the wall contact), fine grained quartz showing jigsaw to mosaic texture (middle) grading into fine-grained carbonate (right); CHM2-89.5, TL-PPL, d) same as c; CHM2-89.5, TL-XPL.

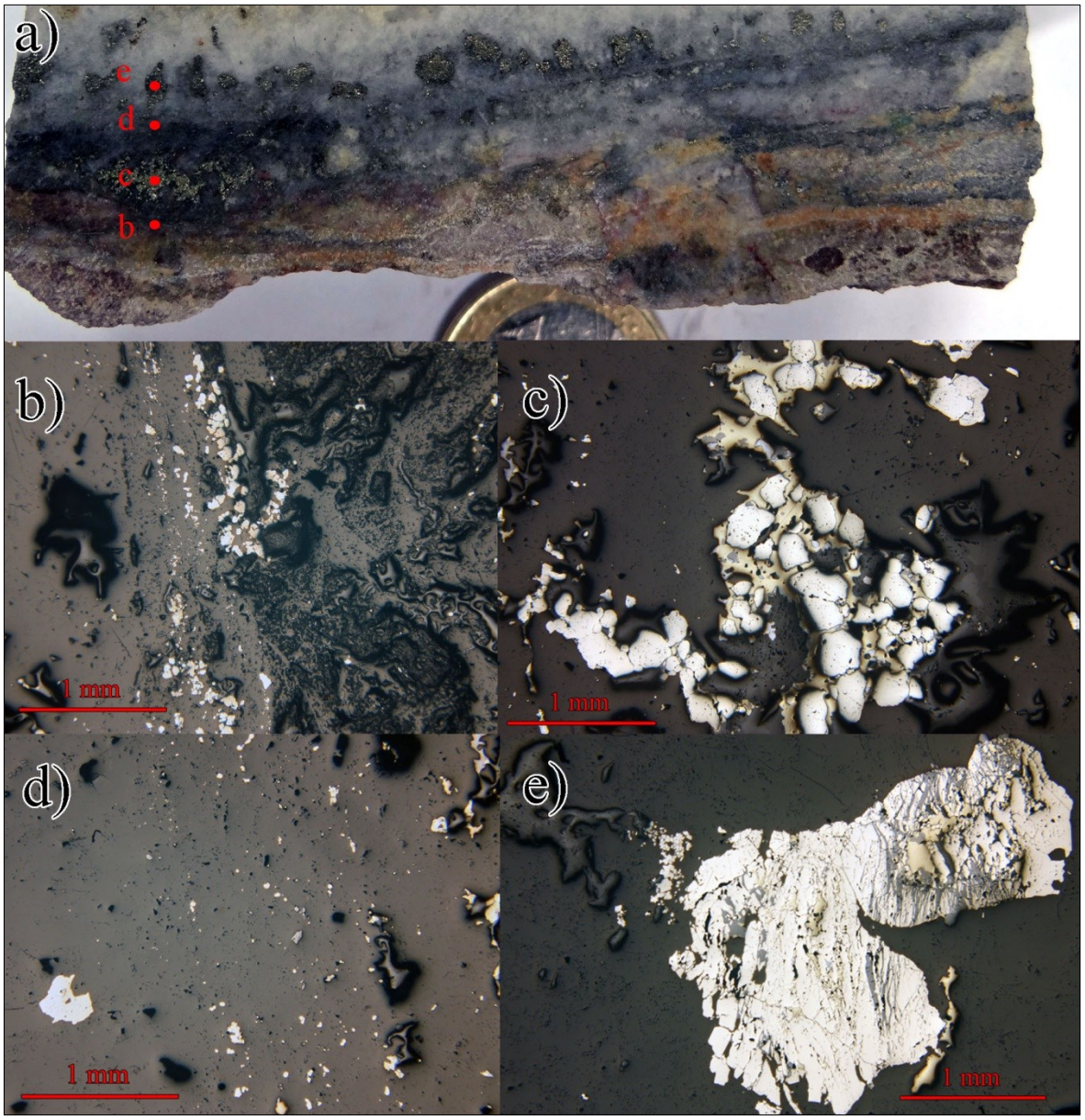

Figure 21: Photo and photomicrographs documenting the vein development in sample CHM4-59. a) Hand specimen showing micro-areas (b-e) from the wall contact to the vein center. b) Fine-grained sulfides (mostly pyrite) are aligned parallel to the vein margins. c) Quartz matrix becoming coarse-grained with large subhedral pyrite grains and interstitial chalcopyrite and sulfosalts. d) Matrix becoming finer grained with small vugs and thin trails of sulfides. e) Polyphase sulfide grain from the interior part of the vein. Large, fragmented pyrite crystals with fillings of chalcopyrite and sphalerite. The micro-fractures are oriented parallel to the vein wall.

Figure 22: Photos of drill core BH-CHM7 documenting massive banded sulfide veins (so called ginguro) in altered volcanics. a) The relatively compact drill core between 21.00 and 24.70 m is dominated by greenish advanced argillic alteration adjacent to intersects of cm thick ginguro bands (e.g. at 21.20, 22.10, 23.70 m depth) and grades into sericitic alteration indicated by brownish-beige colors. b) The altered andesitic wall rock of sample CHM7-23.7 includes a 3 cm thick ginguro veinlet that is bordered by colloform bands of fine-grained quartz along the wall contact. c) Ginguro bands also occur as 10 to 20 cm thick veins of massive sulfides containing lots of voids; the light mineral is anhydrite, which has been partly leached leaving some cavities. d) Sericitic alteration (brown staining) in strongly fragmented drill core BH-CHM7 grading into a greenish-gray rock indicating advanced argillic alteration (partly silicification?) next to the ginguro vein.

4.2.4.3 Crustiform veins

Crustiform veins were defined after Shimizu (2014) and are characterized by successive, narrow, subparallel layers of mineral crusts. These crusts are composed of mostly coarse-grained quartz and carbonate showing a variety of textures with symmetric layering relative to the footwall and hanging wall of the vein. This vein type was only found in the drill cores. They are widely distributed in the middle to deeper sections of Chah-Mesi between 2450 and 2327 m a.s.l. and were intersected by drill cores BH-CHM1 (Figure 23 a), BH-CHM2, BH-CHM4 and BH-CHM7 (Figure 23 e). The individual veins are 3 to 5 cm thick (Figure 23 b, c). Their spatial distribution indicates that crustiform veins occur distally of the massive quartz veins.

Gangue minerals comprise white to gray colored fine- to coarse-grained quartz and carbonates. Comb quartz and euhedral carbonate rhombohedra are typical textures in crustiform veins as well as bands of jigsaw quartz and euhedral quartz hexagons (Figure 24 d). Crustiform veins are mirror-plane symmetric and show similar textural characteristics as the banded veins; i.e., individual layers reflect differences in color, mineralogy and texture. A systematic gradation is to be seen in gangue mineral grain size with rather fine-grained centers and coarse-grained margins. Quartz is the dominant primary gangue mineral, but carbonate is also present (Figure 24 e). Zoning in crustiform veins from wall contact to the vein center commonly starts with a mm thick selvage of wallrock carbonatization (Figure 23 d) followed by barren, coarse quartz bands grading into fine-grained cavity-rich quartz containing Cu-sulfides, carbonate and minor sheet silicates (i.e., illite-sericite, clay minerals). These bands are followed by a layer of comb quartz and subhedral mosaic-textured quartz, which are associated with coarse-grained sphalerite often exceeding 2 mm in size (Figure 24 a). In the innermost zone, commonly comb quartz fills the remaining open spaces; the long axis of quartz is oriented perpendicular to the vein walls.

Ore minerals record a spatial zonation where Cu-Fe-dominated sulfide aggregates occur mostly along the vein margins and grade into a Pb-Zn rich assemblage (Figure 24 a). Cu-Fe sulfides include rounded and partly cataclastic pyrite grains enclosed by chalcopyrite (Fig. 10 c). This sulfide texture is comparable to the one described from the ginguro ore. However, towards the vein center the ore assemblage becomes dominated by Pb-Zn minerals with only minor amounts of pyrite and chalcopyrite (Figure 24, b). In contrast to the grain size of the gangue minerals which decreases towards the center, the grain size of the ore minerals increases towards the vein center.

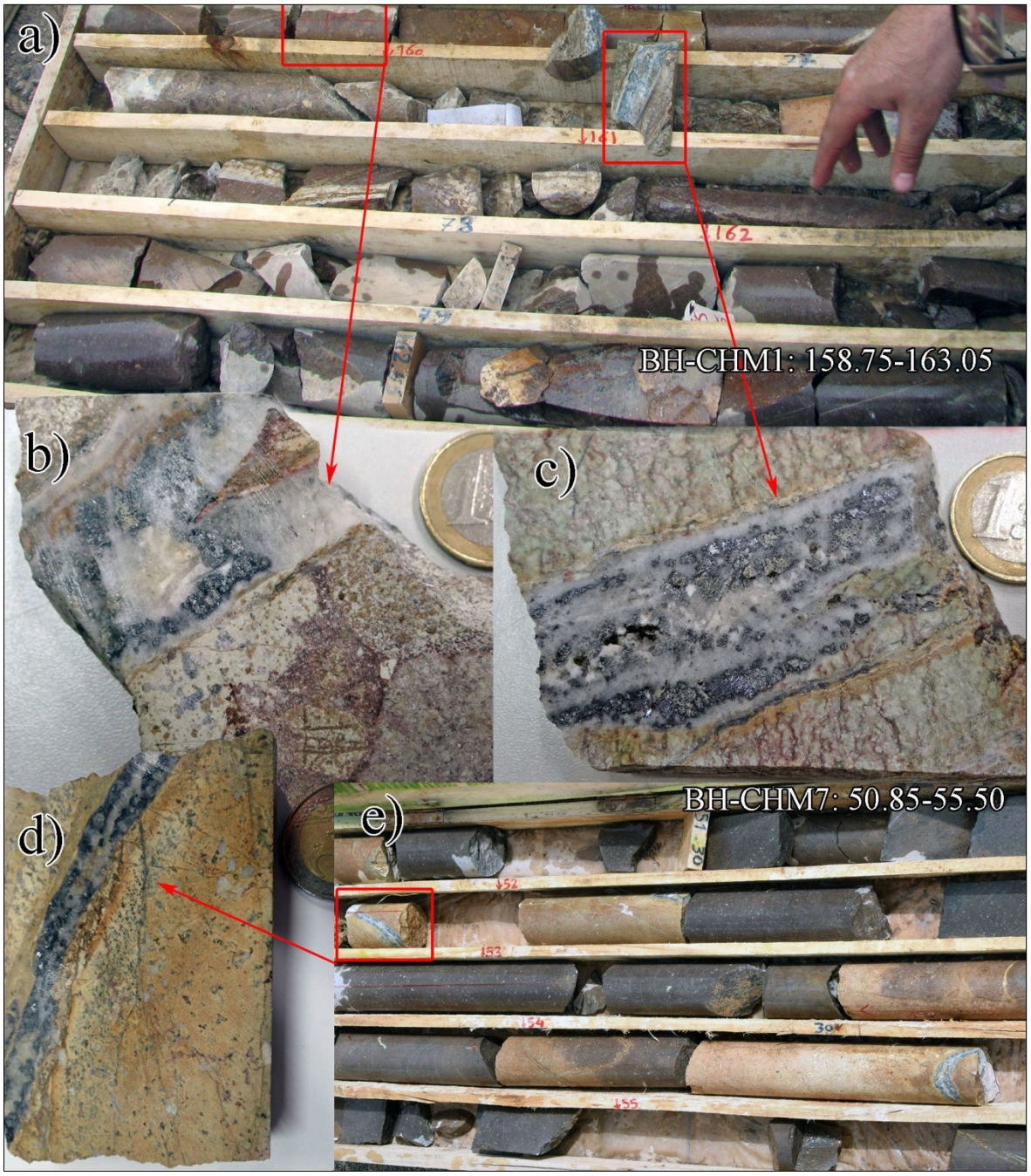

Figure 23: Photographs of crustiform veins and adjacent wallrocks from drill cores BH-CHM1 and BH-CHM7. a) Crustiform veins occurring in altered pyroclastic rocks at about 160.0 m depth in drill hole BH-CHM1. b) Crustiform vein with quartz, sphalerite and galena. An angular wallrock fragment is to be seen in the center of the vein; CHM1-159. c) Vein showing crustiform banding with coarse-grained sulfides (sphalerite, galena); a wallrock fragment (greenish) and voids are also to be seen; CHM1-160. d) 2 cm thick crustiform vein with 2 mm thick carbonate halo and argillic alteration in the adjacent volcanics; CHM7-52. e) Crustiform veins intersecting volcanic host rocks. Light coloring in rocks next to the veins are due to argillic and sericitic alteration; the alteration halos are 0.3-0.5 m thick. Dark colors are caused by propylitic alteration predating argillic /sericitic alteration and vein formation.

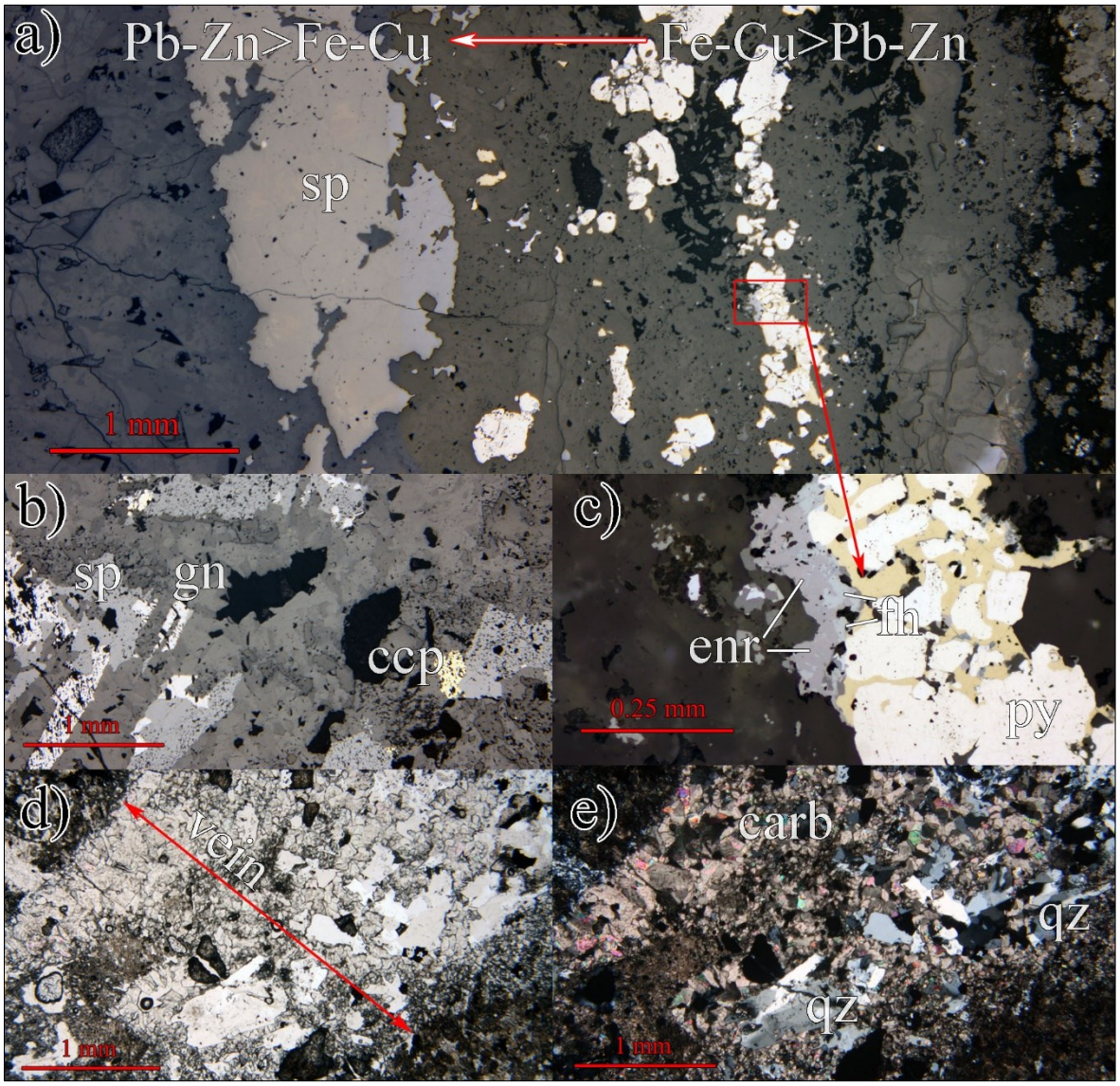

Figure 24: Photomicrographs of crustiform vein textures in samples CHM7-52 and CHM7-94. a) Cross-section through crustiform vein. Fe-Cu-dominated sulfides close to the wall rock (right, close-up image in c) grade into a coarse-grained Pb-Zn-dominated assemblage towards the center (left); CHM7-52, RL-PPL. b) Central part of crustiform vein with sphalerite, galena and minor chalcopyrite; CHM7-94, RL-PPL. c) Detail of a) showing the sulfide assemblage at the vein margin with subhedral pyrite cemented by chalcopyrite and sulfosalts (enargite, luzonite-famatinite, fahlore); CHM7-52, RL-PPL. d) Approximately 3 mm thick veinlet consisting mainly of subhedral to euhedral carbonate (brown-beige) and subhedral quartz (colorless); CHM7-94, TL-PPL. e) Same area as in d) with coarse-grained quartz enclosed in inequigranular carbonates. Carbonate crystals become more fine-grained towards the center; CHM7-94, TL-XPL.

4.2.4.4 Mineralized breccia zones

Although this is not a typical vein-controlled mineralization it is included in this description because of the mineralogical similarities with the veins. Two samples of mineralized breccias were collected from drill cores BH-CHM2 and BH-CHM7 (Figure 25 a, b). Both occur at a depth of 2351 m a.s.l and might represent a slightly inclined breccia body. However, if the two breccia zones are connected is not sure.

This type of breccia mineralization consists of fragmented and altered wallrocks cemented by gangue minerals and sulfides. Normally, intersections of these breccia ores in the cores are 0.3 to 1 m thick, but also thinner, only cm-thick breccia veins were observed in sample CHM2-81 (Figure 26 e). The breccias contain up to several cm large angular to subrounded components of the adjacent pyroclastic wallrocks (Figure 25, c, d). The components are affected by intense advanced argillic alteration resulting in nearly complete decomposition of the primary minerals. Secondary minerals consist of irregularly distributed aggregates of clay minerals, microcrystalline quartz and sericite tracing the cleavage and crystal faces of decomposed primary minerals. Drill core sections adjacent to the breccia zones also show strong argillic alteration of primary minerals and transformation into sheet silicates (Figure 25 a). Gangue minerals of the matrix consist of quartz, carbonate and minor amounts of fluorite and anhydrite (Figure 26 c, d). Quartz often occurs as comb quartz and prismatic subhedral crystals. Carbonates are less abundant, but often forms euhedral rhombohedra. Anhydrite and barite occur as euhedral rectangular crystals and acicular shapes, respectively. Fluorite only forms anhedral isometric crystals (Figure 26, c).

Ore minerals are bound to the breccia matrix and are less than 20 vol%. They mainly consist of Fe-Cu-dominated sulfide aggregates that show similar characteristics to ginguro; i.e. rounded pyrite grains enclosed in chalcopyrite together with sulfosalts, sphalerite and galena. Sphalerite and galena (up to 2 mm) also occur separate from the Fe-Cu-dominated assemblage.

Figure 25: Photographs of mineralized breccias. a) Intersection of mineralized brecciated zone in drill core BH-CHM2 at approx. 136 m depth. b) About 1 m thick intersection of mineralized breccia at 140 m depth in drill core BH-CHM7. The core shows advanced argillic alteration (brownish) grading into propylitic alteration toward depth. c) Angular to subangular altered wallrock fragments embedded in a matrix of quartz (white) and sulfides (dark, metallic lustre); note irregularly shaped vugs of several mm in size; CHM7-140.8. d) Subangular pyroclastic components up to several cm in size cemented by gangue quartz and sulfides; CHM2-136.

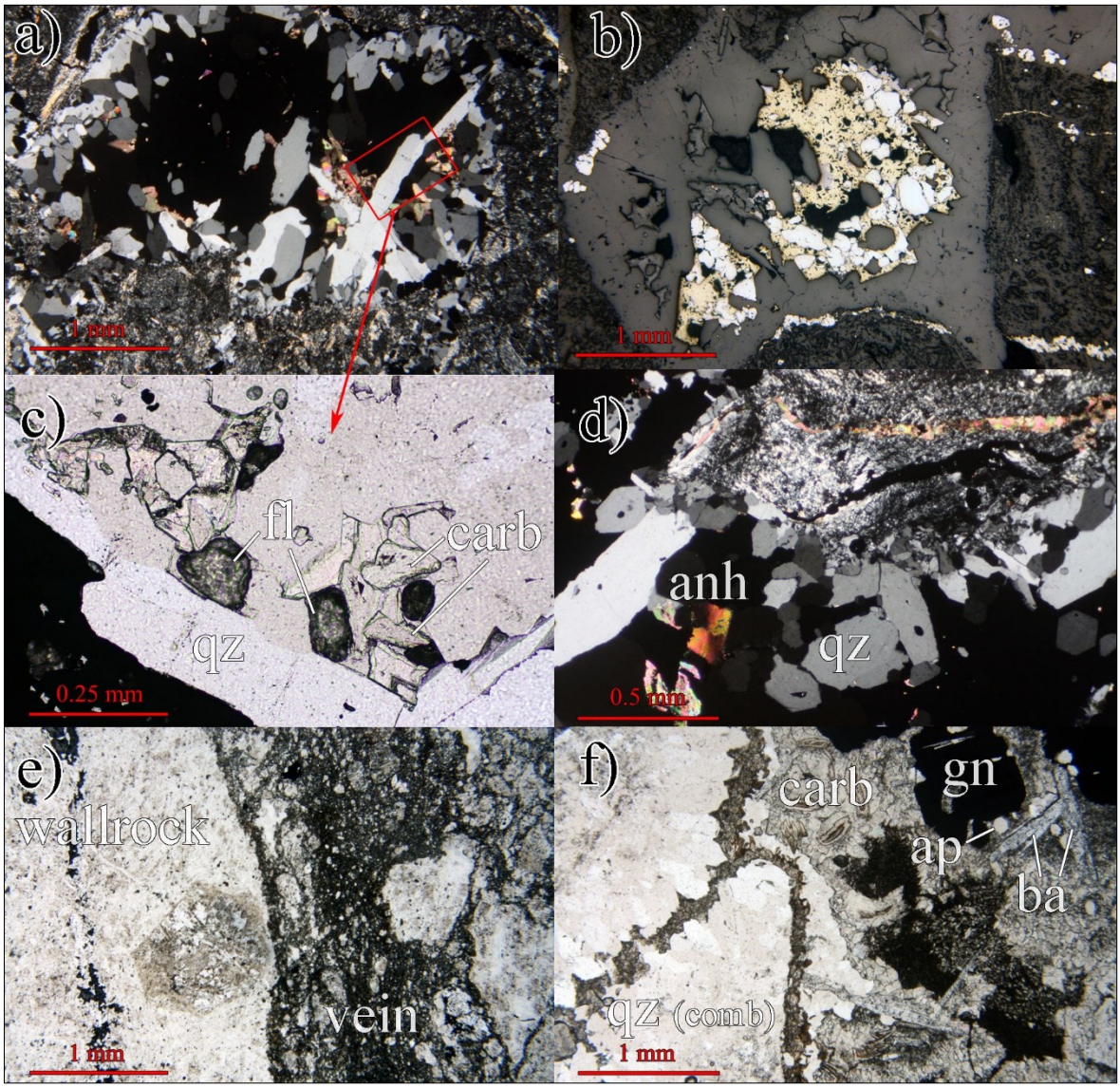

Figure 26: Photomicrographs of breccia microtextures in samples CHM2-136 and CHM2-81. a) Open spaces between breccia components are filled with prismatic quartz and comb quartz. The crystals are partly oriented perpendicular to wall contacts. Opaque phases of the interior part are sulfides (see b); CHM2-136, TL-XPL. b) Sulfides consisting of subhedral pyrite grains enclosed in chalcopyrite and sulfosalts; CHM2-136, RL-PPL. c) Detail of a) showing prismatic quartz associated with carbonate and fluorite; CHM2-136, TL-PPL. d) Strongly silicified breccia component (upper right area) consisting primarily of microcristalline quartz and cut by thin carbonate veinlet. The gangue minerals are subhedral quartz and anhydrite (lower area); CHM2-136, TL-XPL. e) Contact of altered wallrock with highly decomposed pyroxene (?) phenocryst (left) and cm thick breccia vein (right). Opaque phases in altered wallrock are fine-grained Pb-Zn sulfides and pyrite; CHM2-81, TL-PPL. f) Interior part of breccia veinlet consisting of comb quartz, carbonate, small apatite and elongated baryte crystals. Carbonate is coarse-crystalline (right) or forms microcrystalline fringes around comb quartz (left, gray aggregates). Opaque phase is coarse-grained galena; CHM2-81, TL-PPL.

4.2.5 Prehnite-calcite-epidote veins (PCE-type)

In the field, this type of vein forms sheeted veins dissecting the country rocks in a spacing of about 20 cm (e.g., at the summit of the hill south to the open pit, Figure 9 a). The veins are oriented E-W and dip middle-steeply towards the north. They are 4 to 10 cm thick and show banding of varying colors (light to deep green or a yellowish white, Figure 27 a). Wallrock contacts are sharp to slightly undulating. The adjacent host rocks are characterized by propylitic alteration with high contents of calcite together with chlorite, phyllosilicates and slightly altered rutile (Figure 27 d). The dominant vein mineral is prehnite, which has anomalous interference colors (blueish-white) and is intergrown with coarse-grained (up to 2 mm) calcite (Figure 27 b). Both minerals are anhedral. Euhedral acicular and partly zoned clinozoisite/epidote is a minor mineral. Textural relationships indicate that clinozoisite/epidote overprint earlier formed prehnite and calcite (Figure 27 b, c). In reflected light up to 50 µm large grains of native copper have been observed within prehnite (Figure 27 e).

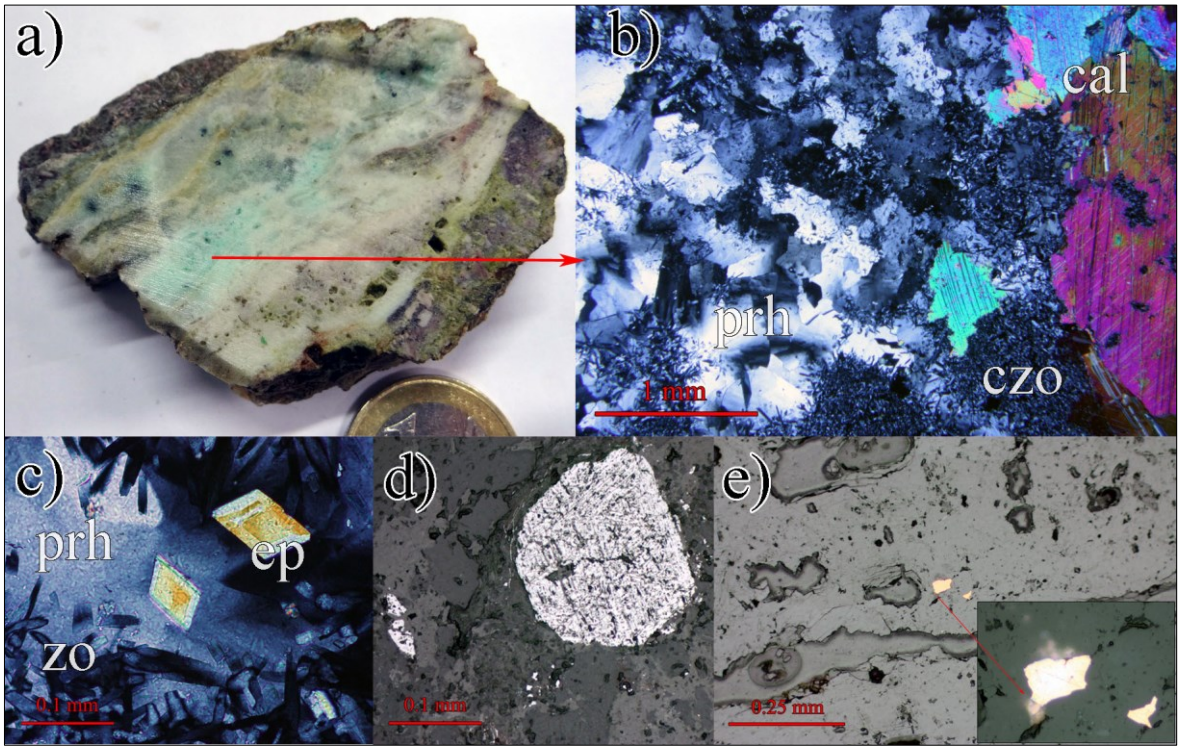

Figure 27: Photograph and microphotographs of PCE veins in sample CHM3B. a) Hand specimen showing layered texture of prehnite-calcite bands (beige-white) and clinozoisite/epidote-in the center (greenish). b) Calcite (high interference colors) associated with prehnite and acicular clinozoisite; TL-XPL. c) Details showing euhedral epidote, acicular clinozoisite and prehnite (bluish grey); TL-XPL. d) Partly altered rutile associated with microcrystalline quartz (dark gray) and phyllosilicates (light gray) from wallrock; RL-PPL. e) Small grain of native copper embedded in prehnite; RL-PPL.

4.2.6 Calcite veins (CC-type)

Calcite veins are ubiquitous occurring throughout the whole Chah-Mesi deposit. Also, in the drill cores they are common and there is no relation to depth or geographic position. The calcite veins are most common in zones of propylitic alteration. They form up to several cm sheeted veins that intersect all other vein types and the host rocks; i.e. they are the youngest ones. In the western part of the open pit, steeply west dipping calcite veins up to 10 cm in thickness crosscut older middle-steeply north dipping PCE-type veins (Figure 9 b). In the deeper sections of the drill holes calcite veins also show breccia texture and include angular fragments of dissected volcanic rocks (Figure 28 a). Commonly, veins have straight to undulating contacts (Figure 28 b).

The CC veins contain coarse-grained calcite and minor amounts of quartz, but they are not mineralized. Quartz is always present as small, anhedral grains and restricted to vein selvages (Figure 28 b). Coarse calcite forms subhedral grains often with straight mutual grain boundaries (Figure 28 a, d, e). Microfractures containing fine-grained calcite are surrounded by mm-thick symmetric halos of strong carbonate alteration. They also crosscut the coarse-grained veins although an alteration halo is not visible in those (Figure 28 c). In contrast to carbonate-bearing mineralized veins, calcite veins do not show any zonation. Microscopic textures show that two generations of calcite veins are present and crosscutting relationships indicate that coarse-grained calcite veins are older than the fine-grained calcite veinlets that tend to preferentially reopen and follow QCS veins.

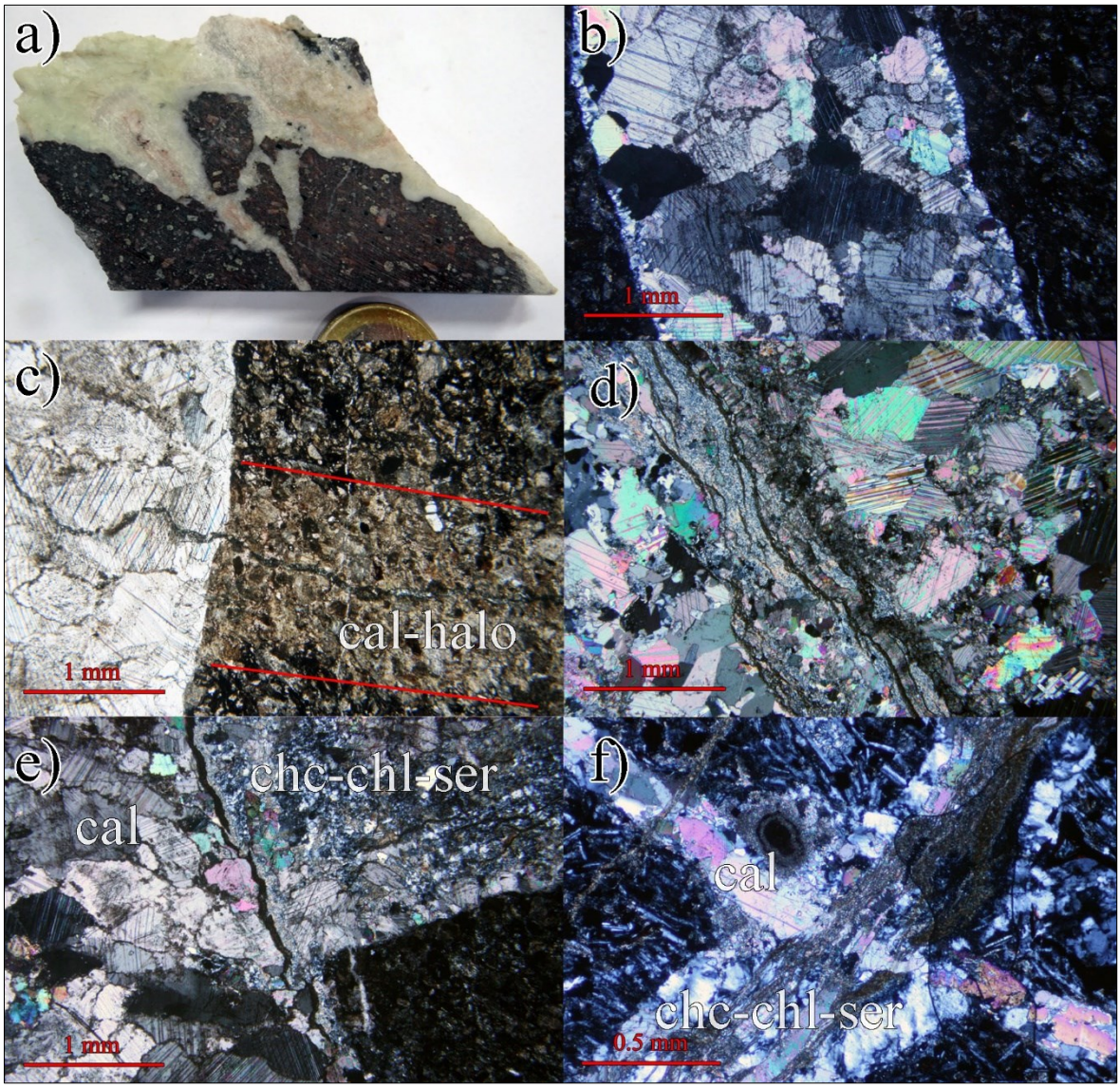

Figure 28: Photo and photomicrographs (b-f, all taken in transmitted light) of calcite veins. a) Anastomosing calcite vein showing fragmentation of pyroclastic wallrock with angular components included in calcite matrix; sample CHM4-117. b) Calcite veinlet with sharp contact to host rock. Inequigranular calcite grains show distinct lamellar twinning; sample CHM1-172, XPL. c) Fine grained microfracture calcite producing a calcite-rich alteration halo in the host rock; it also crosscuts the coarse-grained calcite vein; sample CHM1-172, PPL. d) Vein of coarse calcite interleaved by undulating veinlets containing fine-grained calcite; sample CHM1-115, XPL. e) Coarse calcite vein crosscutting QCS vein and altered host rock (lower right). f) Thin veinlet of coarse calcite (upper left to lower right) crosscutting QCS vein (upper right to lower left). Microfractures with fine-grained follow the QCS direction and crosscut the coarse calcite veinlet.

4.3 Alteration

Several alteration types were documented in the Chah-Mesi deposit (Table 10). Regarding the scale, a more regional alteration (deposit scale) has to be distinguished from local alteration, the latter related to individual veins. Adjacent and within to major fault zones silicification dominates and most of the adjacent O-type veins have advanced argillic alteration halos. Sericitic alteration forms a contiguous zone to advanced argillic alteration and is the most common type of alteration at Chah-Mesi deposit. Propylitic alteration formed distally to the ore deposit. In the northernmost part of Chah-Mesi, towards the Meiduk porphyry copper deposit, potassic alteration has been recorded in BH-CHM4.

Alteration assemblages were only determined by microscope. Thus, a definite distinction of very fine-grained minerals and particularly of the clay minerals was not possible. The nomenclature used in the following is based on the terminology of Thompson and Thompson (1996) and the well-established alteration types recorded from porphyry copper systems as summarized by Sillitoe (2010).

Table 10: Types of hydrothermal alteration at Chah-Mesi.

Alteration	Mineral assemblage	Description
Silicic	Quartz, chalcedony	adjacent to O-type veins, mostly related to massive and banded textures, vuggy-residual silica
Advanced argillic	Clay minerals (kaolinite, montmorillonite, illite-smectite), quartz, pyrite, sericite, APS?, Fe-oxyhydroxides	restricted alteration halos around veins dominated by high-sulfidation mineral assemblages
Sericitic	Sericite, chlorite, clay minerals, calcite	most present alteration type, dominates the central parts of the deposit, transition into shallow argillic and lateral propylitic, borders potassic towards north, QCS-veinlets
Argillic	Clay minerals (illite-smectite, montmorillonite), Fe-oxyhydroxides, quartz	strong decomposition of host rocks into mainly clay minerals at shallow deposit levels
Propylitic	Calcite, chlorite, epidote, sericite, clay minerals, pyrite	occurs as an outer regionally extensive alteration zone, PCE-, CC-veinlets
Potassic	Biotite, chlorite, sericite, anhydrite	forms peripheral alteration zone in wallrocks, associated with porphyry-related veins, in proximity to Meiduk

4.3.1 Silicic alteration

The zones of intense silicification with vuggy-residual silica are found mostly along the NNE-SSW trending fracture zones and are typically associated with the massive O-type veins. This extreme form of acidic leaching (Figure 30 a) decreases in intensity away from mineralized veins with an outward gradational zonation from advanced argillic through sericitic to propylitic alterations. Silicic alteration results in net addition of silica to the adjacent host rock; quartz predominantly replaces rock forming minerals at the contact between veins and their surrounding rocks. Silicic alteration also results in vast amounts of vugs and open spaces due to selective leaching of earlier formed minerals (Figure 18). Often, cavities formed by leaching preserve euhedral shapes of the former minerals. The precipitated silica is mostly inequigranular and ranges from large euhedral quartz crystals to microcrystalline chalcedony.

4.3.2 Advanced argillic alteration

This alteration type forms around veins and adjacent to silicic altered rocks (Table 10). It is dominated by clay minerals, quartz, calcite and minor amounts of sericite. The zone of advanced argillic alteration is mostly observed at around 50 m depth in the drill cores underneath the zone of argillic alteration. A clear distinction between argillic and advanced argillic alteration is not always easy, but usually the latter include higher silica and calcite contents. Altered rocks have a distinct brownish to pale yellow color and if less quartz is included, they feel very smooth. Plagioclase is completely altered into clay minerals and minor sericite. Aggregates of very fine-crystalline calcite are very common and sometimes form spherical shaped crystals (Figure 30 b). Calcite and quartz are homogeneously distributed in the whole rock and preferentially replace the fine-grained volcanic groundmass. Zones of advanced argillic alteration are often interspersed by very thin stockworks of mineralized veins, which comprise banded and crustiform textures. Also, minor amounts of a very fine-grained aluminum-phosphate-sulfate (APS) phase were found close to mineralized veins of ginguro type. The EDS analysis by EPMA (Figure 29) confirmed the presence of Al, P, Pb and minor Ca, which could indicate the presence of the alunite group mineral plumbogummite with the formula $PbAl_3(PO_4)_2(OH)_5xH_2O$. APS minerals are characteristic for advanced argillic alteration zones (Mavrogonatos et al., 2018).

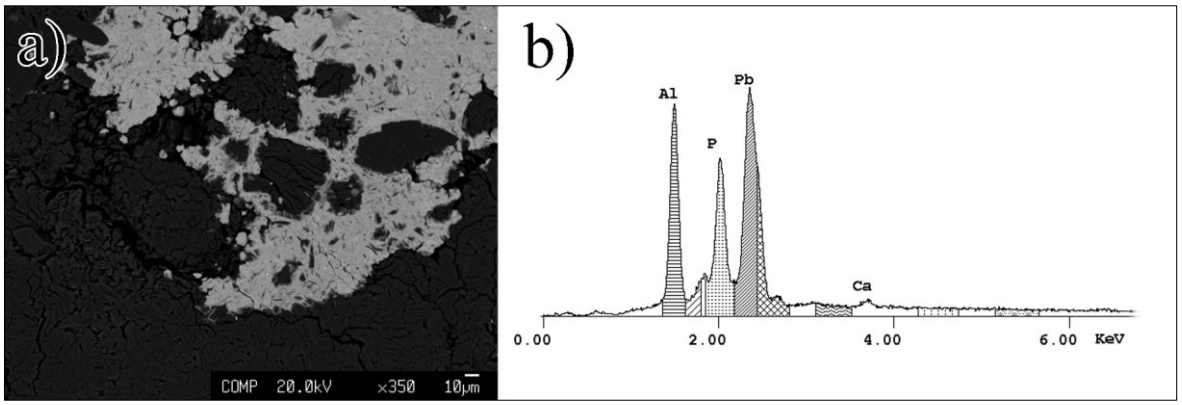

Figure 29: BSE image and EDS spectrum of APS phases occurring in advanced argillic alteration zone. a) Fine-grained aggregates of probably plumbogummite formed interstitial to gangue and ore minerals; CHM7-31.4, BSE image. b) EDS spectrum of APS phase showing the presence of Al, P, Pb and minor Ca.

4.3.3 Sericitic alteration

The sericitic alteration is widely observed in the central parts of the Chah-Mesi deposit and is associated with ore-bearing vein types. The most common mineral is sericite, which is accompanied by calcite, minor quartz, chlorite and clay minerals (Figure 30 c). They occur mostly as pervasive replacement zones of the preexisting mineral phases, whereas particularly plagioclase is affected by strong sericitization. Calcite commonly occurs as fine-grained aggregates in the matrix together with chlorite and clay. Often transition zones of advanced argillic-sericitic as well as sericitic-propylitic alteration are developed. In transitions from advanced argillic to sericitic alteration, phenocrysts are altered completely into sericite, but the silica content is higher than usual for sericitic alteration. In contrast, transitions from sericitic to propylitic alteration provide intense phenocryst decomposition into chlorite and Fe-oxides (Figure 30 d) and lower sericitization of plagioclase. A clear textural relationship between distinct mineral assemblages of two different alteration zones could not be resolved. However, sometimes it seems like sericitization postdates propylitic alteration, because typical features of propylitization occur in zones with high sericite contents. Also typical for sericitic alteration is the presence of QCS-type veinlets with higher sericite abundance. In the northernmost part of Chah-Mesi sericitization grades into potassic (biotite-rich) alteration.

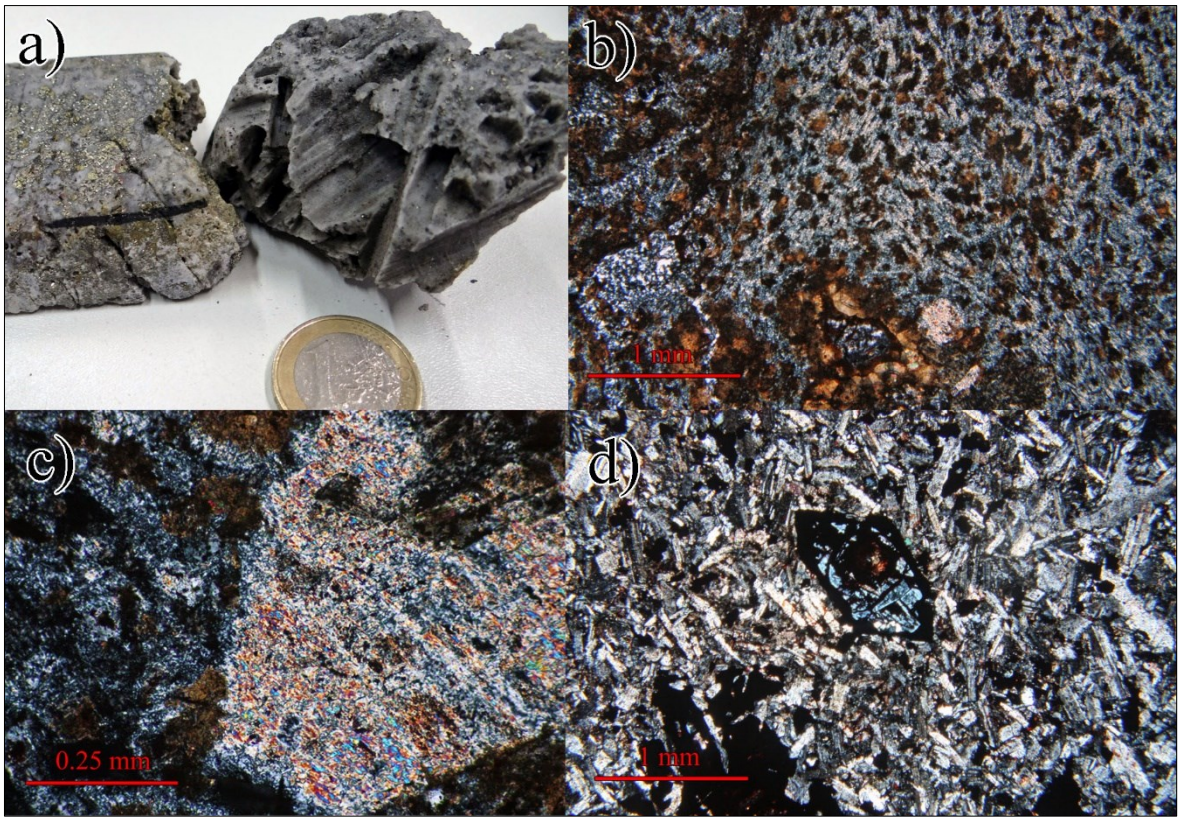

Figure 30: Photograph of a hand specimen affected by intense silicification (a) and photomicrographs showing advanced argillic (b) and sericitic alteration (c, d). a) Andesite adjacent to massive O-type vein showing strong silicification and leaching structures; CHM1-59. b) Zone of advanced argillic alteration with dusty matrix plagioclase, which is completely decomposed into clay and minor sericite (bluish-yellow). Disseminated calcite (brownish) with occasional spherical crystals (below) and fine-crystalline quartz (white-grey, to the left) are also very present; CHM1-45, TL-XPL. c) Intensely sericitized phenocryst embedded in a matrix of clay (bluish-grey) and calcite (brownish); CHM1-45, TL-XPL. d) Strongly decomposed, euhedral Fe-Mg-silicate phenocryst with pseudomorph chlorite (bluish-grey) and opaque hematite along crystal margins and fissures. Groundmass consists of sericitized plagioclase laths; CHM1-116.5, TL-XPL.

4.3.4 Argillic alteration

Rocks affected by argillic alteration were mostly observed in the shallow parts of the deposit and typically show intense decomposition into clay minerals and limonitic aggregates. Colors of weathered rocks are white and tan with dark brown to orange oxidized surfaces. Under the microscope, relict feldspars are associated with clay minerals (Figure 31 a), quartz and iron oxyhydroxides. Sometimes relicts of twinning lamellae of large plagioclase phenocrysts are still visible (Figure 31 b), however, commonly phenocrysts occur very cloudy and are completely altered. Fe-oxyhydroxides often form dendritic aggregates and commonly occur along fractures and fissures of phenocrysts. Minor quartz is irregularly dispersed within the whole rock, but also occurs as veinlets with similar texture of D_1-type veinlets. Pyrite is mostly weathered to Fe-oxyhydroxides (Figure 15 e). Further, veinlets in argillaceous zones often have thin selvages of minor sericite and chlorite.

4.3.5 Propylitic alteration

The rocks affected by propylitic alteration have a greenish color and are to be found in the distal peripheral parts and the deepest parts of the deposit. Propylitic alteration is present as pervasive regional alteration. Characteristic alteration minerals are epidote and chlorite with varying amounts of calcite and minor quartz. Epidote occurs as irregularly distributed euhedral crystals within the matrix (Figure 31 c). Chlorite forms very fine flakes and mostly pseudomorph after primary Fe-Mg-silicates. Commonly, Fe-Mg-silicates are selectively altered and intensely decomposed into an assemblage of chlorite, Fe-oxides and occasionally quartz or calcite. Fe-oxides usually form along the rims and micro-fractures of primary minerals. Calcite is abundant and mostly forms interstitial aggregates. Plagioclase phenocrysts are often replaced by calcite, but also very thin veinlets are present of fine-crystalline calcite. Veinlets of CC-type and PCE-type are associated with propylitic alteration occurring in the deepest parts of the deposit as well as in the peripheral area on the surface.

4.3.6 Potassic (biotite-rich) alteration

The zone of potassic alteration is restricted to the northernmost part of Chah-Mesi, i.e. close to the Meiduk porphyry stock. The diagnostic alteration mineral of the potassic alteration zone is biotite, associated with minor amounts of chlorite, anhydrite and sericite. Rocks affected by potassic alteration are greenish to dark grey though biotitization is only recognizable microscopically. Biotite is present as very fine-grained, equigranular flakes, which selectively replace phenocrysts of Fe-Mg-silicates and also occur disseminated in the matrix. The original rock texture is often well preserved despite the replacement of phenocrysts by biotite aggregates (Figure 31 d). Chlorite is also very common and mostly forms pseudomorph after biotite. Often, plagioclase has corroded margins and is partly to totally replaced by biotite and sericite. Anhydrite is rare and mostly forms anhedral crystals close to mineralized veins. Potassic alteration is associated with porphyry-related D_1-type and B_2-type veins.

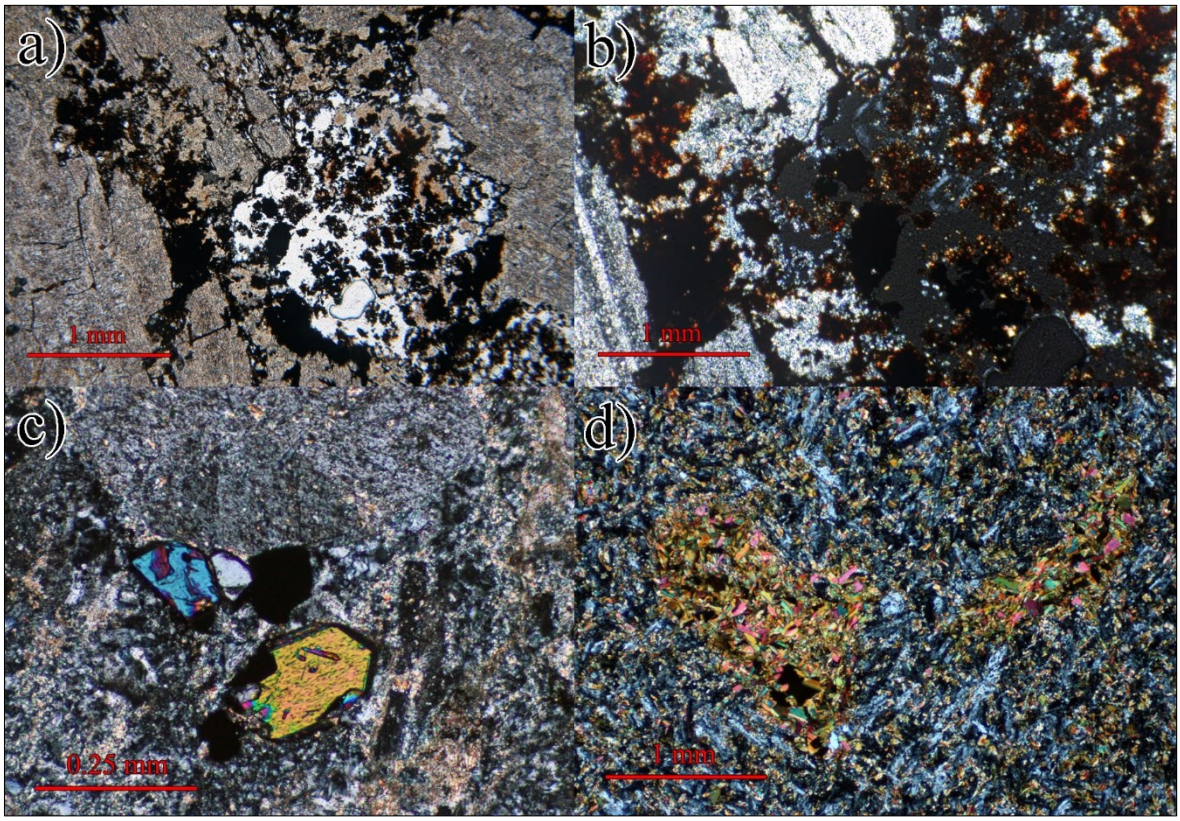

Figure 31: Photomicrographs showing argillic (a, b), propylitic (c) and potassic (d) alteration. a) Plagioclase phenocrysts are totally altered to very fine aggregates of clay minerals plus Fe-oxyhydroxides; CHM1-5, TL-PPL. b) Twinning lamellae are still visible in altered plagioclase phenocryst (lower left corner). Fe-oxyhydroxides occurring as opaque phases with increasing reddish birefringence towards the margins; CHM1-5, TL-XPL. c) Euhedral crystals of epidote (purple-blue to yellow-orange) beneath altered plagioclase with fine-grained calcite (high birefringence, red-orange); CHM1-178, TL-XPL. d) Fine-grained biotite crystals (high birefringence, yellow-green to red) selectively replacing ferromagnesian phenocrysts of a potassic altered andesite and forming a glomerophyric-like texture. Biotite also constitutes the groundmass together with (altered) plagioclase and magnetite; CHM4-20, TL-XPL.

5 Ore mineralogy

At the Chah-Mesi polymetallic vein deposit the predominant sulfide minerals are pyrite, chalcopyrite, galena and sphalerite. Associated minor minerals include enargite, luzonite-famatinite, tetrahedrite-tennantite, covellite and chalcocite. Gold is present as electrum and silver is contained in fahlore group minerals and rare Ag-bearing sulfosalts and sulfides. Ore minerals are predominantly restricted to O-type veins (Chapter 4.2.4) occurring as open space infillings or replacement ores. Gangue minerals comprise quartz and Ca-Mg-Mn-Fe-carbonates together with minor sericite, anhydrite, apatite and barite. Sulfides are either disseminated or form thin layers/bands within the veins parallel to the vein wallrock contacts. In breccia zones, sulfides form ore coatings around fragmented wallrock components and constitute a major part of the matrix. Open space deposition and replacement textures indicate a late stage hydrothermal sulfide deposition. Supergene mineralization comprises chalcocite and covellite together with goethite-limonite, malachite, azurite and anglesite.

On the basis of mineralogy and textural relationships it was tried to establish a paragenetic sequence of mineralization. An unequivocal differentiation into distinct ore assemblages was hardly possible, because almost all samples studied contained the same ore minerals, however, showing varying modal and metal proportions. These differences in metal proportions reflect a deposit-scale spatial as well as time zonation. Fe-Cu-dominated assemblages predominate in massive O-type veins in the center and in shallow ore zones grading into Pb-Zn-richer ores within banded to crustiform veins towards the periphery of Chah-Mesi deposit. Zonation is even documented on the vein scale where the outer parts (earlier) of individual composite veins tend to be richer in Fe and Cu than the interior parts (later) which contain more Pb and Zn.

This metal distribution was used to distinguish four ore zones, which exhibit extensive zonal overlap. Hence, transitions are common. Supergene mineralization is ubiquitous and restricted to superficial areas at Chah-Mesi. The established paragenetic sequence of the ore minerals in the Chah-Mesi polymetallic vein deposit is shown in Figure 37. The mineralogical and textural features of the distinct ore zones are summarized and in Table 11.

The terminology used in this chapter mainly follows Barton (1970) and Einaudi et al. (2003). *Mineral assemblages* are defined as a group of minerals that occur in direct contact (mutual grain contacts) and display no evidence of reaction with one another. Minerals that constitute an assemblage are joined with "+" signs in the text. *Mineral association* is a group of minerals that are characteristic of a given zone of mineralization, however, the minerals are not always in mutual contact and they were not necessarily all deposited at the same time (Einaudi et al., 2003). An *ore zone* designates a restricted section of the deposit, which is characterized by distinct proportions of the metallic species and mineral association (i.e. Fe-Cu- or Pb-Zn-dominated). The term *mineralization stage* is used for a group of phases that represents an interval of deposition during which no discernible chemical or physical change has happened (Barton, 1970). The term *paragenesis* refers to the sequential formation of minerals (Craig and Vaughan, 1994).

5.1 Ore zoning

The study of mineralized samples from four drill cores reveals lateral as well as depth variations of the ore mineral associations in the Chah-Mesi deposit. Four ore zones (OZ) are distinguished on the basis of the metal proportions and mineral associations. Also, the different ore zones can be linked with certain vein-types and ore textures. The characteristic features of the different ore zones are listed in Table 11.

Table 11: Mineralogical and textural characteristics of ore zones.

Ore zone	Mineral association		Vein type	Ore texture	Metal proportion
	major	minor			
OZ 1	py, ccp	enr, luz, bn, sp	(vuggy-) massive	disseminated, cavity fillings, replacement	Fe-Cu > Pb-Zn; <Ag
OZ 2	py, ccp, sp, gn	enr, luz-fm, tn-tt, Au, Ag-sulfides	(massive), banded, crustiform, breccia zones	sulfide layers, ginguro, disseminated, mostly in exterior vein parts	Fe-Cu ≥ Pb-Zn; >Ag
OZ 3	sp, gn	py, ccp, tn-tt, enr, luz-fm, Au	banded, crustiform	coarse sulfide layers, mostly in interior vein parts	Fe-Cu < Pb-Zn; <Ag
OZ 4	py, ccp, sp, gn	cc, cv, mal, goe, az, ang, anh	massive, banded	replacement and decomposition of hypogene minerals	Fe-Cu > Pb-Zn; >Ag

Ore zone 1 is concentrated in the central part of the deposit in the north of the Chah-Mesi open pit and is dominated by Fe-Cu-rich sulfides. This zone preserves mostly ore mineral associations of the early mineralization assemblage grading into main stage assemblages towards the depth and the periphery of the deposit. A key observation is the change of ore minerals with increasing abundance of tennantite-tetrahedrite at costs of enargite and luzonite-famatinite (Figure 32). As will be discussed in chapter 7.3.1 this reflects transition of high-sulfidation state assemblages into intermediate-sulfidation state assemblages. Minor sphalerite postdating Fe-Cu sulfides was observed in the outer parts of OZ 1. Gold is generally absent. The occurrence of massive quartz veins and replacement ores with vuggy quartz texture is restricted to this ore zone. Also, ore textures are dominated by disseminated sulfides filling open spaces and cavities. Gangue minerals are mainly quartz with only minor Ca-Mg-Mn-Fe-carbonates and phyllosilicates.

Ore zone 2 represents a transition zone between Fe-Cu and Pb-Zn dominated areas, respectively, and is characterized by an increase of sphalerite and galena. Ore zone 2 surrounds OZ 1 and is dominated by ore mineral assemblages of the main stage. Chalcopyrite is the prevailing sulfide followed by pyrite, sphalerite and galena, which increase towards the depth and laterally in the deposit. Moreover, fahlore group minerals outweigh enargite and luzonite-famatinite (Figure 33 and Figure 34). Precious metals are also present and occur as small grains of electrum (Figure 38) and Ag-bearing fahlore minerals or exotic Ag-sulfosalts. The majority of mineralized veins in OZ 2 are of the banded and brecciated types, but also transitions of massive-banded and banded-crustiform veins were observed. Ore textures commonly comprise layered sulfides, ginguro veins as well as subordinate disseminated ores. Quartz is still the dominant gangue minerals, but an increase of carbonates and phyllosilicates is apparent.

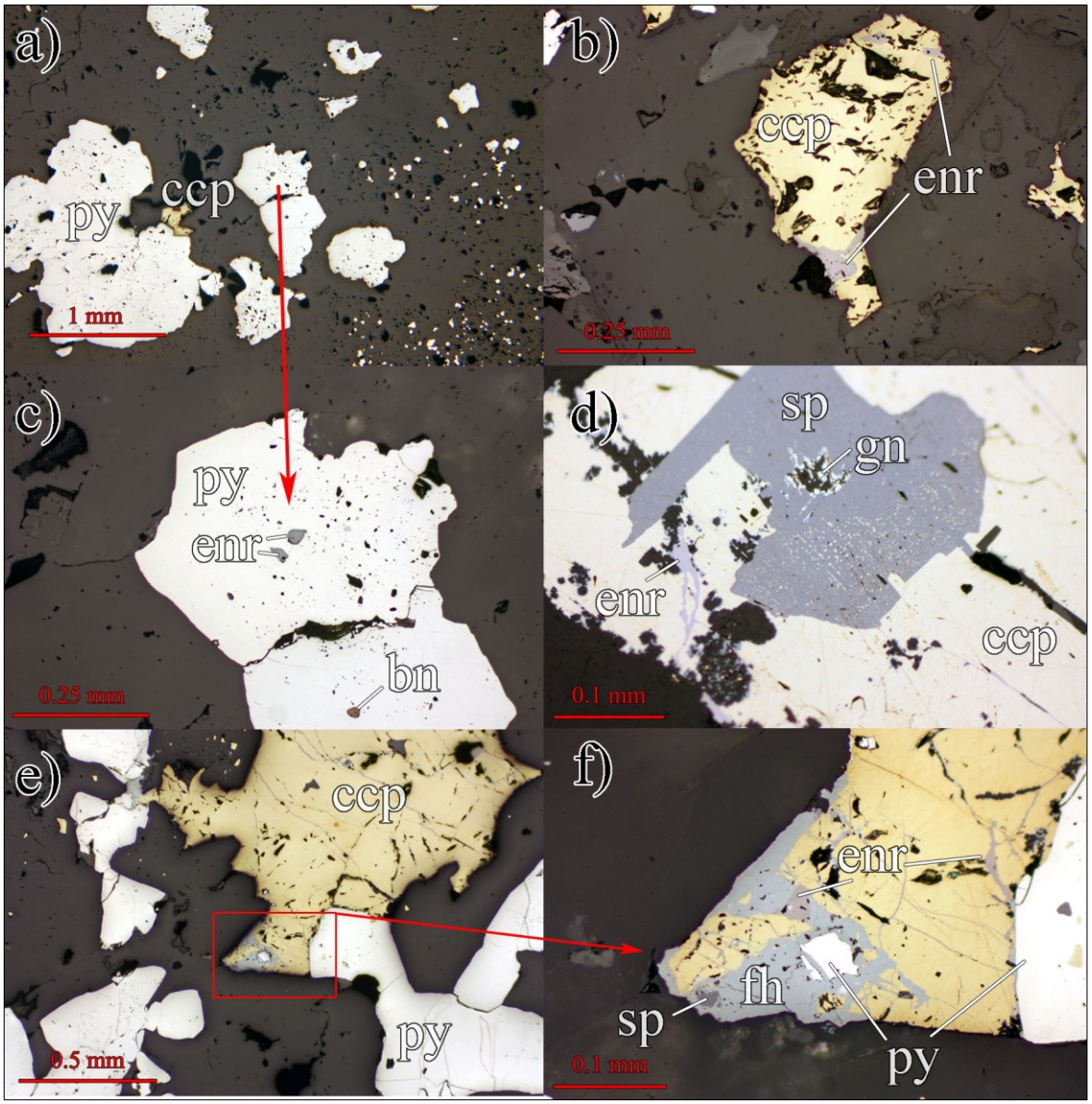

Figure 32: Photomicrographs of ore associations of ore zone 1 under reflected light. a) Coarse subhedral pyrite grains and chalcopyrite in a massive quartz vein; CHM1-55.7, PPL. b) Chalcopyrite intergrown with enargite; CHM1-44, PPL. c) Subhedral pyrite grains with small rounded inclusions of enargite and bornite; CHM1-55.7, PPL. d) Rare sphalerite with tiny crystallographic oriented inclusions of chalcopyrite ("chalcopyrite disease") intergrown with coarse chalcopyrite; tiny euhedral galena in center of sphalerite; CHM1-59, PPL. e) Coexisting chalcopyrite and pyrite intergrown with partly euhedral quartz gangue; CHM1-59, PPL. f) Enlarged micro-area of e) showing overgrowths and micro-fractures filled with enargite and fahlore dissecting chalcopyrite and pyrite; CHM1-59, PPL.

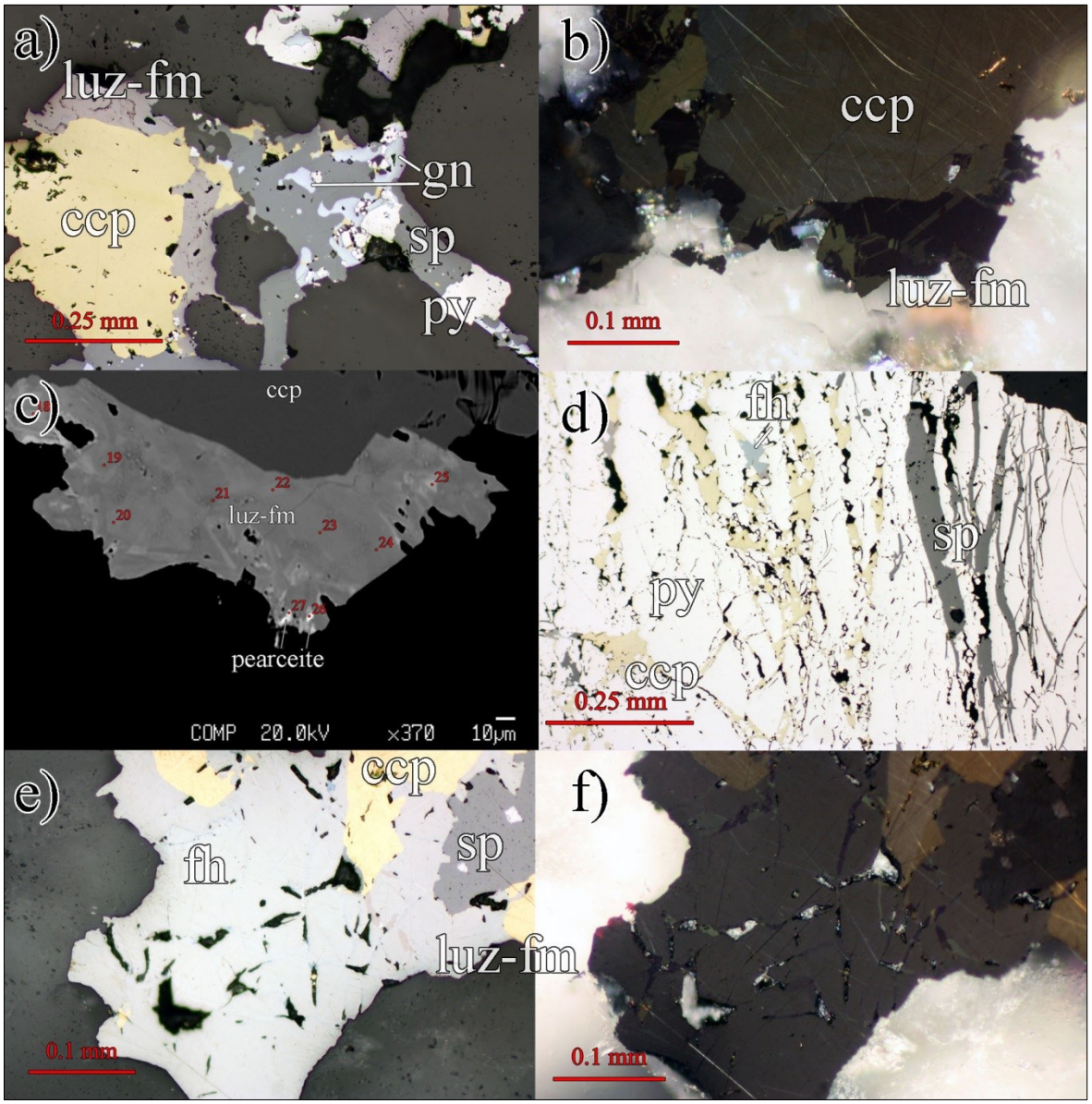

Figure 33: Photomicrographs showing ore associations and microtextures of sulfides in ore zone 2 (increasing Pb-Zn content). a) Chalcopyrite rimmed by luzonite-famatinite. Next to it a polyphase aggregate of sphalerite, galena and pyrite; CHM2-89, RL-PPL. b) Luzonite intergrown with chalcopyrite; luzonite shows distinct lamellar twinning and greenish interference colors under crossed polarizers; sample CHM2-89, RL-XPL. c) Detail of luzonite-famatinite overgrowth shown in a) (turned 180°) documenting the complex internal compositional zonation of these sulfosalts. Minute bright grains of pearceite occur at the margin; sample CHM2-89, BSE image; for EPMA analyses (numbers in red) see appendix III; d) Microfractures of cataclastic pyrite are filled with chalcopyrite and fahlore (left) as well as sphalerite (right); CHM4-59, RL-PPL. e) Sulfosalt assemblage at margin of chalcopyrite showing luzonite-famatinite intergrown with fahlore. Sphalerite with cusp and carious texture overgrows chalcopyrite and luzonite; CHM2-89, RL-PPL. f) Same image as in e) showing rare red internal reflections of fahlore under crossed nicols; CHM2-89, RL-XPL.

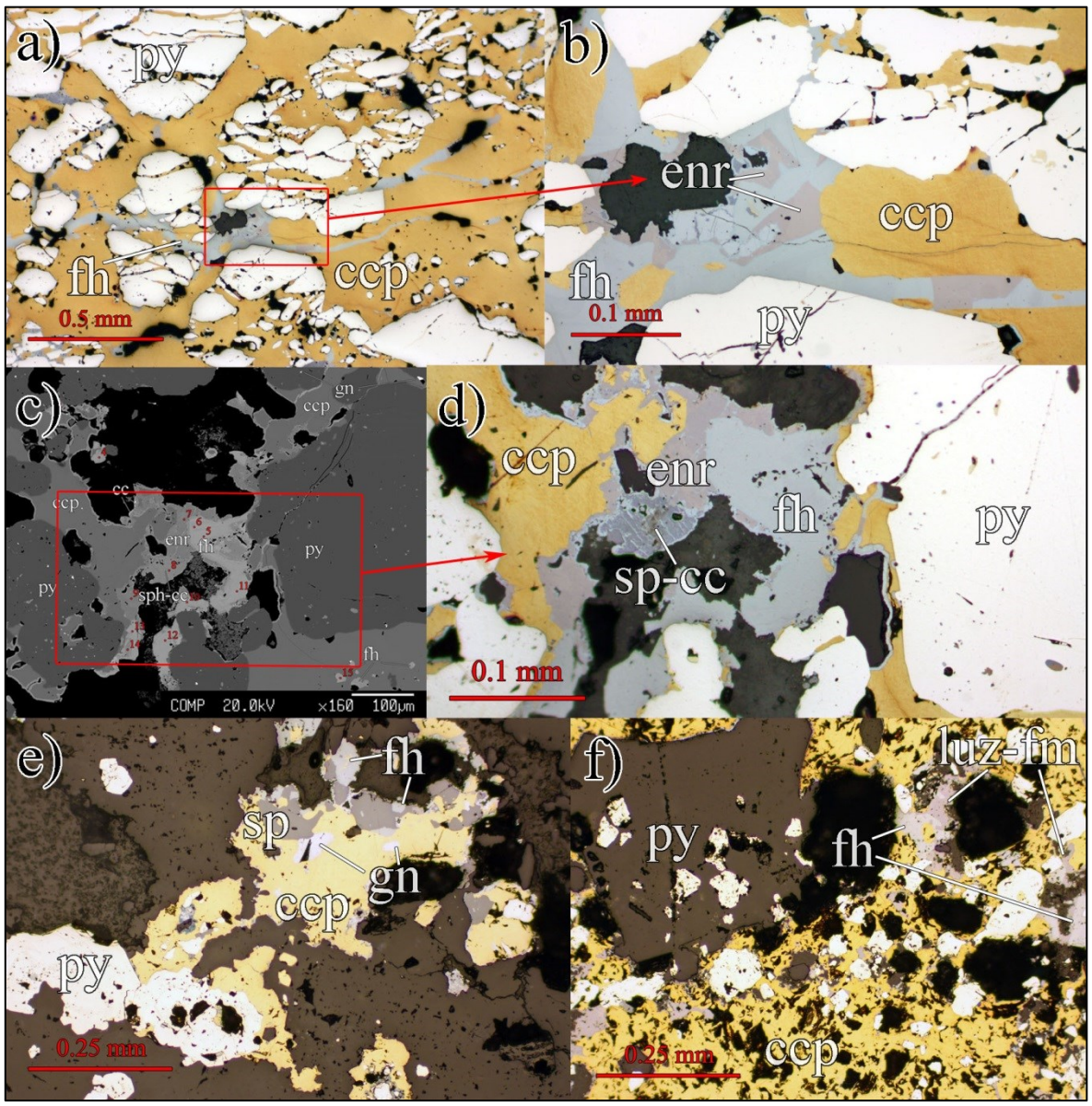

Figure 34: Photomicrographs showing ore textures and mineral associations in ore zone 2 (increasing Pb-Zn content). a) Massive chalcopyrite enclosing fragmented pyrite crosscut by veinlets filled with fahlore and enargite; sample CHM2-69, PPL. b) Detail of a) showing the intergrowth of fahlore and enargite; sample CHM2-69, PPL. c) Zoned sulfosalts (enargite, fahlore) occurring interstitial to massive chalcopyrite and pyrite; CHM2-69, BSE image. d) Main stage sphalerite associated with fahlore and enargite; sphalerite is partly altered to chalcocite; CHM2-69, PPL. e) Late stage sphalerite and galena overgrowing and penetrating main stage chalcopyrite along fractures and fringes; CHM7-31.4, RL-PPL. f) Massive chalcopyrite enclosing pyrite grains, luzonite-famatinite and fahlore; CHM7-23.5, RL-PPL.

Ore zone 3 is Pb-Zn dominated. It was found mainly in the deepest and in the peripheral parts of Chah-Mesi. Late stage sphalerite and galena overprint the ore minerals of earlier stages (Figure 35). They commonly are coarse-grained in contrast to sphalerite and galena from the inner ore zones. Cu-Fe sulfides in OZ 3 comprise chalcopyrite, pyrite, fahlore group minerals and rarely enargite. Electrum enclosed in pyrite was only found in proximity to OZ 2. The Ag-contents decrease due to the low abundance of fahlore minerals. Mineralized veins in ore zone 3 typically show crustiform textures, but also transitions to banded veins were observed.

The crustiform veins contain sphalerite and galena, which preferentially occur in the inner parts of veins and show an increase of the crystal size towards the center. Moreover, Ca-Mg-Mn-Fe-carbonates become important gangue minerals with only minor euhedral quartz.

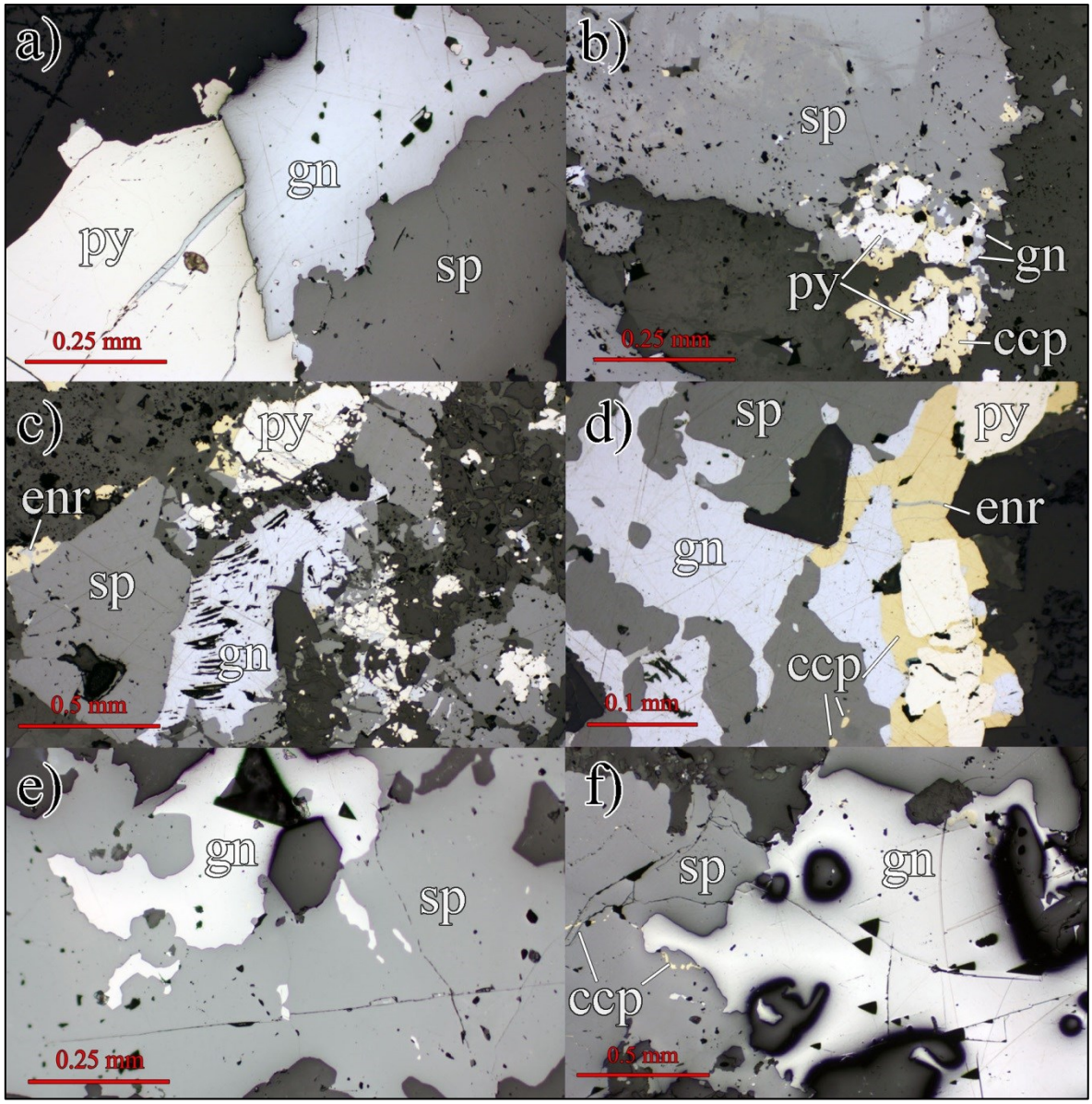

Figure 35: Photomicrographs showing ore associations and microtextures of ore zone 3. a) Galena showing undulating mutual grain boundaries with sphalerite and also filling micro-fracture in pyrite; CHM2-67, RL-PPL. b) Sphalerite, galena and chalcopyrite and pyrite; pyrite and sphalerite partly overgrow chalcopyrite. Note that bireflectance of sphalerite occurs due to an uneven surface of the fluid inclusion thick section; FI-sample CHM7-52, RL-PPL. c) Galena showing slightly deformed cleavage pits ("Bleischweife") indicating minor deformation; CHM7-94, RL-PPL. d) Cusp and carious texture indicating crystal growth of sphalerite at expense of galena; CHM7-94, RL-PPL. e) Coarse-grained sphalerite enclosing galena; CHM1-159, RL-PPL. f) Sphalerite and galena from crustiform vein at deeper level of the deposit. Sphalerite contains small worm-like inclusions of chalcopyrite; CHM1-160, RL-PPL.

Ore zone 4 represents the zone of supergene weathering extending from the surface to a depth of approximately 50 m and affecting all hypogene mineral associations in the various vein types. Characteristic ore minerals of this zone are chalcocite and covellite as well as malachite, azurite, goethite and limonite (Figure 36). Typically, chalcocite and covellite replace hypogene sulfides of the early, main and late stage. Gold was not observed in this zone, but higher Ag contents have been recorded. In contrast to the deeper zones, where tetrahedrite and tennantite act as the main Ag-carrier, chalcocite and covellite seem to be the main Ag-bearing phases in the supergene zone (Chapter 5.3.2).

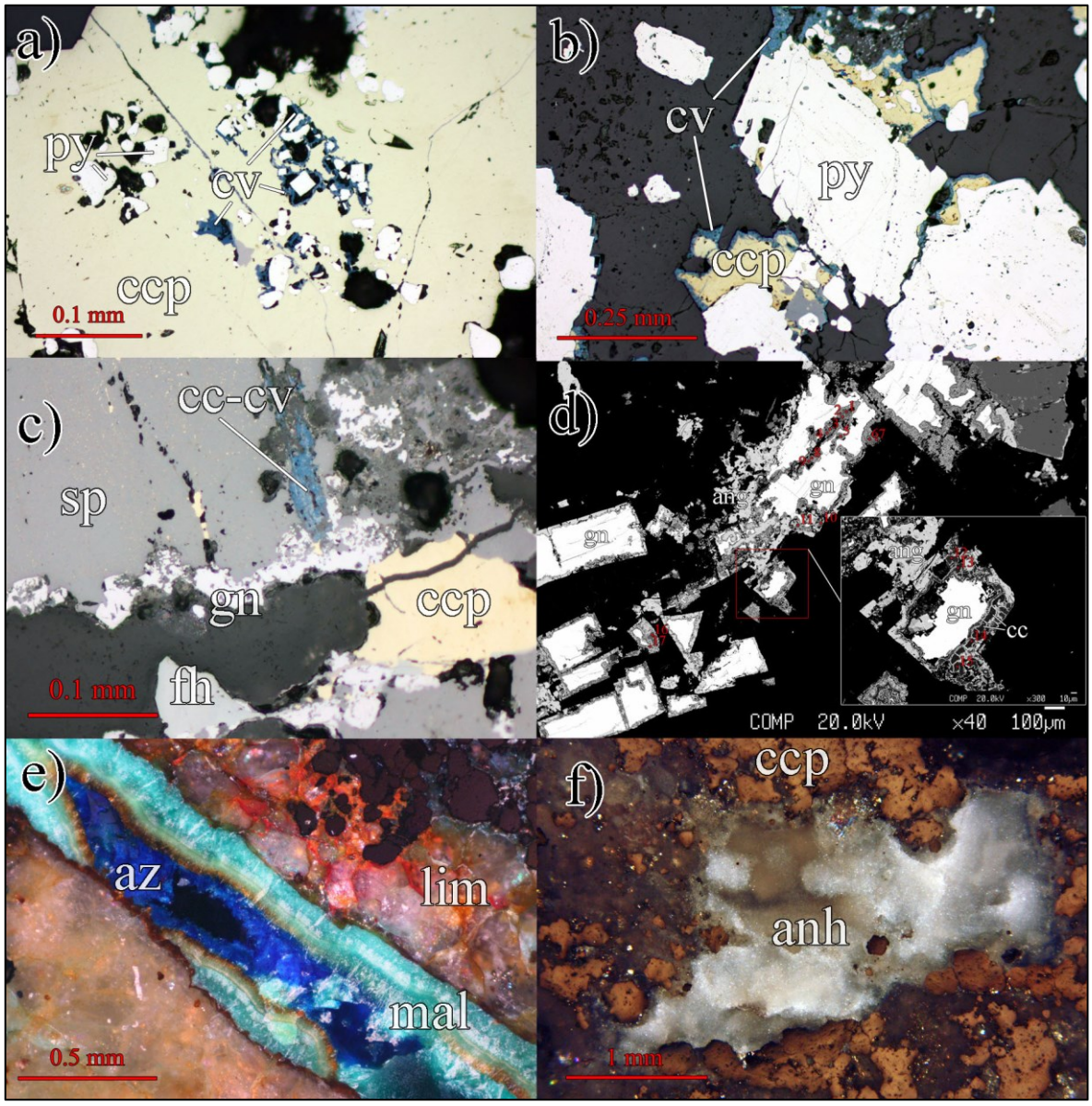

Figure 36: Photomicrographs of supergene mineralization and secondary minerals on the surface of ore zone 4. a) Chalcopyrite showing beginning supergene alteration to covellite, which forms fringes and grows into corrosion-related cavities and open spaces; CHM8.1, RL-PPL. b) Covellite replacing chalcopyrite. Pyrite is commonly unaffected; CHM9.1, RL-PPL. c) Coarse-grained sphalerite with fringe of galena showing beginning replacement by chalcocite and covellite along micro-fracture. Galena is altered to anglesite (dark grey, upper right corner); CHM8.1, RL-PPL. d) Supergene alteration of galena with mainly chalcocite forming in fringes and fissures. Additionally, minor anglesite forms (center); CHM1B, BSE image. e) Fracture-filling with malachite and azurite in limonitic gangue material; banded malachite is composed of fibrous crystals; azurite shows deep blue internal reflections; CHM6, RL-XPL. f) Void-filling microcrystalline anhydrite showing white to milky white internal reflection in weathered chalcopyrite-rich ore; CHM7-31.4, RL-XPL.

5.2 Ore paragenesis and ore textures

Based on mineralogy and textural relationships four mineralization stages were established defining a paragenetic sequence (Figure 37). They reflect ore formation due to continuous (?) changes of physicochemical conditions (e.g. temperature, f_{S2}) and of fluid composition. Based on textural relations an early, main and late hypogene mineralization stage are distinguished. The fourth stage is supergene weathering. The early stage is dominated by pyrite and chalcopyrite with minor enargite/luzonite-famatinite and bornite. The mineral assemblage of this stage reflect formation at higher sulfidation states. The main stage consists of pyrite, chalcopyrite, tennantite-tetrahedrite with minor sphalerite, gold and exotic Ag-sulfosalts. The late stage of hypogene mineralization is mainly represented by sphalerite, galena and pyrite. The main and late stage reflect cooling of the hydrothermal system and intermediate-sulfidation states. Supergene mineralization overprints all hypogene features and shows distinct textures of replacement and decomposition related to weathering.

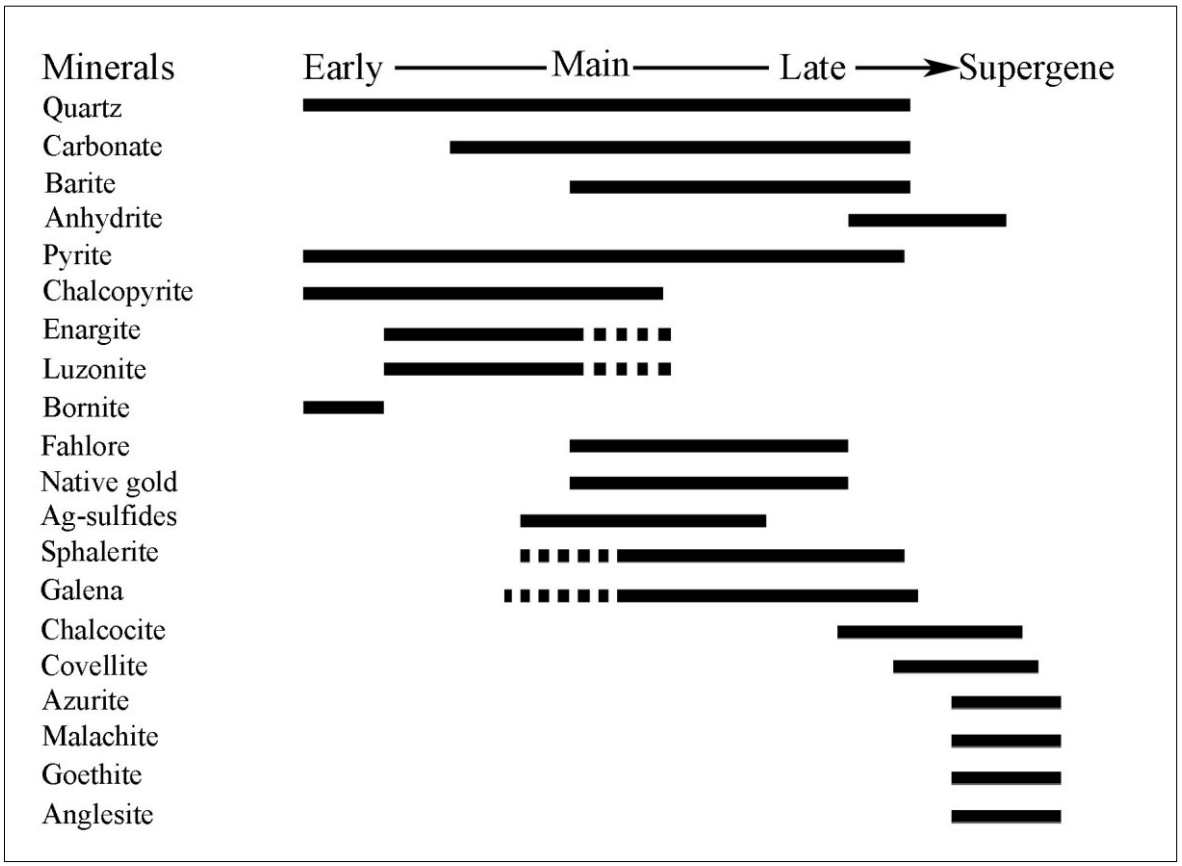

Figure 37: Paragenetic sequence of ore and gangue minerals in the Chah-Mesi polymetallic vein deposit. Early stage mineralization is characterized by quartz rich veins with pyrite, chalcopyrite, enargite-luzonite and minor bornite. The main mineralization stage comprises the associations of quartz-carbonate gangue with chalcopyrite, pyrite, fahlore (tennantite-tetrahedrite), electrum, Ag-sulfides and minor sphalerite plus galena. The late mineralization stage refers to Pb-Zn rich dominated sulfides with mainly sphalerite and galena occurring together with pyrite and small amounts of chalcopyrite and native gold. In the near-surface zone, hypogene mineralization is overprinted by supergene mineralization with abundant chalcocite, covellite and other secondary minerals.

5.2.1 Early stage

The mineral assemblage of the early mineralization stage is concentrated in ore zone 1 of the central part of the deposit where they are found in massive quartz veins and minor replacement bodies. Pyrite and chalcopyrite of the early stage have mutual grain boundaries with smooth to undulating contacts.

Pyrite is the dominant sulfide of the early stage although it is also an important constituent of the later mineralization stages. Usually, it occurs either as inequigranular, granoblastic grains reaching almost 2 mm in size or as nodular pyrite in "porphyritic" ore textures. Pyrite is also present as disseminated cubes within the matrix of adjacent wallrocks. Early stage pyrite often has euhedral to subhedral morphology and contains rounded inclusions that range between 20 and 30 µm in diameter. These inclusions mostly consist of chalcopyrite, enargite/luzonite and minor bornite (Figure 32 c). The latter phase is only present in inclusions; i.e. it is an early stage phase (Figure 37). Compared to enargite or luzonite, bornite inclusions appear slightly darker in color and show rather weak anisotropy.

The dominant Cu-mineral of the early stage assemblage is chalcopyrite. It commonly occurs as subhedral and anhedral grains up to 1 to 2 mm in size. Twinning is often visible under crossed polarizers with non-deformed twin lamellae indicating a stress-free crystallization. Inclusions in chalcopyrite are rare and mostly consist of small grains of pyrite as well as bornite. At shallow depths and particularly on the surface chalcopyrite is commonly fringed and replaced by chalcocite and covellite.

Enargite and luzonite are in grain contact with chalcopyrite and pyrite but seem to have formed slightly later. Commonly, they occur along the rims of chalcopyrite grains or within microfractures (Figure 37, Figure 32 a, b) and develop anhedral to subhedral crystals smaller than 100 µm in size. In some sections, thin microfractures filled with enargite/luzonite crosscut chalcopyrite and minor pyrite (Figure 32 e, f). In addition to chemical composition (Chapter 5.3.2), the distinct lamellar twinning of luzonite, visible under crossed polars in reflected light, was used to distinguish enargite from its dimorph luzonite (Figure 33 b). Enargite and luzonite associated with chalcopyrite are key minerals of the early mineralization stage as they indicate high-sulfidation conditions (Chapter 7.1.2.1).

5.2.2 Main stage

The main stage comprises pyrite, chalcopyrite, the abundant fahlore group minerals tennantite-tetrahedrite, and minor sphalerite. Also, precious metals are assigned to this stage and occur as native gold and Ag-bearing sulfides and sulfosalts (Figure 37). The main stage assemblage is typically found in ore zone 2 and associated with banded textured veins, especially massive sulfide veins (ginguros). The outer zones of crustiform veins, however, also show this typical assemblage. The main stage of mineralization is still characterized by Cu-dominated ore minerals postdating and overprinting the early stage high-sulfidation assemblage (Figure 34 c, d).

Pyrite of the main stage usually forms subhedral crystals smaller than 1 mm with inclusion trails aligned parallel to growth zones. Inclusions comprise enargite-luzonite and fahlore in the central parts grading into sphalerite and galena inclusions outward. Chalcopyrite is also abundant in this stage and commonly occurs as the matrix enclosing most of the other sulfides (Figure 34 a, e, f). Often chalcopyrite fills fractures of cataclastic early-stage pyrite (Figure 33 d). Micro-fractures filled by sulfosalts also affect the main stage chalcopyrite, however, these are predominantly filled by tennantite-tetrahedrite and comprise less amounts of enargite/luzonite compared to the earlier mineralization.

Tennantite and tetrahedrite occur mostly as anhedral grains or overgrowths/reaction rims around chalcopyrite (Figure 33 e, f). Moreover, they form veinlets pervading chalcopyrite or show up as fracture fillings in cataclastic pyrite as well as in chalcopyrite. The grain size of these sulfosalts commonly ranges between 100 µm and 1 mm. Most of the investigated grains are complexly zoned and under crossed nicols thin growth zones can be observed of isotropic fahlore alternating with strongly anisotropic zones of enargite/luzonite. Often fahlore grains contain enargite or luzonite in its core, which are rimmed by 1 to 8 µm thick layers of tennantite-tetrahedrite, but they are present at the outer rims as well. The texture of zoned fahlore grains is reminiscent of colloform banding textures usually observed in banded or crustiform veins. Rare famatinite is restricted to distinct zones in the sulfosalts. Fahlore minerals were identified as the main Ag-carrier at Chah-Mesi and occasionally include exotic Ag-sulfosalts, such as pearceite and benleonardite (Chapter 5.3.1).

Minor sphalerite is part of the main stage too. It occurs as small crystals surrounded by zoned fahlore (Figure 32 f). Often sphalerite is replaced by chalcocite along fractures and fissures (Figure 34 d). As a rare constituent of the assemblage gold was found in samples CHM7-23.4, CHM2-67 and CHM2-89. Gold occurs as electrum with anhedral grains between 10 and 30 µm in size. It has a bright golden-yellow color and very high reflectance under reflected light. Microtextural relationships show that gold is intergrown with pyrite and chalcopyrite, included in pyrite but also in grain contact with sphalerite and fahlore (Figure 38 a, b) (Figure 38 f). Exotic Ag-sulfosalts generally occur as inclusions within pyrite or as small crystals enclosed in zoned fahlore (Figure 33 c). Typically, their grain size is smaller than 10 µm. Hence, it is difficult to observe them under the microscope. EPMA analyses identified pearceite, jalpaite and possibly benleonardite (Chapter 5.3.2).

The fahlore group minerals together with sphalerite are the typical key minerals of this paragenetic stage because they illustrate a transition into intermediate-sulfidation state. Several textures also elucidate the change of sulfidation state and chemical composition of the ore fluids during ore precipitation (Chapter 7.3.1), such as pyrite inclusions. Due to the complex zoning of typical HS- and IS-indicating sulfosalts, a clear separation between the early and main stage is difficult and it might indicate a continuous transition between early and main stage mineralization rather than two separate mineralizing events.

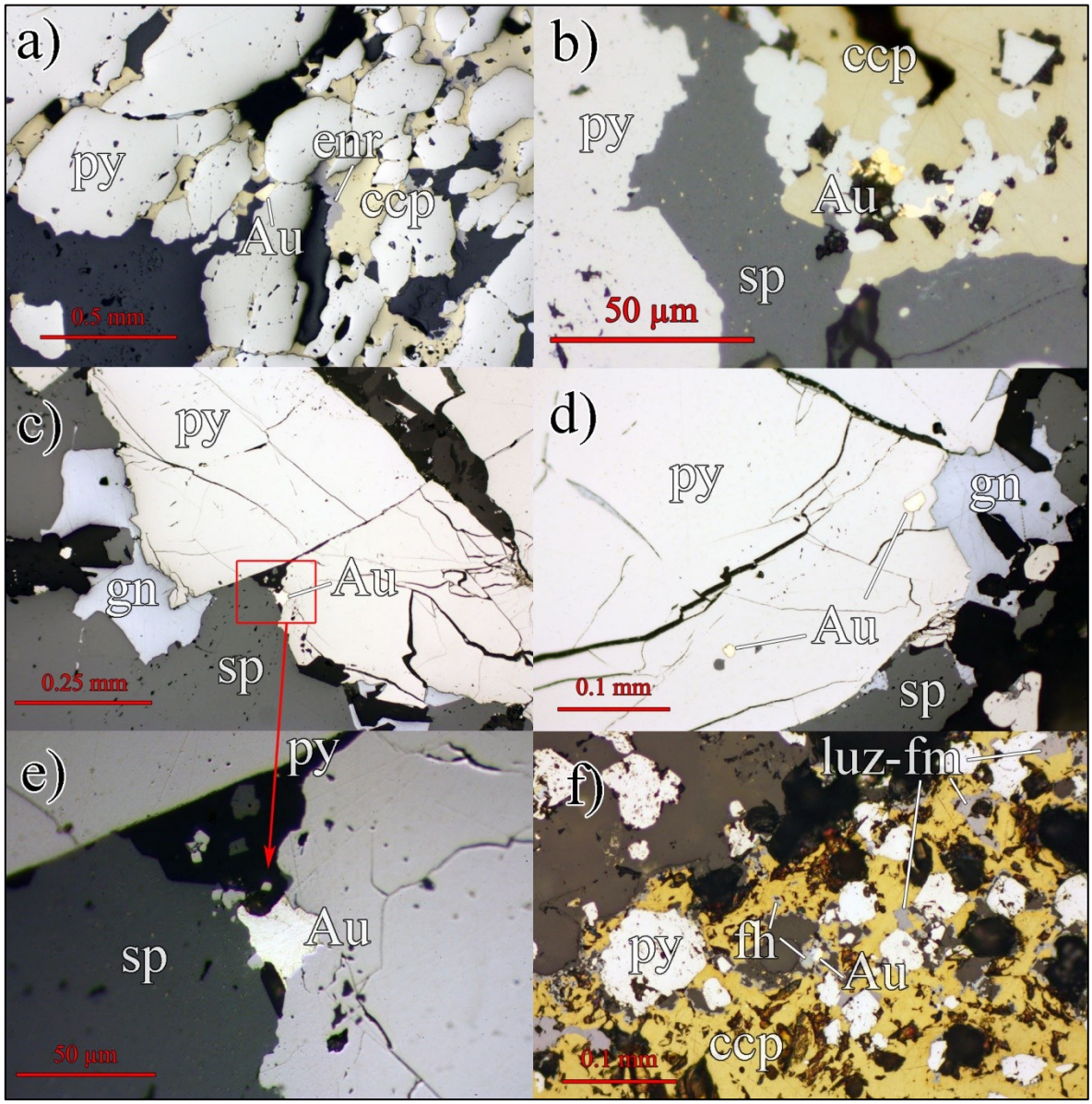

Figure 38: Photomicrographs showing association of gold with main stage (a, b, f) and late stage (c, d, e) ore minerals under reflected light (PPL). a) Gold grain of about 50 µm (center) occurring at the grain boundary of subhedral pyrite; CHM7-23.5. b) Several grains of gold occupying interstitial spaces between small euhedral pyrite grains enclosed by chalcopyrite; cavities and voids of chalcopyrite are black; CHM7-23.5, PPL. c) Gold grain (30 µm) as a part of the late stage assemblage pyrite + sphalerite + galena; CHM2-67, RL-PPL. d) Inclusions of gold (bright golden-yellow) in pyrite that is intergrown with galena; CHM2-67, RL-PPL. e) Detail of c) showing the association of gold with pyrite and sphalerite; CHM2-67, RL-PPL. f) Electrum of the main stage enclosed in a fahlore crystal that is surrounded by massive chalcopyrite; CHM7-32.5, RL-PPL.

5.2.3 Late stage

The late stage mineralization is characterized by galena, sphalerite, pyrite. Rare electrum has also been observed in this assemblage (Figure 37). This stage overprints all previous ore minerals as indicated by galena and sphalerite mostly overgrowing and penetrating chalcopyrite, pyrite, enargite and fahlore minerals of the early and main stage. The Pb-Zn dominated mineralization is more abundant in the distal and deeper parts of the Chah-Mesi deposit associated with ore zone 3. It typically occurs in the crustiform O-type veins. However, this late stage assemblage is also developed in the center of banded veins and in brecciated ores.

Sphalerite is the dominant zinc mineral in Chah-Mesi. In Cu-sulfide dominated veins sphalerite is rather irregularly distributed forming small to medium-grained, anhedral crystals in micro-fractures and between other sulfides. In contrast, Pb-Zn dominated ores show crustiform banding subparallel to vein walls with large, subhedral sphalerite crystals up to 5 mm in size (Figure 35 b). Chalcopyrite is commonly included in this coarse-grained sphalerite. It has varying grain size and minute ovoid grains and spherical droplets are arranged in cloud-like aggregates. Moreover, sphalerite contains inclusions of various sulfosalts and galena.

The color of the internal reflections of sphalerite vary from white to bright yellow. Under reflected light, in some cases, a transition of color and reflectivity can be observed that ranges from light gray with a bluish tinge to lighter gray. Transmitted light microscopy shows that lighter gray sphalerite domains are more transparent and contain numerous primary fluid inclusions (Chapter 6). In the near-surface area chalcocite and covellite replace sphalerite along crystal rims and fissures.

Galena is the dominant lead mineral in Chah-Mesi. It is always associated with sphalerite sharing similar textural characteristics though it is less abundant. Coarse-grained, subhedral galena crystals up to 2 mm in size are observed in veinlets dominated by sphalerite and galena. In Cu-rich assemblages galena forms anhedral to subhedral crystals in micro-fractures and open spaces and is associated with pyrite, chalcopyrite and sulfosalts. Additionally, idiomorphic cubes smaller than 10 µm were observed along grain boundaries and in cavities of finely fragmented sphalerite. Solid inclusions are rare, but if present, it is chalcopyrite and subordinate pyrite, occasionally accompanied by small grains of sphalerite. Deformation textures such as curved cleavage pits (“Bleischweife”) are rarely present and indicate minor deformation (Figure 35 c). Mutual grain boundaries between galena and sphalerite are smooth to undulating (Figure 35 a), although, often sphalerite seems to penetrate galena forming cusp and carious textures (Figure 35 d, e, f).

Pyrite crystals of the late stage are subhedral to anhedral, between 50 µm and 2 mm in size and often overgrow chalcopyrite of the earlier stages. Larger crystals are commonly fragmented, however, open spaces and fractures remained unfilled and no replacement by other sulfides was observed. In comparison to the early and main stage, inclusions in pyrite are rare; if present they mostly comprise fahlore, sphalerite and galena. Electrum of the late stage is associated with pyrite. It occurs as anhedral 10 to 30 µm large inclusions in pyrite (Figure 38 d) or along pyrite-sphalerite grain boundaries (Figure 38 c, e).

5.2.4 Supergene stage

Supergene mineralization represents the final stage of ore formation with chalcocite- and covellite-group minerals, Fe-hydroxides, Cu-carbonate hydroxides, etc. (Figure 37). This mineral assemblage is restricted to the weathered surface area associated with ore zone 4 and progressively decreases towards a depth of approximately 50 m below the surface. Chalcocite and covellite preferentially replace chalcopyrite, sphalerite and galena, less so pyrite (Figure 36 a, b). Commonly, covellite forms irregular reaction rims around chalcopyrite (Figure 36 a, b) with fine granular but more frequently lamellar crystallizations. Chalcocite also forms reaction rims around chalcopyrite. The reflection color has bluish tints and EPMA analysis revealed copper sulfides of composition Cu_xS $1.24 \leq x \leq 1.59$ indicating mainly sulfides of the geerite-covellite series (Chapter 5.3.2). Both minerals also replace sphalerite; this process starts from micro-fractures but can be quite extensive. Successive multiple reaction coronas were observed on galena and sphalerite. Chalcocite formed first and is replaced by covellite (Figure 36 c, d).

Fe-oxyhydroxides are represented by goethite and limonite. Together they form encrustations around non-weathered gangue minerals or acicular crystals in small open cavities. Goethite preferentially replaces chalcopyrite and occasionally forms radial laths. Larger crystals of goethite were only observed in two samples from deeper parts of the weathered zone. Malachite and azurite are abundant in the near-surface zone and occur either as small fracture-fillings or dispersed impregnations (Figure 36 e). Malachite is more common than azurite. Malachite crystals in banded material is preferentially fibrous, whereas azurite rather forms fine-grained aggregates (Figure 36 e). Anglesite and anhydrite are rare (Figure 36 f). Commonly, both occur as fine-crystalline aggregates in open spaces and cavities.

5.3 Mineral chemistry

This chapter reports the EPMA results focusing on sulfides (pyrite, chalcopyrite, sphalerite, chalcocite, covellite) and sulfosalts (tetrahedrite-tennantite, enargite, luzonite-famatinite) of O-type veins from the Chah-Mesi deposit. Gold and tiny Ag-sulfosalts were also analyzed. The EPMA aimed to determine the composition of the ore minerals and to evaluate the distribution of precious metals in these phases. The data were also used to test for possible correlations between the chemical composition of minerals showing extensive solid solution (e.g. fahlore group) and their geographic position within the Chah-Mesi deposit and distance to the Meiduk porphyry system, respectively. Deposit-scale zoning and differences among the different ore zones could be established with this approach. Thus, particular emphasis was placed on the analysis of fahlore group minerals.

5.3.1 Fahlore group minerals

The name fahlore is commonly used for minerals of the tetrahedrite-tennantite solid-solution series with the generalized formula $(Cu,Ag)_6Cu_4(Fe,Zn,Cu,Hg,Cd)_2(Sb,As,Bi,Te)_4(S,Se)_{13}$ (Johnson et al., 1986). The As and Sb endmembers are referred to as tennantite and tetrahedrite having the ideal formulas $(Cu,Ag)_{10}(Fe,Zn)_2As_4S_{13}$ and $(Cu,Ag)_{10}(Fe,Zn)_2Sb_4S_{13}$, respectively. Minerals of the fahlore group are considered to be the most common sulfosalt minerals in epi- to mesothermal vein deposits (e.g., polymetallic sulfide veins) but also in sedimentary exhalative and volcanogenic massive sulfide deposits (Sack et al., 2003). No generally accepted classification exists for fahlore group minerals because of their large chemical variation due to multiple cation and anion substitutions at the different crystallographic sites in the structure in addition to the well-established Sb-As exchange. In this thesis the classification scheme of Kharbish et al. (2007), based on the tetrahedrite content (td%), is used. The td% content is defined as [Sb apfu / (As apfu + Sb apfu) x 100]. According to this scheme tennantite (td% < 5), Sb-rich tennantite (5 ≤ td% < 50), As-rich tetrahedrite (50 < td% ≤ 95) and tetrahedrite (td% > 95) are distinguished.

The chemical analyses were recalculated on the basis of 13 S atoms per formula unit (apfu) and 29 total apfu, respectively; both calculation schemes have been proposed in the literature. The calculated formulas for our analyses were comparable. The recalculation on the basis of 13 S apfu was preferred (for details see Kharbish et al., 2007). A summary of the data with an average formula for each sample is given in Table 34. The complete data set is listed in appendix II and III.

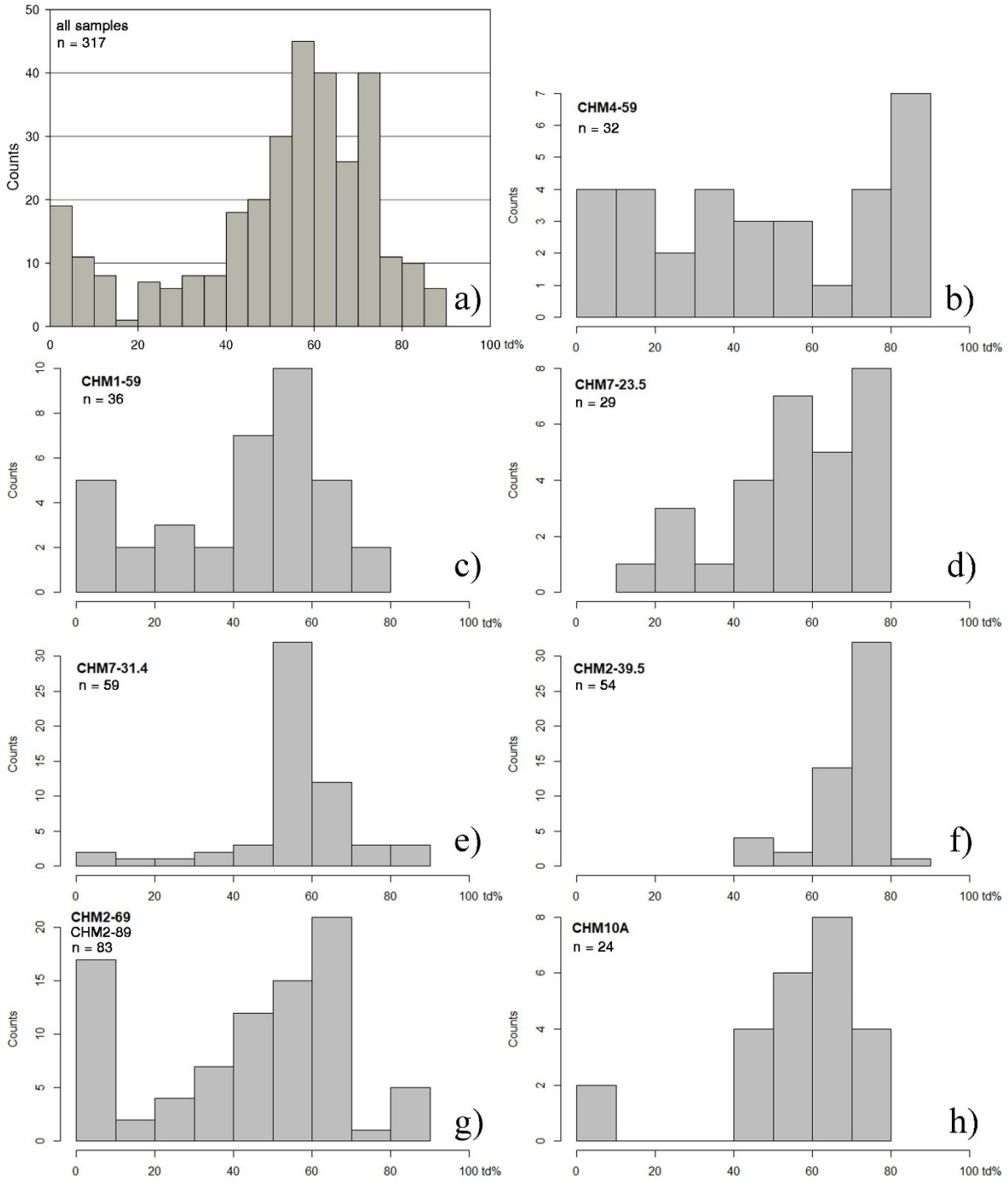

Figure 39: Frequency distribution of the analyzed fahlores from Chah-Mesi deposit regarding their tetrahedrite content (td%). The samples are arranged in increasing distance to the Meiduk deposit. a) All samples included in one histogram; b) CHM4-59 (distance: 1100 m, altitude: 2447 m a.s.l.); c) CHM1-59 (distance: 1400 m, altitude: 2428 m a.s.l.); d) CHM7-23.5 (distance: 1450 m, altitude: 2468 m a.s.l.); e) CHM7-31.4 (distance: 1450 m, altitude: 2461 m a.s.l.); f) CHM2-39.5 (distance: 1500 m, altitude: 2448 m a.s.l.); g) CHM2-69 (distance: 1500 m, altitude: 2418 m a.s.l.) and CHM2-89 (distance: 1500 m, altitude: 2399 m a.s.l.); h) CHM10A (distance: 1600 m, altitude: 2488 m a.s.l.).

Generally, two populations of fahlores can be distinguished based on their td% (Figure 39 a). The first has its maximum at 0-5 td% representing the almost pure As-endmember tennantite, whereas the second one constitutes As-rich tetrahedrite with a well-defined mode at ~60 td% within a wide compositional range between 40 and 75 td%. The data set reveals a nearly complete solid solution with Sb/(As+Sb) ratios within the range of td 0 to 90%. The Sb/(As+Sb) values show a wider range in samples from the deeper levels (CHM2-69-89, CHM4-59, CHM1-59, Figure 39 b, c, g). There, the compositions range from pure tennantite to As-rich tetrahedrite with ~85 td%. Most samples from shallower areas (CHM7-23.5-31.4, CHM2-39.5, CHM10A, Figure 39 d, e, f, h) comprise mainly As-rich tetrahedrite and minor Sb-rich tennantite with compositions between 40 and 80 td%.

The individual samples exhibit a distinct distribution of fahlore composition. As the closest sample to the Meiduk deposit (distance about 1100 m), sample CHM4-59 (2447 m a.s.l.) shows the widest range of composition between 0 and 90 td% and a maximum at 80 to 90 td%, which correlates to almost pure tetrahedrite (Figure 39 b). About 300 m to the south, fahlores of sample CHM1-59 (2428 m a.s.l.) have still a wide range between 0 and 80 td%, but a separation of two fahlore populations is visible between 0 and 10 td% and 40 and 70 td%, respectively (Figure 39 c). Within the Chah-Mesi open pit, drill core BH-CHM7 shows a lack of tennantite in a depth of 23.5, corresponding to 2468 m a.s.l., and the composition of fahlores ranges from 10 to 80 td%. The highest counts are in the range of As-rich tetrahedrite between 50 and 80 td% (Figure 39 d). At a depth of 31.4 (2461 m a.s.l.) the fahlore chemistry extends from 0 to 90 td% but shows a well-defined mode at ~60 td%. However, the abundance of pure and Sb-rich tennantite is very low (Figure 39 e).

In drill core BH-CHM2 the shallow sample from 39.5 m depth (2448 m a.s.l.) is characterized by a narrow range of fahlore composition between 40 and 90 td% and dominated by As-rich tetrahedrite with a well-defined mode at ~75 td% (Figure 39 f). In the deeper sections of the drill core, at a depth of 69 and 89 m, corresponding to 2418 and 2399 m a.s.l., the range of fahlore chemistry widens from 0 to 90 td% and the abundance of As increases. Two fahlore populations are apparent, whereas one showing pure tennantite composition and the other has its highest counts between 40 to 70 td%. The most distant sample CHM10A is dominated by As-rich tetrahedrite with a range between 40 to 80 td% and a mode at ~70 td% but also minor amounts of pure tennantite are present.

Most fahlore grains are complexly zoned showing oscillatory zoning of As and Sb (Figure 40 and Figure 41). This is best seen in back-scattered electron images and mainly reflects different concentrations of Sb and As. However, there is also some zoning to be seen for Zn, which exhibits a positive correlation with Sb-rich sections in sample CHM2-69 (Figure 40). Yet, this observation cannot be determined in sample CHM1-59 (Figure 41). Oscillatory zoning caused by exclusive variation in the Sb, As, Fe and Zn contents were also reported by Plotinskaya et al. (2015) and (Marushchenko et al., 2018). The reasons for oscillatory zoning are currently unclear, but Shore and Fowler (1996) reported the major reasons as extrinsic (e.g. change in solution composition, pressure or temperature) and intrinsic (e.g. adsorption of growth inhibitors) mechanisms. Plotinskaya et al. (2015) reports that the oscillatory zoning of the tennantite-tetrahedrite solid solution is caused by variable activities of As and Sb in the mineralizing fluids due to growth rate kinetics of the fahlore crystals. This is controlled by the concentrations of these elements in the reaction zone of growing crystals.

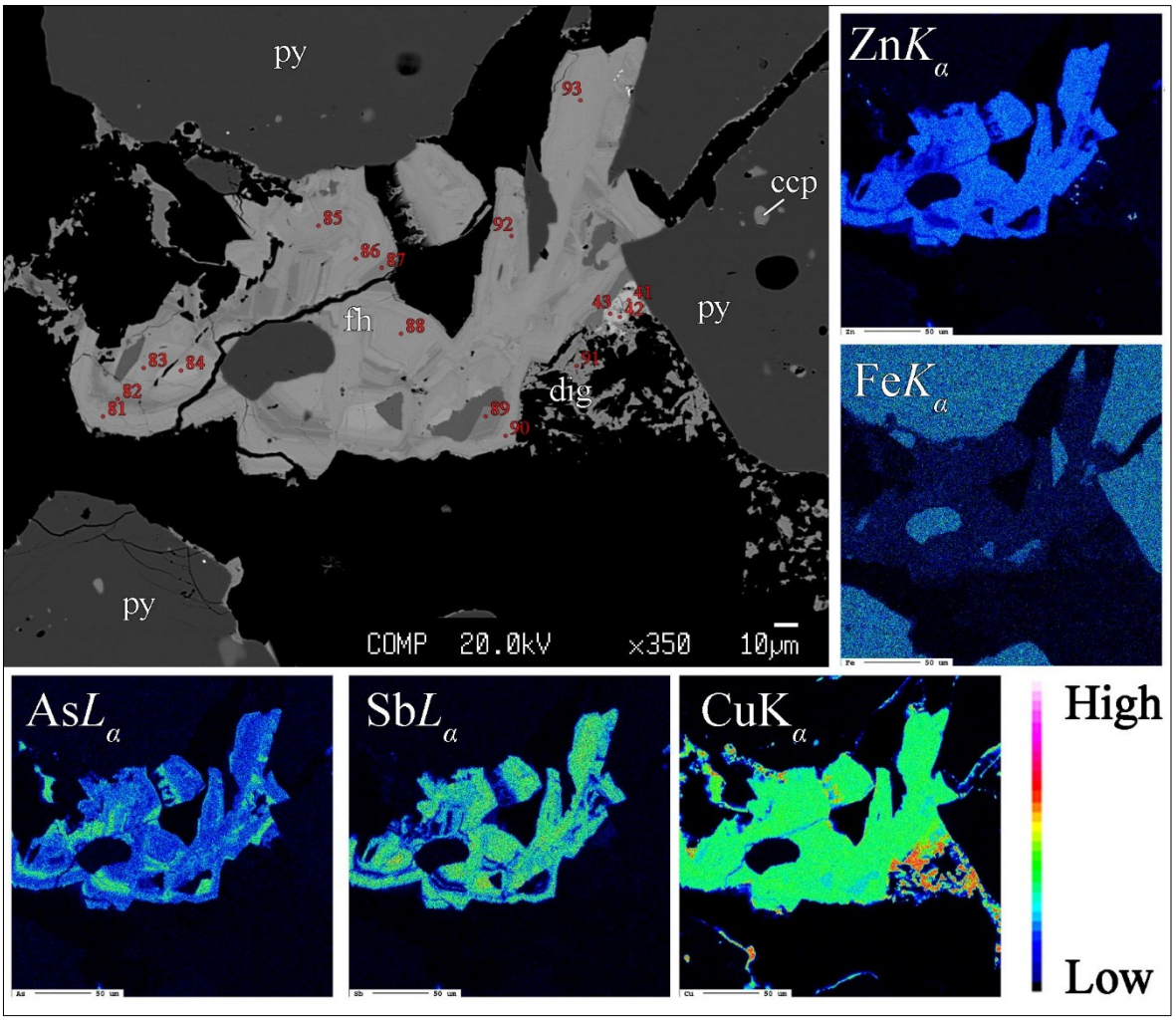

Figure 40: Back-scattered electron image of zoned fahlore crystals (see red numbers in appendix III) and WDS element mappings of AsL_α, SbL_α, CuK_α, FeK_α and ZnK_α. X-ray images elucidate that the complex zoning is mainly due to oscillating As-Sb contents. Sample CHM2-69.

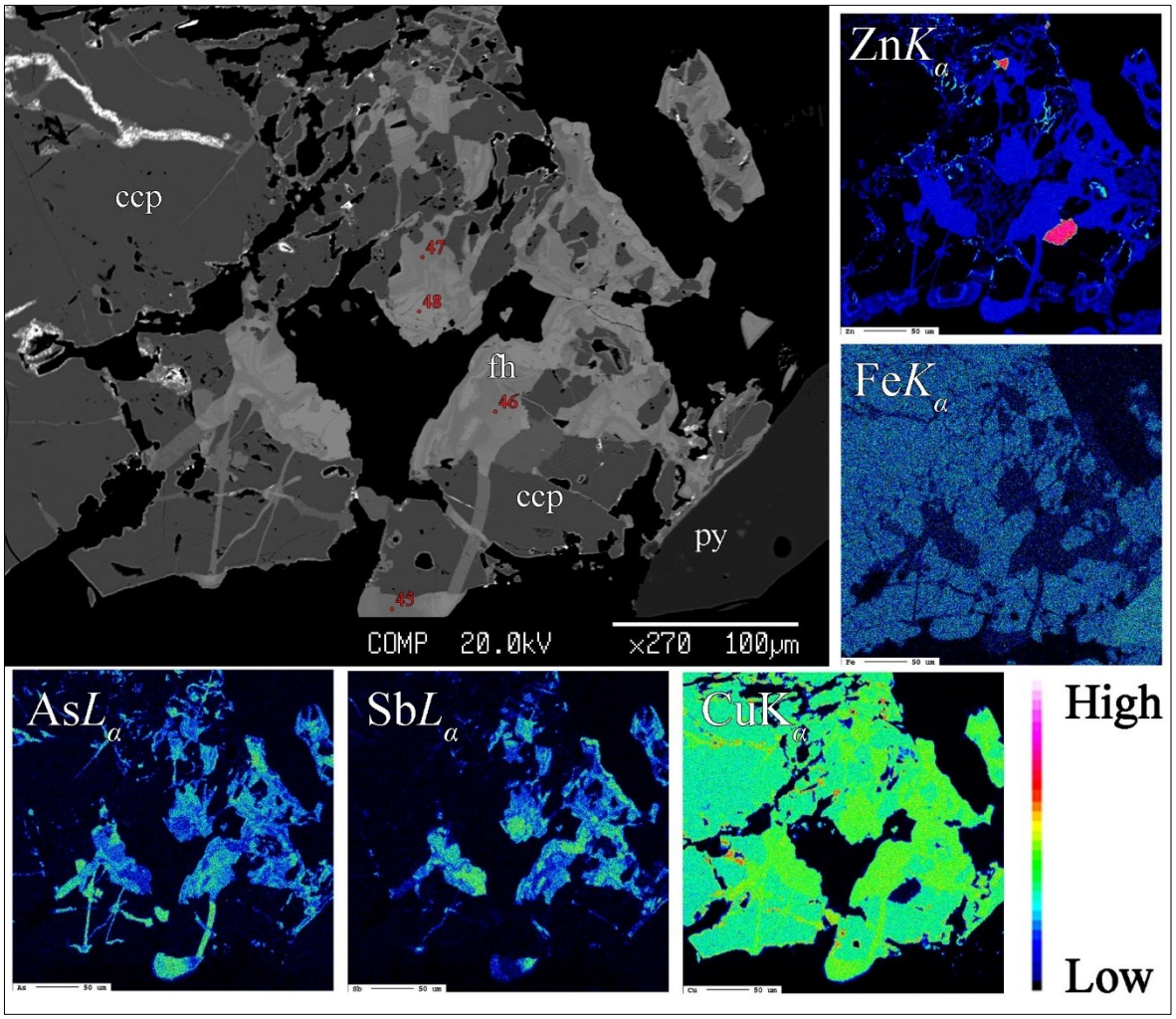

Figure 41: Back-scattered electron image of zoned fahlore crystals of sample CHM1-59 (see red numbers in appendix III) and AsL_α, SbL_α, CuK_α, FeK_α and ZnK_α X-ray images elucidating the complex zoning of sulfosalts.

Table 12: Chemical composition of fahlores from the Chah-Mesi deposit. The samples are grouped according to the distance to the Meiduk porphyry Cu-(Au) deposit with CHM4-59 as the northern most (closest to Meiduk) and CHM10 as the most distant sample collected.

Sample		Cu		Ag		Fe		Zn		total *apfu*	As		Sb		total *apfu*	S		total *apfu*	total wt%	td-conten	Average formula (for 13 S apfu)
		wt%	*apfu*	wt%	*apfu*	wt%	*apfu*	wt%	*apfu*		wt%	*apfu*	wt%	*apfu*		wt%	*apfu*				
CHM4-59	**min**	29.01	8.88	0.04	0.01	0.53	0.15	3.98	1.00	11.29	2.24	0.49	0.23	0.03	3.54	19.73	13.00	27.83	72.02	0.72	
	max	43.55	10.19	2.57	0.40	4.40	1.31	8.42	1.98	12.79	20.74	4.22	26.14	3.54	4.39	28.25	13.00	29.87	102.36	87.65	$(Cu_{9.81}Ag_{0.12})_{9.93}(Fe_{0.46}Zn_{1.76})_{2.22}(As_{2.16}Sb_{1.87})_{4.02}S_{13}$
	avg	39.13	9.81	0.79	0.12	1.61	0.46	7.23	1.76	12.15	10.27	2.16	14.01	1.87	4.02	26.15	13.00	29.18	99.20	46.76	
CHM1-59	**min**	38.67	9.50	0.09	0.01	0.53	0.15	5.60	1.25	12.02	5.05	1.08	0.14	0.02	3.06	25.69	13.00	28.30	99.92	0.42	
	max	43.73	10.35	0.32	0.05	6.30	1.76	8.73	2.06	12.96	19.82	3.91	21.91	2.92	4.08	28.58	13.00	29.92	102.70	72.62	$(Cu_{10.05}Ag_{0.03})_{10.08}(Fe_{0.51}Zn_{1.91})_{2.42}(As_{2.22}Sb_{1.66})_{3.88}S_{13}$
	avg	41.03	10.05	0.18	0.03	1.85	0.51	8.01	1.91	12.49	10.79	2.22	12.82	1.66	3.88	26.79	13.00	29.38	101.46	42.56	
CHM7-23.5	**min**	38.99	10.01	0.17	0.03	0.37	0.11	3.63	0.85	12.16	3.83	0.84	2.99	0.37	3.57	25.08	13.00	29.17	98.92	10.12	
	max	43.50	10.51	0.85	0.13	4.15	1.14	8.46	2.11	13.00	16.33	3.33	23.33	3.15	4.13	27.37	13.00	29.94	102.32	78.93	$(Cu_{10.26}Ag_{0.07})_{10.33}(Fe_{0.43}Zn_{1.77})_{2.20}(As_{1.77}Sb_{2.19})_{3.96}S_{13}$
	avg	40.67	10.26	0.45	0.07	1.51	0.43	7.19	1.77	12.52	8.35	1.77	16.52	2.19	3.96	26.00	13.00	29.49	100.68	55.02	
CHM7-31.4	**min**	37.39	9.59	0.04	0.01	0.08	0.02	6.41	1.53	11.82	2.07	0.46	1.98	0.25	3.43	24.29	13.00	28.83	97.88	6.05	
	max	42.60	10.66	0.31	0.05	6.18	1.70	9.84	2.44	13.01	18.88	3.95	26.98	3.80	4.67	27.85	13.00	30.49	103.38	88.92	$(Cu_{10.15}Ag_{0.02})_{10.17}(Fe_{0.26}Zn_{2.05})_{2.31}(As_{1.83}Sb_{2.32})_{4.15}S_{13}$
	avg	39.82	10.15	0.14	0.02	0.88	0.26	8.29	2.05	12.48	8.50	1.83	17.36	2.32	4.15	25.74	13.00	29.63	100.73	55.99	
CHM2-39.5	**min**	32.24	8.66	0.19	0.03	0.36	0.10	5.40	1.31	11.64	2.05	0.45	13.53	1.77	3.14	23.12	13.00	28.06	97.23	42.77	
	max	41.14	10.38	11.58	1.94	3.79	1.05	8.92	2.18	14.02	11.14	2.37	26.97	3.66	4.17	28.12	13.00	30.55	103.08	89.00	$(Cu_{9.88}Ag_{0.21})_{10.09}(Fe_{0.40}Zn_{1.93})_{2.33}(As_{1.22}Sb_{2.74})_{3.96}S_{13}$
	avg	38.64	9.88	1.33	0.21	1.35	0.40	7.76	1.93	12.41	5.63	1.22	20.53	2.74	3.96	25.66	13.00	29.37	100.92	68.98	
CHM2-69	**min**	38.97	9.85	0.09	0.01	0.06	0.02	1.69	0.37	11.88	2.50	0.55	0.07	0.01	3.75	24.95	13.00	28.86	99.14	0.20	
	max	44.76	10.69	0.34	0.05	6.28	1.67	8.88	2.12	12.92	20.23	3.96	25.29	3.43	4.36	28.76	13.00	30.14	103.15	85.75	$(Cu_{10.24}Ag_{0.03})_{10.27}(Fe_{0.65}Zn_{1.53})_{2.18}(As_{2.26}Sb_{1.77})_{4.03}S_{13}$
	avg	41.45	10.24	0.17	0.03	2.36	0.65	6.32	1.53	12.44	10.95	2.26	13.46	1.77	4.03	26.56	13.00	29.47	101.26	43.60	
CHM2-89	**min**	39.60	10.13	0.36	0.05	0.09	0.02	5.66	1.32	12.26	4.98	1.07	2.77	0.35	3.48	25.62	13.00	29.14	99.18	9.94	
	max	45.64	10.97	2.08	0.30	1.06	0.31	8.32	2.05	13.11	15.64	3.25	22.00	2.91	4.09	27.40	13.00	29.74	101.49	73.11	$(Cu_{10.54}Ag_{0.16})_{10.70}(Fe_{0.16}Zn_{1.76})_{1.92}(As_{2.20}Sb_{1.60})_{3.80}S_{13}$
	avg	42.49	10.54	1.10	0.16	0.56	0.16	7.28	1.76	12.62	10.57	2.20	12.09	1.60	3.80	26.42	13.00	29.42	100.51	40.21	
CHM10A	**min**	38.22	9.82	0.00	0.00	0.09	0.03	7.84	1.87	11.94	5.25	1.16	0.10	0.01	3.62	24.40	13.00	28.87	98.32	0.29	
	max	44.50	10.89	0.13	0.02	1.04	0.30	8.78	2.19	13.24	21.00	4.30	22.48	3.05	4.45	27.88	13.00	30.69	102.50	72.48	$(Cu_{10.37}Ag_{0.01})_{9.93}(Fe_{0.13}Zn_{2.04})_{2.17}(As_{1.84}Sb_{2.30})_{4.14}S_{13}$
	avg	40.83	10.37	0.04	0.01	0.46	0.13	8.24	2.04	12.55	8.64	1.84	17.18	2.30	4.14	25.82	13.00	29.69	101.21	55.32	

The average formulae of the studied fahlores show that the cation sum of (Cu+Ag) is commonly >10 apfu in comparison to the ideal stoichiometric formula $(Cu,Ag)_{10}(Fe,Zn)_2(As,Sb)_4S_{13}$ (Table 12). Except for sample CHM4-59 and CHM2-39, Cu excess was observed in most samples and ranges between 10.05 and 10.54 Cu apfu, which are far beyond the analytical error. Analysis determined that Ag is always present showing wide concentration range, as discussed below. Also, most samples have sums of (Fe+Zn) higher than the ideal formulae ranging from 2.17 to 2.42 apfu with only sample CHM2-89 from the more distal and deeper section showing a slight depletion. The Zn/(Fe+Zn) values range from 0.19 to 0.99 and show that either Fe-rich as well as Zn-rich fahlores are present. Sums of (As+Sb) also comprise deviations from the ideal formula in the range of 3.80 and 4.15 total apfu. Whereas the sums of (Cu+Ag) and (Fe+Zn) have relatively constant values, a significant variation is recognized of As and Sb, and therefore of the tetrahedrite content (td%, Figure 39).

The analyzed fahlores also contain small amounts of silver. The highest contents with 1.24 and 1.94 apfu Ag were observed in sample CHM2-39.5, which was taken from the central area of the Chah-Mesi mine. Higher Ag contents are also shown by sample CHM7-23.5 and the closest sample to Meiduk CHM4-59. The surface sample (CHM10A) is the one showing the lowest Ag/(Cu+Ag) values. However, the overall Ag-content is relatively low with an average of 0.42 wt% Ag, corresponding to 0.06 Ag apfu. As the Ag contents in each sample has a wide range, the median values are shown in Figure 42 with decreasing distance to the Meiduk deposit from left to right. Also, many analyses yielded very low Ag contents with a minimum at 0.003 wt% Ag, corresponding to $4.4x10^{-4}$ Ag apfu (Appendix II). Nevertheless tetrahedrite-tennantite has been identified as the main Ag-carrier in the deposit.

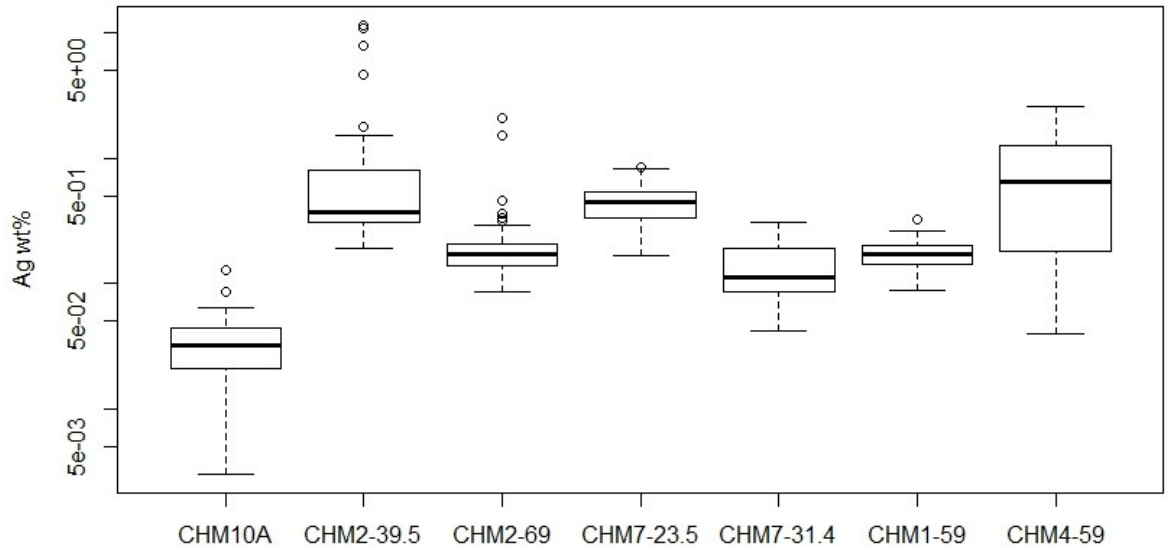

Figure 42: Boxplots showing silver contents of individual samples arranged in decreasing distance to Meiduk (left to right).

For individual samples (e.g. CHM4-59, CHM7-23.5) the Ag content increases systematically with the tetrahedrite component as seen by the positive correlation of Ag/(Cu+Ag) vs. Sb/(As+Sb). However, this is not true for sample CHM-39.5 showing the highest Ag contents of all analyses (Figure 43 a).

The Zn/Fe values vary between 0.2 and 1.0. The plot of Zn/(Fe+Zn) vs. Sb/(As+Sb) indicates that most fahlores contain more Zn than Fe; notable exceptions are samples CHM2-39.5 and CHM2-69 (Figure 43 b). These samples also show a clear increase of Zn/Fe with tetrahedrite component. Hence, the composition of fahlores extends from Fe-rich or Zn-rich tennantite to rather Zn-rich tetrahedrite. Maximum Zn/(Fe+Zn) values are reached at about 50-70 td%. Some samples show a weak positive correlation of Zn and Sb in the first part between 0.0 to 0.6 Sb/(As+Sb). The strongest trend is visible in sample CHM2-69 starting with Fe-rich tennantite and proceeding to Zn-rich tetrahedrite with up to 70 td%. Beyond 0.6 Sb/(As+Sb) a slight negative correlation of Zn and Sb is visible in some samples (e.g. CHM4-59, CHM1-59).

The correlation of Ag/(Cu+Ag) and Zn/(Fe+Zn) exhibits that the highest Ag-contents are associated with Zn/(Fe+Zn) values between 0.6 and 0.8 (Figure 43 c). At lower Zn/(Fe+Zn) values, usually almost constant values of Ag/(Cu+Ag) dominate, however, beyond 0.8 Zn/(Fe+Zn) the range of Ag-content widens significantly. A weak positive correlation of Ag and Zn is indicated by sample CHM2-69, whereas also negative trends are apparent in measured fahlores from samples CHM4-59 and CHM1-59. The negative trends usually occur in the range between 0.8 to 1.0 Zn/(Fe+Zn).

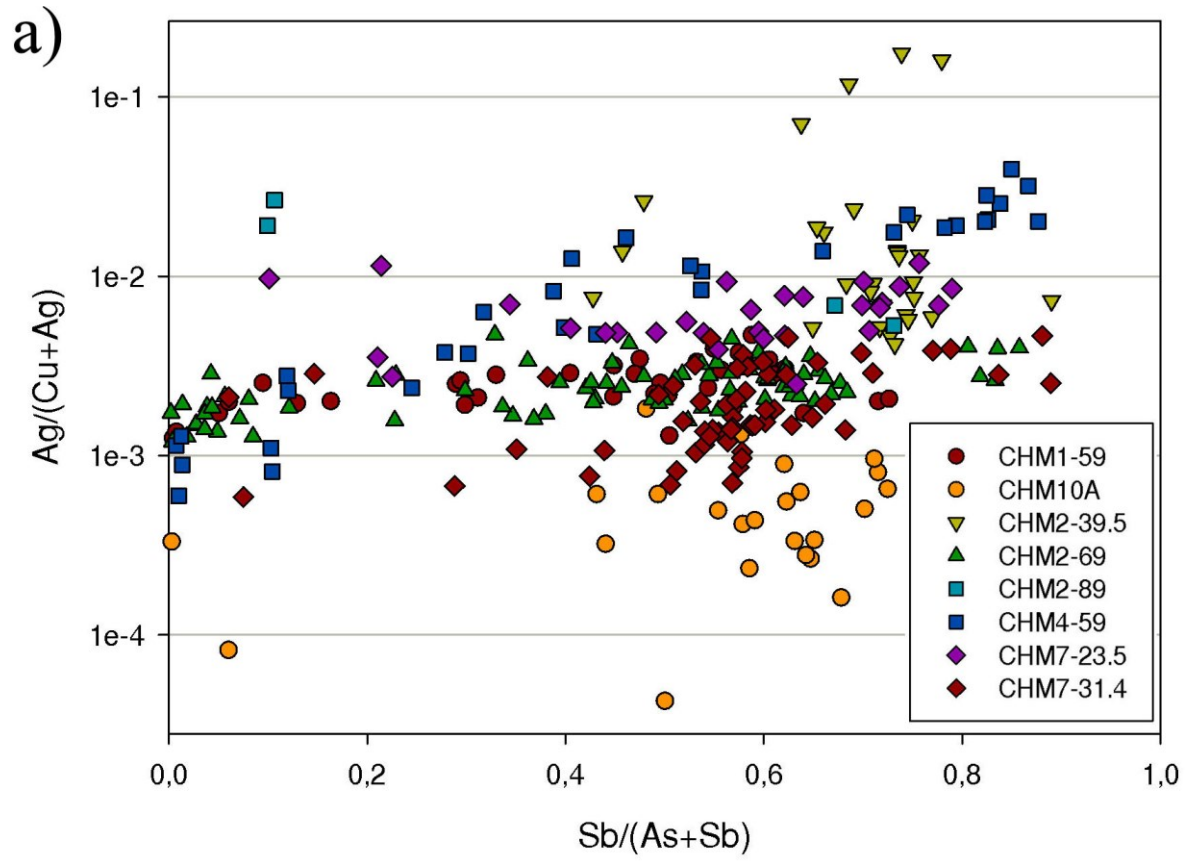

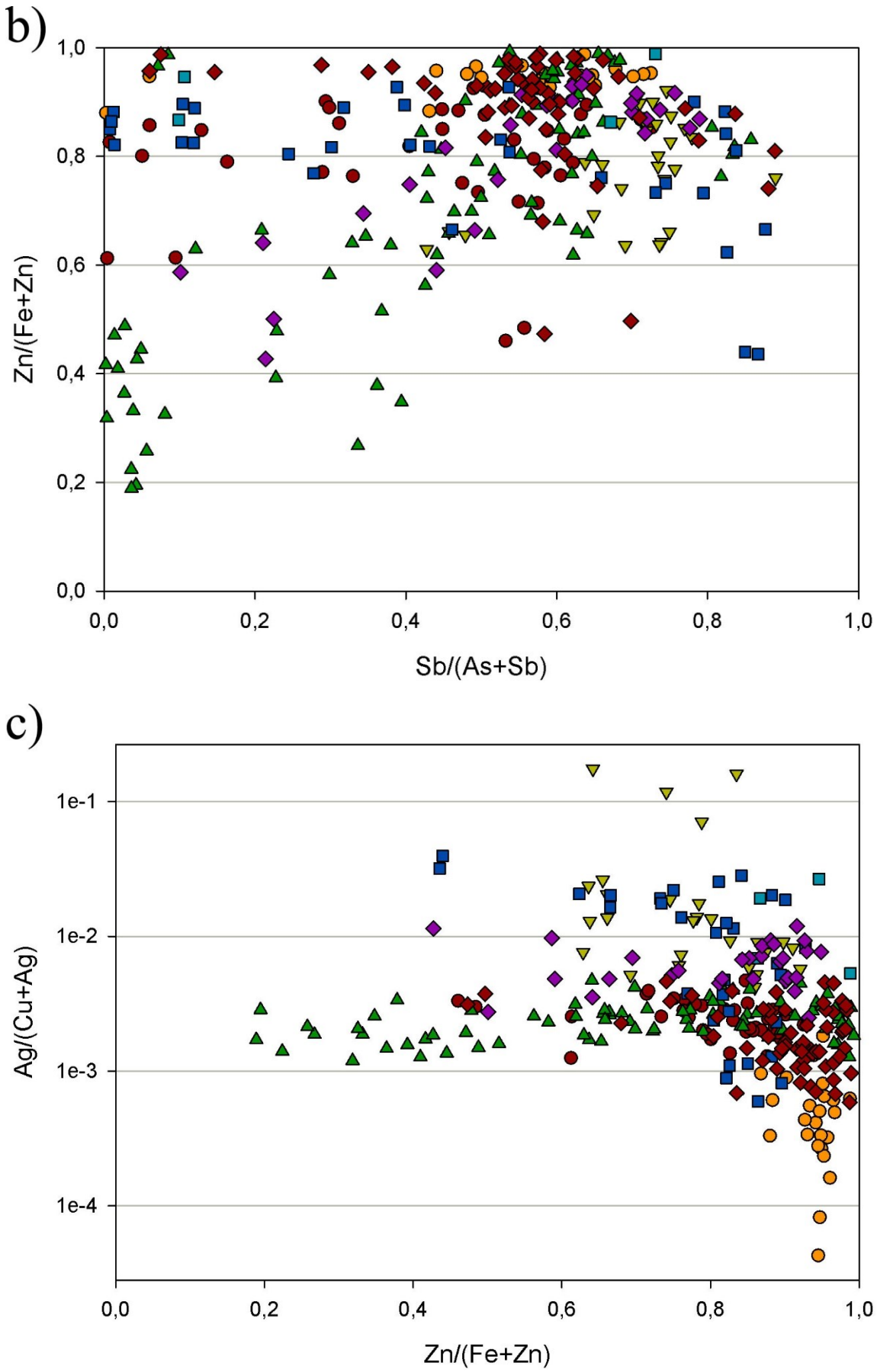

Figure 43: Correlation plots for fahlores from the Chah-Mesi deposit: a) Sb/(As+Sb) vs. Ag/(Cu+Ag); b) Sb/(As+Sb) vs. Zn/(Fe+Zn); c) Zn/(Fe+Zn) vs. Ag/(Cu+Ag).

5.3.2 Other sulfides and sulfosalts

In addition to fahlores, enargite, luzonite-famatinite, chalcopyrite, pyrite and sphalerite were analyzed by EPMA. The exotic Ag-minerals have been identified as members of the pearceite-polybasite series, jalpaite and likely benleonardite. Gold is classified as electrum. The mineral formulae were obtained by recalculating the analyses on the basis of the respective number of S apfu for each phase (i.e. 4 S for enargite, 2 S for chalcopyrite). The data are listed in appendix II and III.

The distinction of enargite and its dimorph luzonite is hardly possible by using only EPMA analyses. Also, optically it is often difficult to distinguish these phases in the sections studied because of their rather small grain size. Arsenic can be partly substituted by Sb in enargite; in general As contents are <7 wt% (Ramdohr, 1969). As luzonite with Sb/(As+Sb) values ≤0.1 is probably not stable under most natural conditions (Luce et al. (1977) analyses of Cu_3AsS_4 phases showing values ≤0.1 Sb/(As+Sb) were designated as enargite. Thus, analyses of these phases with >0.1 Sb/(As+Sb) were declared as being part of the luzonite-famatinite solid solution. After Luce et al. (1977) luzonite refers to all compositions falling in the range 50 to 100 atom % As. The antimony analogue of luzonite is famatinite and refers to compositions in the range 0 to 50 atom % As.

The analyses revealed that enargite, luzonite and famatinite show a significant deviation from the ideal composition $Cu_3(As,Sb)S_4$ in the Chah-Mesi deposit. Cu is commonly substituted by small amounts of Ag, Fe and Zn (Table 13). Enargite has an average calculated formula of $(Cu_{3.02}Ag_{0.01}Fe_{0.08}Zn_{0.01})_{3.12}(As_{0.94}Sb_{0.04})_{0.98}S_4$ with a mean Sb/(As+Sb) value of 0.04. Most of the analyzed enargite grains contain small amounts of Ag averaging 0.01 Ag apfu with a maximum of 0.02 apfu. The iron contents range from 0.01 to 0.20 apfu, those of zinc may reach up to 0.03 apfu. Luzonite has an average formula of $(Cu_{3.02}Ag_{0.02}Fe_{0.09}Zn_{0.01})_{3.12}(As_{0.75}Sb_{0.24})_{0.99}S_4$ with a mean Sb/(As+Sb) value of 0.24. Silver contents reach up to 0.34 Ag apfu and an average of about 0.02 Ag apfu. Iron contents vary between 0.01 and 0.91 apfu, zinc has maximum values of 0.05 apfu. The average formula of famatinite can be given as $(Cu_{3.10}Fe_{0.04}Zn_{0.01})_{3.12}(As_{0.38}Sb_{0.64})_{1.02}S_4$ with a mean Sb/(As+Sb) value of 0.63. In comparison to luzonite, famatinite contains less Fe and Zn and hardly any Ag.

Table 13: Chemical composition of enargite. luzonite and famatinite from the Chah-Mesi deposit.

		Cu		Ag		Fe		Zn		total *apfu*	As		Sb		total *apfu*	S		total *apfu*	total wt%
		wt%	*apfu*	wt%	*apfu*	wt%	*apfu*	wt%	*apfu*		wt%	*apfu*	wt%	*apfu*		wt%	*apfu*		
Enargite	**min**	46.67	2.90	0.02	0.00	0.19	0.01	0.01	0.00	2.92	15.54	0.82	0.10	0.00	0.90	30.50	4.00	7.90	97.75
	max	49.86	3.16	0.53	0.02	2.81	0.20	0.42	0.03	3.29	19.02	1.02	2.93	0.10	1.03	32.82	4.00	8.28	101.89
	avg	47.94	3.02	0.22	0.01	1.10	0.08	0.10	0.01	3.12	17.49	0.94	1.24	0.04	0.98	32.01	4.00	8.09	100.10
Luzonite	**min**	41.07	2.68	0.03	0.00	0.12	0.01	0.01	0.00	2.90	7.77	0.45	2.95	0.10	0.75	29.29	4.00	7.83	97.66
	max	48.81	3.21	8.43	0.34	12.29	0.91	0.77	0.05	3.59	16.84	0.91	14.40	0.50	1.12	32.70	4.00	8.36	102.94
	avg	46.75	3.02	0.44	0.02	1.20	0.09	0.14	0.01	3.14	13.64	0.75	6.96	0.24	0.98	31.24	4.00	8.12	100.38
Famatinite	**min**	45.06	3.02	0.02	0.00	0.09	0.01	0.05	0.00	3.07	3.29	0.19	14.88	0.52	1.01	28.96	4.00	8.08	100.54
	max	46.68	3.16	0.26	0.01	1.05	0.08	0.21	0.01	3.25	8.61	0.49	23.51	0.86	1.05	30.11	4.00	8.27	101.41
	avg	45.79	3.10	0.09	0.00	0.51	0.04	0.15	0.01	3.16	6.61	0.38	18.16	0.64	1.02	29.79	4.00	8.18	101.10

The recalculated chalcopyrite analyses provide the average formula $Cu_{1.07}Fe_{1.01}S_2$ and show only minor deviation from the ideal stoichiometric composition. Occasionally, chalcopyrite showing an excess in Cu and deficiency in Fe incorporates minor amounts of Ag with a maximum of 0.09 Ag apfu. The average of the pyrite analyses gives a formula of $Fe_{1.06}S_2$. Occasionally, minor copper was analyzed with up to 0.02 Cu apfu. Contamination due to small inclusions of chalcopyrite cannot be ruled out.

Sphalerite is characterized by (very) low Fe contents ranging from 0.09 to 2.73 wt% Fe and recalculation revealed an ideal stoichiometric average formula of $Zn_{0.99}Fe_{0.1}S$. Some analyses show elevated Cu contents of up to 0.07 apfu, probably associated with "chalcopyrite disease".

The compounds of the Cu-S system were mostly observed in the near-surface area replacing galena (Figure 36 d) and other sulfides. Analyses show mainly non-stoichiometric compositions with Cu/S ratios varying between 1.24 and 1.59. These ratios refer to the geerite-covellite series, including the Cu_xS minerals geerite ($Cu_{1.5\text{-}1.6}S$), spionkopite ($Cu_{1.4}S$), yarrowite ($Cu_{1.1}S$) and covellite (CuS) (Gablina, 1997). Most recalculations of the analyzed Cu_xS phases reveal a composition of $1.31 \leq x \leq 1.46$, which is suggested to represent spionkopite with an average formula of $Cu_{1.36}S$. However, also geerite and probably yarrowite with an average formula of $Cu_{1.57}S$ and $Cu_{1.24}S$, respectively, were determined. The minerals of the geerite-covellite series include Ag contents of up to 0.1 apfu.

Exotic Ag-bearing minerals that were only detected by EPMA include phases of the pearceite-polybasite series, jalpaite and benleonardite (Figure 44 a. b). Pearceite-polybasite occurs as small inclusions of fahlore and luzonite-famatinite crystals. The calculated average formula $(Ag_{8.10}Cu_{7.84}Fe_{0.18}Zn_{0.15})_{16.27}(As_{1.66}Sb_{0.24})_{1.90}S_{10.98}$ shows significant deviation from the ideal formula $(Ag,Cu)_{16}(As,Sb)_2S_{11}$. The high value of Cu and low content of Sb indicates that the measured phases are pearceite (Bindi et al., 2007). The main substitution is that of Ag and Cu. Their values range from 6.00 to 11.56 Ag apfu and 4.45 to 10.77 Cu apfu. The Sb/(As+Sb) value is relatively constant with an average of about 0.12. One small grain of jalpaite was detected as an inclusion of pyrite. It has a calculated formula of $Ag_{2.86}Cu_{0.98}S_{2.02}$ what is close to the ideal formula Ag_3CuS_2. In sample CHM2-89, significant amounts of Te were detected in an Ag-rich phase by EDS (Figure 44 d). This phase that is interstitial to pyrite, chalcopyrite and enargite was not fully quantitatively analyzed, because of a missing Te standard. Neglecting Te only analyses with totals of about 87 wt% could be obtained. Assuming that the difference to 100 wt% is all tellurium, recalculation results in the formula $Ag_{15.19}Cu_{2.55}(Sb_{2.13}As_{0.17})_{2.30}S_{8.82}Te_{2.69}$. This phase could therefore be benleonardite, which has the ideal formula $Ag_{15}Cu(Sb,As)_2S_7Te_4$.

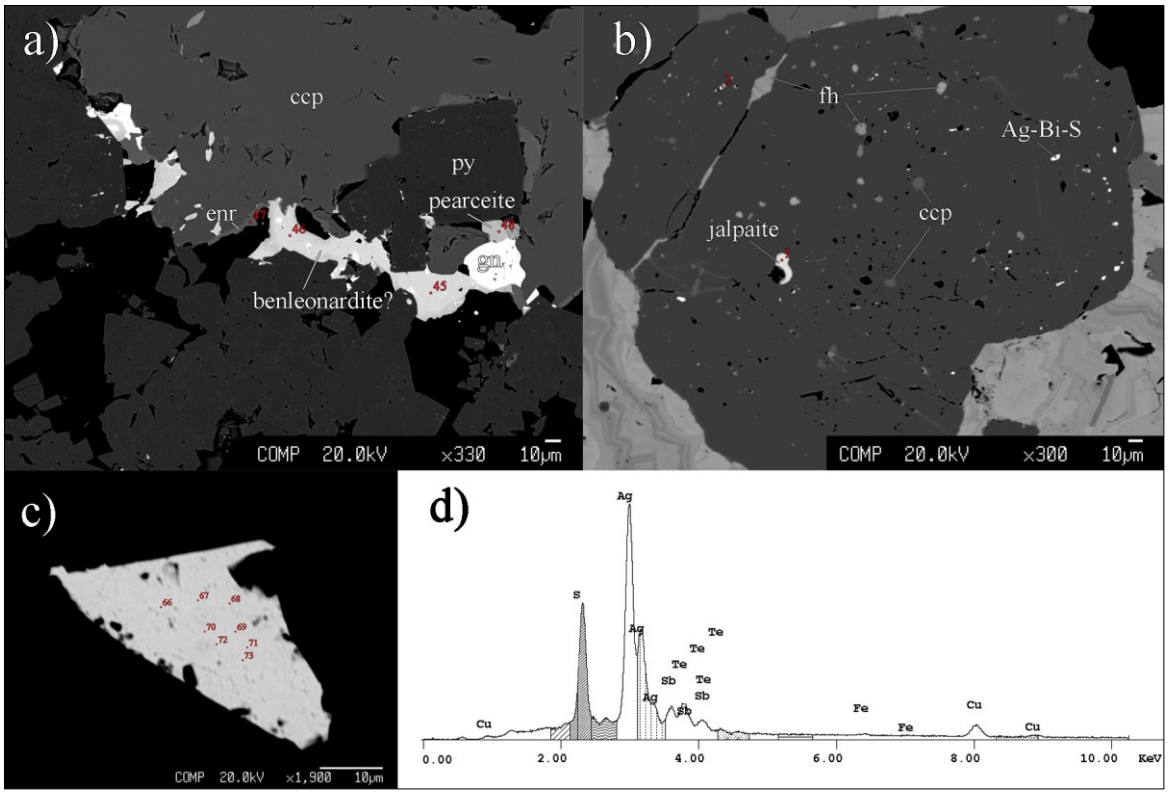

Figure 44: BSE-images of a) Pearceite and "benleonardite" associated with chalcopyrite, pyrite, enargite and galena; CHM2-89. b) Jalpaite occurring as minute inclusion in pyrite; CHM2-69. c) Gold grain reaching almost 40 µm in size; for analyses (red numbers see appendix III); CHM7-23.5. d) EDS spectra of "benleonardite" confirming the presence of Te in this phase.

Several analyses of one gold grain associated with pyrite in sample CHM7-23.5 (Figure 44 c) yielded the average composition of 76.32 % Au, 22.42 % Ag and 0.50 % Cu. Hence, gold it is classified as electrum.

5.3.3 Ca-Mg-Mn-Fe-carbonates

Ca-Mg-Mn-Fe-carbonates commonly occur as gangue minerals in the banded and crustiform O-type veins, less commonly in mineralized veins with massive and brecciated texture. These gangue carbonates were only analyzed qualitatively by EDS. Normally, euhedral carbonate crystals show zoning, which is well visible in back-scattered electron images (Figure 45). EDS analyses revealed that the cores of carbonates mostly show compositions of ankerite (Figure 46 a) and towards the rim the composition corresponds to siderite (Figure 46 b). Often, the siderite rims include significant amounts of Zn in addition to Mn. In addition to Ca and Fe, high Mn-contents were detected in the inner crystal parts, suggesting the presence of Mn-rich carbonates such as kutnohorite (Figure 46 c).

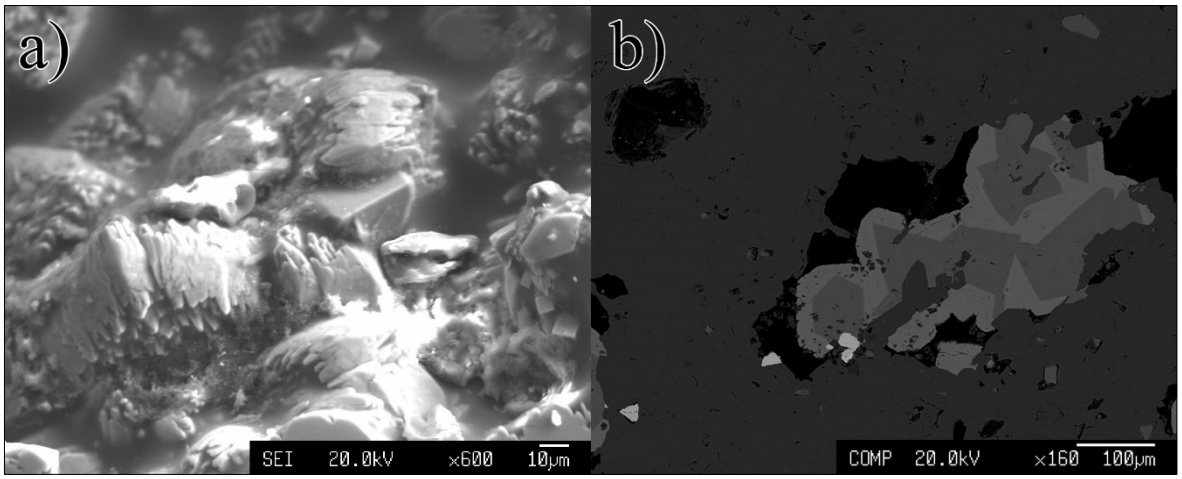

Figure 45: a) Secondary electron (SEM) image showing elongated to bladed aggregates of Ca-Mg-Mn-Fe-carbonates overgrowing rhombohedral carbonate (center of photo); CHM2-39.5. b) Back-scattered electron (BSE) image showing distinct zoning of euhedral carbonate crystals filling voids and open spaces. Commonly, the ankerite cores show darker hues than the rims consisting of siderite; CHM1-44.

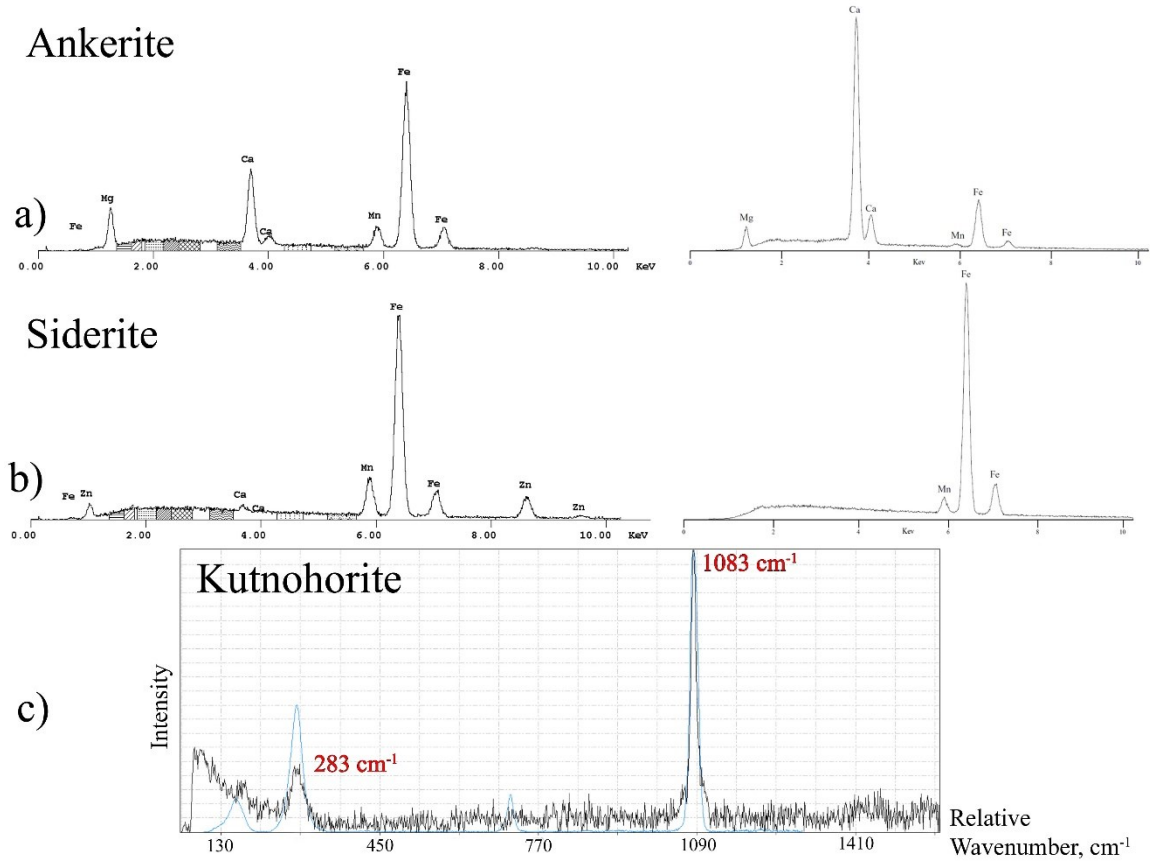

Figure 46: EDS spectra of Ca-Mg-Mn-Fe-carbonates (see Figure 40 b). a) Cores are Mn-bearing ankerite b) rims are Mn- and Zn- bearing siderite. As a reference the published spectra of ankerite and siderite after Severin (2004) are shown. c) Raman spectra of kutnohorite: measured sample (black) compared to the reference (blue, RRUFF ID: R060473) showing a match of about 76 %.

6 Fluid inclusions

In order to constrain the PT-X conditions of ore formation and check if there exists a genetic link of the Chah-Mesi deposit to the Meiduk porphyry system, fluid inclusions were studied of mineralized O-type veins using microthermometry and Raman spectroscopy. Two samples of O-type veins were studied: the first is a banded (CHM2-68.5, ~2419 m a.s.l) the second a crustiform (CHM7-52, ~2440 m a.s.l.) O-type vein (Figure 47 a, b). The horizontal distance of the two drill cores from where the samples were taken is approximately 50 m (Figure 7).

Fluid inclusions are abundant in quartz and sphalerite in both veins. The size of the fluid inclusions ranges from <1 to 45 µm. The majority of inclusions examined during this study were 4 to 15 µm big. To constrain the initial conditions of ore and gangue crystallization, most measurements were done on inclusions showing micro-textural characteristics of primary fluid inclusions as defined by Roedder (1984). Thus, microthermometric investigation focused on fluid inclusion assemblages belonging to inclusion-rich growth zones and oriented parallel to crystal faces (Figure 47 c - e).

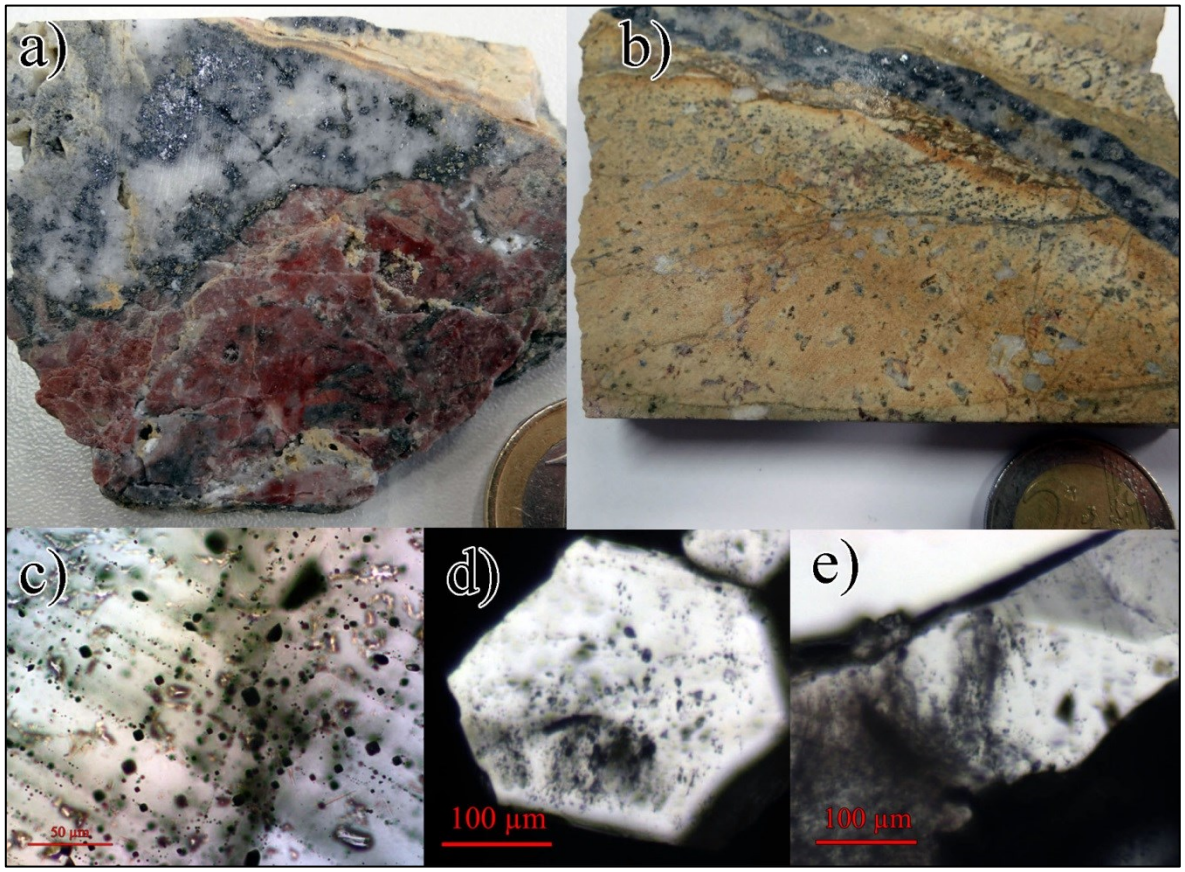

Figure 47: Photographs of the banded (a, sample CHM2-68.5) and the crustiform (b, sample CHM7-52) O-type veins studied. c) Primary fluid inclusions oriented along crystal growth zones in sphalerite; CHM2-68.5, TL-PPL. d) Euhedral quartz embedded in sphalerite showing fluid inclusions parallel to growth zones; CHM2-68.5, TL-PPL. e) Elongated quartz crystal showing fluid inclusions parallel to crystal faces; CHM2-68.5, TL-PPL.

6.1 Fluid inclusion petrography and types of inclusions

Fluid inclusions were classified following the scheme used by Hezarkhani (2008) for the Meiduk PCD; this allows for better comparison of the data. Two types of fluid inclusions have been identified.

Type 1: Two phase liquid-vapor (LV) inclusions are the dominant type of inclusion. They contain liquid + vapor ± solid phases (Figure 48 a, b) with the liquid phase being the volumetrically dominating phase. The distribution of LV inclusions is homogeneous in both O-type veins and also in sphalerite and quartz crystals. They are present as primary inclusions in growth zones parallel to crystal faces, but also occur as trails along healed fractures, representing secondary inclusions. The fluid inclusions are from 1 to 20 µm in size. The L:V ratio varies but commonly the vapor bubble occupies less than 25 % of the inclusion volumes and homogenization is into the liquid phase. Inclusions in quartz crystals rarely contain solid phases; higher refractive index and moderate birefringence suggest accidently trapped phyllosilicates (illite-muscovite) (Figure 48 b). In sphalerite solid phases in the inclusions are more abundant. They are irregularly distributed and of variable quantity. Due to fluorescence effects of sphalerite during Raman measurements it was difficult to identify these solid phases. From morphology and optical features anhydrite and/or phyllosilicates could be present (Figure 48 d).

Type 2: Mono-phase L and V type inclusions generally occur in minor amounts. They contain only a liquid or gas phase, respectively (Figure 48 b, f). Due to their very small size of mostly <10 µm the determination of melting temperatures in L type inclusions was hardly possible and not accurate enough. Moreover, most mono-phase L inclusions occur together with LV type inclusions. They likely formed by necking down of LV inclusions. V type inclusions were not observed in quartz but only in sphalerite. Due to the very dark color and poor transparency of sphalerite, however, a clear distinction between LV inclusions with high V proportion and pure V type inclusions was not always possible.

In quartz, fluid inclusions are of variable shape. Larger and isolated inclusions commonly are of irregular shape (Figure 48 b). Assemblages of smaller inclusions oriented along fractures or growth zones typically show more regular elongated morphology, sometimes with a tendency to develop negative crystal shape (Figure 48 c). However, subordinate irregular elongated shapes of smaller inclusions were also observed. In sphalerite, fluid inclusions commonly are equidimensional to slightly elongated and form mostly rectangular inclusions that are aligned in clusters (Figure 48 d). The predominance of LV type inclusions showing similar liquid to vapor ratios indicates a homogeneous trapping process. Although minor amounts of immeasurable monophase L type inclusions are present in both vein types no clear evidence for fluid immiscibility/boiling has been observed.

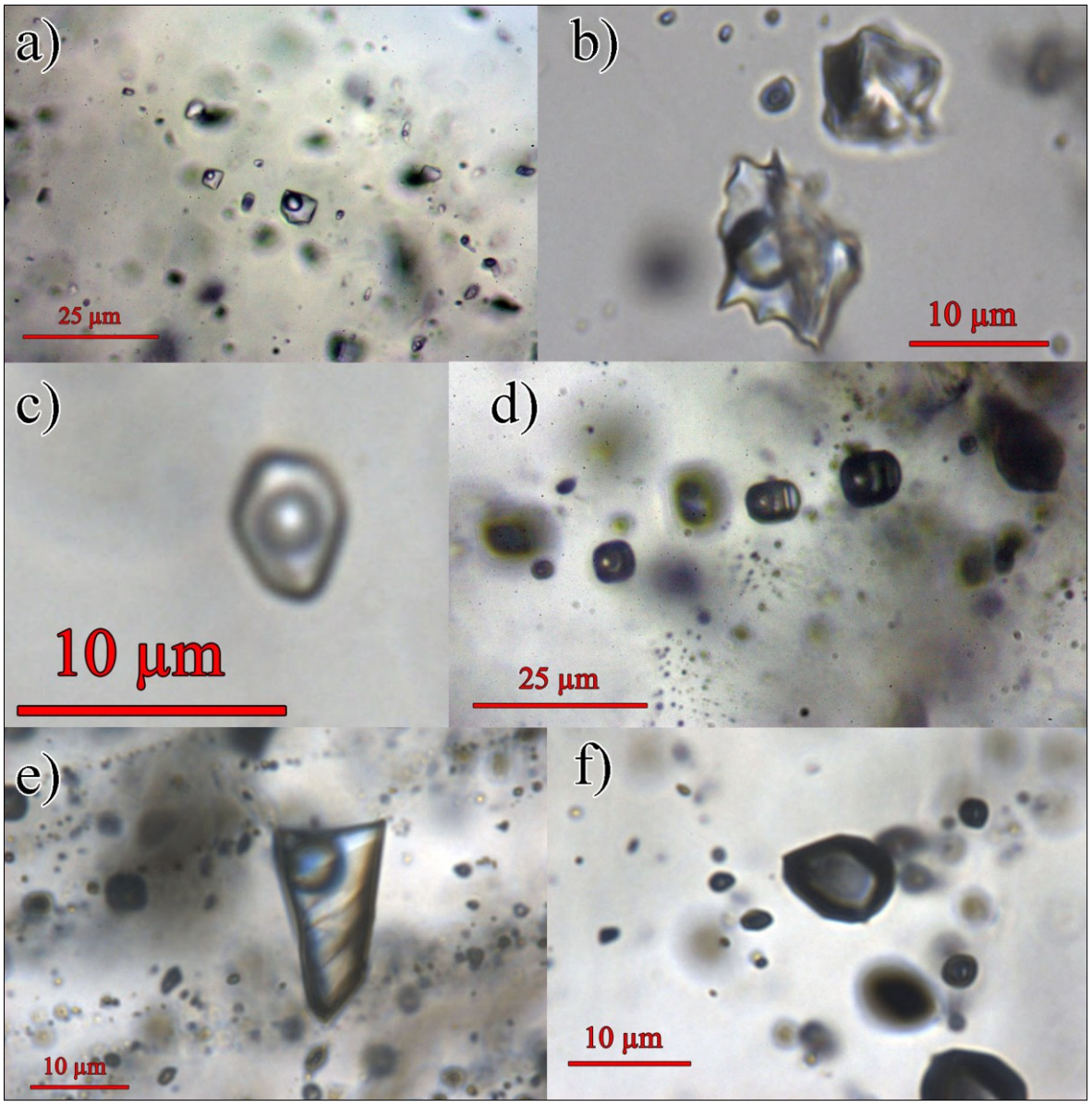

Figure 48: Photomicrographs of fluid inclusions observed in sample CHM2-68.5 under transmitted light with parallel nicols. All photographs were taken at room temperature (~22 °C). a) Fluid inclusion assemblage in quartz showing Type 1 LV inclusions with constant bubble sizes occupying about 25 % of inclusion volumes. b) Large LV inclusion in quartz showing an irregular shape next to a liquid-rich inclusion and smaller LV type inclusions (above). c) Regular shaped equidimensional inclusion in quartz forming a hexagonal negative crystal. d) Fluid inclusion assemblage in sphalerite exhibiting square to rectangular LV type inclusions. The inclusion in the middle contains a rectangular solid phase. e) Large inclusion in sphalerite with elongated shape. f) Monophase Type 2 vapor (or liquid?) inclusion in sphalerite. Microthermometric investigation was hardly possible due to the dark color.

6.2 Fluid inclusion microthermometry

Microthermometric measurements were carried out on both quartz and sphalerite of samples CHM2-68.5 and CHM7-52, respectively (Table 14). The temperatures of final melting of ice ($T_{m(ice)}$) and the nucleation of ice during cooling ($T_{n(ice)}$) were measured only in LV type inclusions, because L type inclusions were too small to allow accurate measurements. Clathrate formation was not observed in any of the inclusions indicating the low content of CO_2 (<1.5 mole%, Roedder, 1984) in the system. The $T_{m(ice)}$ values for fluid inclusions in sphalerite from sample CHM2-68.5 range from -0.7 ° to -5.5 °C, corresponding to salinities of 1.2 to 8.6 wt% NaCl equiv., respectively (Bodnar, 1993). The nucleation of ice in these inclusions occurred between -39.0 ° and -45.6 °C. Sphalerite inclusions in sample CHM7-52 yielded $T_{m(ice)}$ values ranging from -1.2 ° to -6.5 °C, corresponding to a salinities of 2.1 to 9.9 wt% NaCl equiv. $T_{n(ice)}$ values in these inclusions range from -33.2 ° to -46.5 °C.

Fluid inclusions hosted in quartz from sample CHM2-68.5 yielded $T_{m(ice)}$ values between -3.3 ° and -6.0 °C, corresponding to salinities of 5.4 to 9.2 wt% NaCl equiv. with $T_{n(ice)}$ values between -36.3 ° and -45.4 °C. In sample CHM7-52, $T_{m(ice)}$ values in quartz hosted inclusions range from -1.2 ° to -4.3 °C corresponding to salinities of 2.1 to 6.9 wt% NaCl equiv. $T_{n(ice)}$ values of these inclusions were measured between -37.8 ° and -44.5 °C. Histograms of the salinity data show that the banded O-type vein sample CHM2-68.5 (Figure 49 a, b) shows comparatively higher salinity values than the crustiform vein sample CHM7-52 (Figure 49 c, d).

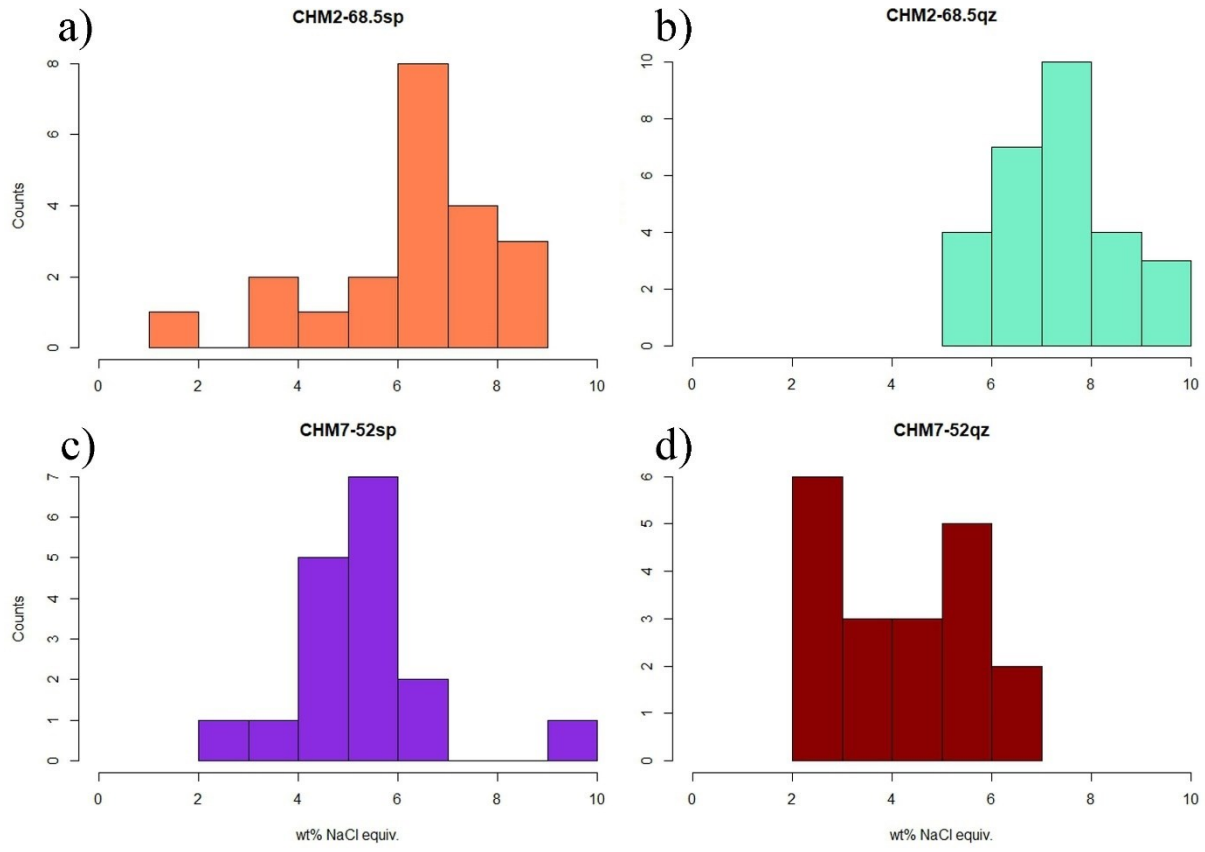

Figure 49: Histograms of the calculated salinities of a) sphalerite grains from sample CHM2-68.5, b) quartz grains from sample CHM2-68.5, c) sphalerite grains from sample CHM7-52 and d) quartz grains from sample CHM7-52.

Table 14: Summary of fluid inclusion data of this study from the Chah-Mesi deposit (CHM) compared to published data from Meiduk (MD) and Latala (BH) (Padyar et al. (2017). Mean values are in brackets.

Symbol	Type	Class	$T_{m(ice)}$ [°C]	T_h [°C]	Salinity [wt% NaCl equiv.]	Density [g/m³]	Pressure [MPa]
CHM2-68.5sp	L+V	P+PS	-5.5 to -0.7	127.6 to 294.6 (218.0)	1.2 to 8.6 (6.2)	0.79 to 0.93 (0.88)	0.68 to 7.69 (2.81)
CHM2-68.5qz	L+V	P+PS+S	-6.0 to -3.3	153.0 to 396.5 (270.8)	5.4 to 9.2 (7.3)	0.60 to 0.90 (0.79)	2.08 to 26.40 (9.23)
CHM7-52sp	L+V	P+PS	-6.5 to -1.2	114.6 to 275.4 (200.6)	2.1 to 9.9 (5.4)	0.82 to 1.02 (0.90)	0.15 to 5.80 (2.70)
CHM7-52qz	L+V	P+PS+S	-4.3 to -1.2	144.8 to 322.8 (234.8)	2.1 to 6.9 (4.2)	0.74 to 0.96 (0.85)	0.40 to 11.36 (3.72)
				Padyar et al., 2017			
MD-I_a	L+V	P+PS+S	-9.3 to -0.7	162.0 to 411.0	1.2 to 13.2	0.53 to 0.95 (0.77)	-
MD-I_b	V+L	P+PS+S	-15.5 to -1.3	205.0 to 492.0	2.2 to 19.0	0.88 to 0.95 (0.88)	-
BH-I_a	L+V	P+PS+S	-7.1 to -0.1	135.0 to 325.0	0.2 to 10.6	0.71 to 0.96 (0.81)	-
BH-I_b	V+L	P+PS+S	-0.9 to -0.6	235.0 to 335.0	1.1 to 1.5	-	-
BH-$I_{Sphalerite}$	L+V	P+PS	-4.9 to 0.1 (2.8)	144.0 to 285.0 (217.2)	0.2 to 7.8 (4.5)	0.8 to 1.0 (0.9)	-

The heating of LV type inclusions results in homogenization of the vapor into the liquid phase at homogenization temperatures (T_h) from 114.6 ° to 396.5 °C (Figure 50). Inclusions in sphalerite of sample CHM2-68.5 show T_h values from 127.6 ° to 294.6 °C, with a mean value of 218 °C and a well-defined mode at ~ 220 °C (Figure 50 a). The histogram of the T_h values of inclusions in sphalerite crystals from sample CHM7-52 indicates the presence of two fluid populations. One population has T_h values at lower temperatures between 114.6 ° to 141.5 °C, the second one at higher T_h values between 231.7 to 275.4 °C (Figure 50 c). Fluid inclusions hosted in quartz generally homogenize at higher temperatures and in both samples, they exhibit maxima at around 270 °C. The T_h values range between 153.0 ° and 396.5 °C in sample CHM2-68.5 and between 144.8 to 322.8 in sample CHM7-52 (Figure 50 b, d).

The microthermometric data were plotted on T_h vs. salinity diagrams (Figure 37). In sample CHM2-68.5 the T_h values increase with higher salinity; this is very obvious for the sphalerite data (Figure 51 a). In sample CHM7-52 T_h decreases with higher salinity in the case of quartz hosted inclusions (Figure 51 b). Moreover, inclusions in sphalerite of the latter sample are split into two subgroups, the first one exhibiting higher homogenization temperatures at around 250 °C and a salinity of 4 to 5 wt% NaCl equiv. and the second one exhibiting lower T_h values of about 120 °C and a wider range of salinity (2 to 10 wt% NaCl equiv.), respectively. This suggests the presence of two distinct generations of fluids hosted by sphalerite.

Concerning the host minerals of fluid inclusions, fluids measured in sphalerite of sample CHM2-68.5 have higher salinities (3 to 8.5 wt%) than in sample CHM7-52 (2 to 6.5 wt%, except one outlier at almost 10 wt% NaCl equiv.), but in sample CHM-68.5 only one fluid generation is indicated and homogenizes at temperatures (170 to 300 °C) between the high (250 to 300 °C) and low (~120 °C) tempered fluid generations of sample CHM7-52 (Figure 51). Quartz inclusions of the banded vein sample CHM2-68.5 generally show higher salinities (6 to 9 wt%) as well as higher temperatures of homogenization (220 to

400 °C) than inclusions of quartz in the crustiform sample CHM7-52 with salinities ranging from 2 to 6.5 wt% NaCl equiv. and T_h values between 150 and 300 °C (Figure 51). The comparison of sphalerite and quartz within the same sample shows that that sphalerite has a wider salinity range than quartz in sample CHM2-68.5, but a similar salinity range of both minerals is apparent in sample CHM7-52. However, in both samples T_h values of fluid inclusions hosted by quartz tend to be higher temperatures than those in sphalerite.

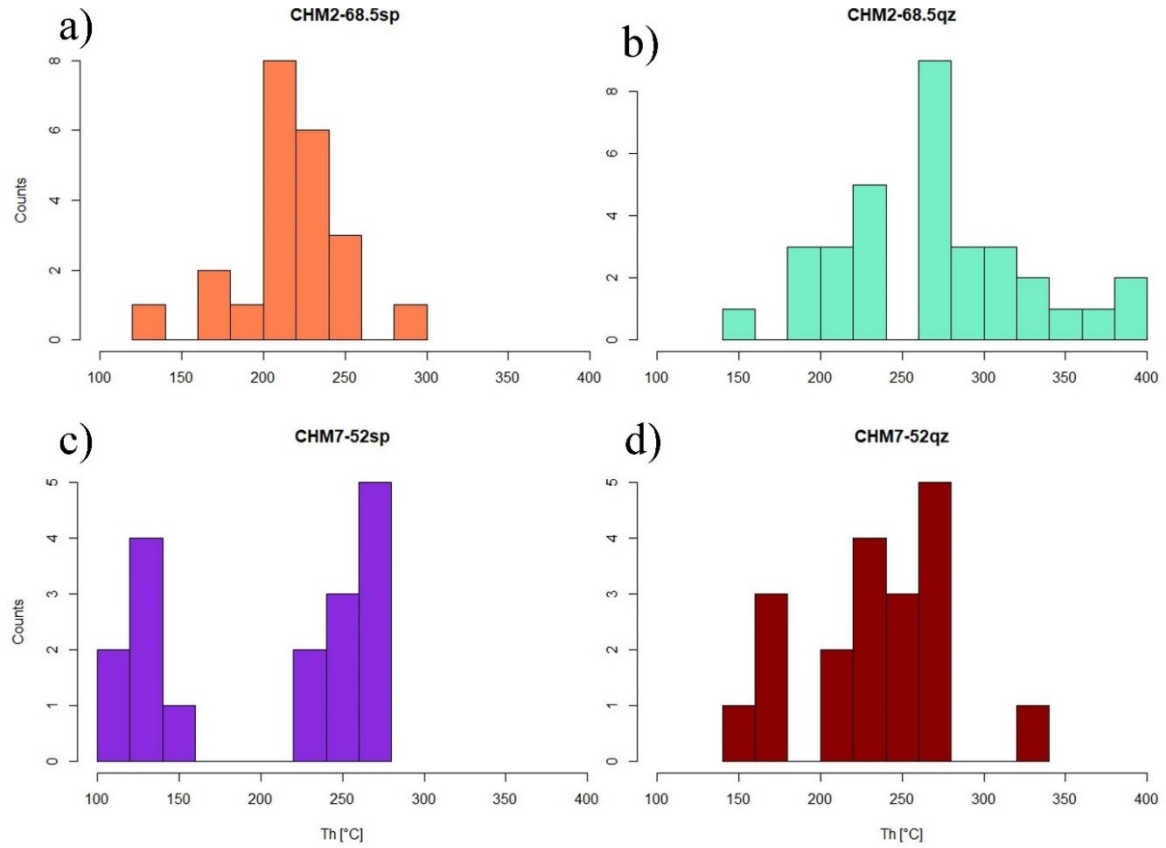

Figure 50: Histograms of the measured temperature of homogenization (T_h) of two-phase L+V inclusions in a) sphalerite from sample CHM2-68.5, b) quartz from sample CHM2-68.5, c) sphalerite from sample CHM7-52 and d) quartz from sample CHM7-52.

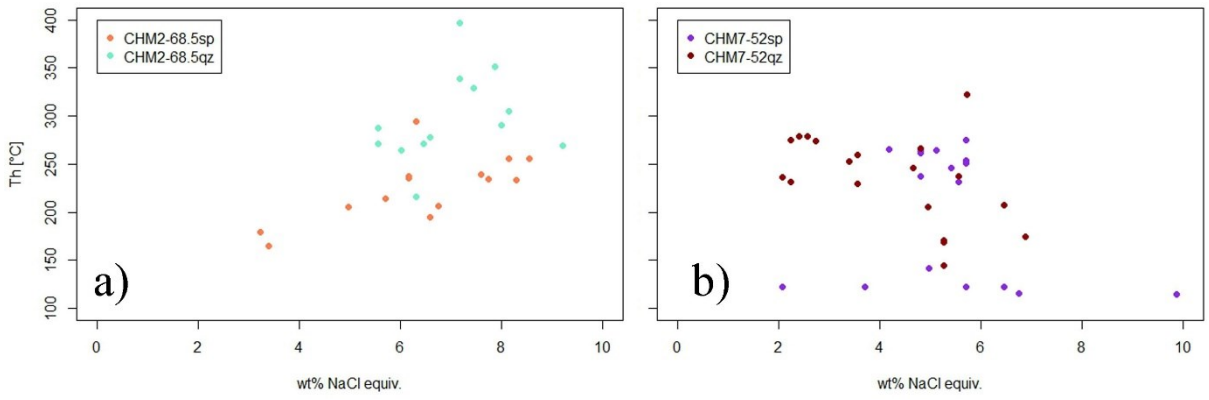

Figure 51: Plots of homogenization temperature (Th) vs. salinity (wt% NaCl equiv.). a) sample CHM2-68.5 and b) sample CHM7-52 with distinction of host mineral of fluid inclusions: sphalerite (sp) and quartz (qz).

6.3 Raman spectroscopy of fluid inclusions

The results of the laser Raman spectroscopic analyses on fluid inclusions of one sample are illustrated in Figures 38 and 39. In the banded vein sample CHM2-68.5 H_2O is dominant in the liquid phase in both sphalerite and quartz; this is indicated by the broad asymmetric H_2O stretching band in the wave number range 2800 and 4000 cm^{-1} consisting of three overlapping Raman peaks at about 3227 cm^{-1}, 3419 cm^{-1} and 3622 cm^{-1} (Figure 52 a). In the case of sphalerite, fluorescence makes the determination of the Raman peaks difficult. Thus, the spectrum of the liquid phase has been compared with the background measurement of sphalerite (Fig. 39). The slight intensity increase in the spectrum in the 3000-4000 cm^{-1} range is interpreted to be due to presence of H_2O (Figure 53 a). Hence, it is assumed that the liquid phase in both the sphalerite and quartz hosted FI is water.

The Raman spectrum of the gas (vapor) phase in quartz shows peaks at 1286 cm^{-1} and 1389 cm^{-1} (Figure 53 b) confirming the presence of minor amounts of CO_2. The peak at 1161 cm^{-1} is from host quartz. Raman peaks indicating CO_2 were also observed in the gas phase of sphalerite hosted inclusions at 1287 cm^{-1} and 1389 cm^{-1} (Figure 53 b). Therefore, it is assumed that the gas phase of inclusions in sphalerite and quartz have identical composition. Due to the very low content of CO_2, it was neglected for the calculation of salinities.

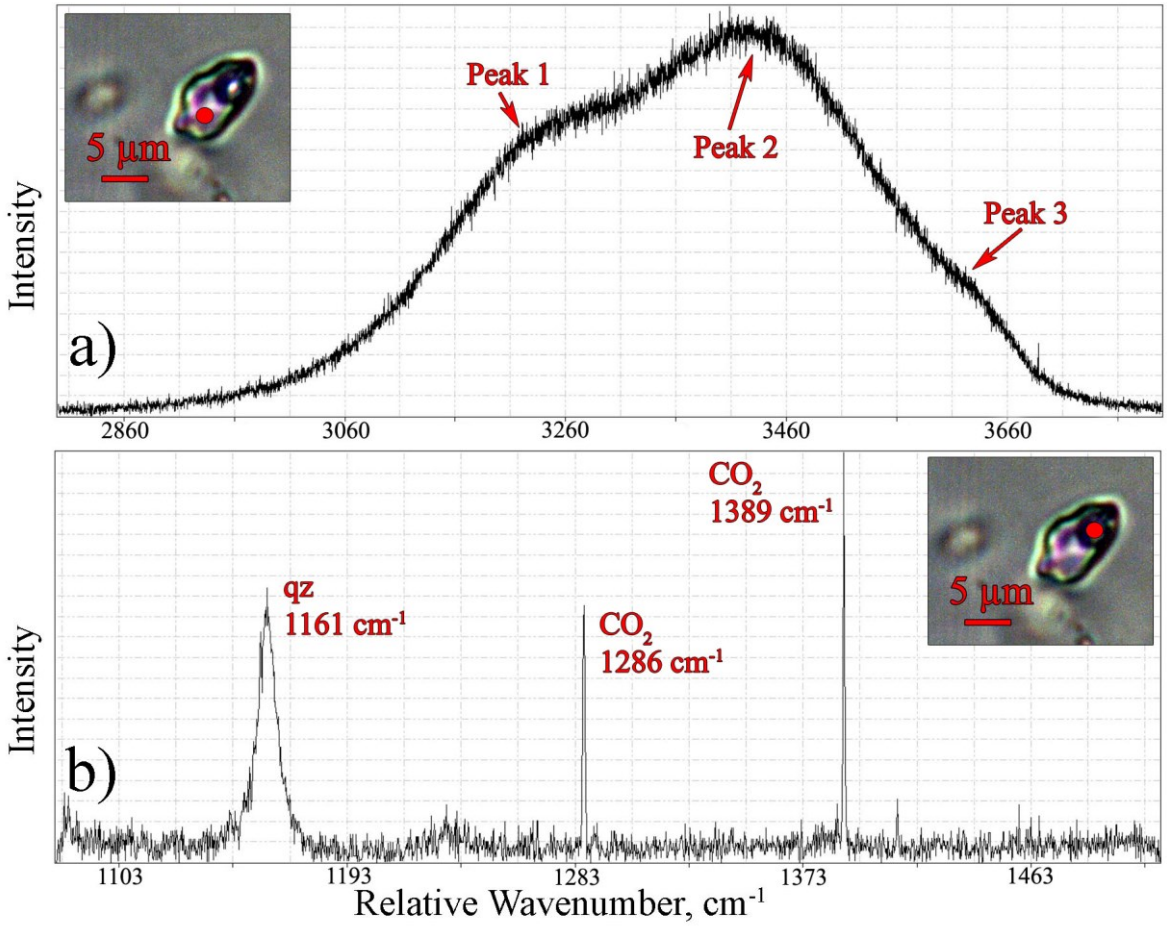

Figure 52: Raman spectra of the a) liquid and b) gas phase in a fluid inclusion of quartz from sample CHM2-68.5 suggesting the presence of H_2O (Peak 1: 3227 cm^{-1}, Peak 2: 3419 cm^{-1}, Peak 3: 3622 cm^{-1}) and minor amounts of CO_2 in the vapor phase (1286 cm^{-1} and 1389 cm^{-1}). Red dots illustrate the spots of the measurement in the inclusion.

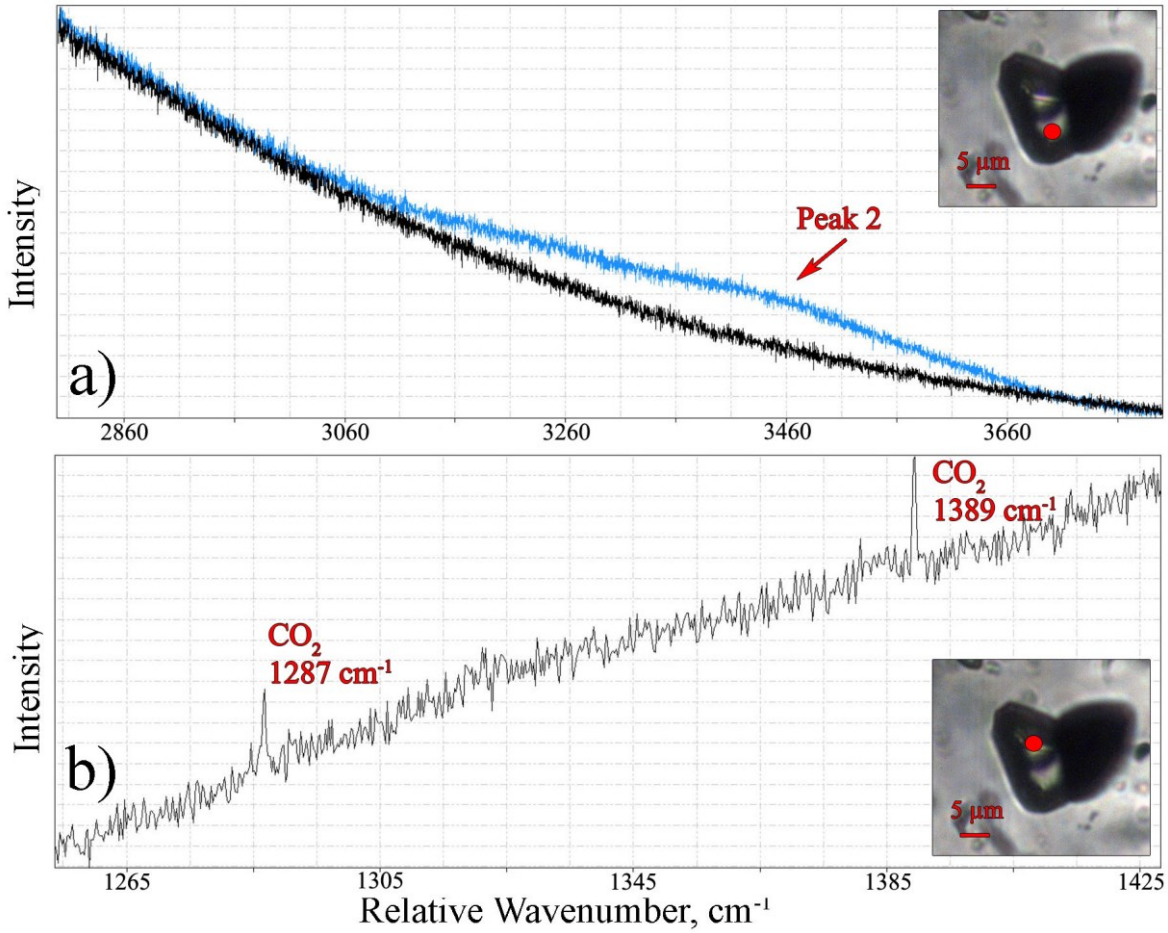

Figure 53: Raman spectra of the a) liquid and b) gas phase in a fluid inclusion of sphalerite from sample CHM2-68.5 suggesting the occurrence of H_2O (Peak 2: 3420 cm^{-1}) and CO_2 (1287 cm^{-1} and 1389 cm^{-1}). a) The fluorescence of sphalerite interferes with the Raman bands of H_2O. Therefore, the background spectrum of sphalerite (black) is illustrated together with the obtained spectrum for the liquid phase (blue) showing the second peak of H_2O. b) Spectrum of the gas phase showing two small peaks of CO_2. The decrease respectively increase in intensity is due to fluorescence of sphalerite. Red dots illustrate the spots of measurement in the inclusion.

7 Discussion

This Master thesis focused on the investigation of the polymetallic Chah-Mesi vein deposit, which is located close to the Meiduk porphyry system in the Kerman Copper Belt of SE Iran. The study aimed to obtain mineralogical data on the precious and base metal bearing veins. The data was used to interpret the physicochemical conditions of ore formation, to estimate the evolutionary path of hydrothermal fluids in space and time and to classify the deposit. Investigation included the sampling of five exploration drill cores brought down by the National Iranian Copper Industries Company in 2007. Macroscopic studies of the samples as well as microscopic and microanalytical data permitted the definition of several vein types, establishing the spatial distribution of the ore and alteration zones and the identification of a paragenetic sequence of mineral formation. In the following discussion the obtained data are compared to the general characteristics of epithermal deposits as e.g. summarized by Cooke and Simmons (2000) and Einaudi et al. (2003). A special focus was to establish regional trends on the deposit scale based on metal and ore associations. For this purpose, fahlore composition proved to be a valuable tool. Preliminary fluid inclusion studies allowed to constrain the PTX-conditions of ore formation. Finally, the possible genetic link of the polymetallic veins at Chah-Mesi with the nearby Meiduk porphyry deposit is discussed in the light of our new and previously published data (Hezarkhani, 2008; Hosseinkhani, 2009; Padyar et al., 2017). Conclusively, in order construct a genetic model, a synthesis of all obtained data discussed in this study and previously published information about Chah-Mesi and Meiduk is used.

7.1 Porphyry copper and epithermal deposits reviewed

As an introduction and for setting the background of the discussion the following chapter reviews important characteristics of porphyry copper deposits (PCDs) and summarizes general features of porphyry and epithermal systems.

7.1.1 Porphyry copper deposits

Porphyry systems involve some of the most widely distributed deposit types forming at convergent plate boundaries, including porphyry copper deposits (PCDs) centered around shallow intrusions, skarn, carbonate-replacement, and sediment-hosted Au deposits in peripheral locations as well as high- and intermediate-sulfidation epithermal deposits (Figure 54). Porphyry systems presently supply about 75 % of the world's Cu, 50 % Mo, 20 % Au, most of the Re, and minor amounts of other metals, such as Ag, Pd, Te, Se, Bi, Zn and Pb (Sillitoe, 2010). PCDs are characterized by low- to moderate metal grade (~0.3-2.0 % Cu) but are large tonnage (>100 Mt of ore) ore bodies that extend over several km² and allow profitable mining in huge open pit operations. Mineralization is disseminated, breccia and vein-hosted and forms in altered and genetically-related porphyry intrusions and adjacent wall rocks; stockwork-like mineralization is very typical. Commonly, these systems are connected to broadly coeval volcanism, shallowly emplaced (<10 km depth) stocks and dikes as well as underlying plutons and batholiths (John et al., 2010; Pohl, 2011).

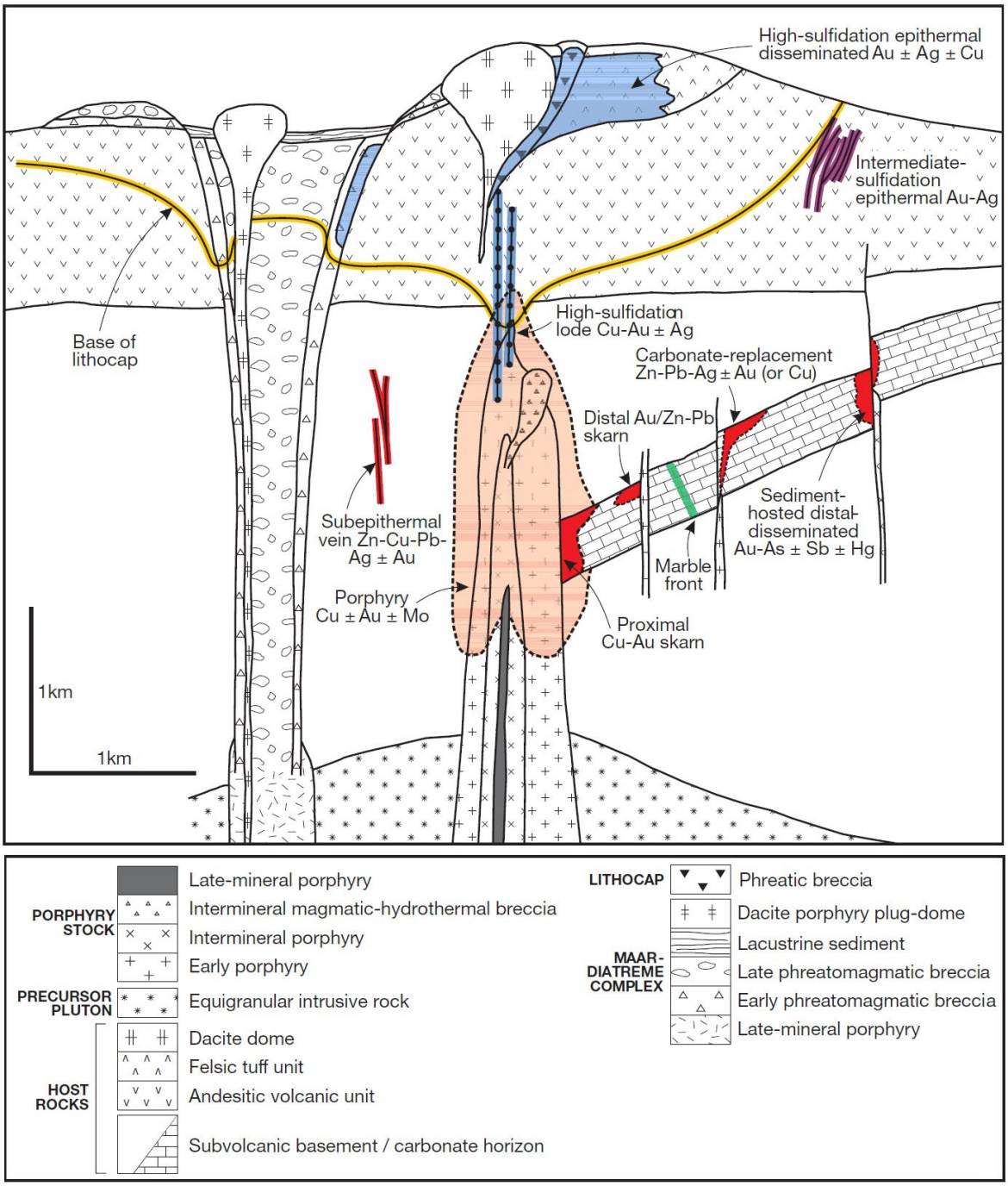

Figure 54: Anatomy of a telescoped porphyry Cu system showing spatial interrelationships of a centrally located porphyry Cu deposit in a multiphase porphyry stock and its immediate host rocks. Porphyry-related deposits of the periphery comprise proximal and distal skarn, carbonate-replacement (chimney-manto) and sediment-hosted (distal-disseminated) deposits in carbonate rocks as well as subepithermal veins in noncarbonate rocks. High- and intermediate-sulfidation epithermal deposits occur in and alongside the overlying lithocap environment. Temporal sequence of rock types is explained in the legend with the porphyry stock predating maar-diatreme emplacement, which in turn overlaps lithocap development and phreatic brecciation. Individual systems rarely contain several of the deposits types illustrated, however, the cartoon adds little to the understanding of porphyry Cu genesis and embodies the relationships observed in the field. Reproduced from Sillitoe (2010).

Typically, porphyry Cu deposits are centered above cylindrical stock-like, composite intrusions (Figure 54) having dimensions of about 1.5 x 2 km. Igneous rocks typically show porphyritic textures in the inner core surrounded by an outer shell of equigranular medium-grained rock. The porphyritic texture indicates rapid crystallization to produce the finer grained groundmass surrounding earlier formed phenocrysts (plagioclase, hornblende, biotite) (Evans, 1993). The porphyry intrusions comprise multiple intrusive phases, that were emplaced before (early porphyries), during (inter-mineral porphyries), near the end of (late mineral porphyries), and after (post-mineral porphyries) the alteration and mineralization event (Sillitoe, 2010).

7.1.1.1 Geodynamic setting

Most porphyry systems form at convergent plate margins and range from Precambrian to Quaternary in age, though the most known deposits formed during the Cenozoic and Mesozoic (Cooke et al., 2005; John et al., 2010). However, porphyry Cu deposits have also been discovered in ancient fold belts and in post-collisional settings (Asadi, 2018; Richards, 2009). At convergent margins, porphyry deposits are genetically linked to intermediate to felsic calc-alkaline magmas in volcano-plutonic arcs above active subduction zones (Figure 55 A) at continental margins (e.g. Andean porphyries) and at intra-oceanic island arcs (e.g. Pacific island porphyries). The magmas derive their fundamental characteristics of relatively high oxidation state and enrichments in water, alkalis, S, and Cl, H_2O, and some metals from the subduction process. These characteristics are critical to the formation of magmatic-hydrothermal ore deposits of this type: the high oxidation state suppresses the formation of significant amounts of magmatic sulfide phases, which would strip the magma of chalcophile and siderophile metals (Richards, 2005); the high water content results in saturation of the magma in an aqueous fluid phase upon ascent into the upper crust, into which these metals will efficiently partition (Candela and Holland, 1984). In most cases, arc crust is relatively thick with evidence for broadly coeval contractional or transpressional tectonism (John et al., 2010). It is suggested that most porphyry deposits formed during specific periods of subduction and changes in the tectonic regime (e.g. stress field) is important for porphyry ore genesis (Cooke et al., 2014). Cooke et al. (2005) showed that many giant copper- and gold-rich porphyries are inferred to be associated with regions where flat or shallow subduction was induced by subduction of buoyant oceanic features, such as ridges, ocean plateaus or seamount chains and synchronous with ore formation. These collisions do not cause a cessation of subduction but do result in crustal thickening, rapid uplift and exhumation.

Although most PCDs are present in subduction-related magmatic arcs, the recent recognition of porphyry-style mineralization in parts of Tibet, China and SE Iran (Asadi, 2018) revealed that some porphyry copper deposits are related to post-subduction magmatism. Richards (2009) proposes that post-subduction porphyry copper deposits can form from remelting of subduction-metasomatized mantle in both extensional and compressional environments (Figure 55 B, C, D). These environments include: (1) areas of post-subduction arc extension where decompressional melting occurs in upwelling subduction-metasomatized asthenosphere and lithosphere, which generates mafic alkaline magmas of shoshonitic or hawaiitic composition (Figure 55 B); and (2) post-subduction arc contraction caused by collision that can lead to crustal thickening and delamination of the subcontinental lithospheric mantle. The partial melting of lower crustal rocks results from depression of lower crustal rocks as isotherms rebound or due to invasion of hot asthenosphere. During these processes, melts with more felsic, calc-alkaline or

mildly alkaline compositions are generated (Figure 55 C, D). The magmas of both extensional and compressional post-subduction settings tend to be small volume, spatially isolated and mildly (high-potassium ± sodium calc-alkaline) to strongly alkaline in composition. The remelting of rocks containing residual copper- and gold-rich sulfides left in cumulates during earlier subduction-related magmatism provide a fertile source of copper and gold that eventually are redeposited in these post-subduction porphyry deposits (John et al., 2010; Richards, 2009).

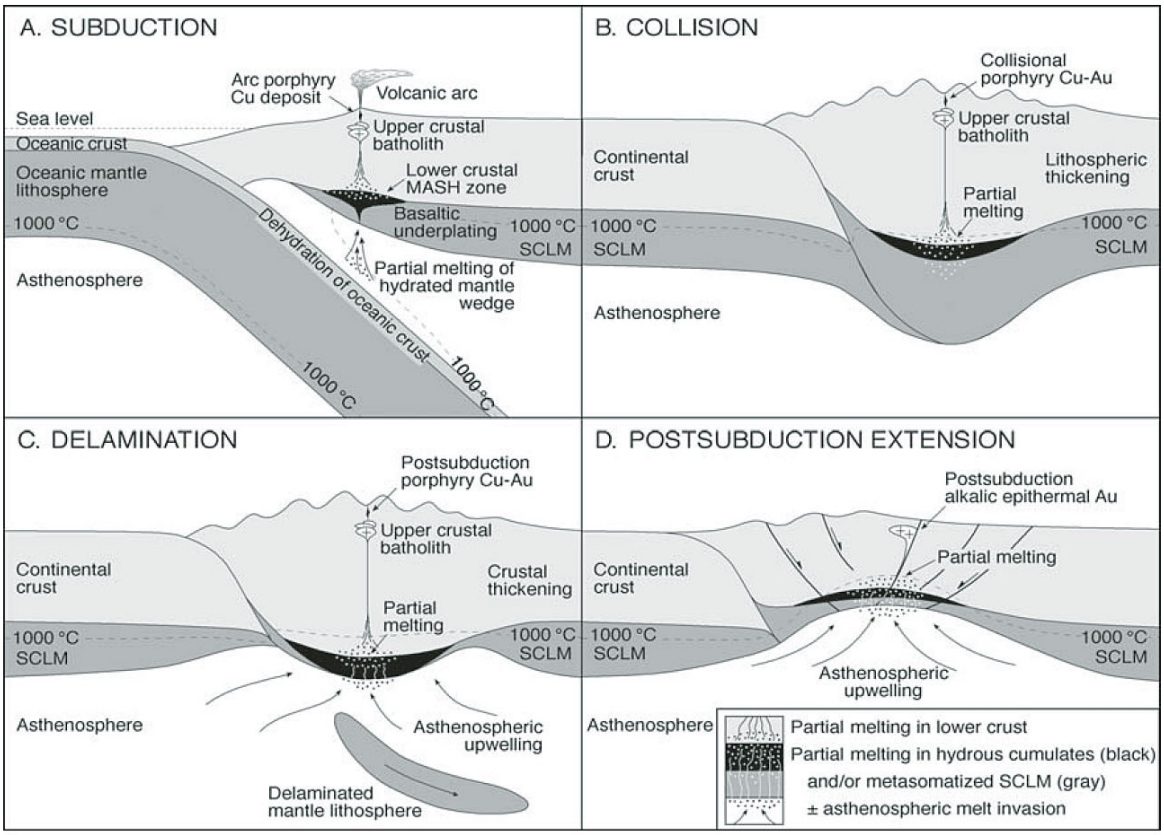

Figure 55: Geodynamic setting of porphyry Cu deposits. A) Typical continental margin arc above subduction zone. Porphyry copper generation as a product of normal arc magmatism. B) Collisional lithospheric thickening. C) Post-collisional lithospheric mantle delamination. D) Post-subduction lithospheric extension. MASH: zone of melting, assimilation, storage, and homogenization; SCLM: subcontinental lithospheric mantle; B-D) Remelting of subduction-metasomatized SCLM or lower crustal hydrous cumulate zones (black layer) leading to potential porphyry copper-gold and epithermal gold deposit formation. High Sr/Y and La/Yb magmas may be generated in all cases by residual or fractionating hornblende (± garnet, titanite) in the lower crust (John et al., 2010). Reproduced from Richards (2009).

7.1.1.2 Magma characteristics of PCDs

Porphyry intrusions are exclusively of I-type and magnetite-series affiliation, and typically metaluminous and medium K calc-alkaline, but magmas may also show high K calc-alkaline (shoshonitic) or even alkaline characteristics. The range of compositions comprises calc-alkaline diorite and quartz diorite through granodiorite to quartz monzonite as well as alkaline diorite through monzonite and subordinate syenite (Sillitoe, 2010). Host intrusions in island arc settings have primitive initial $^{87}Sr/^{86}Sr$ isotope ratios (0.705-0.702) and the melts therefore presumably derived from the upper mantle and/or recycled oceanic crust. Higher Sr isotope ratios in mineralized intrusions in continental settings indicate derivation from or contamination by crustal material (Evans, 1993; Seedorff et al., 2005).

Investigation on the geochemical evolution of low-mineralized to well-mineralized porphyry copper systems of the UDMB has shown that in general all porphyry intrusions exhibit LREE enrichment relative to HREE. However, economic deposits (e.g. Sungun, Sar Cheshmeh, Meiduk) exhibit a relatively steep LREE to HREE profile reflecting a higher LREE abundance than in sub-economic porphyry copper systems (e.g. Reagan and Daraloo; Habibi and Hezarkhani, 2013; Hezarkhani, 2006b). Moreover, Eu anomalies vary from distinct negative in sub-economic deposits (Eu/Eu* = 0.28-0.70) to either markedly less negative or positive anomalies (Eu/Eu* = 0.45-1.67) in economic deposits. The lack of distinct negative Eu anomalies is referred to more oxidized PCD magmas, where all REEs occur trivalent (including Eu^{3+}). Also, the lack of significant plagioclase fractionation reflects the high magmatic water contents and depression of plagioclase fractionation. High La/Sm and Sm/Yb values may indicate economic porphyry deposits and reflect high crustal assimilation in a relatively thickened crust and the fractionation of hornblende with garnet. The steep downward LREE to MREE and flatter MREE to HREE slopes in economic deposits indicate hornblende involvement with magma evolution toward more volatile content. Thus, it is proposed that in an ongoing process of subduction, during compression and crustal shortening, sub-economic intrusions are followed by adakite-like hydrous economic Cu-bearing intrusions (Zarasvandi et al., 2015).

7.1.1.3 Hydrothermal alteration and mineralization

Hydrothermal alteration and mineralization are essential features of porphyry deposits. Ideally, alteration zones form concentric shells around the intrusions. Alteration affects a large volume of wallrocks around and above the intrusions. The classical model of Lowell and Guilbert (1970) is the result of fundamental comparative studies on several porphyry copper deposits. It demonstrates that the nature and distribution of the zones of hydrothermal wallrock alteration is the best reference framework to which all the other features of these deposits can be related (Lowell and Guilbert, 1970). Alteration of wallrocks includes alkali-dominated assemblages (potassic, sodic, sodic-calcic), acid assemblages (advanced argillic, sericitic) and propylitic alteration. The hydrothermal alteration varies from early high-temperature and proximal alkali-rich minerals (potassic alteration zone) to later and mostly distal sheet silicate- and pyrite-rich mineral zones (sericitic or phyllic, intermediate argillic and advanced argillic alteration types) (John et al., 2010).

Subsequent to the Lowell-Guilbert model that is based on porphyry deposits related to intrusives with high silica to alkali ratios, deposits in association with intrusives that show a low ratio of these elements are best pictured by the diorite model of Hollister (1978). These porphyry deposits related to diorites differ in a number of ways from the Lowell-Guilbert model. One of the main reasons could be that sulfur concentrations were relatively low in the mineralizing fluids in the latter. As a result, not all iron in the host rocks is converted to pyrite and much iron remains fixed in chlorite and biotite while excess iron tends to occur as magnetite that may be present in all alteration zones.

Regarding alteration zoning, the phyllic and argillic zones are usually absent in diorite-hosted porphyry systems. In this case, the potassic zone is directly bordered by propylitic alteration. Diorite-hosted porphyry systems are present in both island arc and continental arc settings. Concerning the mineralization, the main difference is that significant amounts of gold may occur, and molybdenum usually is low. Fractures containing gangue silicates and copper sulfides are mostly devoid of quartz and commonly rich in chlorite, epidote and albite.

7.1.1.3.1 Hydrothermal alteration

The model after Sillitoe (2010) summarizes alteration patterns of porphyry Cu deposits, which display a broad-scale alteration-mineralization zoning that comprises, centrally from the bottom upward, sodic-calcic, potassic, chlorite-sericite, sericitic and advanced argillic alteration. Chloritic and propylitic alteration zones develop distally at shallow and deeper levels, respectively. Opaque mineral assemblages are intrinsic parts of each alteration type because of the direct linkage between sulfidation state, the chief control on sulfide assemblages, and solution pH, a principal control of alteration type (Einaudi et al., 2003; Meyer and Hemley, 1967). Sulfidation state (Chapter 7.1.2.1) changes from low through intermediate to high as temperature declines (Einaudi et al., 2003). Generally, the alteration-mineralization types become progressively younger upward, with the result that the shallower alteration-mineralization zones overprint and partly reconstitute deeper ones (Figure 56 a). The sequence, from potassic with peripheral propylitic through chlorite-sericite and sericitic to advanced argillic, is the result of increasing acidity consequent upon the declining temperature of the hydrothermal fluids (Figure 56 b). A parallel simultaneous increase in sulfidation state of the fluids results in changes in the sulfide assemblage from chalcopyrite-bornite, through chalcopyrite-pyrite and pyrite-bornite, to pyrite-enargite or pyrite-covellite. Cu-bearing sulfides are commonly absent in the early, high-temperature advanced argillic zone (Sillitoe, 2010).

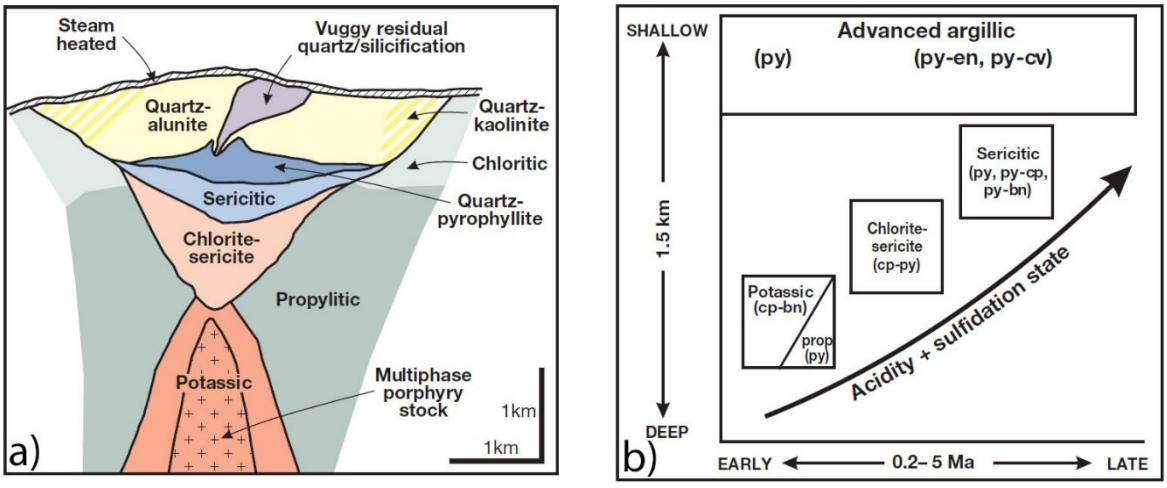

Figure 56: a) Generalized alteration-mineralization zoning pattern for porphyry Cu deposits. Shallow alteration-mineralization types consistently overprint deeper ones. Volumes of the different alteration types vary markedly from deposit to deposit. Sericitic alteration may project vertically downward and often separates the potassic and propylitic zones as well as cutting the potassic zone centrally. Alteration-mineralization in the lithocap is commonly far more complex than shown. See text for further details. b) Schematic representation of generalized alteration-mineralization sequence in relation to paleodepth and system life span. Both figures are from Sillitoe (2010) and modified after Sillitoe (2000).

Sodic-calcic alteration affects commonly the immediate wallrocks to the porphyry intrusions and is normally poorly preserved at depth with only minor amounts of sulfides and metals. Large parts of many porphyry Cu deposits, especially deeply formed, are made up predominantly of potassic alteration, which grades marginally into weakly developed propylitic zones. *The potassic zone alteration* is characterized by the alteration assemblage quartz + K-feldspar ± biotite ± sericite ± anhydrite (Lowell and Guilbert, 1970). This alteration affects mainly the early and inter-mineral porphyry generations (Figure 54) and is generally pervasive (Sillitoe, 2010). Alteration minerals replace primary magmatic

orthoclase, plagioclase and mafic minerals (Pirajno, 1992). Common ore minerals are pyrite, chalcopyrite, bornite with minor magnetite and molybdenite. This assemblage is ascribed to high-temperature magmatic-hydrothermal fluids.

Chlorite-sericite alteration is widespread in the shallower parts and overprints preexisting potassic assemblages. The alteration is typified by partial to complete transformation of mafic minerals to chlorite, plagioclase to sericite-illite as well as magmatic and any hydrothermal magnetite to hematite (martite and/or specularite). The zone of sericitization (also known as phyllic alteration) overprints and wholly or partially destroys the potassic and chlorite-sericite assemblages (Sillitoe, 2010).

Sericitic alteration is characterized by the assemblage quartz-sericite-pyrite (QSP zone). It usually includes minor chlorite, illite and rutile. Pyrophyllite may be present, but carbonate and anhydrite are very rare. The inner part of this zone is dominated by sericite, whereas further outward clay minerals become more important. Sericitization affects feldspars and primary biotite and results in silica-generating reactions producing much secondary quartz causing silicification. The contact with the potassic zone is gradational over tens of meters and disseminated and veinlet pyrite shows its major abundance within zones of sericitic alteration (Pirajno, 1992).

Advanced argillic alteration occurs in the near-surface lithocaps and often the root zones overprint the upper parts of porphyry Cu deposits. Sericitic alteration is commonly transitional upward to quartz-pyrophyllite, an assemblage widespread in the deep, higher temperature parts of many lithocaps. The assemblage of quartz-kaolinite is related to lower temperatures and also known as argillic alteration after Lowell and Guilbert (1970). The argillic zone (also known as intermediate argillic alteration) comprises mainly clay minerals with kaolinite being dominant close to the orebody and montmorillonite further away. In comparison to the sericitic zone, pyrite is less abundant, but still very common. It occurs in veinlets rather than disseminated. Biotite may be unaffected or converted to chlorite and feldspars are generally only slightly decomposed.

As the outermost zone, the *propylitic alteration* zone is always present and chlorite is the most common mineral there. Calcite and epidote usually join the alteration assemblage and primary mafic minerals (biotite and hornblende) are altered partially or completely to chlorite and carbonate. The propylitic zone fades out into the unaltered surrounding rocks over several hundreds of meters (Evans, 1993).

7.1.1.3.2 Mineralization in PCD

Copper is the dominant metal produced from porphyry copper deposits with important by-products being Mo, Au and lesser amounts of Ag, Re and PGEs. Copper minerals include chalcopyrite, bornite, chalcocite, enargite and digenite in hypogene ore and chalcocite, covellite, tenorite, chrysocolla, malachite, azurite, and native copper in supergene ore. The distribution of metals (Cu, Mo, Au, Zn, Pb, Ag) varies and zonation often broadly correlates with fluid flow directions (pressure gradients), reactivity of wall rocks (alteration types) and gradients of both temperature and reduced sulfur species in the hydrothermal fluids with the more soluble base metals (Zn, Pb) mostly found distally (John et al., 2010). Ore deposition may occur totally within the intrusive stock, in the stock and within the country rocks or only in the country rocks.

The shape of many porphyry copper deposits mimic those of their host intrusions and many of them have vertically extensive orebodies, which become progressively lower grade both outward and

downward (Sillitoe, 2010). Mineralization tends to develop in zones with a central barren to low grade zone with disseminated to subordinate fracture-controlled chalcopyrite, molybdenite and pyrite forming only a few percent of the rock, but occasionally ranging up to 10 %. Going outwards, a first increase in molybdenite is followed by chalcopyrite as the main ore constituent and develops to veinlet mineralization. Pyrite mineralization also increases in intensity outwards to form a peripheral pyrite-rich halo with 10-15 % pyrite but only minor chalcopyrite and molybdenite. A spatial relationship to the wallrock alteration is indicated with the highest copper values often being developed at the boundary between the potassic and sericitic zones. Commonly, mineralization is not found in the argillic zone, which appears to have been formed later and to be superimposed on the other alteration zones. Weak, but non-economic mineralization continues outwards into the propylitic zone (Evans, 1993).

Distal ore formation in porphyry Cu systems may occur in permeable wallrocks, within propylitic halos, where fault- and fracture-controlled, subepithermal Zn-Pb-Cu-Ag ± Au veins of currently limited economic importance tend to be developed. The advanced argillic alteration dominated lithocap environment is commonly located above and overprints porphyry Cu deposits (Figure 54). High-sulfidation epithermal Au, Ag, and/or Cu deposits are typical, however, preserved parts of many lithocaps are essentially barren. The deeper level high-sulfidation deposits tend to be characterized by massive sulfides, commonly rich in the Cu-bearing sulfosalts of enargite, luzonite and/or famatinite, which mostly occur as tabular veins overprinting porphyry Cu deposits.

Intermediate-sulfidation epithermal precious metal deposits, containing Zn-Pb-Ag ± Cu ± Au as well as Mn-bearing carbonates, rhodonite and quartz occur alongside lithocaps. They are mostly spatially separated from the high-sulfidation orebodies but may display transitional mineralogic relationships. The intermediate-sulfidation epithermal veins are the shallow-level (<1 km paleodepth) counterparts of the Zn-Pb-Cu-Ag ± Au veins located alongside porphyry Cu deposits, but no direct connection between the two types is evident (Figure 54).

Superficially, PCDs often display a variety of weathering features including exotic copper deposits in which copper has been transported laterally from the original hypogene ore, leached caps, supergene enrichment blankets and oxide copper deposits formed in situ (John et al., 2010).

7.1.1.4 Genesis of porphyry systems

Porphyry Cu systems are initiated by injection of hydrous, oxidized magma saturated with S- which and exsolve metal-rich, aqueous fluids from the cooling and fractionating parental chambers during magma convection as well as later stagnant magma crystallization (Shinohara and Hedenquist, 1997). The required magmatic fluid volume is produced during the focused and episodic ascent of magma and fluid for as long as about 5 million years in the case of long-lived porphyry Cu systems (Sillitoe, 2010). Parental magmas need to be water rich (>4 wt%) and oxidized in order to maximize the metal contents endowment of the resultant exsolved aqueous phase. High water contents result in magmas becoming saturated with the aqueous phase, into which the ore metals can partition efficiently. High oxidation state suppresses magmatic sulfide precipitation, a process that may cause sequestration of metals before they can partition into the aqueous phase (Richards, 2005).

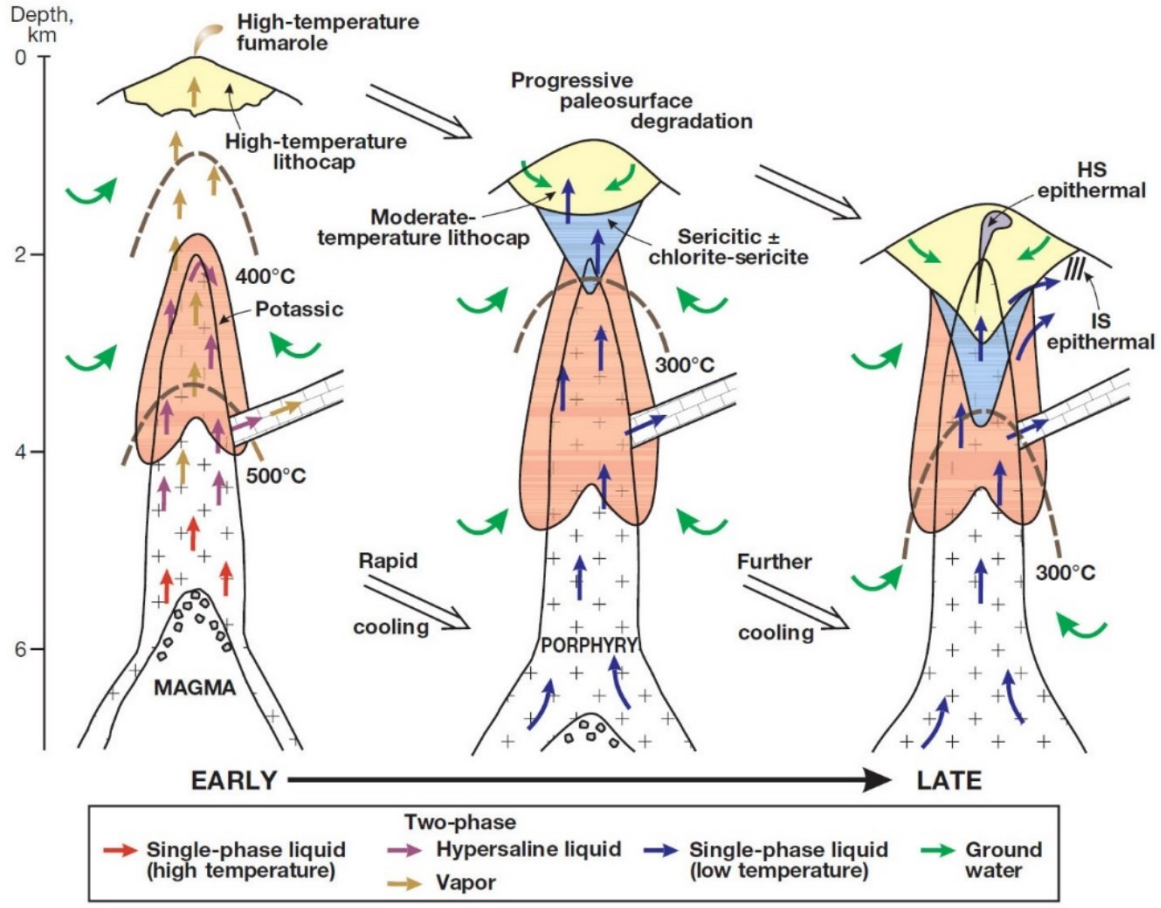

Figure 57: Schematic time slices through a telescoped porphyry Cu system illustrated in Figure 54 based on modeling by Sillitoe and Hedenquist (2003) and Heinrich (2005). The illustration after Sillitoe (2010) is showing the evolution of the main magmatic fluid and alteration-mineralization types together with progressive downward magma solidification, cooling and paleosurface degradation. For detailed explanation of the individual genetic stages see text.

The sequence of alteration-mineralization events is a consequence of progressive rock and fluid cooling (from >700 °C to <250 °C) caused by solidification of the underlying parental plutons and downward propagation of the lithostatic-hydrostatic transition as well as paleosurface degradation. At the early stage (Figure 57, left side), magma is present at the top of the parental chamber and, a single-phase, low- to moderate-salinity (2-10 wt% NaCl equiv.), fluid exsolves from the magma (Heinrich, 2005). This aqueous liquid phase decompresses, cools and therefore undergoes phase separation during ascent to generate immiscible hypersaline liquid fluid (brine) and larger volume of low-density vapor. The liquid phase/brine is enriched in Na, K and Fe chlorides, whereas the vapor phase contains acidic volatile species, such as SO_2, H_2S, CO_2, HCl and HF (Giggenbach, 1992). Phase separation causes the selective fractionation of specific element suites between the vapor and hypersaline liquid with vapor containing appreciable amounts of the Cu, Au, Ag and S, plus much of the As, Sb, Te and B. However, Fe, Zn, Pb, Mn and possibly Mo preferentially partition into the hypersaline liquid (Heinrich, 2005). During the cooling of the porphyry Cu system through the 700° to 550 °C temperature range, the fluids initiate potassic alteration plus low-sulfidation state high-temperature porphyry Cu mineralization that affects mainly early to inter-mineral porphyries and their immediate wall rocks. Quartz-veined cores of the potassic zones remain barren because temperatures are too high to permit Cu-Fe ± Au sulfide deposition, potentially giving rise to the bell- and cap-shaped ore zones described by the Lowell and Guilbert (1970)

model and documented from many porphyry deposits. Coincident with the potassic alteration, heated external water, largely meteoric with subordinate connate component, generates the peripheral propylitic alteration. The convective circulation of the external water takes place where rock permeabilities are adequately high and causes moderate-temperature hydration reactions (Meyer and Hemley, 1967). Upward-escaping, low-pressure vapor that does not reach the paleosurface as high-temperature fumaroles (Hedenquist et al., 1993) undergoes disproportionation of the contained SO_2 (to H_2SO_4 and H_2S) that, eventually, condenses together with HCl into ground water (Giggenbach, 1992). This acidic condensate produces the extremely low pH fluid responsible for the generally barren advanced argillic alteration of the lithocap environment on top of the porphyry system (Figure 56 a) and the generation of the vuggy, residual quartz cores (Meyer and Hemley, 1967).

As magma solidification advances downward (Figure 57, middle), the entire porphyry system cools rapidly and the rock can fracture in a brittle fashion on cooling below 400 °C, hence, lithostatic gives way to hydrostatic pressure. Due to lower temperature conditions the aqueous liquid phase exsolves more slowly from the still crystallizing magma and, in turn, advects more slowly and cools, what may prevent the intersection of its solvus. A single-phase, low- to moderate-salinity (5-20 wt% NaCl equiv.) liquid in the 350° to 250 °C temperature range ascends directly from the parental chambers into the overlying porphyry Cu system (Shinohara and Hedenquist, 1997). The mixing of the magmatic fluid with meteoric water is often responsible for the formation of the late sericitic ± chlorite (phyllic) alteration zones, particularly at the margins of systems where the advecting magmatic fluid may entrain and mix with convecting meteoric water. Sericitic alteration may be related with variable degrees of Cu ± Au mobilization and cooling of hypersaline liquids fluids in contact with external wallrocks that are diluted with meteoric water causes Zn, Pb, Ag and Mn precipitation giving rise to geochemical halos and localized veins in the propylitic halos.

The fluid most likely induces high-sulfidation (HS) epithermal Au ± Ag ± Cu mineralization (Figure 57, right side) in the relatively barren, early formed lithocaps whereas the low- to moderate-salinity, H_2S-rich, aqueous fluid produced the underlying sericitic alteration zone. On entering the lithocap environment, this intermediate-sulfidation state fluid becomes unbuffered and easily evolves to a higher sulfidation state on cooling. These fluids may pass into adjoining, less altered rocks and undergo sufficient neutralization and reduction during outward flow and wallrock reaction to produce fluids capable of forming intermediate-sulfidation (IS) epithermal deposits. Alternatively, the intermediate-sulfidation state fluids derived from deeper parts of the system may bypass the lithocaps entirely and produce epithermal intermediate-sulfidation mineralization at shallow levels (Einaudi et al., 2003; Sillitoe and Hedenquist, 2003).

7.1.2 Epithermal deposits

Epithermal systems are defined as those formed at low to moderate temperatures (between about 50 and 300° C) and low pressures (< 500 bar or depth equivalent of < 1 to 1.5 km) from hydrothermal fluids of low to moderate salinity (<1 to 5-15 wt% NaCl equivalent). The fluids often have a magmatic-meteoric signature with HCl, CO_2 and H_2S being of magmatic derivation. Due to their formation at near-surface levels in geotectonic settings characterized by rapid erosion the preservation potential of epithermal systems in the ancient geological record is generally poor. Therefore, most known epithermal systems are of Cenozoic age and, like porphyry systems, they are especially abundant at convergent plate margins as well as in rift-related settings.

Common and distinct mineralogical features of epithermal mineralization are the presence of fine-grained chalcedonic silica, calcite, quartz pseudomorphs after calcite (indicative of boiling fluids) as gangue minerals. The elemental association typically is typically Au, Ag, As, Sb, Hg, Tl, Te, Pb, Zn and Cu, whereas these elements commonly form sulfides and Cu-bearing sulfosalts (enargite, luzonite-famatinite and/or tennantite-tetrahedrite). Characteristic ore textures include open space fillings (low pressure environment), crustifications, colloform banding and comb structures. Mineralization is formed from the surface to approximately 1.5 km below the surface and consists of veins, stockworks and disseminations occurring either together or as single entities. Hydrothermal breccias can also be present. Generally, epithermal deposits provide easy mining targets with Au and Ag being the main metals of interest. They are either mined as open cast or shallow underground operations depending on tonnage and grades (Pirajno, 2009).

7.1.2.1 Classification

Modern classification schemes of epithermal deposits are based on alteration assemblages, hypogene sulfide-oxide assemblages and the oxidation/sulfidation states (Einaudi et al., 2003; Sillitoe and Hedenquist, 2003). The term sulfidation state was originally defined by Barton (1970) and has been used analogous to oxidation state, whereas nowadays the frame of reference is temperature and the fugacities of S_2 (f_{S2}) and O_2 (f_{O2}), respectively. The sulfur respectively oxygen fugacity of a system, at any temperature, is compared to standard mineral reactions (buffers), such as

$$\underset{\text{magnetite}}{4Fe_3O_4} + O_2 = \underset{\text{hematite}}{6Fe_2O_3} \quad (1)$$

for oxygen, or

$$\underset{\text{pyrrhotite}}{2FeS} + S_2 = \underset{\text{pyrite}}{2FeS_2} \quad (2)$$

for sulfur. The basis for assigning relative sulfidation or oxidation states are the differences between the sulfur or oxygen fugacity deduced for the natural mineral assemblage compared to that of a buffer reaction. In nature the most stable species of sulfur in the oxidized state is SO_4^{2-} and in the reduced state H_2S. In hydrothermal systems, sulfidation state controls the speciation of sulfur and the deposition of ore minerals whereby ore-forming fluids contain S in various valence states (Seedorff et al., 2005).

Einaudi et al. (2003) designed a pioneering phase diagram distinguishing five arrays of sulfidation states based on sulfidation reactions among minerals in the system Cu-Fe-As-S distinguishing “very low”, “low”, “intermediate”, “high” and “very high” sulfidation fields (Figure 58). These arrays comprise a complex transition from porphyry (500-350 °C) to high- and low-sulfidation (<350 °C) environments (Pirajno, 2009).

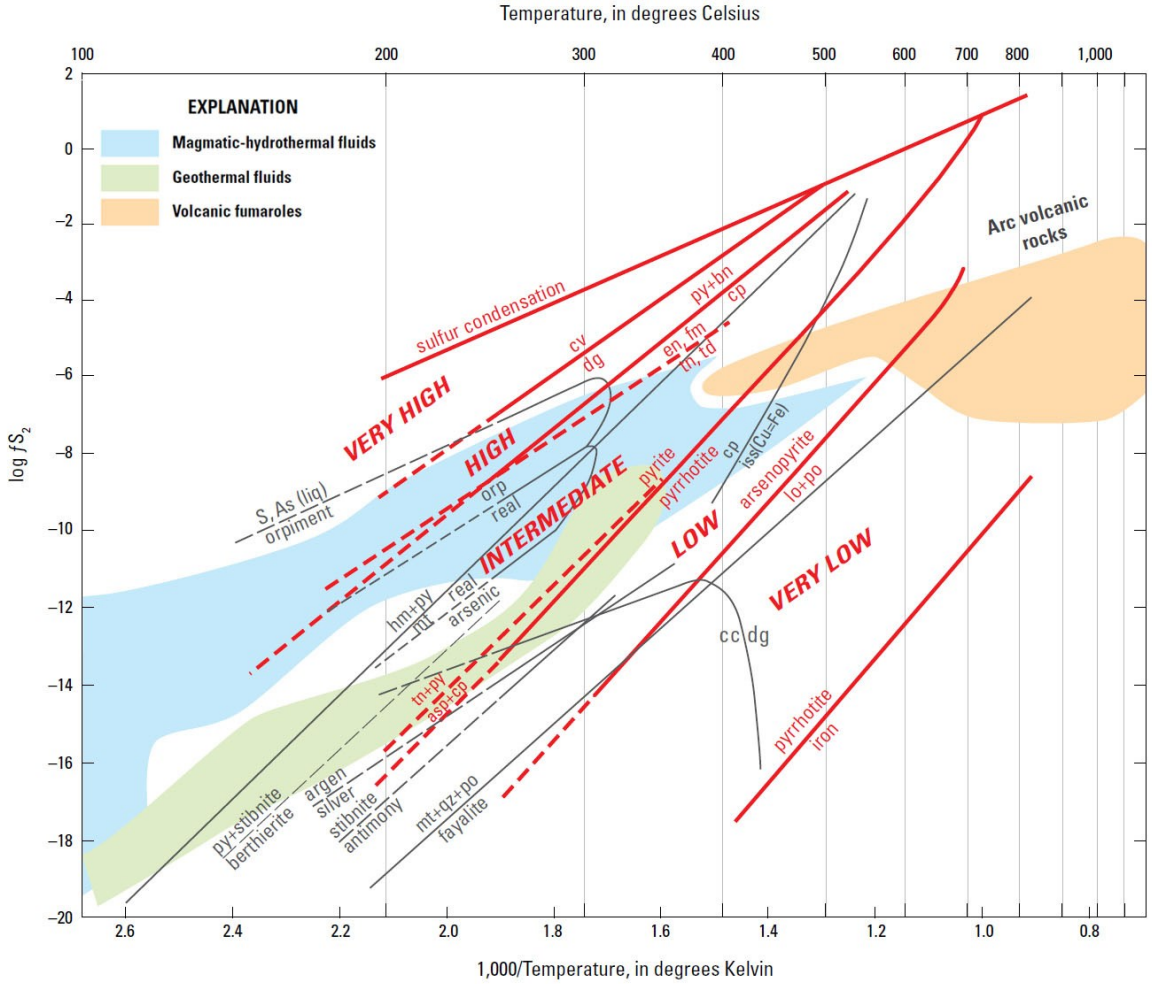

Figure 58: Sulfur fugacity (fS_2)-temperature diagram showing the variety of sulfide assemblages in hydrothermal ore deposits and reflecting sulfidation state, from very low to very high. Thick red lines mark boundaries between these sulfidation states. Compositional fields of arc volcanic rocks, high-temperature volcanic fumaroles, magmatic-hydrothermal fluids, and geothermal fluids also are shown, as discussed by Einaudi et al. (2003). Figure after John et al. (2018) modified from Sillitoe and Hedenquist (2003). Element and mineral abbreviations: argentite (argen); arsenic (As); arsenopyrite (asp); bornite (bn); chalcocite (cc); chalcopyrite (cp); copper (Cu); covellite (cv); digenite (dg); enargite (en); famatinite (fm); iron (Fe); hematite (hm); intermediate solid solution (iss); loellingite (lo); magnetite (mt); orpiment (orp); pyrite (py); pyrrhotite (po); quartz (qz); realgar (real); sulfur (S); tennantite (tn); tetrahedrite (td).

Considering the sulfidation state, epithermal deposits are nowadays commonly classified into three subtypes; low-, intermediate- and high-sulfidation epithermal deposits. Low-sulfidation epithermal deposits are characterized by the low-sulfidation state assemblage of pyrite, arsenopyrite, with minor chalcopyrite and pyrrhotite in some deposits. Intermediate-sulfidation epithermal deposits are characterized by intermediate-sulfidation state assemblages containing pyrite, chalcopyrite, tetrahedrite-tennantite, and iron-poor sphalerite. High-sulfidation epithermal deposits typically contain sulfide-rich assemblages of high-sulfidation state, including pyrite-bornite, pyrite-enargite, pyrite-luzonite, pyrite-

famatinite, and pyrite-covellite (Einaudi et al., 2003; Sillitoe and Hedenquist, 2003). Silver sulfides and selenides, silver-bearing sulfosalts and electrum (>20 wt% Ag) are mostly restricted to low- and intermediate-sulfidation deposits, whereas enargite and silver-poor gold (<10 wt% Ag) are common in nearly all high-sulfidation deposits. Geological features and metal contents also differ between low- and intermediate-sulfidation deposits. Low-sulfidation deposits commonly consist of multiple stages of sheeted veins, vein stockworks and breccias with comb and crustiform textures. These mineralized veins include fine concordant and discordant layered mineral assemblages. Intermediate-sulfidation deposits consist of multistage veins and associated breccias that contain significant amounts of other base metals like Cu, Pb and Zn in addition to gold and silver (Cooke and Simmons, 2000; John et al., 2018).

Hydrothermal alteration assemblages (Chapter 7.1.1.3.1) typically are zoned laterally and vertically around the ore bodies and relative to the paleowater table. Alteration associated with low- and intermediate-sulfidation deposits includes near-neutral pH alkali-dominated assemblages formed below the water table and steam-heated acid assemblages formed at and above the water table. Below the paleowater table, hydrothermal alteration around ore zones is commonly zoned with silicification and potassic (adularia-illite) alteration in the inner zones grading outward to argillic and propylitic assemblages. Argillic and advanced argillic alteration is present at and above the paleowater table. Hydrothermal alteration associated with high-sulfidation deposits results from intense acid leaching by low-pH fluids formed by condensation of HCl- and SO_2-rich fluid in groundwater. Characteristically, alteration is zoned with residual (vuggy) quartz and quartz-alunite assemblages around fluid conduits in the innermost zone grading outward into advanced argillic (kaolinite/dickite or pyrophyllite), argillic (illite-montmorillonite) and propylitic assemblages (John et al., 2018).

Geological and geochemical evidence demonstrates that subaerial epithermal mineralization and associated cogenetic hydrothermal alteration form predominantly from meteoric waters with variable amounts of magmatic volatiles released during emplacement and crystallization of temporally and spatially associated mafic to silicic magmas. High-sulfidation deposits typically show hydrothermal alteration assemblages, geochemical characteristics and isotopic compositions reflecting stronger magmatic fluid input than intermediate- and low-sulfidation deposits. The ultimate source of gold, silver and other metals in epithermal gold-silver deposits is uncertain, but likely includes multiple sources in the upper mantle and crust (John et al., 2018). Sillitoe (2008) suggested that many mineral deposits may be associated with, and in some cases are transitional to, epithermal deposits (Figure 59). These deposit types include hot spring mercury (Hg), porphyry copper (Cu, Mo, Au), skarn (Cu, Fe, Au, Zn), polymetallic vein (Au, Ag, Cu, Zn, Pb, Mn, As), polymetallic replacement (“manto”, Ag, Pb, Zn, Cu, Au), intrusion-related breccia pipe (Au, Ag, Cu, Pb, Zn), sedimentary-rock hosted gold (Au) and distal-disseminated gold-silver (Au, Ag), placer (Au) and stratiform sulfur (S).

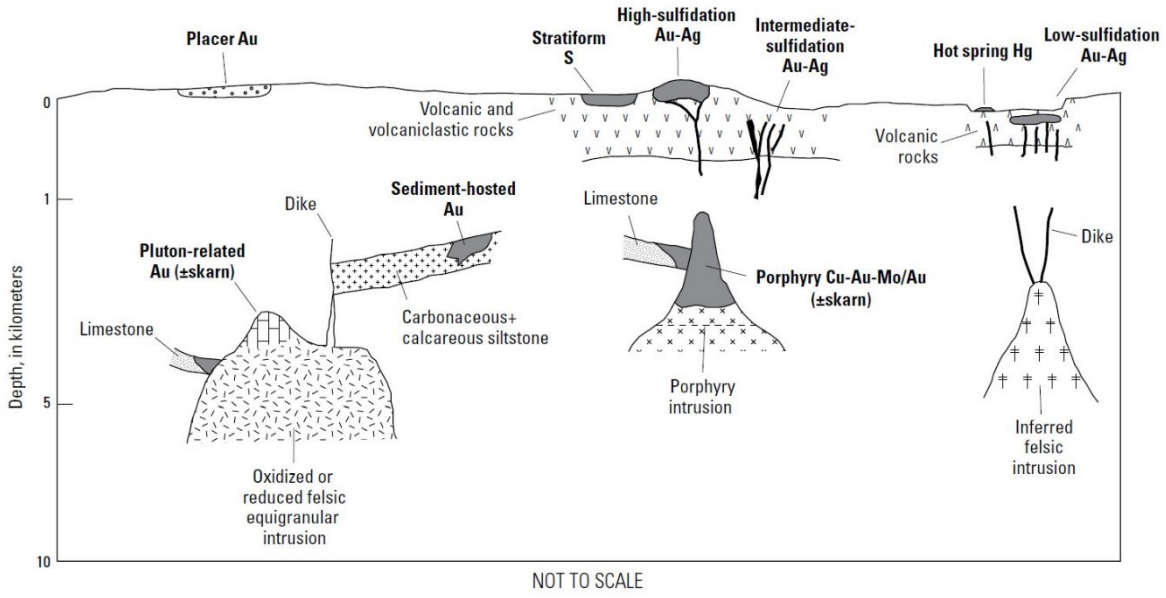

Figure 59: Sketch showing position (depth) of epithermal gold-silver deposits in the upper crust and of other ore deposit types of which some may be genetically related to the epithermal deposits. Figure from John et al. (2018) based on Sillitoe (2008).

In the following chapters the most important characteristics of epithermal deposits and their classification will be summarized (Table 15). The modern classification of this class of magmatic hydrothermal ore deposits is based on ore and gangue mineralogy as well as physicochemical characteristics (temperature, pH, oxidation/sulfidation state) of the mineralizing fluids. Herein, the widely accepted classification by Hedenquist et al. (2000) is used distinguishing high-sulfidation, intermediate-sulfidation and low-sulfidation deposits. Other features considered in classifying epithermal deposits are their tectonic setting, host rocks, deposit geometry, age and temperatures and depths of formation the ore, gangue and alteration mineral assemblages, zoning, and sources of fluids (Table 15).

The three deposit subtypes included in this class, i.e. high-, intermediate- and low-sulfidation epithermal deposits, are named to reflect the differences in the sulfidation state of the ore-fluids that results in distinct hypogene ore mineral assemblages (Figure 58 and Figure 60). Sulfidation state refers to sulfide assemblages that are stable at certain temperature and sulfur fugacities; for details the reader is referred to Einaudi et al. (2003). Sulfidation state also affects the solubilities of Au, Ag and base metals as a function of the available complexes. Whereas Au is preferably transported as thiosulfide complexes Ag and base metals can be transported as chloride complexes in the epithermal temperature regime. Hydrothermal alteration and gangue mineral assemblages are an important indicator of fluid composition, particularly of the reactivity (i.e. the acidity) of a fluid. Yet, it is the ore mineral assemblage itself that reflects the nature of the ore fluid (Sillitoe and Hedenquist, 2003).

7.1.2.2 High-sulfidation deposits (HS-type)

This type is mainly associated with calc-alkaline andesitic-dacitic rocks formed in compressional arc environments. Many large high-sulfidation deposits formed in arcs subjected to neutral to mildly extensional stress regime. However, once extension becomes more advanced high-sulfidation deposits are not normally generated. Compressive arcs also host both small, high-grade and large, low-grade high-sulfidation deposits.

HS deposits contain sulfide assemblages of high-sulfidation state, typically pyrite + enargite, pyrite + luzonite, pyrite + famatinite and pyrite + covellite. Enargite and Ag-poor gold (<10 wt% Ag) are present in almost all high-sulfidation deposits. HS deposits are hosted by leached silicic rocks surrounded by a halo of advanced argillic alteration. This alteration results from intense acid leaching by low-pH fluids formed by the condensation of HCl- and SO_2-rich magmatic-hydrothermal fluid when it came into contact with groundwater. In this zone of mixing so-called lithocaps form (Cooke et al., 2017). Characteristically, alteration progressively grades outward from inner residual (vuggy) quartz and quartz-alunite assemblages to advanced argillic, argillic and propylitic assemblages. Stable isotopes evidence that epithermal mineralization and associated hydrothermal alteration form predominantly from mixing of meteoric waters with variable amounts of magmatic fluids released from crystallizing mafic to silicic magmas. Typically, high-sulfidation deposits have hydrothermal alteration assemblages, geochemical characteristics and isotopic compositions reflecting larger magmatic fluid input than intermediate- and low-sulfidation deposits.

High-sulfidation ore fluids are commonly highly acidic causing extreme leaching and formation of quartz-alunite assemblages in the lithocap. Leaching requires fluids with pH <2 to mobilize Al, and alunite most likely forms at a pH of 2 to 3 (Stoffregen, 1987). The early leaching fluid is a condensate of magmatic vapor with very low salinity of <1 wt% NaCl equiv. However, fluids with a wide range of salinities, from <1 to 45 wt% NaCl equiv., were present during formation of HS deposits. Hypersaline fluids are associated with sericitic and K-silicate alteration in deeper parts of these systems (Arribas, 1995). Fluid inclusions of high-sulfidation deposits commonly show dilute (<1 to 6 wt% NaCl equiv.), moderate temperature (T_h = 155 to 330 °C, some excess 400 °C), two-phase fluid inclusions (Cooke and Simmons, 2000; John et al., 2018).

7.1.2.3 Low-sulfidation deposits (LS-type)

Andesite-dacite-rhyolite arcs comprising alkaline and calc-alkaline series are more favorable for the formation of low-sulfidation deposits. Many of these deposits are formed in continental and island-arcs characterized by bimodal volcanism and extension. Extension may occur in intra-, near- and back-arc settings during subduction of oceanic lithosphere and is typically attributed to slab rollback, oblique subduction, asthenospheric upwelling, post-collisional collapse or hot-spot activity (Sillitoe and Hedenquist, 2003).

LS deposits contain the characteristic low-sulfidation assemblage pyrite + arsenopyrite, with the latter in rather minor quantities. Minor Cu is present as chalcopyrite or, less commonly, tetrahedrite-tennantite. Often, minor Fe-rich sphalerite and galena join the assemblage and pyrrhotite is present in trace amounts. LS deposits are associated with high gold and silver contents with low Ag/Au ratios. Gold-silver selenides, silver-bearing sulfosalts and electrum (>20 wt% Ag) are a common feature of LS deposits. Gangue minerals comprise quartz, chalcedony and adularia plus subordinate calcite; the latter often with characteristic bladed morphology. Low-sulfidation deposits commonly consist of multistage veins, stockworks, sheeted veins and also breccia bodies (Sillitoe and Hedenquist, 2003). Veins are commonly characterized by lattice textures (platy calcite and its pseudomorphs) as well as shallowly formed crustiform and colloform quartz. In deeper parts, veins consist mostly of coarse crystalline comb quartz (Cooke and Simmons, 2000).

The hydrothermal alteration from the vein selvage into the adjacent country rock shows that adularia gives way to illite and also quartz abundance diminishes. These minerals reflect mineralization in the presence of a reduced and near-neutral pH low-salinity fluid. The deeper levels and peripheral alteration consist of a propylitic assemblage containing quartz, chlorite, illite, pyrite, calcite, albite, adularia and epidote. Silica sinter is deposited where boiling or boiled low-sulfidation fluids discharge at the surface (Cooke and Simmons, 2000). Fluid inclusions of LS deposits are mostly two phases (L+V) and are liquid-rich (>65 vol%), but also vapor-rich (>98 vol%) inclusions might be present. Homogenization temperatures range from <130° to 290 °C. Diluted low-salinity values (<3 wt% NaCl equiv.) are a characteristic feature (John et al., 2018).

7.1.2.4 Intermediate-sulfidation deposits (IS-type)

Most intermediate-sulfidation epithermal deposits, like their high-sulfidation brethren, occur in calc-alkaline andesitic-dacitic arcs. Generally, IS deposits show a wide geodynamic distribution and can develop under variable stress states (compressive, neutral and extensional) in magmatic arcs, back arcs and post-collisional orogenic belts. However, local extensional and neutral stress regimes are reported to be more favorable for the formation of IS deposits (Wang et al., 2019).

Mineralization in most intermediate-sulfidation deposits occurs as veins and/or brecciated bodies extending laterally up to several kilometers. Precious metal-bearing orebodies are commonly found within a depth interval between 300 to 800 m (Hedenquist et al., 2000). Textures of ore and gangue minerals in IS veins share much similarity with those in LS veins. Most common textures include crustiform and symmetric banding, vugs, cockade and comb textures. Often, mineral textures, such as colloform quartz and lattice-bladed (or platy) calcite), indicate boiling in IS deposits. Many IS-type deposits host polyphase and multi-stage veins, which appear to be the product of an episodic process of cracking and sealing of veins (Wang et al., 2019).

Intermediate-sulfidation deposits possess sulfidation states between the two above mentioned epithermal endmembers. Sulfide mineral assemblage in the majority of IS deposits can be relatively simple and include combinations of pyrite, chalcopyrite, tetrahedrite-tennantite, Fe-poor sphalerite and galena. Precious metals are represented by electrum, native gold, acanthite-argentite and many other silver sulfosalts (Sillitoe and Hedenquist, 2003). Silver is the major commercial element in many IS deposits, which hosted in sulfides, sulfosalts, tellurides or occurs as native silver. The gangue minerals in IS are primarily quartz, Mn-carbonates, commonly rhodochrosite and manganoan calcite, as well as adularia. Locally, barite, fluorite, dolomite-ankerite, muscovite, albite and Mn-silicates may be present. The relative contents of ore and gangue minerals in veins can be used as diagnostic features to distinguish IS and LS deposits in the field (Wang et al., 2019).

Hydrothermal alteration mineral assemblages are commonly zoned laterally and vertically around the ore bodies. Alteration below the paleowater table in intermediate-sulfidation deposits is commonly zoned around former fluid conduits and ore zones. Silicification and potassic (adularia, illite) alteration in the inner zones grades outward to argillic and propylitic assemblages. Above the paleowater table argillic and advanced argillic alteration is normally developed (John et al., 2018).

Intermediate-sulfidation ore fluids have a wider range of salinity due to fluctuations in salinity between the different ore stages (Sillitoe and Hedenquist, 2003). John et al. (2018) report a range of homogenization temperature between ~135-385 °C for liquid rich and vapor-rich fluid inclusions. Salinities vary from 1 to 12 wt% NaCl equiv. with distinctly different value ranges among districts and deposits. Elevated salinities have been interpreted to reflect a magmatic water component in ore-forming fluids what is supported by stable isotope studies.

7.2 Characteristics of Chah-Mesi and comparison to epithermal subtypes

In order to correctly classify the Chah-Mesi deposit the results of this study are compared to the characteristics of HS, IS and LS deposits (Table 16). Obviously, Chah-Mesi shows common characteristics with each subtype regarding host rocks and geodynamic setting, deposit style, hydrothermal mineralization and alteration, precious metals as well as epithermal ore-fluid compositions. In the following arguments for assigning Chah-Mesi to the IS subtype are discussed in more detail.

7.2.1 Host rocks and geodynamic setting

Petrography of the host rocks (Chapter 4.1) shows that Chah-Mesi is mainly hosted by a calc-alkaline sequence of andesitic rocks with underlying dacitic pyroclastics and minor microdioritic intrusions. Although the modal mineralogy of andesites might indicate a transition into basaltic andesite towards the deeper levels, they were mainly designated as andesites (Aliani et al., 2009; Taghipour et al., 2008) due to the high abundance of plagioclase either as phenocrysts or in the groundmass.

Concerning the geodynamic setting, there have been several recent papers dealing with the geochemistry and age of the intrusive rocks hosting porphyry Cu deposits within the UDMB including the Meiduk (e.g. Aliani et al., 2009; Alirezaei et al., 2017). These studies confirm that the fertile intrusions in UDMB chemically differ from normal calc-alkaline series showing adakite-like chemical and mineralogical signatures (Alirezaei et al., 2017). Age data of the PCD deposits in UDMB also support their post-subduction formation during the post-collision stage (Aliani et al., 2009).

Chah-Mesi shows a close spatial relation to the Meiduk porphyry. With about 1.5 km distance a common geodynamic evolution is therefore assumed. Geochemical data from Aliani et al. (2009) and Alirezaei et al. (2017) suggest that the porphyry stock at Meiduk is an adakite-like, H_2O-enriched, high-pressure differentiated product of hydrous mafic partial melts of lithospheric mantle. The melting probably resulted from slab break-off and upwelling of the hot asthenospheric mantle. Thus, the porphyry system of Meiduk is proposed to have been formed in a continental arc setting during post-collisional tectonic processes after the continental collision between the Arabian and Iranian plates at the final evolution stage of the UDMB (Aliani et al., 2009).

The petrographic features of the investigated country rocks actually correlate with all three subtypes of epithermal deposits. However, as LS deposits commonly have a wider range of host rock compositions and are often associated with bimodal magmatism, it is more likely that the country rocks represent an environment more typical of HS and IS deposits.

Table 15: Principal characteristics of epithermal deposit types after Sillitoe and Hedenquist (2003) and John et al. (2018).

	High-sulfidation deposits	Low-sulfidation deposits	Intermediate-sulfidation deposits
Associated volcanic rocks	Calc-alkaline, andesite-dacite	Calc-alkaline, andesite-rhyolite; tholeiitic, bimodal basalt-rhyolite	Calc-alkaline, andesite-rhyolite
Tectonic setting	Compressional-transpressional continental-margin arc or back arc; compressional-transpressional, neutral stress to mildly extensional continental-margin arc	Extensional continental-margin and island arcs; extensional back arc; post-arc continental extension	Extensional continental-margin arc; compressional island arc; continental rift
Deposit style and mineralized structures	Breccias; diatremes; residual vuggy quartz; veins and stockworks; veins generally late; disseminated ore, massive sulfide;	Multiple stage veins and breccias; sheeted veins; vein stockworks and breccias; fault intersections; disseminated and fine layered ores	Multistage veins and associated breccias; diatremes; coarse layered and disseminated ore
Sulfide abundance	5 to 90 vol%	<1 to 2 vol. % (in basalts ~20 vol%)	5 to >20 vol%
Key sulfide minerals	Enargite, luzonite, famatinite, covellite, acanthite, stibnite	minor arsenopyrite ± pyrrhotite; minor sphalerite, galena, tetrahedrite-tennantite, chalcopyrite	Sphalerite (FeS-poor), galena, tetrahedrite-tennantite, chalcopyrite
Main metals	Cu, As-Sb, Au-Ag	Au ± Ag	Zn, Pb, Cu, Ag-Au
Minor metals	Zn, Pb, Bi, W, Mo, Sn, Hg	Zn, Pb, Cu, Mo, As, Sb, Hg	Mo, As, Sb
Te and Se minerals	Au-Ag tellurides common; selenides present locally	Au-Ag selenides, Se sulfosalts common	Tellurides common locally; selenides uncommon
Precious metals	Gold, electrum, Au-Ag tellurides, acanthite, Ag-bearing tennantite, tetrahedrite, enargite, luzonite, chalcopyrite	Electrum, Ag sulfides, selenides and sulfosalts; low Ag/Au	Electrum, Ag sulfides and sulfosalts; high Ag/Au; chalcopyrite, galena, sphalerite
Silica gangue and textural features	Structurally and stratigraphically controlled fine-grained silicification and residual, vuggy quartz	Vein-filling crustiform and colloform chalcedony and quartz	Fault zone replacement and vein-filling by fine- to coarse-grained equigranular quartz, and crustiform and comb quartz
Carbonate gangue	Absent	Present but typically minor and late	Common, typically including manganiferous varieties
Other gangue	Minor barite common, typically late	Barite uncommon; fluorite present locally	Barite and manganiferous silicates present locally
Proximal alteration minerals	Quartz-alunite/aluminium-phosphate-sulfate (APS) minerals; vuggy quartz; quartz-pyrophyllite at depth	Illite/smectite-adularia	Sericite; adularia generally uncommon
Fluid inclusions	Mostly 155 to 330 °C (220 to 270 °C modes); ~0–6 weight % NaCl equiv.; halide saturated fluids in some deposits	<100 to 390 °C (<130 to 290 °C modes); 0 to 6 weight % NaCl equiv. (mostly <3%)	135 to 385 °C (220 to 310 °C modes); as much as 23 weight % NaCl equiv. (mostly 1 to 12%)

Table 16: Summary of petrographic and mineralogical features of the Chah-Mesi deposit compared to principal characteristics of epithermal deposit types. + common, ~ probable, - uncommon

	Chah-Mesi deposit	High-sulfidation deposit	Low-sulfidation deposit	Intermediate-sulfidation deposits
Associated volcanic rocks	intermediate calc-alkaline, (basaltic) andesite-dacite	+	~	+
Tectonic setting	post-collision, extensional	~	+	~
Deposit style	Residual vuggy quartz, multistage veins and associated breccias	+	-	+
Sulfide abundance	Mostly 20 to 30 vol%, >50 vol% in ginguros	+	-	+
Sulfide minerals	Sphalerite, galena, chalcopyrite, tetrahedrite-tennantite, enargite/luzonite, famatinite, bornite, covellite, chalcocite	~	-	+
Main metals	Cu, Zn, Pb, As-Sb, (Au-Ag)	~	-	+
Minor metals	Mo, Te	-	-	+
Te and Se minerals	Minor tellurides (benleonardite)	~	-	+
Precious metals	Electrum, Ag-sulfides and -sulfosalts; low Ag/Au	-	~	+
Silica gangue and textural features	Fault zone replacement and vein-filling by massive and banded fine- to coarse-grained quartz, crustiform and comb quartz	~	~	+
Carbonate gangue	Very common; siderite and ankerite, typically including Mn	-	~	+
Other gangue	Minor barite, fluorite, apatite, anhydrite	+	+	+
Proximal alteration minerals	Mostly sericite; vuggy quartz; adularia generally uncommon	~	-	+
Fluid inclusions	115 to 397 °C (modes at 210 to 270 °C); 1.2–9.9 weight % NaCl equiv. (mostly 4 to 7 %); CO_2-bearing H_2O-NaCl system	+	-	+

7.2.2 Deposit style and ore zonation

Ore minerals in Chah-Mesi are mainly hosted by O-type veins, which comprise multistage and polyphase veins, occasionally with smaller adjacent stockwork-veinlets and local replacement bodies (Figure 8 e). Also, at depths of around 2351 m a.s.l a flat lying, mineralized breccia body is indicated (Figure 25 and Figure 26). The spatial distribution of ore veins indicates a zoning with Fe-Cu-dominated assemblages in the proximal and Pb-Zn-dominated assemblages in the peripheral (distal) areas. This observation is interpreted as deposit-scale ore zoning. The central ore zone 1 (OZ 1, Figure 32) including high-sulfidation assemblages grades into Pb-Zn richer high- and intermediate-sulfidation zone (OZ 2, Figure 33 and Figure 34) and Pb-Zn-dominated, intermediate-sulfidation zones (OZ 3, Figure 35) laterally and with increasing depth. A sheet-like surface zone (OZ 4, Figure 36) with about 50 m thickness is related to supergene weathering. It must be noted that this interpretation of the zoning is based on only 5 drill cores studied along a N-S profile (Figure 7). To confirm the 3D geometry of ore zoning in the Chah-Mesi deposit more drill cores would need to be investigated.

The multistage and crustiform to comb textured quartz veins as seen at Chah-Mesi are a common characteristic of LS and IS type deposits. However, the presence of intense silicification in the central part is rather unusual for low-sulfidation deposits but is commonly observed in IS types. These central silica-rich parts including HS assemblages would rather correspond to high-sulfidation type deposits. Anyhow, the fact that they are limited to fault zones rather than comprising the whole deposit and the high abundance of veins hosting multistage and polyphase ore minerals favors the assignment as intermediate-sulfidation deposit.

7.2.3 Ore mineralogy and mineral distribution

Mineralization in Chah-Mesi is subdivided into several stages of ore formation (Figure 37). The abundance of ore minerals in O-type veins (Chapter 4.2.4) ranges between 20 and 30 vol%, however, ginguro veins even contain up to 50-60 vol% sulfides. Early mineral assemblages comprise pyrite + chalcopyrite + enargite + luzonite-famatinite ± bornite and are mainly present in ore zone 1. This assemblage is referred to be of high-sulfidation state due to the presence of key minerals, such as enargite, luzonite-famatinite and minor bornite. Early mineralization is followed by the main stage assemblage with pyrite + chalcopyrite + tennantite-tetrahedrite + sphalerite + galena ± Au ± Ag-sulfosalts ± enargite/luzonite. This assemblage is designated as main stage because it is the most abundant one in the whole deposit and occupies the most extensive ore zone 2. The presence of tennantite-tetrahedrite coexisting enargite/luzonite and the increase in Pb-Zn minerals indicate that this stage was formed under transitional high to intermediate-sulfidation conditions. Late stage sphalerite, galena, chalcopyrite, pyrite with minor tennantite-tetrahedrite is mainly present in ore zone 3. Fe-poor sphalerite is the most prominent sulfide in ore zone 3. The spatial distribution of ore minerals demonstrates that Chah-Mesi is dominated by veins including mainly intermediate-sulfidation assemblages. Ore textures indicate that lower sulfidation state assemblages generally overprint higher sulfidation assemblages and that the outer Pb-Zn richer ore zones likely postdate and encroach on the inner Cu-rich zone. It is obvious that low-sulfidation key minerals, such as arsenopyrite and pyrrhotite are lacking at Chah-Mesi. This together with presence of Fe-poor sphalerite is typical for IS deposits.

Regarding the HS-dominated centers surrounded by IS assemblages, Einaudi et al. (2003) mention that many high-sulfidation deposits record a shift to lower sulfidation states with time, whereby enargite is replaced by tennantite at the time of gold deposition. However, intermediate-sulfidation deposits also feature such a decrease in sulfidation state. This is because HS and IS fluids are in disequilibrium with the wallrocks outside the silicified zone and therefore the natural long-term tendency is for hydrothermal fluids to become more reduced due to enhanced fluid rock interaction.

Nevertheless, differences between these two subtypes are evident. IS deposits typically are well zoned, whereas high-sulfidation deposits are commonly telescoped. The mineralogy of intermediate-sulfidation deposits is more complex and the metal suite includes Cu, Zn, Pb, and Ag and tends to be associated with molybdenum-bearing, gold-poor porphyries, such as Meiduk. In contrast, many HS deposits are associated with gold-rich porphyry Cu deposits containing only minor Mo and other metals.

The ore mineralogy at Chah-Mesi is rather complex and dominated by transitional high to intermediate-sulfidation assemblages. Zoning is established on the deposit scale by distribution of Cu-Zn-Pb minerals but also by the chemical composition of fahlore group minerals (see below). Moreover, the

predominating metal association of Cu, Zn, Pb and Ag and the proximity to the Mo-bearing (0.007 wt%) and Au-poor (0.08 g/t) porphyry of Meiduk (Chapter 2.4.2) favors Chah-Mesi to be an epithermal intermediate-sulfidation deposit.

7.2.4 Precious metals

Based on ore microscopy and microanalytical studies the deposit is characterized by the metals Cu, Zn, Pb, As, Sb with minor Ag and Au. Geochemical analysis conducted on samples from the Chah-Mesi open pit during a previous exploration program from the KAN Iran Consulting Engineers (2006) showed that Au contents range between 0.01 and 57.9 ppm. Most analysis are below 1 ppm and have a mode at 0.7 ppm. Ag contents vary from 0.5 to 100 ppm with a median at 38.2 ppm. Ag/Au ratios are between 2 and 425, with a mode at around 32. As shown in this study the precious metals occur mostly as electrum, Ag-sulfides and Ag-sulfosalts. Ag-bearing sulfides include chalcopyrite and Cu_xS minerals. On average chalcopyrite contains 0.02 Ag apfu and Cu_xS phases include 0.01 Ag apfu. Ag-bearing sulfosalts include enargite, luzonite-famatinite with an average Ag content of 0.02 apfu and up to a maximum of 0.34 apfu. Further, exotic silver minerals that were documented, are phases of the polybasite-pearceite solid solution series. Trace metals present in Chah-Mesi ores comprise Mo and Te. Molybdenum was only observed in porphyry-related veins (Chapter 4.2.1) close to the Meiduk porphyry. Tellurium was only proven in an accessory sulfosalt phase interpreted as benleonardite.

The dominating metal suite with Cu, Zn, Pb, As, Sb as well as the high Ag-contents in gold are typical features of IS deposits. The low contents of Au and Ag and the high Ag/Au ratio support this interpretation.

7.2.5 Gangue mineralogy and textures

Mineralization at Chah-Mesi is structurally controlled and mainly hosted in veins and in the surrounding altered host rocks. Vuggy quartz textures in the central parts of the deposit are indicative of high-sulfidation environments. Yet, this zone constitutes only a small area in comparison to the surroundings, where veins with banded, crustiform and comb quartz texture and carbonate gangue minerals are more common, features which are more typical for LS and IS types. Importantly, the presence of Mn-carbonates at Chah-Mesi is a diagnostic feature to discern IS from LS deposits (Wang et al., 2019) and support the interpretation of Chah-Mesi as an intermediate-sulfidation deposit.

7.2.6 Hydrothermal alteration

Hydrothermal alteration in Chah-Mesi (Chapter 4.3) shows a distinct zoning and consists of central structure-related silicification, which includes minor replacement bodies and vuggy quartz textures. Silicic alteration is associated with the HS assemblage bearing, massive O-type veins and grades into advanced argillic and argillic alteration halos. Pervasive sericitization with QCS-type veinlets becomes the predominant alteration of the deposit either close or with increased distance to O-type veins. Sericitic alteration grades into propylitic alteration with PCE- and CC-type veinlets. The transition between sericitic and propylitic alteration shows characteristics of the chlorite-sericite zone (Sillitoe, 2010), which occurs very close to porphyry Cu core zones. Potassic (biotite-rich) alteration represents the outermost alteration at Chah-Mesi in the north closest to the Meiduk porphyry deposit. The potassic zone also includes the porphyry-related D_1- and B_2-type veins. It is hypothesized that potassic alteration

and these veins in drill core BH-CHM4 already belong to the Meiduk PCD. Unfortunately, the relative time relations of these veins/potassic alteration to the Chah-Mesi veins could not be established from studying a single drill core.

The hydrothermal alteration in the central part of Chah-Mesi is well comparable to HS-type deposits due to the presence of leached host rocks and strong silicification indicative of strongly acidic fluids. However, the diagnostic assemblage of quartz plus aluminum-phosphate-sulfate (APS) minerals, such as alunite, which is a characteristic HS deposit mineral, could not be determined. The only APS mineral observed was plumbogummite (Figure 29), which was found in the (advanced argillic) alteration halo around a ginguro vein.

Adularia is a very common mineral in mineralized veins in LS deposits. Yet, adularia could not be determined at Chah-Mesi either. Therefore, the lack of alunite and adularia and the ubiquitous presence of sericite proximal to O-type veins further support the classification of Chah-Mesi as intermediate-sulfidation deposit.

7.2.7 Fluid inclusions

Most of the fluid inclusion assemblages described in this study are aqueous H_2O-NaCl fluids with minor amounts of CO_2 and dominated by liquid-rich LV type inclusions with subordinate occurrence of vapor-rich VL (Chapter 6.1). Minute solid phases were present, but mostly recognized as trapped mineral phases, such as quartz or phyllosilicates, rather than daughter minerals (Figure 48). Thus, halide saturated fluid inclusions were not determined, which indicates that hypersaline fluids were probably not involved in ore-forming processes. Anyhow, the composition of fluid inclusions commonly showed a relatively low-salinity. The obtained $T_{m(ice)}$ values in sphalerite and quartz were recalculated to total salinities of 1.2 to 9.9 wt% and 2.1 to 9.2 wt% NaCl equiv., respectively. The measured high-temperature phase changes into the liquid phase and comprised T_h values in the range of 114.6 to 294.6 °C with modes at ~220 °C for sphalerite and 153.0 to 396.5 °C with modes at ~270 °C for quartz. Commonly, the minimum homogenization temperatures are represented by sphalerite hosted inclusions (114.6 – 127.6 °C) and maximum temperatures were observed mainly in quartz crystals (322.8 – 396.5 °C).

The determined information of fluid inclusions shows that the range of salinity is too high for typical low-sulfidation fluid inclusions, which might range between 0 and 6 wt% but mostly are below 3 wt% NaCl equiv. Also, the measured T_h values are usually too high for LS environments. Hence, an affiliation to LS deposits is highly unlikely. The fluid inclusion properties of Chah-Mesi correspond rather to HS and IS deposits regarding salinity and T_h values. The measured inclusions accord well to the characteristic HS fluids, despite a wider range of T_h values at Chah-Mesi and halide saturated fluids are completely absent. This could be also referred to the local HS type characteristics at Chah-Mesi. However, the wider range of salinity and T_h is rather a typical feature of IS type deposits, which would also be the favored interpretation for the studied fluid inclusions.

7.3 Mineralization and regional trends on the ore deposit scale

The Chah-Mesi deposit hosts several types of mineralized veins, which are classified as O-type veins and comprise mainly massive, banded and crustiform textures. Minor mineralization occurs also as replacement bodies and in breccia zones within the deposit. The spatial distribution of O-type veins suggests a zoning of mineralization in respect of sulfidation state. One of the most common minor ore minerals is tennantite-tetrahedrite. Due to its complex zoning and variation of As-Sb ratio, particular emphasis was placed on the analysis of fahlore group mineral to gather information about their spatial distribution and to find out if there is a relation to the nearby porphyry system.

7.3.1 Conditions of ore formation and physicochemical fluid evolution

The paragenetic sequence (Figure 37) of ore minerals is interpreted to start with high-sulfidation assemblages with pyrite + chalcopyrite + enargite + luzonite-famatinite ± bornite during the early stage and mainly occupies OZ 1 close to the central NNE-SSW trending fault zones. This stage grades into intermediate-sulfidation assemblages with pyrite + chalcopyrite + tennantite-tetrahedrite + sphalerite + galena. Gold and only minor enargite also formed during the main stage in OZ 2. The late Pb-Zn dominated stage is characterized by sphalerite + galena + chalcopyrite + pyrite ± tennantite-tetrahedrite in OZ 3 distal to fault zones. Gold and silver are also present in this stage.

Textural relationships show that IS assemblages commonly overprint HS assemblages. This is also illustrated in individual ore samples, which include both HS and IS assemblages containing enargite/luzonite as well as tennantite-tetrahedrite. From the coexistence of these phases, it is proposed that ore-forming fluids evolved from high- to intermediate-sulfidation states crossing the important sulfidation reaction:

$$\underset{\text{tennantite}}{0.67Cu_{12}As_4S_{13}} + S_2 = \underset{\text{enargite}}{2.67Cu_3AsS_4} \qquad (3)$$

This coexistence might also relate to a continuous mineralization process rather than several pulses of ore formation. By contrast, banded and crustiform O-type veins often show HS-IS assemblages at the vein-wallrock contact and mainly IS assemblages (dominated by sphalerite and galena) in the central parts. These two mineralized layers are often separated by barren zones consisting only of carbonate and quartz. This could indicate a temporal separation between the main and late stage of ore formation, reflecting several pulses of ore-forming fluids. The late stage formation of sphalerite and galena in the central parts of veins (Figure 21) and in the outer ore zones in the deposit suggests that the late fluids were characterized by decreased sulfidation state and even more reduced conditions.

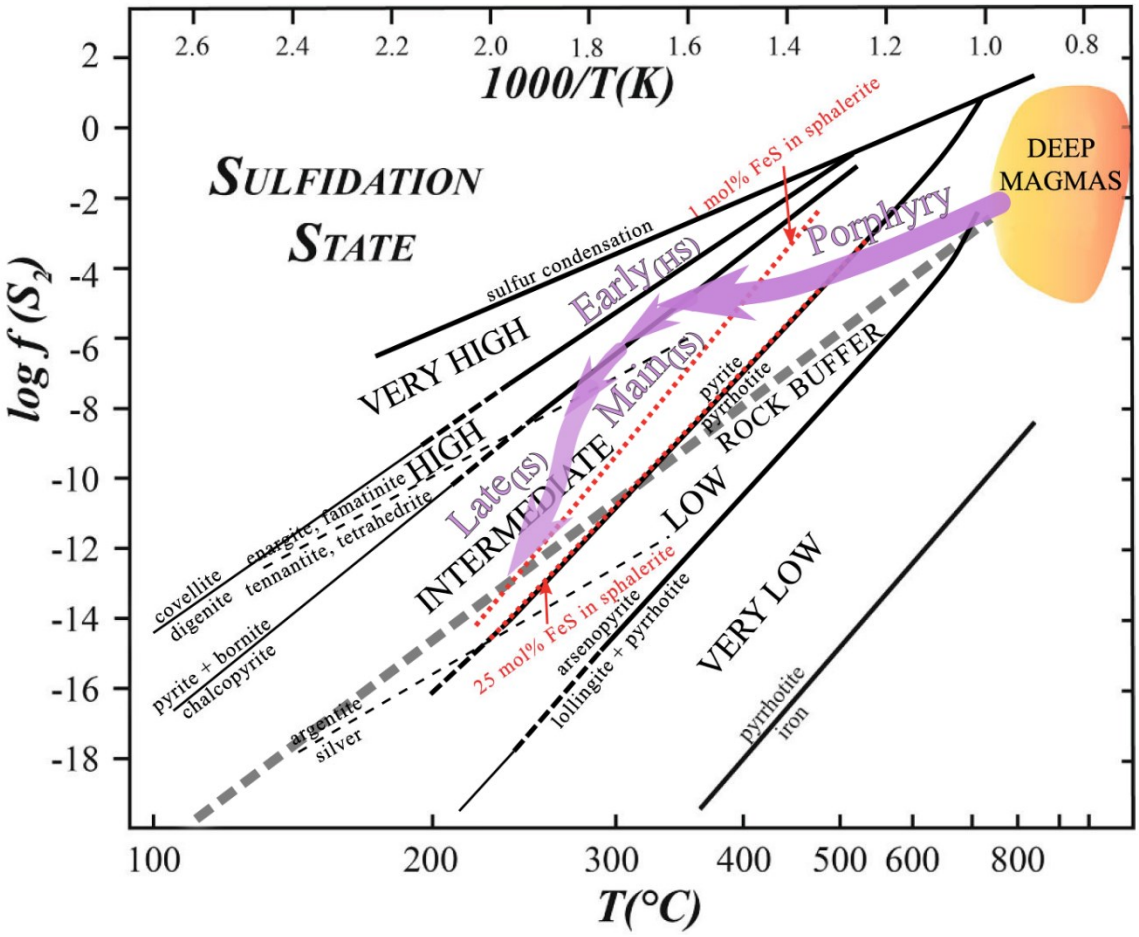

Figure 60: Temperature vs. sulfur fugacity diagram showing mineral reactions used for distinguishing different sulfidation stages and evolution of magmatic hydrothermal fluids according to Einaudi et al. (2003). Trajectories (purple) show the proposed fluid evolution path from early (HS – high-sulfidation state) to late (IS – intermediate-sulfidation state) stage mineralization that could explain the sulfidation evolution deduced for the Chah-Mesi deposit. Adapted after Wang et al. (2019) and Einaudi et al. (2003).

The carbonate-bearing, IS assemblage-dominated, banded and crustiform O-type veins of OZ 2 are interpreted to have formed coeval or shortly after the adjacent HS assemblage-dominated massive O-type veins. The IS-dominated veins contain gold adjacent to the HS epithermal domain. This relationship was also reported by Rinne (2015) and suggested that higher gold grades occur at the transition from high- to intermediate-sulfidation styles. This implies that either both the HS and IS fluids were gold-bearing, and coincidently deposited gold in the same region at the boundary between ore zone 1 and 2. Another and more likely possibility is that the high-sulfidation fluid was probably at least in part the parental fluid of the intermediate-sulfidation fluid and gold mineralization occurred during the transition from HS to IS conditions. This would be supported by the observation of a probably continuous process of ore precipitation from the early to the main stage of mineralization.

7.3.1.1 Iron content of sphalerite

Sphalerite occurs together with pyrite and tennantite near the outer margins of high-sulfidation dominated ore zones (OZ1). Sphalerite is reported to occur in many high-sulfidation deposits and is generally interpreted to record a change (either spatial or temporal) from high- to intermediate-sulfidation state (Einaudi et al., 2003). The sphalerites contained in the different vein types were found

to have low Fe concentrations ranging from 0.05 to 1.5 mole% FeS substituting for ZnS in the sphalerite structure. Studies of Einaudi et al. (2003) showed that the Fe content of sphalerite can be related to the sulfidation state of epithermal fluids, assuming that sphalerite coexists with either pyrite or pyrrhotite. High-sulfidation fluids are associated with low-Fe sphalerite containing less than approximately 0.1 mole% FeS, whereas Fe concentrations of ZnS are above this value in IS deposits. Sphalerite forming under low-sulfidation conditions are expected to have very high Fe concentrations exceeding 20 mole% Fe (Einaudi et al., 2003). Based on the range of Fe concentrations encountered in sphalerite of the different vein stages, it is concluded that the epithermal fluids that precipitated the sphalerite were indeed characterized by an intermediate-sulfidation state (Figure 60).

EPMA analyses of sphalerite contained in mineralized breccia zones show an average Fe concentration of about 0.19 mole% FeS indicating a relatively high-sulfidation state. As it is assumed, that the sulfidation state decreased over time and space, as indicated by the paragenetic sequence and ore zoning, mineralized breccia zones are assigned to an early stage of ore formation and fluid evolution.

Moreover, banded veins closest to the silicified HS assemblage-bearing fault zones show average Fe concentrations of 0.11 mole% FeS. In contrast, sphalerites hosted by ginguro veins further away from fault zones have FeS values of about 1.16 mole%, hence indicating a decreasing sulfidation state. This decrease is explained with increasing influence of fluid-rock interactions upon cooling and increasing transport distance of the fluids (Einaudi et al., 2003). The decrease in sulfidation state reflects a decrease in fluid/rock ratios and increasingly reducing conditions which causes a shift in sphalerite precipitation from lower Fe to higher Fe contents with increasing distance to the silicified veins.

7.3.1.2 Witnesses of hydrothermal fluid processes: gangue textures and fluid inclusions

According to the textures and gangue minerals of mineralized veins it is suggested that ore and gangue mineral deposition occurred under non-boiling conditions. This is evidenced by the presence of crustiform bands with fine-grained Ca-Mg-Mn-Fe-carbonate often having rhombic textures. However, minute occurrence of lattice bladed calcite and colloform quartz may indicate boiling (Dong et al., 1995; Shimizu et al., 1998). Other minerals inferred to boiling processes, such as adularia, are completely missing (Guzman; Shimizu, 2014). Fluid inclusions show a constant proportion of liquid and vapor in LV type inclusions in banded and crustiform vein types. The subordinate occurrence of vapor-rich VL type inclusions also suggests that probably no or only limited boiling has happened. The low homogenization temperature of quartz and sphalerite of 200.6 – 270.8 °C and salinities between 5 to 10 wt% NaCl equiv. support the fact that no phase separation (i.e. boiling process) has happened during ore precipitation.

A temporal or at least spatial difference of ore formation is indicated by fluid inclusion studies conducted on two different vein types. Banded and crustiform O-type veins comprise low-salinity fluids with slightly different T_h values. The minimum homogenization temperatures are represented by sphalerite hosted inclusions (114.6 – 127.6 °C) and maximum temperatures were observed in quartz crystals (322.8 – 396.5 °C). Primary sphalerite inclusions commonly show lower average T_h values (200.6 – 218.0 °C) than inclusions in quartz (234.8 – 270.8 °C) and indicate that sphalerite postdates quartz crystallization, when the mineralizing fluids were already cooling down. The spatial distribution of T_h values shows that the vein sample located closer to HS-bearing fault zone structures contains inclusions with higher

homogenization temperature than the one located more in the distal parts. Also, the salinity of the observed inclusions seems to decrease with increasing distance. Although only two samples were studied, the decreasing salinity and homogenization temperature could be referred to the dilution of hot, higher saline waters by cold, near-surface meteoric water during their ascent and lateral flow, respectively. This is illustrated by the extrapolation of the dilution trend to zero salinity (0 wt% NaCl equiv.; Figure 62), indicating that the dilutant could have been groundwater with T <100 °C (Hurai et al., 2015). In fact, the effect of meteoric water is also supported by $\delta^{18}O$ values of fluid in equilibrium with quartz ranging between +1.9 and +6.0 ‰ (Hosseinkhani, 2009). This study also assumed a dilution of magmatic fluids with meteoric water. Further, $\delta^{18}O$ and δD values of fluid in equilibrium with sericite range from -5.2 to -9.6 ‰, and from -95.5 to -108.5 ‰, respectively. Hence, the oxygen and hydrogen isotope composition indicate meteoric water as one source of fluids that caused sericitic alteration.

7.3.1.3 The role of wallrock buffering

The gradation of high-sulfidation state into intermediate state assemblages can be explained with to the model by Sillitoe and Hedenquist (2003). They propose two possibilities for IS fringing HS centers. One option is that deep fluids bypass the lithocap along fractures to directly form IS veins in distal portions. The other possibility is that deep IS fluid evolves to HS conditions on entering the unbuffered lithocap, followed by sufficient neutralization and reduction during outward flow and water-rock reaction to return to intermediate stability. The latter process is supported by the increasing Fe contents of sphalerite towards the periphery indicating decreasing sulfidation states of fluids.

Wallrock buffering is a process where rock-forming minerals interact with a hydrothermal fluid at submagmatic temperatures and mediate its sulfidation/oxidation state and total acidity (Barton, 1970). Minerals that are likely to be act as buffers are the ferromagnesian minerals with iron in different valence states, such as Fe^{2+} in pyroxene, olivine, biotite and magnetite and Fe^{3+} in biotite and magnetite (Einaudi et al., 2003). At Chah-Mesi totally decomposed phenocrysts of former Fe-Mg-silicates in altered rocks may be attributed to this process.

As discussed by Einaudi et al. (2003), epithermal systems are only capable to achieve intermediate- or high-sulfidation states if the fluid chemistry is buffered by the presence of H_2S and SO_2. This requires the input of magmatic volatiles into the hydrothermal system. Upon cooling and increases in transport distance, the sulfidation state of hydrothermal fluids becomes increasingly influenced by fluid-rock interactions. Wallrock buffering at low temperatures (T_h of sphalerite ~230 °C, Figure 60) may explain the decrease in the sulfidation state. It is assumed that wallrock buffering as evidenced by the strong alteration of Fe-Mg-silicates, was an important process affecting the chemistry of the ore-forming fluids at Chah-Mesi.

7.3.2 Regional zoning seen in fahlore chemistry

The regional distribution of fahlore composition as shown in the contour plot (Figure 61) indicates some systematic variation of the Sb/(Sb+As) with depth and distance from the Meiduk PCD. The vertical distribution indicates that the tetrahedrite content of fahlores is lower in deeper sections (ca. 40 td%), progressively increases towards intermediate depths (with max. 70 td%), but slightly decreases again near the surface. Horizontally, an increase of Sb is also obvious with increasing distance to the Meiduk PCD. A high Sb-zone with >70 td% is outlined between about 1450 to 1600 m distance from Meiduk and depths of 2430 to 2480 m a.s.l. This corresponds with the Chah-Mesi mine but about 30 to 40 m below the deepest mining level at 2488/2487 m a.s.l. in the open pit.

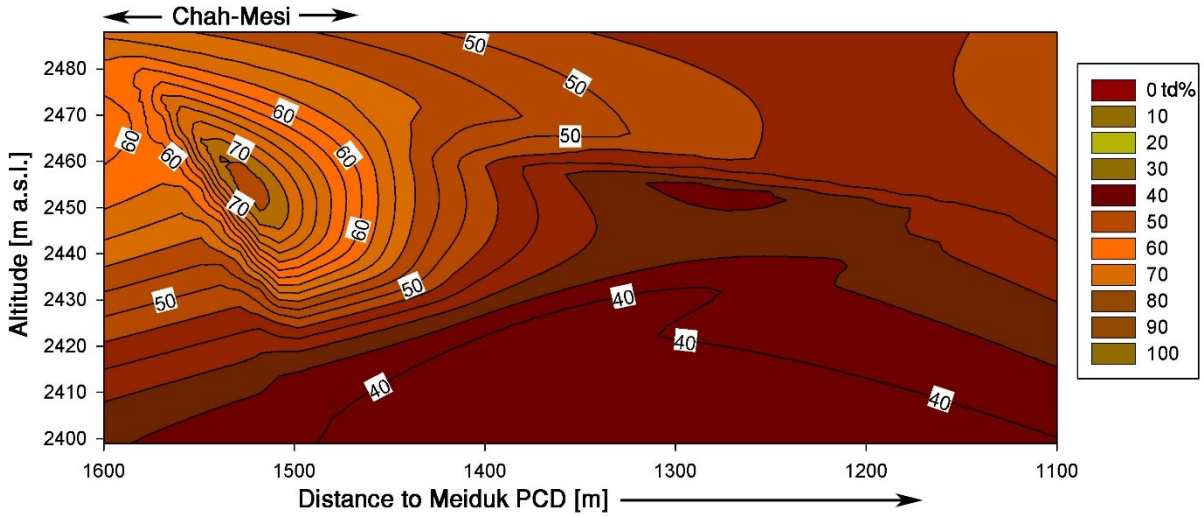

Figure 61: Contour plot of the tetrahedrite content (td%) showing the distribution of fahlore composition relative to drill core depth (m a.s.l.) and distance to the Meiduk PCD (in meters). The diagram illustrates a N-S cross section from the Meiduk deposit in the north (at theoretically 0 m distance, to the right) and the Chah-Mesi deposit (located between 1500 to about 1800 m away from Meiduk). Vertical scale is exaggerated.

The fahlore composition at Chah-Mesi ranges from Zn-rich and Fe-rich tennantite to Zn-rich tetrahedrite. Samples CHM2-39.5 and CHM2-69 show a trend from Fe-rich tennantite to Zn-rich tetrahedrite. All other samples comprise mainly Zn-rich tennantite and Zn-rich tetrahedrite. A clear trend in zoned fahlore grains could not be observed, though some crystals in sample CHM2- 69 might comprise As-rich but also Sb-rich cores, whereas margins are mainly dominated by Sb (Figure 40, Appendix III). However, in between Sb/As ratios vary too strong to identify a clear progression. In sample CHM1-59 different fahlore generations are present and show crosscutting relationships (Figure 41). Thin veinlets of Sb-rich fahlore dissect earlier formed As-rich ones and point out to an increase of Sb during later stages. Yet, this observation was also limited to few crystals and data do therefore not allow to obtain a clear picture of fahlore evolution.

Similar to Chah-Mesi deposit oscillatory zoning of fahlores,, caused by the variable Sb, As, Fe and Zn contents, was reported from Peschanka deposit and Nakhodka ore field occurring in the Baimka Cu-Mo-Au porphyry-epithermal trend, Russia (Marushchenko et al., 2018), and of the Biksizak porphyry-epithermal system, Russia (Plotinskaya et al., 2015), but also in the historic Schwaz and Brixlegg mining areas, Austria (Krismer et al., 2011).

Marushchenko et al. (2018) distinguished different evolution trends for fahlore group minerals of porphyry, transitional epithermal-porphyry and IS epithermal settings. In PCDs they evolve from Fe-rich tennantite to Zn-rich tetrahedrite, whereas in transitional deposits they evolve from Zn-rich tetrahedrite to Zn-rich tennantite exhibiting oscillatory zoned fahlore grains. IS epithermal-related fahlore evolves from Zn-rich tennantite to Zn-rich tetrahedrite. It has therefore been suggested that the character of the chemical evolution of fahlore minerals is a criterion to discriminate porphyry, transitional and epithermal mineralization. The evolution from tennantite to tetrahedrite at the porphyry and epithermal setting is caused by the Sb increase in the fluid. The concentrations of Fe and Zn are largely the function of f_{S2} in mineralizing fluid, with higher f_{S2} corresponding to higher Zn concentration (Krismer et al., 2011). The progression of transitional fahlores indicates fluctuations in As and Sb regime in fluid.

A complimentary increase of Sb and Ag content in fahlores from early to late generation was previously reported (Dimitrova et al., 2007; Vassileva et al., 2014). Plotinskaya et al. (2015) determined higher Sb and Ag contents and wider variations in fahlores with increasing distance from the dioritic porphyry intrusion at Biksizak. Hackbarth and Petersen (1984) described this feature in detail at Coeur d'Alene, Idaho, United States and Orcopampa and Julcani, Peru, and established a correlation between the contents of Sb and Ag. They suggested that the zoning of fahlore composition is caused by the evolution of fluid. This implies that fahlores enriched in As and Cu firstly precipitate from the fluid moving from center towards the margins of the hydrothermal system. The result is the enrichment of residual fluid in Sb and Ag and therefore fahlores of the assemblages latest and furthest from hydrothermal centers are enriched in Sb and Ag.

The spectrum of fahlore composition in Chah-Mesi ranging from Fe- and Zn-rich tennantite to Zn-rich tetrahedrite could be referred to all three settings proposed by Marushchenko et al. (2018). A clear evolutionary trend could not be determined but it is assumed that the Sb content increased over time in Chah-Mesi as evidenced by crosscutting fahlore veinlets and Sb-dominated grain margins. This could be due to Sb increase in the hydrothermal solution and also increasing f_{S2} conditions. However, this trend must have been accompanied by periods of significant fluctuations in the As and Sb concentrations, as evidenced by the oscillatory zoning of the fahlore grains.

Spatially, the Sb/(Sb+As) values are highest away from the Meiduk PCD with an increase of td% with distance and from deeper levels towards intermediate depths. This zoning is comparable to the model of Hackbarth and Petersen (1984) and might indicate the flow-direction and evolution of mineralizing fluids from Meiduk to Chah-Mesi, whereas hydrothermal fluids became enriched in Sb with increasing distance and decreasing depth. A correlation of Ag content could not be determined and an evolutionary trend is not visible for this element.

7.4 Chah-Mesi and Meiduk: porphyry to epithermal transition?

The hypothesis that Chah-Mesi can be classified as an epithermal deposit is supported by the fact that the majority of measured fluid inclusions plot in the field typical for epithermal environments (Figure 62). Although epithermal deposits are not exclusively porphyry-related, many epithermal deposits have a clear spatial and genetic relationship with underlying or adjacent porphyry systems. The genetic relationship between porphyry systems and spatially adjacent high-sulfidation epithermal deposits was already demonstrated by Muntean and Einaudi (2001) in the Refugio, Aldebarán, and La Pepa districts of the Maricunga belt, northern Chile, and Pudack et al. (2009) at Famatina, northwest Argentina. Similar to HS deposits, some intermediate-sulfidation deposits also exhibit close relations with PCDs. Examples reported are Far Southeast (PCD) – Lepanto (HS) – Victoria (IS) in the Philippines (Chang et al., 2011) or Golpu (PCD) – Wafi (IS) in Papua New Guinea (Rinne, 2015).

Epithermal deposits can be part of a continuum of PCDs developed in the deeper part of a system, with HS deposits close to the intrusion and IS veins generally located more distally (Figure 54). Since intermediate-sulfidation deposits are often found in the surroundings of PCDs it is likely that the epithermal veins were partially formed from the same fluids forming the porphyry mineralization (Rinne et al., 2018). Key processes in formation of this transitional porphyry-epithermal systems involve the separation of magmatic fluid into magmatic brine and low density vapor, followed by the interaction of the low density vapor component with overlying and laterally adjacent wallrock and groundwater, which results in epithermal vein precipitation and alteration (Hedenquist et al., 2000).

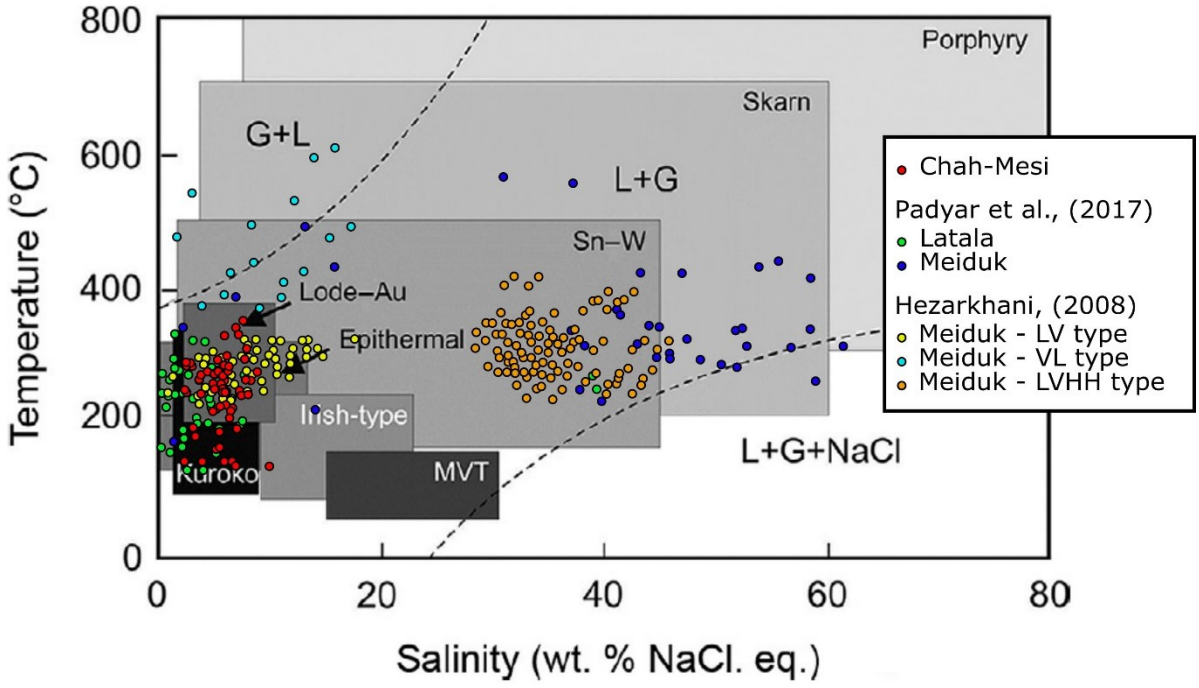

Figure 62: Comparison of liquid-vapor homogenization temperature vs. salinity plots of the Chah-Mesi deposit, Latala deposit and Miduk porphyry deposit. Critical curve (upper-left dashed curve) and vapor-saturated halite liquidus of the NaCl-H_2O system (lower-right dashed curve) separate the fields of vapor-dominated (G+L), aqueous liquid-dominated, halite-undersaturated (L+G) and halite-oversaturated (L+G+NaCl) fluids. Fields for various other ore deposits are shown as rectangles for comparison (different shading): MVT Mississippi Valley-type deposits; Sn-W metasomatic granite-related (tin-wolfram) greisen deposits etc. Modified from Wilkinson (2001).

The observed small CO_2-contents in fluid inclusions could indicate a magmatic origin that might be associated with magmatic brines derived from the Meiduk porphyry. Kokh et al. (2017) suppose that fluid mixing with CO_2-rich waters in porphyry systems may be an important process for the formation of epithermal deposits. CO_2-rich fluid pulses from the underlying magma chamber can mix with metal-bearing fluids and result in the precipitation of more than half of the Au and the initial Cu and Fe load of the aqueous fluid in porphyry Cu-Au deposits. This CO_2-rich fluid may pass through the porphyry, mix with epithermal ore fluids and trigger precipitation of ore minerals, forming Ca-Mg-Mn-Fe-carbonate at the same time when HCO_3^- decomposes and combines with Ca^{2+}, Fe^{2+}, Mn^{2+} and Mg^{2+}.

Further, the gathered information of fluid inclusions was compared to fluids determined by Hezarkhani (2008) for his group I and group III veins (Chapter 2.4.2). Veins of group I include the sulfide assemblage molybdenite + pyrite ± chalcopyrite ± bornite and correlate well with the observed B_2-type veins of the potassic zone. Group III vein sulfide assemblage of pyrite ± chalcopyrite correlates in part with the described D_1-type veins consisting of pyrite ± chalcopyrite ± bornite, despite the missing anhydrite gangue and additional bornite. Fluids studied from group I and group III veinlets include LV type, VL type and LVHH type inclusions.

Both vein groups comprise LV type inclusions consisting of liquid + vapor ± solid, VL type of vapor + liquid ± solid and LVHH type inclusions are multiphase and consist of liquid + vapor + halite + other solids. All these inclusion types were compared to LV type inclusions at Chah-Mesi and are compiled in the T_h-salinity plot after Wilkinson (2001) shown in Figure 62. Hezarkhani (2008) proposed that early hydrothermal fluids are represented by high-temperature (380 to 550 °C), high-salinity (~60 wt% NaCl equiv.) LVHH inclusions and high-temperature (320 to 550 °C), low-salinity VL inclusions. These are interpreted as orthomagmatic fluid that boiled episodically and caused potassic alteration. Additionally, they are associated with the deposition of group I veins. The influx of meteoric water into the central part of the system and mixing with magmatic fluid produced a lower temperature (200 to 350 °C), low- to intermediate-salinity (1 to 20 wt% NaCl equiv.), Ca-rich, evolved meteoric fluid associated with LV type inclusions. This type was mainly responsible for propylitic alteration and formation of group III veins.

Data of Chah-Mesi overlap with LV type inclusions of Meiduk (Figure 62). These comprise salinities of 3.9 to 10.2 wt% for group I and 4.1 to 17.9 wt% NaCl equiv. for group III. LV type fluid inclusions homogenize to liquid at temperatures between 180 and 350 °C with well-defined modes at ~270 C° for group I and around 300 C° for group III. These microthermometric data are well comparable to the ore-forming fluids at Chah-Mesi. However, the Meiduk fluids also show slightly higher salinities and homogenization temperatures. Hence, it must be assumed that they have been affected by continuing dilution and cooling until they reached the epithermal environment at Chah-Mesi.

The Chah-Mesi data are also well comparable to the inclusions from the epithermal Latala deposit (Table 14, Figure 62), which is situated about 8 km to the north of Meiduk and for which a genetic link to the nearby porphyry system was suggested (Padyar et al., 2017). Properties of fluids at Latala are consistent with a magmatic-hydrothermal fluid circulating from deeper levels to shallower environments and also $\delta^{34}S$ values of ore minerals (mostly between -2.5 to +0.9 ‰) support a magmatic-hydrothermal source. Padyar et al. (2017) proposed a genetic model in which epithermal mineralization occurred upon

dilution of the high-salinity magmatic fluid with meteoric water, which entered the hydrothermal system as it cooled.

Fluid mixing has also been deduced from $\delta^{18}O$ values of quartz at Chah-Mesi. Calculated fluid compositions range between +1.9 and +6.0 ‰ (Hosseinkhani, 2009) in accordance with the interpretation that magmatic fluids derived from Meiduk were diluted by meteoric water during their circulation and ascent.

The regional extent of the hydrothermal alteration also indicates the proximity and close relation to the Meiduk porphyry system. Alteration zoning consists of silicification and advanced argillic alteration close to structure-related fluid conduits and a transition into sericitic, argillic and propylitic and eventually potassic alteration; the latter one is closest to the Meiduk porphyry system and points to Meiduk as source of ore-forming hydrothermal-magmatic fluids. Similar zoning associated with porphyry Cu-Mo deposits has been recorded by Darabi-Golestan et al. (2013). However, what seems very unusual is that potassic alteration at Meiduk was recognized upon 3366900 N and represents an about 50 m thick halo surrounding the porphyry stock. In Chah-Mesi potassic alteration starts at 3365300 N, which corresponds to about 1600 m distance to the outer boundary of Meiduk potassic alteration. Therefore, a direct connection between these two zones is very unlikely.

7.5 Regional geodynamics and ore genesis

This chapter gives an interpretation of the possible metallogenetic evolution of Chah-Mesi and presents a genetic model (Figure 63) from the author's viewpoint. For this purpose, the results of this study are discussed in combination with other published data and ideas.

7.5.1 Regional geodynamics and metallogeny

The epithermal deposit Chah-Mesi and the nearby porphyry copper deposit Meiduk are located in the Kerman Porphyry Copper Belt of the southeastern UDMB. The formation of the UDMB is closely related to the subduction of oceanic lithosphere of the Neotethys. The opening of the Neotethys started in the Permian and the collision of the Arabian and Iranian plates occurred during the end of the Eocene (Alirezaei et al., 2017; Berberian and King, 1981). The subduction of the Neotethys caused the formation of an active continental margin environment and initiated the deposition of calc-alkaline volcanic rocks in the Meiduk area (Aliani et al., 2009). The main volcanic activity of this area started during the Lower Eocene with the Bahraseman complex. Andesitic and dacitic-pyroclastic host rocks described in this study belong to the overlying Middle-Upper Eocene Razak complex, which was deposited at 37.5 ± 1.4 Ma (Hassanzadeh, 1993). The uppermost Oligocene Hezar complex was formed at 32.7 ± 6.3 Ma Hassanzadeh (1993).

The Mid- to Late Miocene post-collisional and late orogenic slab breakoff (Allen et al., 2011) following the collision of the Arabian and Iranian plates is widely considered to have caused uplift and adakite-like magmatism in the UDMB (Omrani et al., 2008). Shafiei et al. (2009) proposed that post-collisional calc-alkaline magmas involved a significant fraction of remobilized subduction-modified lower crust and argue that this process is key to the fertility of these Middle-Miocene magmas, which are related to the formation of the largest porphyry Cu-Mo deposits in Iran (e.g. Sar Cheshmeh, Meiduk). During this time the Meiduk porphyry granitic stocks, related to the Kuh-Panj type granitoids, intruded into the

Razak complex at 12.5 ± 0.1 Ma (zircon U-Pb, McInnes et al., 2005) at shallow crustal levels (2-3 km, Alirezaei et al., 2017). Taghipour et al. (2008) reported Re-Os molybdenite ages of 12.23 ± 0.07 Ma for mineralization. Geochemical results of Alirezaei et al. (2017) show that Meiduk was formed in a post-collisional and late orogenic geodynamic setting with an extensional stress regime (Figure 55 C). The main mineralization phases at Meiduk are hosted by quartz-diorite, granodiorite and diorite with calc-alkaline, metaluminous to weakly peraluminous and I-type nature. The geochemical characteristics such as high Sr, low Yb, strongly differentiated REE patterns and lack of Eu anomaly indicate an adakitic-like signature (Aliani et al., 2009; Alirezaei et al., 2017).

7.5.2 Genetic model for Chah-Mesi – Meiduk

Hezarkhani (2008) demonstrates that multiple intrusions at Meiduk are associated with repeated fracturing and hydrothermal activity. The fluid inclusion studies indicate that the earliest fluid at Meiduk was magmatically derived and characterized by high temperatures and moderate to high salinities. Moreover, it was responsible for potassic alteration and the wide distribution of early veinlets including molybdenite + pyrite ± chalcopyrite ± bornite (B_2-type, Taghipour et al., 2008). Early stage mineralization is ascribed to episodical boiling at temperatures ranging from 370 to 530 °C. During the main stage of mineralization, the influx of meteoric water into the central part of the porphyry system and mixing with magmatic fluid produced a lower temperature (200 to 350 °C), low- to intermediate-salinity (1 to 20 wt% NaCl equiv.), oxidized fluid. This fluid caused peripheral propylitic alteration as well as local argillic alteration and formed veinlets with pyrite ± chalcopyrite (D_1-type?, Taghipour et al., 2008).

A fluid of mainly mixed meteoric and magmatic origin circulated later in the central part of the stock, at temperatures between 230 and 450 °C. Hezarkhani (2008) proposed that at temperatures around 350 °C, partial boiling and subsequent mixing with meteoric fluids was responsible for the variation in salinity in the vein-hosted fluid inclusions. Destabilization of previously formed K-feldspar from the potassic alteration zone caused formation of biotite-rich potassic alteration, which is documented in the northern part of Chah-Mesi.

Alizadeh and Arian (2015) concluded that brittle structures are an important prerequisite for transferring hydrothermal fluids towards the surface in PCD deposits in the Kerman Belt. The cooling intrusion at Meiduk caused dense fracturing in the porphyry stock and the surrounding wallrocks (Shafiei and Ghiyasi, 2014). These fractures provided pathways for the late hydrothermal fluid to ascend in the upper levels of the intrusion and produce widespread lower temperature sericitization there. As a result of lower pH and higher f_{O2}, earlier formed copper sulfides were remobilized and reprecipitated into highly fractured zones. Therefore, it has been assumed that the magmatic-hydrothermal fluids ascended from the Meiduk porphyry system towards the south through major faults and transported magmatic volatiles (e.g. CO_2) as well as sulfur and metals into the near-surface area of Chah-Mesi (IS epithermal in Figure 54 and Figure 57, right). Cooling and mixing of this moderately saline (1.2 to 9.9 wt% NaCl equiv.) magmatic fluid and meteoric water could explain the “inclined” trend represented by the transition of LV type fluid inclusions from Meiduk and Chah-Mesi in the homogenization temperatures vs. salinity diagram (Figure 62). This is supported by very low CO_2 contents observed in the vapor phase and $\delta^{18}O$ values of fluid in equilibrium with quartz ranging between +1.9 and +6.0 ‰ reported by Hosseinkhani

(2009), which indicate a dilution of these magmatic fluids with meteoric water upon epithermal mineralization.

The formation of mineralized O-type veins at Chah-Mesi started with an early highly acidic fluid of high-sulfidation state that caused strong silicification and local replacement bodies with vuggy quartz. These textures are limited to the NNE-SSW striking major faults (OZ1) and are associated with massive silica-rich O-type veins including the early ore assemblage pyrite + chalcopyrite + enargite + luzonite-famatinite ± bornite. With increasing distance to the central fault zones (OZ2) the mineralizing fluids were affected by continuous reaction with the surrounding wallrock and further dilution with meteoric water. This caused an increase in pH and the reduced as well as cooled conditions provided a decrease into intermediate-sulfidation state. The physicochemical change resulted in widespread sericitization and open space precipitation of banded and crustiform veins hosting the main stage assemblage pyrite + chalcopyrite + tennantite-tetrahedrite + sphalerite + galena ± enargite ± Ag-sulfides ± electrum. The mineralized breccia zone of the deeper level is probably related to the transition between early (HS) and main (IS) mineralization due to very low Fe contents of sphalerite.

Petrographic features and fluid inclusion data do not support boiling as an ore deposition mechanism but cannot completely rule it out either. The contribution of meteoric water as the source of fluids that caused sericitic alteration is supported by stable isotope data (Hosseinkhani, 2009). The systematic variation of the fahlore composition with oscillatory zoned crystals reflect significant fluctuations in the As and Sb concentrations of the ore-forming fluids. However, a general trend of Sb increase with time is recorded by fahlores and in space with increasing tetrahedrite content away from the Meiduk deposit and shallow depths.

It can be speculated that a separate pulse of ore-forming fluids caused the late stage hypogene mineralization, which is Pb-Zn dominated and occurs distal to the major fault zones (OZ3) and overprints earlier Cu-rich assemblages. It consists of sphalerite + galena + chalcopyrite + pyrite ± tennantite-tetrahedrite with predominately Ca-Mg-Mn-Fe-carbonates as gangue mineral.

The final stage of mineralization is associated with supergene weathering and oxidation. It is characterized by the replacement of chalcopyrite, sphalerite and galena by secondary copper and iron minerals. Hence, the assemblage of chalcocite- and covellite-group minerals, Fe-hydroxides, Cu-carbonate hydroxides, etc. is restricted to the weathered surface area and progressively decreases towards a depth of approximately 50 m below the surface.

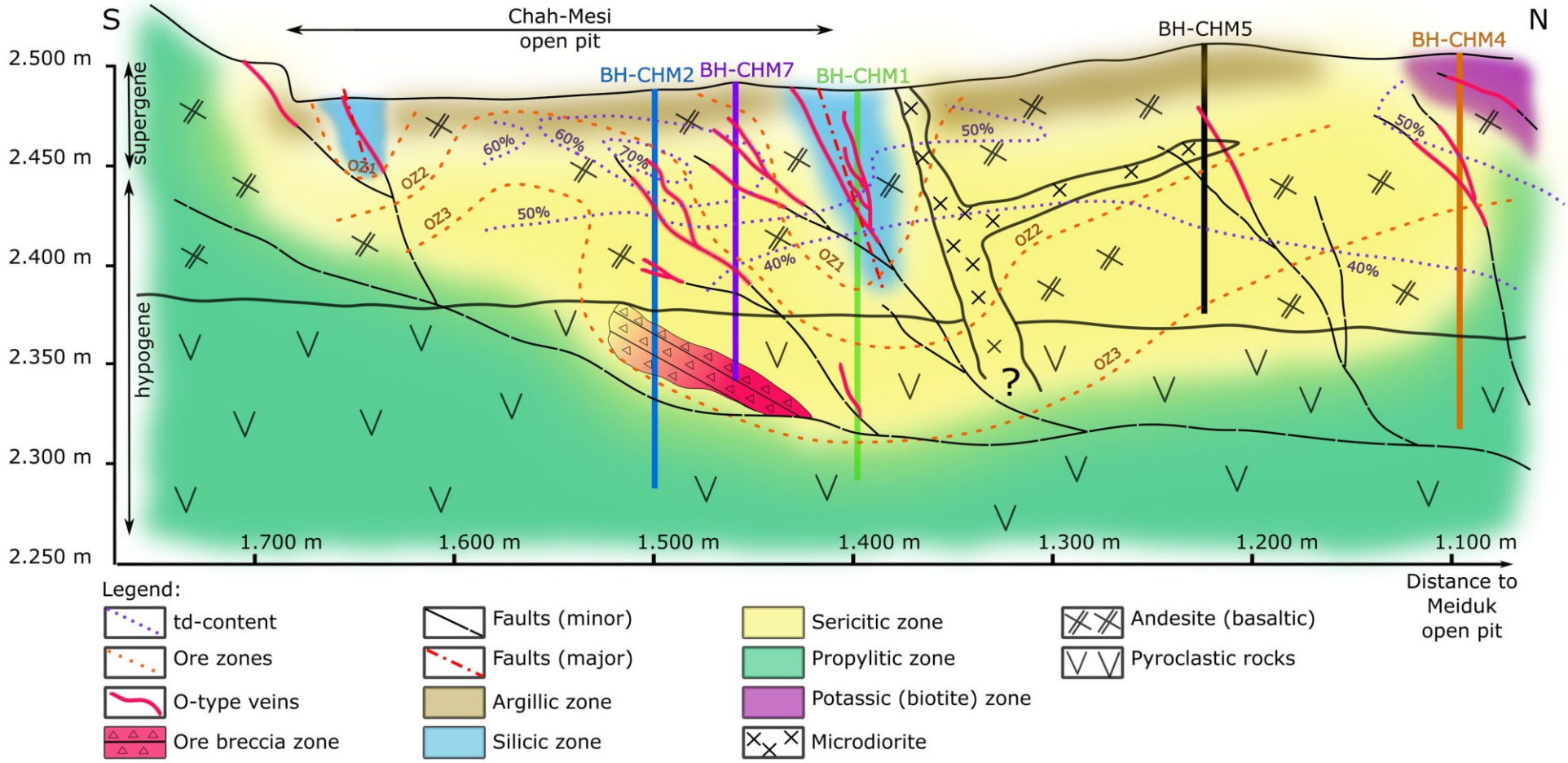

Figure 63: N-S crossection of Chah-Mesi deposit schematically showing the distribution of tetrahedrite content (dotted purple lines), ore zones (dashed orange lines), alteration zones and host rocks. Ore zone 1 (OZ1) surrounds areas of intense silicification associated with Fe-Cu-dominated sulfides and grades through the transitional ore zone 2 (OZ2) into the Pb-Zn-dominated ore zone 3 (OZ3) affected by mainly sericitic to minor propylitic alteration. Ore zone 4 is associated with supergene alteration on the surface and was excluded for reasons of clarity. Tetrahedrite content (td%) indicating Sb-enrichment towards shallow levels and increasing distance to Meiduk (contour lines are taken from Figure 61).

8 Conclusions

This Master's thesis presents a detailed investigation of the epithermal veins at Chah-Mesi deposit in the Kerman Porphyry Copper Belt in southeastern Iran. The main purpose of this study was to correctly classify Chah-Mesi regarding epithermal deposit types. Detailed textural and mineralogical studies allowed to distinguish different vein types, establish a paragenetic sequence of ore mineralization and provide new data on the mineral chemistry of the ore minerals and their deposit-scale distribution. The physicochemical conditions of ore-forming fluids and their evolution through time and space were reconstructed on the basis of ore mineral assemblages, mineral chemistry and fluid inclusion studies. It is discussed that hydrothermal fluids derived from the porphyry system and that there exists a causal link of epithermal mineralization at Chah-Mesi with the Meiduk porphyry.

The polymetallic Chah-Mesi Cu-Pb-Zn-(Ag-Au) vein type deposit is classified as intermediate-sulfidation (IS) state epithermal deposit. This is supported by the following data:

(1) Chah-Mesi deposit is hosted by a calc-alkaline succession of intermediate volcanic rocks (andesites, pyroclastics of dacitic composition) and minor hypabyssal rocks (microdiorite) formed in a post-collisional arc setting within an extensional stress regime. Mineralized polymetallic epithermal veins are related to NNE-SSW striking fault zones.

(2) Polymetallic mineralization is restricted to multistage veins, associated breccias and minor replacement bodies with residual vuggy quartz. The main metals are Cu, Zn, Pb, As, Sb with minor Ag and Au and trace amounts of Mo and Te. The average sulfide abundance is between 20 and 30 vol% and may exceed 50 vol% in ginguro veins. Hypogene ore minerals include sphalerite, galena, chalcopyrite, tetrahedrite-tennantite, enargite, luzonite-famatinite and minor bornite. Precious metals occur as electrum, Ag-bearing sulfides and sulfosalts (e.g. jalpaite, pearceite, benleonardite). Supergene mineralization contains chalcocite and covellite together with Fe-oxyhydroxides and Cu-carbonate hydroxides.

(3) Textural features of silica gangue comprise fault zone replacement and vein filling by massive and banded fine- to coarse-grained quartz as well as crustiform and comb quartz textures. Common carbonate gangue minerals in the banded and crustiform veins are Mn and Zn bearing siderite, ankerite and rare kutnohorite. Other gangue minerals involve barite, fluorite, apatite and anhydrite.

(4) Hydrothermal alteration zoning consists of central structure-controlled silicification grading into local advanced argillic and argillic alteration halos. Pervasive sericitization grading into regional propylitic alteration is commonly further away from the deposit. Potassic (biotite-rich) alteration is found in the north closest to the Meiduk porphyry deposit.

(5) The investigated fluid inclusions contain aqueous H_2O-NaCl fluids with minor CO_2. Low salinity liquid-rich LV type inclusions dominate the assemblages determined in sphalerite and quartz; total salinities are 1.2 to 9.9 wt% in sphalerite and 2.1 to 9.2 wt% NaCl equiv. in quartz. T_h values range from 114.6 to 294.6 °C for sphalerite and 153.0 to 396.5 °C for quartz.

A total of 59 representative drill core and surface samples from the various vein types and lithologies were collected. These were taken from 5 drill cores from different depths and locations within the Chah-Mesi deposit. Optical microscopy was conducted to constrain the textural and mineralogical characteristics of the mineralization and alteration and to establish an ore paragenetic sequence and alteration zoning for the Chah-Mesi deposit. The study of the samples allowed to draw the following conclusions:

(1) Two types of veins are directly linked with porphyry mineralization and occur in the potassic alteration zone very close to Meiduk. They include B_2-type (quartz, carbonate, pyrite, molybdenite, chalcopyrite and bornite) and D_1-type (mainly quartz and pyrite with minor carbonate, chalcopyrite, bornite and Fe-oxyhydroxides) veins and represent the earliest veins. Furthermore, three barren alteration-related vein types were distinguished, termed QCS-type (quartz, chlorite, sericite and minor calcite), PCE-type (prehnite, calcite, clinozoisite, epidote with minor rutile and native copper) and CC-type (calcite and minor quartz) veins. Mineralization is restricted to O-type veins which are subdivided into four subtypes; i.e. massive, banded and crustiform veins as well as mineralized breccia zones.

(2) The paragenetic sequence of ore minerals is initiated by a high-sulfidation stage with pyrite + chalcopyrite + enargite + luzonite-famatinite ± bornite, which mainly occurs in ore zone 1 (OZ 1) close to the central NNE-SSW trending fault zones. This early stage assemblage grades into intermediate-sulfidation assemblages with pyrite + chalcopyrite + tennantite-tetrahedrite + sphalerite + galena. Gold and only minor enargite also formed during the main stage, which mainly occurs in OZ 2. The subsequent Pb-Zn dominated stage is characterized by sphalerite + galena + chalcopyrite + pyrite ± tennantite-tetrahedrite to be found mostly in OZ 3 distal to fault zones. The fourth stage represents supergene weathering and is characterized by the mineral assemblage of chalcocite + covellite + malachite + azurite + goethite + limonite. It is restricted to OZ 4 extending from the surface to a depth of approximately 50 m.

(3) Alteration associated with the HS massive O-type veins consists of central structure-related silicification grading into advanced argillic and argillic alteration halos. Sericitization is associated with QCS-type veinlets, propylitic alteration with PCE- and CC-type veinlets. In the north closest to the Meiduk porphyry deposit potassic (biotite-rich) alteration is associated with the porphyry-related D_1- and B_2-type veins.

Electron microprobe analysis was conducted on fahlore group minerals and other sulfides and sulfosalts. It allowed to establish a spatial distribution of Sb/As ratios of fahlore group minerals and to identify the main Ag carriers.

(1) Fahlore group minerals define a trend of increasing Sb content (td%) with increasing distance from Meiduk and from deeper towards intermediate depths at Chah-Mesi. However, individual samples record significant compositional zoning and grain-scale variations of As and Sb due to fluctuations of these elements in the hydrothermal fluid.

(2) Fahlore group minerals are identified as the main Ag carriers with contents up to 1.94 apfu Ag in the central part of Chah-Mesi. The overall Ag content shows an average of 0.06 Ag apfu. In some samples the Ag content increases systematically with the tetrahedrite component. Moreover, enargite and luzonite contain small amounts of Ag averaging 0.01 Ag apfu with a maximum of 0.02

apfu. Chalcopyrite showing an excess in Cu and deficiency in Fe incorporates minor amounts of Ag with a maximum of 0.12 Ag apfu. The minerals of the geerite-covellite series have Ag contents of up to 0.1 apfu. Exotic Ag-bearing minerals identified comprise phases of the pearceite-polybasite series, jalpaite and benleonardite.

(3) The sphalerite contained in the different vein types has low Fe concentrations ranging from 0.05 to 1.5 mole% FeS substituting for ZnS in the sphalerite structure.

The combined mineralogical and fluid inclusion studies permit to constrain changes in the physicochemical conditions of ore forming fluids and to establish a genetic link to Meiduk porphyry deposit:

(1) Banded and crustiform O-type veins formed from H_2O-NaCl fluids with subordinate CO_2 content, indicating a magmatic origin. The properties of LV type fluid inclusions of these veins are similar to those reported from the nearby epithermal Latala deposit. Moreover, there is a strong overlap with low salinity LV type inclusions reported from Meiduk PCD. Thus, it is suggested that epithermal mineralization at Chah-Mesi is linked with magmatic-hydrothermal fluids derived from the Meiduk porphyry system. These fluids migrated upward and laterally from the deep high-temperature porphyry level into shallow epithermal environments where, upon cooling, they were diluted by meteoric water.

(2) The early stage magmatic hydrothermal fluids were highly acidic and high-sulfidation state fluids that caused the intense silicification and replacement of host rocks along the major faults at Chah-Mesi. They produced the HS sulfide assemblages. Due to cooling, fluid-wallrock interaction and mixing with meteoric water the fluids were neutralized and the sulfidation state changed to intermediate towards the peripheral parts of the deposit as well as in the younger parts of multiple sulfide veins. This change in physicochemical conditions triggered the formation of Au- and Ag-bearing IS assemblages and strong sericitization. Fluid inclusions and vein textures indicate that mineralization occurred under non-boiling conditions. Hence, mixing of fluids and fluid-rock interaction controlling the sulfidation state are interpreted to have played key roles in ore precipitation at Chah-Mesi.

9 References

Adeli, Z., Rasa, I., and Darvishzadeh, A., 2014, Fluid inclusion study of the ore-quartz veins at Haftcheshmeh porphyry copper (Mo) deposit, Ahar–Arasbaran Magmatic Belt, NW Iran, Ore Geology Reviews, 502-511 p.:

Agard, P., Omrani, J., Jolivet, L., and Mouthereau, F., 2005, Convergence history across Zagros (Iran): constraints from collisional and earlier deformation: International Journal of Earth Sciences, v. 94, no. 3, p. 401-419.

Aghanabati, A., 2004, Geology of Iran, Tehran, Geological Survey of Iran, 606 p.:

Aghazadeh, M., Castro, A., Badrzadeh, Z., and Vogt, K., 2011, Post-collisional polycyclic plutonism from the Zagros hinterland: the Shaivar Dagh plutonic complex, Alborz belt, Iran: Geological Magazine, v. 148, no. 5-6, p. 980-1008.

Ahmadzadeh, G., Jahangiri, A., Lentz, D., and Mojtahedi, M., 2010, Petrogenesis of Plio-Quaternary post-collisional ultrapotassic volcanism in NW of Marand, NW Iran: Journal of Asian Earth Sciences, v. 39, no. 1, p. 37-50.

Alaminia, Z., Karimpour, M. H., Homam, S. M., and Finger, F., 2013, The magmatic record in the Arghash region (northeast Iran) and tectonic implications: International Journal of Earth Sciences, v. 102.

Alavi, M., 1980, Tectonostratigraphic evolution of the Zagrosides of Iran: Geology, v. 8, no. 3, p. 144-149.

-, 1991, Sedimentary and structural characteristics of the paleo-Tethys remnant in NE Iran: Geological Society of America Bulletin, v. 103, p. 983-992.

-, 1994, Tectonics of the zagros orogenic belt of iran: new data and interpretations: Tectonophysics, v. 229, no. 3, p. 211-238.

-, 2007, Structures of the Zagros fold-thrust belt in Iran, American Journal of Science - AMER J SCI, 1064-1095 p.:

Ali, S. A., Buckman, S., Aswad, K. J., Jones, B. G., Ismail, S. A., and Nutman, A. P., 2013, The tectonic evolution of a Neo-Tethyan (Eocene–Oligocene) island-arc (Walash and Naopurdan groups) in the Kurdistan region of the Northeast Iraqi Zagros Suture Zone: Island Arc, v. 22, no. 1, p. 104-125.

Aliani, F., Alirezaei, A., Moradian, A., and Abbasloo, Z., 2009, Geochemistry and petrography of the Meiduk porphyry copper deposit, Kerman, Iran: Australian Journal of Basic and Applied Sciences, v. 3, p. 3786-3800.

Alirezaei, A., Arvin, M., and Dargahi, S., 2017, Adakite-like signature of porphyry granitoid stocks in the Meiduk and Parkam porphyry copper deposits, NE of Shahr-e-Babak, Kerman, Iran: Constrains on geochemistry: Ore Geology Reviews, v. 88, p. 370-383.

Alizadeh, H., and Arian, M., 2015, Rule of structural factors in formation of porphyry copper deposits in south western part of Kerman area, Iran: Open Journal of Geology, v. 5, no. 7, p. 489-498.

Alizadeh Sevari, B., and Hezarkhani, A., 2014, Hydrothermal evolution of Darrehzar porphyry copper deposit, Iran: evidence from fluid inclusions: Arabian Journal of Geosciences, v. 7, no. 4, p. 1463-1477.

Allen, M. B., Ghassemi, M. R., Shahrabi, M., and Qorashi, M., 2003, Accommodation of late Cenozoic oblique shortening in the Alborz range, northern Iran: Journal of Structural Geology, v. 25, no. 5, p. 659-672.

Allen, M. B., Kheirkhah, M., Emami, M. H., and Jones, S. J., 2011, Right-lateral shear across Iran and kinematic change in the Arabia—Eurasia collision zone: Geophysical Journal International, v. 184, no. 2, p. 555-574.

Allen, M. B., Saville, C., Blanc, E. J. P., Talebian, M., and Nissen, E., 2013, Orogenic plateau growth: Expansion of the Turkish-Iranian Plateau across the Zagros fold-and-thrust belt: Tectonics, v. 32, no. 2, p. 171-190.

Arribas, A., 1995, Characteristics of high-sulfidation epithermal deposits, and their relation to magmatic fluid: Mineral. Asso. Canada Short Course Series, v. 23, p. 419-454.

Asadi, S., 2018, Triggers for the generation of post–collisional porphyry Cu systems in the Kerman magmatic copper belt, Iran: New constraints from elemental and isotopic (Sr–Nd–Hf–O) data: Gondwana Research, v. 64, p. 97-121.

Atalou, S., Nezafati, N., Lotfi, M., and Aghazadeh, M., 2017, Fluid Inclusion Investigations of the Masjed Daghi Copper-Gold Porphyry-Epithermal Mineralization, East Azerbaijan Province, NW Iran, Open Journal of Geology, 1110-1127 p.:

Bakker, R., 2011, The use of quantities, units and symbols in fluid inclusion research, Berichte der Geologischen Bundesanstalt, Volume 87, p. 5-11.

-, 2018, AqSo_NaCl: Computer program to calculate p-T-V-x properties in the H 2 O-NaCl fluid system applied to fluid inclusion research and pore fluid calculation: Computers & Geosciences, v. 115.

Ballato, P., Uba, C. E., Landgraf, A., Strecker, M. R., Sudo, M., Stockli, D. F., Friedrich, A., and Tabatabaei, S. H., 2011, Arabia-Eurasia continental collision: Insights from late Tertiary foreland-basin evolution in the Alborz Mountains, northern Iran: GSA Bulletin, v. 123, no. 1-2, p. 106-131.

Barton, P. B., 1970, Sulfide petrology: Mineral. Soc. Amer. Spec. Pap., v. 3, p. 187-198.

Berberian, F., and Berberian, M., 1981, Tectono-Plutonic Episodes in Iran, *in* Gupta, H. K., and Delany, F. M., eds., Zagros-Hindu Kush-Himalaya Geodynamic Evolution, Geodynamic Series, Volume 3: Washington DC, American Geophysical Union, p. 5-32.

Berberian, M., and King, G. C. P., 1981, Towards a paleogeography and tectonic evolution of Iran: Canadian Journal of Earth Sciences, v. 18, no. 2, p. 210-265.

Bindi, L., Evain, M., Spry, P. G., and Menchetti, S., 2007, The pearceite-polybasite group of minerals: Crystal chemistry and new nomenclature rules: American Mineralogist, v. 92, no. 5-6, p. 918-925.

Bodnar, R. J., 1993, Revised equation and table for determining the freezing point depression of H2O-NaCl solutions: Geochimica Et Cosmochimica Acta, v. 57, no. 3, p. 683-684.

Brunet, M.-F., 2009, South Caspian to Central Iran Basins, Volume 312: London U6 - ctx_ver=Z39.88-2004&ctx_enc=info%3Aofi%2Fenc%3AUTF-8&rfr_id=info%3Asid%2Fsummon.serialssolutions.com&rft_val_fmt=info%3Aofi%2Ffmt%3Akev%3Amtx%3Ajournal&rft.genre=article&rft.atitle=South+Caspian+to+Central+Iran+Basins&rft.au=Brunet%2C+Marie-Fran%C3%A7oise&rft.series=Geological+Society+special+publication&rft.date=2009-01-01&rft.pub=Geological+Soc&rft.volume=312&rft.externalDocID=LG00006581&paramdict=en-US U7 - Web Resource, Geological Soc.

Byrne, D. E., Sykes, L. R., and Davis, D. M., 1992, Great thrust earthquakes and aseismic slip along the plate boundary of the Makran Subduction Zone: Journal of Geophysical Research: Solid Earth, v. 97, no. B1, p. 449-478.

Calais, E., and Amarjargal, S., 2000, New constraints on current deformation in Asia from continuous GPS measurements at Ulan Baatar, Mongolia: Geophysical Research Letters, v. 27, no. 10, p. 1527-1530.

Candela, P. A., and Holland, H. D., 1984, The partitioning of copper and molybdenum between silicate melts and aqueous fluids: Geochimica et Cosmochimica Acta, v. 48, no. 2, p. 373-380.

Chang, Z., Hedenquist, J. W., White, N. C., Cooke, D. R., Roach, M., Deyell, C. L., Garcia, J., Jr., Gemmell, J. B., McKnight, S., and Cuison, A. L., 2011, Exploration Tools for Linked Porphyry and Epithermal Deposits: Example from the Mankayan Intrusion-Centered Cu-Au District, Luzon, Philippines*: Economic Geology, v. 106, no. 8, p. 1365-1398.

Colman-Sadd, S. P., 1978, Fold development in Zagros simply folded belt, Southwest Iran: AAPG Bulletin, v. 62, no. 6, p. 984-1003.

Cooke, D. R., Hollings, P., and Walshe, J. L., 2005, Giant porphyry deposits; characteristics, distribution, and tectonic controls: Economic Geology and the Bulletin of the Society of Economic Geologists, v. 100, no. 5, p. 801-818.

Cooke, D. R., Hollings, P., Wilkinson, J. J., and Tosdal, R. M., 2014, Geochemistry of Porphyry Deposits, *in* Holland, H. D., and Turekian, K. K., eds., Treatise on Geochemistry, Second Edition, Volume 13: Oxford Elsevier, p. 357-381.

Cooke, D. R., and Simmons, S. F., 2000, Characteristics and Genesis of Epithermal Gold Deposits, *in* Hagemann, S. G., and Brown, P. E., eds., Gold in 2000, Volume 13, Society of Economic Geologists, p. 221-244.

Cooke, D. R., White, N. C., Zhang, L.-J., Chang, Z., and Chen, H., 2017, Lithocaps – characteristics, origins and significance for porphyry and epithermal exploration, Mineral Resources to Discover - Proceedings of the 14th SGA Biennial Meeting, Volume 1, SGA, p. 291-294.

Craig, J. R., and Vaughan, D. J., 1994, Ore microscopy and ore petrography, New York, John Wiley & Sons, Inc., 434 p.:

Darabi-Golestan, F., Ghavami-Riabi, R., and Asadi-Harooni, H., 2013, Alteration, zoning model, and mineralogical structure considering lithogeochemical investigation in Northern Dalli Cu-Au porphyry: Arabian Journal of Geosciences, v. 6, no. 12, p. 4821-4831.

Davidson, J., Hassanzadeh, J., Berzins, R., Stockli, D. F., Bashukooh, B., Turrin, B., and Pandamouz, A., 2004, The geology of Damavand volcano, Alborz Mountains, northern Iran: GSA Bulletin, v. 116, no. 1-2, p. 16-29.

Deere, D. U., 1964, Technical description of rock cores for Engineering purposes: Felsmechanik und Ingenieurgeologie, v. 1, no. 1, p. 16-22.

Delvigne, J. E., 1999, Atlas of Micromorphology of Mineral Alteration and Weathering, Ottawa, Ontario, Mineralogical Association of Canada (in collaboration with ORSTOM, Paris), Canadian Mineralogist Special Publication 3.

Desmons, J., and Beccaluva, L., 1983, Mid-ocean ridge and island-arc affinities in ophiolites from Iran: Palaeographic implications: Complementary reference: Chemical Geology, v. 39, no. 1, p. 39-63.

Dimitrijević, M. D., 1973, Geology of Kerman region, Teheran, Ministry of Economy, Geological Survey of Iran.

Dimitrova, D., Kerestedjian, T., Petrova, M., and Ilieev, T., 2007, Compositional variations in the tetrahedrite-tennantite fahlores and polybasite-pearceite series from the Chiprovtsi Ag-Pb deposit, Northwestern Bulgaria, Geol. Tutkimuslaitos, 39-44 p.:

Dong, G., Morrison, G., and Jaireth, S., 1995, Quartz textures in epithermal veins, Queensland; classification, origin and implication: Economic Geology, v. 90, no. 6, p. 1841-1856.

Ebadi Rajoli, M., Afzal, P., and Moarefvand, P., 2015, Classification of mineralized veins using concentration volume (C–V) fractal modeling: a case study from Chah-Mesi Cu–Au vein deposit, SE Iran: Arabian Journal of Geosciences, v. 8, no. 10, p. 8249-8262.

Einaudi, M. T., Hedenquist, J. W., and Inan, E. E., 2003, Sulfidation State of Fluids in Active and Extinct Hydrothermal Systems: Transitions from Porphyry to Epithermal Environments: Society of Economic Geologists Special Publication, v. 10, p. 285-313.

Evans, A. M., 1993, Ore Geology and Industrial Minerals: An Introduction, Blackwell Science Ltd, 400 p.:

Falcon, N. L., 1974, Southern Iran: Zagros Mountains: Geological Society, London, Special Publications, v. 4, no. 1, p. 199-211.

Förster, H. J., 1978, Mesozoic-Cenozoic metallogenesis in Iran, Journal of The Geological Society - J GEOL SOC, 443-455 p.:

Fürsich, F. T., Wilmsen, M., Seyed-Emami, K., and Majidifard, M. R., 2009, Lithostratigraphy of the Upper Triassic–Middle Jurassic Shemshak Group of Northern Iran, *in* Brunet, M. F., Wilmsen, M., and Granath, J. W., eds., South Caspian to Central Iran Basins, Volume 312, Geological Society of London, p. 0.

Gablina, I., 1997, Copper sulfides as indicators of the Ore-forming environment: Dokl. Earth Sci., v. 357, p. 1133-1137.

Garzanti, E., and Gaetani, M., 2002, Unroofing history of Late Paleozoic magmatic arcs within the "Turan Plate" (Tuarkyr, Turkmenistan): Sedimentary Geology, v. 151, no. 1, p. 67-87.

Geological Survey of Iran, 1989, Geological map of Iran 1:2.500.000, Tehran, Geological Survey of Iran.

-, 2009, International geological map of the Middle East, Tehran, Geological Survey of Iran.

Ghalamghash, J., Bouchez, J.-L., Vosoughi-Abedini, M., and Nedelec, A., 2009, The Urumieh Plutonic Complex (NW Iran): Record of the geodynamic evolution of the Sanandaj–Sirjan zone during Cretaceous times – Part II: Magnetic fabrics and plate tectonic reconstruction: Journal of Asian Earth Sciences, v. 36, p. 303-317.

Ghasemi, A., and Talbot, C. J., 2006, A new tectonic scenario for the Sanandaj-Sirjan Zone (Iran): J. Asian Earth. Sci., v. 26, p. 683-693.

Ghorbani, M., 1999, Petrological investigations of tertiary-quaternary magmatic rocks and their metallogeny in Takab areaPhD thesis]: Shahid Beheshti University.
-, 2009, Antimony, arsenic and mercury as strategic metals in industries and key elements in exploration geology of epithermal gold deposits: Sang va Maadan Q, v. 13, p. 4-15.
-, 2013, The Economic Geology of Iran: Mineral Deposits and Natural Resources, Dordrecht, Springer Netherlands, 87-197 p.:
Ghorbani, M., and Momenzadeh, M., 1994, Mineralization phases of Iran, 13th congregation of earth scientists, Geological Survey of Iran (In Farsi).
-, Explanation of mineralization phases in Iran, *in* Proceedings Proceedings of the 13th conference on GeoScience, Geological Survey of Iran, 1995.
Ghorbani, M., Tajbakhsh, P., and Khoi, N., 2000, Lead-zinc deposits in Iran, Teheran, Geological Survey of Iran.
Giggenbach, W. F., 1992, Magma degassing and mineral deposition in hydrothermal systems along convergent plate boundaries: Economic Geology and the Bulletin of the Society of Economic Geologists, v. 87, no. 7, p. 1927-1944.
Glennie, K. W., 2000, Cretaceous Tectonic Evolution of arabia's Eastern Plate Margin: A Tale of Two Oceans, Middle East Models of Jurassic/Cretaceous Carbonate Systems, Volume 69, Spec. Publ., SEPM (Society for Sedimentary Geology), p. 9-20.
Gustafson, L. B., and Hunt, J. P., 1975, The porphyry copper deposit at El Salvador, Chile: Economic Geology, v. 70, no. 5, p. 857-912.
Guzman, M., Geology, vein petrography and mineral chemistry of the North Amethyst Deposit, Creede mining district, Creede, ColoradoMaster's], 180 p.
Habibi, T., and Hezarkhani, A., 2013, Hydrothermal evolution of Daraloo porphyry copper deposit, Iran: evidence from fluid inclusions: Arabian Journal of Geosciences, v. 6, no. 6, p. 1945-1955.
Hackbarth, C. J., and Petersen, U., 1984, A fractional crystallization model for the deposition of argentian tetrahedrite: Economic Geology, v. 79, no. 3, p. 448-460.
Hassanzadeh, J., 1993, Metallogenic and tectonomagmatic events in the SE sector of the Cenozoic active continental margin of central Iran (Shahr e Babak area, Kerman Province)Unpublished Ph.D. dissertation]: University of California, 204 p.
Hedenquist, J. W., Arribas, A., and Gonzalez-Urien, E., 2000, Exploration for Epithermal Gold Deposits: Reviews in Economic Geology, v. 13, p. 245-277.
Hedenquist, J. W., Simmons, S. F., Giggenbach, W. F., and Eldridge, C. S., 1993, White Island, New Zealand, volcanic-hydrothermal system represents the geochemical environment of high-sulfidation Cu and Au ore deposition: Geology, v. 21, no. 8, p. 731-734.
Heinrich, C. A., 2005, The physical and chemical evolution of low-salinity magmatic fluids at the porphyry to epithermal transition: a thermodynamic study: Mineralium Deposita, v. 39, no. 8, p. 864-889.
Hezarkhani, A., 2006a, Hydrothermal evolution of the Sar-Cheshmeh porphyry Cu-Mo deposit, Iran; evidence from fluid inclusions: Journal of Asian Earth Sciences, v. 28, no. 4-6, p. 409-422.
-, 2006b, Mineralogy and fluid inclusion investigations in the Reagan Porphyry System, Iran, the path to an uneconomic porphyry copper deposit: Journal of Asian Earth Sciences, v. 27, no. 5, p. 598-612.
-, 2008, Hydrothermal evolution of the Miduk porphyry copper system, Kerman, Iran; a fluid inclusion investigation: International Geology Review, v. 50, no. 7, p. 665-684.
-, 2009, Hydrothermal fluid geochemistry at the Chah-Firuzeh porphyry copper deposit, Iran; evidence from fluid inclusions: Journal of Geochemical Exploration, v. 101, no. 3, p. 254-264.
Hollingsworth, J., Fattahi, M., Walker, R., Talebian, M., Bahroudi, A., Bolourchi, M. J., Jackson, J., and Copley, A., 2010, Oroclinal bending, distributed thrust and strike-slip faulting, and the accommodation of Arabia–Eurasia convergence in NE Iran since the Oligocene: Geophysical Journal International, v. 181, no. 3, p. 1214-1246.
Hollister, V. F., 1978, Geology of the porphyry copper deposits of the Western Hemisphere, New York, Society of Mining Engineers of the American Institute of Mining, Metallurgical, and Petroleum Engineers.
Homke, S., Vergés, J., Serra-Kiel, J., Bernaola, G., Sharp, I., Garcés, M., Montero-Verdú, I., Karpuz, R., and Goodarzi, M. H., 2009, Late Cretaceous-Paleocene formation of the proto-Zagros

foreland basin, Lurestan Province, SW Iran: Society of America Bulletin, v. 121, no. 7-8, p. 963-978.

Hooper, R. J., Baron, I., Hatcher, R. D., and Agah, S., 1994, The development of the southern Tethyan margin in Iran after the break up of Gondwana: Implications of the Zagros hydrocarbon province: Geosciences, v. 4, p. 72-85.

Horton, B. K., Hassanzadeh, J., Stockli, D. F., Axen, G. J., Gillis, R. J., Guest, B., Amini, A., Fakhari, M. D., Zamanzadeh, S. M., and Grove, M., 2008, Detrital zircon provenance of Neoproterozoic to Cenozoic deposits in Iran: Implications for chronostratigraphy and collisional tectonics: Tectonophysics, v. 451, no. 1, p. 97-122.

Hosseinkhani, A., 2009, Geology, tectonomagmatic setting and evaluation of the economic potential of copper-gold mineralization in Chah-Mesi deposit (N of Shahr Babak)Unpublished MSc thesis]: Shahid Behesthi University.

Hurai, V., Huraiová, M., Slobodník, M., and Thomas, R., 2015, Geofluids: Developments in Microthermometry, Spectroscopy, Thermodynamics, and Stable Isotopes, Elsevier, 504 p.:

Jafarzadeh, A., Ghorbani, M., and Pezeshkpour, M., 1995, Iron deposits, geology of Iran, Teheran, Geological Survey of Iran (Persian book).

John, D. A., Ayuso, R. A., Barton, M. D., Blakely, R. J., Bodnar, R. J., Dilles, J. H., Gray, F., Graybeal, F. T., Mars, J. C., McPhee, D. K., Seal, R. R., Taylor, R. D., and Vikre, P. G., 2010, Porphyry copper deposit model, U.S. Geological Survey Scientific Investigations Report 2010–5070–B, 169 p.

John, D. A., Vikre, P. G., du Bray, E. A., Blakely, R. J., Fey, D. L., Rockwell, B. W., Mauk, J. L., Anderson, E. D., and Graybeal, F. T., 2018, Descriptive models for epithermal gold-silver deposits: Chapter Q in <Mineral deposit models for resource assessment, 2010-5070Q.

Johnson, N. E., Craig, J. R., and Rimstidt, J. D., 1986, Compositional trends in tetrahedrite: The Canadian Mineralogist, v. 24, no. 2, p. 385-397.

KAN Iran Consulting Engineers, 2006, Final report: Geological and alteration studies, Chah-Mesi, scale 1:1000 (in Farsi), Iran Mines and Mining Industries Development and Renovation Organization; National Iranian Copper Industries Company (Deputy of Planning and Development), p. 95.

Kharbish, S., Götzinger, M., and Beran, A., 2007, Compositional variations of fahlore group minerals from Austria: Austrian Journal of Earth Sciences, v. 100, p. 44-52.

Kokh, M. A., Akinfiev, N. N., Pokrovski, G. S., Salvi, S., and Guillaume, D., 2017, The role of carbon dioxide in the transport and fractionation of metals by geological fluids: Geochimica et Cosmochimica Acta, v. 197, p. 433-466.

Krismer, M., Vavtar, F., Tropper, P., Kaindl, R., and Sartory, B., 2011, The chemical composition of tetrahedrite-tennantite ores from the prehistoric and historic Schwaz and Brixlegg mining areas (North Tyrol, Austria), European Journal of Mineralogy, 925-936 p.:

Lowell, J. D., and Guilbert, J. M., 1970, Lateral and vertical alteration-mineralization zoning in porphyry ore deposits: Economic Geology, v. 65, no. 4, p. 373-408.

Luce, F. D., Tuttle, C. L., and Skinner, B. J., 1977, Studies of sulfosalts of copper; V, Phases and phase relations in the system Cu-Sb-As-S between 350 degrees and 500 degrees C: Economic Geology, v. 72, no. 2, p. 271-289.

Marushchenko, L. I., Baksheev, I. A., Nagornaya, E. V., Chitalin, A. F., Nikolaev, Y. N., and Vlasov, E. A., 2018, Compositional evolution of the tetrahedrite solid solution in porphyry-epithermal system: A case study of the Baimka Cu-Mo-Au trend, Chukchi Peninsula, Russia: Ore Geology Reviews, v. 103, p. 21-37.

Masoodi, M., Yassaghi, A., Nogole Sadat, M. A. A., Neubauer, F., Bernroider, M., Friedl, G., Genser, J., and Houshmandzadeh, A., 2013, Cimmerian evolution of the Central Iranian basement: Evidence from metamorphic units of the Kashmar–Kerman Tectonic Zone: Tectonophysics, v. 588, p. 189-208.

Mavrogonatos, C., Voudouris, P., Spry, P., Melfos, V., Klemme, S., Berndt, J., Baker, T., Moritz, R., Bissig, T., Monecke, T., and Zaccarini, F., 2018, Mineralogical Study of the Advanced Argillic Alteration Zone at the Konos Hill Mo-Cu-Re-Au Porphyry Prospect, NE Greece: Minerals, v. 8.

McInnes, B. I. A., Evans, N. J., Fu, F. Q., Garwin, S., Belousova, E., Griffin, W. L., Bertens, A., Sukarna, D., Permanadewi, S., Andrew, R. L., and Deckart, K., 2005, Thermal history analysis of selected

Chilean, Indonesian and Iranian Porphyry Cu-Mo-Au deposits., *in* Porter, T. M., ed., Super porphyry copper and gold deposits: a global perspective: Adelaide, PGC publishing, p. 1-16.

Meyer, C., and Hemley, J. J., 1967, Wall rock alteration, *in* Barnes, H. L., ed., Geochemistry of hydrothermal ore deposits: New York, Holt Rinehart & Winston, p. 166-235.

Mirzaie, A., Bafti, S. S., and Derakhshani, R., 2015, Fault control on Cu mineralization in the Kerman porphyry copper belt, SE Iran: A fractal analysis: Ore Geology Reviews, v. 71, p. 237-247.

Mohajjel, M., and Fergusson, C. L., 2014, Jurassic to Cenozoic tectonics of the Zagros Orogen in northwestern Iran: International Geology Review, v. 56, no. 3, p. 263-287.

Mohajjel, M., Fergusson, C. L., and Sahandi, M. R., 2003, Cretaceous–Tertiary convergence and continental collision, Sanandaj–Sirjan Zone, western Iran: Journal of Asian Earth Sciences, v. 21, no. 4, p. 397-412.

Molinaro, M., Zeyen, H., and Laurencin, X., 2005, Lithospheric structure beneath the south-eastern Zagros Mountains, Iran: recent slab break-off?: Terra Nova, v. 17, no. 1, p. 1-6.

Momenzadeh, M., and Walther, H. W., 1984, Mineral Deposits and Metallogenic Epochs in the Area of the Geotraverse Across Iran - a Review: N. Jb. Geol. Paläont. Abh., v. 168, no. 2/3, p. 468-478.

Mouthereau, F., Lacombe, O., and Vergés, J., 2012, Building the Zagros collisional orogen: Timing, strain distribution and the dynamics of Arabia/Eurasia Plate convergence, Tectonophysics, 27–60 p.:

Muntean, J. L., and Einaudi, M. T., 2001, Porphyry-Epithermal Transition: Maricunga Belt, Northern Chile: Economic Geology, v. 96, no. 4, p. 743-772.

Muttoni, G., Mattei, M., Balini, M., Zanchi, A., Gaetani, M., and Berra, F., 2009, The drift history of Iran from the Ordovician to the Triassic, *in* Brunet, M. F., Wilmsen, M., and Granath, J. W., eds., South Caspian to Central Iran Basins, Volume 312, Geological Society of London, p. 0.

Nabatian, G., Rastad, E., Neubauer, F., Honarmand, M., and Ghaderi, M., 2015, Iron and Fe–Mn mineralisation in Iran: implications for Tethyan metallogeny: Australian Journal of Earth Sciences, v. 62, no. 2, p. 211-241.

Nabavi, M. H., 1976, An introduction to geology of Iran, Tehran, Geological Survey of Iran.

National Iranian Copper Industries Company, 2012, National Iranian Copper Industries Company: International Copper Study Group Meeting, 39th, Lisbon, Portugal, April 25-27, 2012.

Omaljev, V., 1972, Report on exploration of Chah-Mesi copper deposit, Report no. 43/Yu, Iran, Geological Survey of Iran.

Omrani, J., Agard, P., Whitechurch, H., Benoit, M., Prouteau, G., and Jolivet, L., 2008, Arc-magmatism and subduction history beneath the Zagros Mountains, Iran: A new report of adakites and geodynamic consequences: Lithos, v. 106, no. 3–4, p. 380-398.

Padyar, F., Rahgoshay, M., Alirezaei, S., Tarantola, A., Vanderhaeghe, O., and Caumon, M. C., 2017, Evolution of the Mineralizing Fluids and Possible Genetic Links between Miduk Porphyry Copper and Latala Vein Type Deposits, Kerman Copper Belt, South Iran: Journal Geological Society of India, v. 90, p. 558-568.

Pang, K.-N., Chung, S.-L., Zarrinkoub, M. H., Mohammadi, S. S., Yang, H.-M., Chu, C.-H., Lee, H.-Y., and Lo, C.-H., 2012, Age, geochemical characteristics and petrogenesis of Late Cenozoic intraplate alkali basalts in the Lut–Sistan region, eastern Iran: Chemical Geology, v. 306-307, p. 40-53.

Perelló, J., Razique, A., Schloderer, J., and Asad-ur-Rehman, 2008, The Chagai Porphyry Copper Belt, Baluchistan Province, Pakistan: Economic Geology, v. 103, no. 8, p. 1583-1612.

Pirajno, F., 1992, Hydrothermal Mineral Deposits: Principles and Fundamental Concepts for the Exploration Geologist, Springer-Verlag Berlin Heidelberg, 709 p.:

-, 2009, Hydrothermal Processes and Mineral Systems, Springer Netherlands, 1250 p.:

Plotinskaya, O. Y., Grabezhev, A. I., and Seltmann, R., 2015, Fahlores compositional zoning in a porphyry-epithermal system: Biksizak occurrence, South Urals, Russia as an example: Geology of Ore Deposits, v. 57, no. 1, p. 42-63.

Pohl, W., 2011, Economic Geology Principles and Practice: Metals, Minerals, Coal and Hydrocarbons – Introduction to Formation and Sustainable Exploitation of Mineral Deposits, Chicester, United Kingdom, John Wiley and Sons Ltd, 663 p.:

Pudack, C., Halter, W. E., Heinrich, C. A., and Pettke, T., 2009, Evolution of Magmatic Vapor to Gold-Rich Epithermal Liquid: The Porphyry to Epithermal Transition at Nevados de Famatina, Northwest Argentina: Economic Geology, v. 104, no. 4, p. 449-477.

Rahmati-Ilkhchi, M., 2009, Metamorphism and Geotectonic Position of the Shotur Kuh Complex, Central Iranian Block [Ph.D. dissertation]: Charles University, 119 p.

Ramdohr, P., 1969, The ore minerals and their intergrowths, Oxford, Pergamon Press, International series of monographs in earth sciences, XVI, 1174 p.:

Regard, V., Bellier, O., Thomas, J. C., Bourlès, D., Bonnet, S., Abbassi, M. R., Braucher, R., Mercier, J., Shabanian, E., Soleymani, S., and Feghhi, K., 2005, Cumulative right-lateral fault slip rate across the Zagros—Makran transfer zone: role of the Minab—Zendan fault system in accommodating Arabia—Eurasia convergence in southeast Iran: Geophysical Journal International, v. 162, no. 1, p. 177-203.

Richards, J. P., 2005, Cumulative factors in the generation of giant calc-alkaline porphyry Cu deposits, *in* Porter, T. M., ed., Super porphyry copper and gold deposits: A global perspective, Volume 1: Adelaide, PGC Publishing, p. 7-25.

-, 2009, Postsubduction porphyry Cu-Au and epithermal Au deposits: Products of remelting of subduction-modified lithosphere: Geology, v. 37, no. 3, p. 247-250.

-, 2015, Tectonic, magmatic, and metallogenic evolution of the Tethyan orogen; from subduction to collision: Ore Geology Reviews, v. 70, p. 323-345.

Richards, J. P., Spell, T., Rameh, E., Razique, A., and Fletcher, T., 2012, High Sr/Y magmas reflect arc maturity, high magmatic water content, and porphyry Cu+ or -Mo+ or -Au potential; examples from the Tethyan arcs of central and eastern Iran and western Pakistan: Economic Geology and the Bulletin of the Society of Economic Geologists, v. 107, no. 2, p. 295-332.

Rinne, M. L., 2015, Geology, alteration, and mineralisation of the Golpu Porphyry and Wafi Epithermal deposit, Morobe Province, Papua New Guinea [PhD thesis]: University of Tasmania, 255 p.

Rinne, M. L., Cooke, D. R., Harris, A. C., Finn, D. J., Allen, C. M., Heizler, M. T., and Creaser, R. A., 2018, Geology and Geochronology of the Golpu Porphyry and Wafi Epithermal Deposit, Morobe Province, Papua New Guinea: Economic Geology, v. 113, no. 1, p. 271-294.

Robert, A. M. M., Letouzey, J., Kavoosi, M. A., Sherkati, S., Müller, C., Vergés, J., and Aghababaei, A., 2014, Structural evolution of the Kopeh Dagh fold-and-thrust belt (NE Iran) and interactions with the South Caspian Sea Basin and Amu Darya Basin: Marine and Petroleum Geology, v. 57, p. 68-87.

Roedder, E., 1984, Fluid Inclusions, Washington D.C., Mineralogical Society of America, Reviews in Mineralogy, v. 12, 644 p.:

Sack, R. O., Lynch, J. V. G., and Foit, F., 2003, Fahlore as a petrogenetic indicator: Keno Hill Ag-Pb-Zn District, Yukon, Canada, Mineralogical Magazine, Volume 67, p. 1023.

Sadeghi, M., Borg, G., and Cornelia, G., 2008, Relationship between large-scale ring structures and lineaments with big porphyry copper deposits in Iran: Geosciences, v. 17, no. 1, p. 199-205.

Samani, B., 1998, Distribution, Setting and Metallogenesis of Copper Deposits in Iran, *in* Porter, T. M., ed., Porphyry and Hdrothermal Copper and Gold Deposits: A Global Perspective: Adelaide, PGC Publishing, p. 151-174.

Saric, A., Djordjevic, M., and Dimitrijevic, M. N., 1971, Geological map of Shahr-Babak, Scale 1:100.000, Teheran, Iran, Geological Survey of Iran.

Scotese, C. R., 2007, Atlas of Earth History, Paleogeography, Volume 1, University of Texas at Arlington. Department of Geology. PALEOMAP Project, p. 52.

Seedorff, E., Dilles, J. H., Proffett, J. M., Jr., Einaudi, M. T., Zurcher, L., Stavast, W. J. A., Johnson, D. A., and Barton, M. D., 2005, Porphyry deposits; characteristics and origin of hypogene features, *in* Hedenquist, J. W., Thompson, J. F. H., Goldfarb, R. J., and Richards, J. P., eds., Economic Geology One Hundreth Anniversary Volume 1905-2005: Liitleton, CO, Society of Economic Geologists, Littleton, CO, p. 251-298.

Severin, K. P., 2004, Energy Dispersive Spectrometry of Common Rock Forming Minerals, Dordrecht, Kluwer Academic Publishers, IX, 225 p.:

Shafiei, B., 2008, Metallogenic model of Kerman orphyry copper belt and its exploratory approaches, Unpublished Ph.D. thesis: Iran, Shaheed Bahonar University of Kerman, p. 257.

Shafiei, B., Haschke, M., and Shahabpour, J., 2009, Recycling of orogenic arc crust triggers porphyry Cu mineralization in Kerman Cenozoic arc rocks, southeastern Iran: Mineralium Deposita, v. 44, no. 3, p. 265.

Shafiei, S., and Ghiyasi, M., 2014, Analysis of Structural Control on Chahmesi Deposit, Miduke Area, SE Iran: Scientific Quaterly Journal, GEOSCIENCES, v. 23, no. 92, p. 177 - 186.

Shahabpour, J., 2007, Island-arc affinity of the Central Iranian Volcanic Belt: Journal of Asian Earth Sciences, v. 30, p. 652-665.

Shahabpour, J., and Kramers, J. D., 1987, Lead isotope data from the Sar-Cheshmeh porphyry copper deposit, Iran: Mineralium Deposita, v. 22, no. 4, p. 278-281.

Shimizu, T., 2014, Reinterpretation of Quartz Textures in Terms of Hydrothermal Fluid Evolution at the Koryu Au-Ag Deposit, Japan: Economic Geology, v. 109, no. 7, p. 2051-2065.

Shimizu, T., Matsueda, H., Ishiyama, D., and Matsubaya, O., 1998, Genesis of epithermal Au-Ag mineralization of the Koryu Mine, Hokkaido, Japan: Economic Geology, v. 93, no. 3, p. 303-325.

Shinohara, H., and Hedenquist, J. W., 1997, Constraints on Magma Degassing beneath the Far Southeast Porphyry Cu–Au Deposit, Philippines: Journal of Petrology, v. 38, no. 12, p. 1741-1752.

Shore, M., and Fowler, A. D., 1996, Oscillatory zoning in minerals; a common phenomenon: The Canadian Mineralogist, v. 34, no. 6, p. 1111-1126.

Sillitoe, R. H., 2000, Gold-Rich Porphyry Deposits: Descriptive and Genetic Models and Their Role in Exploration and Discovery, *in* Hagemann, S. G., and Brown, P. E., eds., Gold in 2000, Volume 13, Society of Economic Geologists, p. 315-345.

-, 2008, Special Paper: Major Gold Deposits and Belts of the North and South American Cordillera: Distribution, Tectonomagmatic Settings, and Metallogenic Considerations: Economic Geology, v. 103, no. 4, p. 663-687.

-, 2010, Porphyry Copper Systems: Economic Geology, v. 105, no. 1, p. 3-41.

Sillitoe, R. H., and Hedenquist, J. W., 2003, Linkages between volcanotectonic settings, ore-fluid compositions, and epithermal precious-metal deposits, Society of Economic Geologists: Special Publication, 315-343 p.:

Singer, D. A., Berger, V. I., and Moring, B. C., 2008, Porphyry copper deposits of the world; database and grade and tonnage models, 2008: Open-File Report - U. S. Geological Survey, p. 45.

Stampfli, G. M., and Borel, G. D., 2002, A plate tectonic model for the Paleozoic and Mesozoic constrained by dynamic plate boundaries and restored synthetic oceanic isochrons: Earth and Planetary Science Letters, v. 196, p. 17-33.

Stampfli, G. M., and Borel, G. D., 2004, The TRANSMED Transects in Space and Time: Constraints on the Paleotectonic Evolution of the Mediterranean Domain, *in* Cavazza, W., Roure, F., Spakman, W., Stampfli, G. M., and Ziegler, P. A., eds., The TRANSMED Atlas. The Mediterranean Region from Crust to Mantle: Geological and Geophysical Framework of the Mediterranean and the Surrounding Areas: Berlin, Heidelberg, Springer Berlin Heidelberg, p. 53-80.

Stampfli, G. M., and Kozur, H. W., 2006, Europe from the Variscan to the Alpine cycles, *in* Gee, D. G., and Stephenson, R. A., eds., European lithosphere dynamics, Volume 32: London, Geological Society of London, p. 57-82.

Stöcklin, J., 1974a, Northern Iran: Alborz Mountains: Geological Society, London, Special Publications, v. 4, no. 1, p. 213.

-, 1974b, Possible Ancient Continental Margins in Iran, *in* Burk, C. A., and Drake, C. L., eds., The Geology of Continental Margins: Berlin, Heidelberg, Springer Berlin Heidelberg, p. 873-887.

-, 1977, Structural correlation of the alpine ranges between Iran and Central Asia: Mémoires hors Série de la Société Géologique de France, v. 8, p. 333-353.

Stöcklin, J., and Nabavi, M. H., 1973, Tectonic Map of Iran, scale 1:2.500.000, *in* Iran, G. S., ed., report no. 31, Tehran Offset Press, p. 100.

Stoffregen, R. E., 1987, Genesis of acid-sulfate alteration and Au-Cu-Ag mineralization at Summitville, Colorado: Economic Geology, v. 82, no. 6, p. 1575-1591.

Taghipour, N., Aftabi, A., and Mathur, R., 2008, Geology and Re-Os geochronology of mineralization of the Miduk porphyry copper deposit, Iran: Resource Geology (Tokyo. 1998), v. 58, no. 2, p. 143-160.

Takin, M., 1972, Iranian Geology and Continental Drift in the Middle East: Nature, v. 235, no. 5334, p. 147-150.

Tangestani, M. H., and Moore, F., 2002, The use of Dempster–Shafer model and GIS in integration of geoscientific data for porphyry copper potential mapping, north of Shahr-e-Babak, Iran: International Journal of Applied Earth Observation and Geoinformation, v. 4, no. 1, p. 65-74.

Thompson, A. J. B., and Thompson, J. F. H., 1996, Atlas of alteration : a field and petrographic guide to hydrothermal alteration minerals: St. John's, Nfld., Geological Association of Canada, Mineral Deposits Division.

Vassileva, R., Atanassova, R., and Kouzmanov, K., 2014, Tennantite-tetrahedrite series from the Madan Pb-Zn deposits, Central Rhodopes, Bulgaria: Mineralogy and Petrology, v. 108, p. 515-531.

Verdel, C., Wernicke, B. P., Hassanzadeh, J., and Guest, B., 2011, A Paleogene extensional arc flare-up in Iran: Tectonics, v. 30, no. 3.

von Raumer, J., Stampfli, G. M., Borel, G., and Bussy, F., 2002, Organization of pre-Variscan basement areas at the north-Gondwanan margin: International Journal of Earth Sciences, v. 91, no. 1, p. 35-52.

Wang, L., Qin, K., Song, G., and Li, G., 2019, A review of intermediate sulfidation epithermal deposits and subclassification, v. 107, p. 434-456.

Waterman, G. C., and Hamilton, R. L., 1975, The Sar Cheshmeh porphyry copper deposit: Economic Geology and the Bulletin of the Society of Economic Geologists, v. 70, no. 3, p. 568-576.

White, R. S., 1982, Deformation of the Makran accretionary sediment prism in the Gulf of Oman (north-west Indian Ocean): Geological Society, London, Special Publications, v. 10, no. 1, p. 357.

Wilkinson, J. J., 2001, Fluid inclusions in hydrothermal ore deposits: Lithos, v. 55, p. 229-272.

Zarasvandi, A., Liaghat, S., and Zentilli, M., 2005, Geology of the Darreh-Zerreshk and Ali-Abad porphyry copper deposits, central Iran: International Geology Review, v. 47, no. 6, p. 620-646.

Zarasvandi, A., Rezaei, M., Sadeghi, M., Lentz, D., Adelpour, M., and Pourkaseb, H., 2015, Rare earth element signatures of economic and sub-economic porphyry copper systems in Urumieh-Dokhtar magmatic arc (UDMA), Iran: Ore Geology Reviews, v. 70, p. 407-423.

Zuercher, L., Bookstrom, A. A., Hammarstrom, J. M., Mars, J. C., Ludington, S., Zientek, M. L., Dunlap, P., Wallis, J. C., Drew, L. J., Sutphin, D. M., Berger, B. R., Herrington, R. J., Billa, M., Kuscu, I., Moon, C. J., and Richards, J. P., 2015, Porphyry copper assessment of the Tethys region of western and southern Asia: Scientific Investigations Report, p. 232.

Appendices

I. List of mineral abbreviations and formulas

amph	amphibole	$AX_2Z_5((Si,Al,Ti)_8O_{22})(OH,F,Cl,O)_2$ A = □, Na, K, Ca, Pb^{2+} X = Li, Na, Mg, Fe^{2+}, Mn^{2+}, Ca Z = Li, Na, Mg, Fe^{2+}, Mn^{2+}, Zn, Co, Ni, Al, Fe^{3+}, Cr^{3+}, Mn^{3+}, V^{3+}, Ti, Zr
ap	apatite	$Ca_5(PO_4)_3(Cl/F/OH)$
ba	barite	$BaSO_4$
benleo	benleonardite	$[Ag_6(Sb,As)_2S_6Te]$ $[Ag_9Cu(S,Te)_2Te_2]$
bn	bornite	Cu_5FeS_4
bt	biotite	$K(Fe^{2+}/Mg)_2(Al/Fe^{3+}/Mg)([Si/Al]Si_2O_{10})(OH/F)_2$
cal	calcite	$CaCO_3$
carb	carbonate	minerals incl. CO_3^{2+}
cc	chalcocite	Cu_2S
ccp	chalcopyrite	$CuFeS_2$
chc	chalcedony	SiO_2
cov	covellite	CuS
czo	clinozoisite	$\{Ca_2\}\{Al_3\}(Si_2O_7)(SiO_4)O(OH)$
enr	enargite	Cu_3AsS_4 (orthorhombic)
ep	epidote	$\{Ca_2\}\{Al_2Fe^{3+}\}(Si_2O_7)(SiO_4)O(OH)$
fh	fahlore	td-tn solid solution
fl	fluorite	CaF_2
fm	famatinite	Cu_3SbS_4
gn	galena	PbS
gr	geerite	Cu_8S_5
hm	hematite	Fe_2O_3
jalp	jalpaite	Ag_3CuS_2
luz	luzonite	Cu_3AsS_4 (tetragonal)
mag	magnetite	$Fe^{2+}Fe^{3+}{}_2O_4$
mo	molybdenite	MoS_2
pbgm	plumbogummite	$PbAl_3(PO_4)(PO_3OH)(OH)_6$
pearc	pearceite	$[Ag_9CuS_4][(Ag,Cu)_6(As,Sb)_2S_7]$
plag	plagioclase	$Na(AlSi_3O_8)$ to $Ca(Al_2Si_2O_8)$
po	pyrrhotite	Fe_{1-x} (x = 0 to 0.17)
prh	prehnite	$Ca_2Al_2Si_3O_{10}(OH)_2$
px	pyroxene	$XY(Si,Al)_2O_6$ X = Li, Na, Mg, Fe^{2+}, Mn^{2+}, Ca Y = Mg, Fe^{2+}, Mn, Zn, Co, Ni, Al, Fe^{3+}, Cr^{3+}, V^{3+}, Ti, Zr
py	pyrite	FeS_2
qz	quartz	SiO_2
rt	rutile	TiO_2
ser	sericite	$KAl_2(AlSi_3O_{10})(OH)_2$
sp	sphalerite	ZnS
spk	spionkopite	$Cu_{39}S_{28}$
td	tetrahedrite	$Cu_6Cu_4(Fe^{2+},Zn)_2Sb_4S_{12}S$
tn	tennantite	$Cu_6Cu_4(Fe^{2+},Zn)_2As_4S_{12}S$
yr	yarrowite	Cu_9S_8

II. EPMA data of the studied sulfides and sulfosalts

CHM1-44

	Cu		Ag		Fe		Zn		total apfu	As		Sb		total apfu	S		total apfu	total wt%	Sb/(As+Sb)	
	wt%	*apfu*	wt%	*apfu*	wt%	*apfu*	wt%	*apfu*		wt%	*apfu*	wt%	*apfu*		wt%	*apfu*				Mineral
an1	21.49	7.37	50.82	10.27	0.58	0.23	0.01	0.00	17.88	6.76	1.97	0.69	0.12	2.09	19.11	13.00	32.97	99.45	0.059	pearc
an2	20.64	7.27	52.54	10.90	1.00	0.40	0.00	0.00	18.58	6.53	1.95	0.53	0.10	2.05	18.62	13.00	33.62	99.85	0.047	pearc
an3	34.45	0.99	0.03	0.00	31.02	1.02	0.05	0.00	2.01	0.00	0.00	0.00	0.00	0.00	34.98	2.00	4.01	100.53		ccp
an4	48.27	2.99	0.17	0.01	0.44	0.03	0.03	0.00	3.03	17.44	0.92	0.44	0.01	0.93	32.54	4.00	7.96	99.32	0.015	enr

CHM1-59

	Cu		Ag		Fe		Zn		total apfu	As		Sb		total apfu	S		total apfu	total wt%	Sb/(As+Sb)	
	wt%	*apfu*	wt%	*apfu*	wt%	*apfu*	wt%	*apfu*		wt%	*apfu*	wt%	*apfu*		wt%	*apfu*				Mineral
an1	39.72	9.98	0.25	0.04	2.83	0.81	8.29	2.02	12.85	7.98	1.70	17.52	2.30	4.00	26.11	13.00	29.85	102.70	0.575	As-td
an2	39.74	9.95	0.21	0.03	1.86	0.53	8.09	1.97	12.48	7.02	1.49	18.72	2.45	3.94	26.19	13.00	29.42	101.83	0.621	As-td
an3	40.06	10.06	0.21	0.03	1.96	0.56	8.12	1.98	12.64	7.78	1.66	17.75	2.33	3.98	26.12	13.00	29.62	102.01	0.584	As-td
an4	47.57	2.96	0.14	0.01	1.65	0.12	0.07	0.00	3.08	17.38	0.92	1.88	0.06	0.98	32.45	4.00	8.06	101.13	0.062	enr
an5	47.90	2.96	0.17	0.01	1.65	0.12	0.02	0.00	3.08	17.57	0.92	1.04	0.03	0.95	32.69	4.00	8.04	101.06	0.035	enr
an6	48.01	3.02	0.21	0.01	1.31	0.09	0.04	0.00	3.13	17.15	0.92	2.14	0.07	0.99	32.05	4.00	8.11	100.91	0.071	enr
an7	40.21	10.08	0.23	0.03	2.02	0.58	7.71	1.88	12.57	7.38	1.57	18.39	2.41	3.97	26.17	13.00	29.54	102.12	0.605	As-td
an8	49.05	3.05	0.13	0.00	0.85	0.06	0.05	0.00	3.12	17.97	0.95	0.96	0.03	0.98	32.48	4.00	8.09	101.49	0.032	enr
an9	49.41	3.08	0.11	0.00	0.75	0.05	0.06	0.00	3.14	17.67	0.93	1.07	0.03	0.97	32.38	4.00	8.11	101.44	0.036	enr
an10	46.87	2.98	0.15	0.01	2.02	0.15	0.26	0.02	3.15	16.68	0.90	3.14	0.10	1.00	31.73	4.00	8.15	100.84	0.104	luz
an11	45.94	2.97	0.10	0.00	1.74	0.13	0.11	0.01	3.11	11.05	0.61	10.87	0.37	0.97	31.25	4.00	8.08	101.05	0.377	luz
an12	47.34	2.97	0.18	0.01	1.17	0.08	0.07	0.00	3.06	17.85	0.95	0.75	0.02	0.97	32.19	4.00	8.04	99.54	0.025	enr
an13	38.67	9.51	0.20	0.03	6.30	1.76	6.92	1.65	12.96	7.50	1.57	15.34	1.97	3.53	26.67	13.00	29.49	101.61	0.557	As-td
an14	47.36	2.97	0.13	0.00	2.14	0.15	0.02	0.00	3.13	18.20	0.97	0.47	0.02	0.98	32.21	4.00	8.11	100.54	0.016	enr
an15	47.10	2.90	0.17	0.01	2.08	0.15	0.03	0.00	3.05	18.44	0.96	0.22	0.01	0.97	32.77	4.00	8.02	100.80	0.007	enr
an16	40.96	10.23	0.24	0.04	2.34	0.66	8.25	2.00	12.93	9.91	2.10	14.56	1.90	4.00	26.27	13.00	29.92	102.53	0.475	Sb-tn
an17	47.60	3.04	0.17	0.01	1.52	0.11	0.07	0.00	3.16	14.79	0.80	5.78	0.19	0.99	31.62	4.00	8.15	101.55	0.194	luz
an18	46.12	2.98	0.16	0.01	1.93	0.14	0.09	0.01	3.14	12.12	0.66	8.32	0.28	0.95	31.21	4.00	8.08	99.95	0.297	luz
an19	40.25	10.06	0.16	0.02	1.44	0.41	8.25	2.00	12.50	8.27	1.75	16.01	2.09	3.84	26.24	13.00	29.34	100.61	0.544	As-td
an20	47.62	3.01	0.16	0.01	1.27	0.09	0.42	0.03	3.13	16.59	0.89	3.11	0.10	0.99	31.95	4.00	8.12	101.13	0.104	luz
an21	47.91	3.02	0.14	0.01	1.41	0.10	0.04	0.00	3.13	17.16	0.92	1.89	0.06	0.98	32.02	4.00	8.11	100.58	0.064	enr
an22	41.44	10.16	0.22	0.03	1.27	0.35	8.43	2.01	12.56	9.97	2.07	13.18	1.69	3.76	26.74	13.00	29.32	101.25	0.449	Sb-tn
an23	40.31	10.16	0.32	0.05	1.28	0.37	8.28	2.03	12.60	7.72	1.65	17.89	2.35	4.00	26.03	13.00	29.60	101.83	0.588	As-td
an24	38.97	9.83	0.26	0.04	2.66	0.76	7.87	1.93	12.55	8.54	1.83	16.93	2.23	4.05	26.01	13.00	29.61	101.23	0.550	As-td
an25	41.46	9.66	0.18	0.02	4.17	1.11	7.75	1.76	12.55	15.57	3.08	2.65	0.32	3.40	28.14	13.00	28.95	99.92	0.095	Sb-tn
an26	41.39	9.50	0.23	0.03	5.60	1.46	5.60	1.25	12.24	7.36	1.43	13.61	1.63	3.06	28.58	13.00	28.30	102.37	0.532	As-td
an27	41.69	10.06	0.15	0.02	1.06	0.29	7.64	1.79	12.16	12.97	2.65	9.54	1.20	3.86	27.19	13.00	29.02	100.24	0.312	Sb-tn
an28	40.82	9.94	0.18	0.03	2.49	0.69	8.03	1.90	12.55	9.24	1.91	14.77	1.88	3.79	26.94	13.00	29.34	102.47	0.496	Sb-tn
an29	42.83	9.96	0.09	0.01	3.30	0.87	6.10	1.38	12.23	19.82	3.91	0.14	0.02	3.93	28.20	13.00	29.15	100.47	0.004	tn
an30	40.86	10.12	0.20	0.03	0.92	0.26	8.22	1.98	12.38	9.95	2.09	14.32	1.85	3.94	26.50	13.00	29.32	100.95	0.470	Sb-tn
an31	41.39	10.22	0.15	0.02	0.92	0.26	8.40	2.02	12.52	10.32	2.16	13.62	1.76	3.92	26.56	13.00	29.44	101.36	0.448	Sb-tn
an32	42.47	9.93	0.14	0.02	1.33	0.35	8.71	1.98	12.28	16.39	3.25	3.95	0.48	3.73	28.06	13.00	29.01	101.06	0.129	Sb-tn
an33	41.03	10.16	0.20	0.03	1.56	0.44	8.26	1.99	12.61	11.20	2.35	12.37	1.60	3.95	26.50	13.00	29.56	101.11	0.405	Sb-tn
an34	40.28	10.11	0.19	0.03	1.42	0.41	8.26	2.01	12.55	7.33	1.56	18.61	2.44	3.99	26.15	13.00	29.55	102.24	0.610	As-td
an35	40.68	10.26	0.17	0.03	0.98	0.28	8.19	2.01	12.57	6.91	1.48	19.31	2.54	4.02	26.01	13.00	29.59	102.25	0.632	As-td
an36	41.41	10.16	0.20	0.03	1.96	0.55	7.40	1.76	12.50	12.77	2.66	10.22	1.31	3.96	26.74	13.00	29.46	100.69	0.330	Sb-tn
an37	41.28	9.92	0.18	0.02	2.06	0.56	8.13	1.90	12.41	13.46	2.74	8.91	1.12	3.86	27.29	13.00	29.27	101.32	0.289	Sb-tn
an38	40.80	9.99	0.15	0.02	0.57	0.16	8.20	1.95	12.12	9.18	1.91	14.31	1.83	3.74	26.79	13.00	28.86	100.00	0.490	Sb-tn
an39	42.17	10.12	0.14	0.02	1.82	0.50	8.01	1.87	12.51	16.40	3.34	5.20	0.65	3.99	27.32	13.00	29.50	101.06	0.163	Sb-tn
an40	40.59	10.06	0.09	0.01	1.03	0.29	8.52	2.05	12.41	9.34	1.96	15.46	2.00	3.96	26.47	13.00	29.37	101.50	0.505	As-td
an41	40.65	10.19	0.12	0.02	0.84	0.24	8.31	2.02	12.47	6.71	1.43	19.40	2.54	3.97	26.17	13.00	29.44	102.20	0.640	As-td
an42	42.65	9.96	0.13	0.02	1.86	0.49	8.73	1.98	12.46	18.63	3.69	1.61	0.20	3.89	28.08	13.00	29.34	101.69	0.051	Sb-tn
an43	39.88	10.18	0.14	0.02	1.06	0.31	8.21	2.04	12.55	5.37	1.16	21.91	2.92	4.08	25.69	13.00	29.63	102.26	0.715	As-td
an44	40.03	10.07	0.13	0.02	1.86	0.53	8.45	2.06	12.69	8.15	1.74	17.54	2.30	4.04	26.07	13.00	29.73	102.22	0.570	As-td
an45	43.73	10.34	0.15	0.02	1.17	0.31	8.20	1.89	12.56	18.14	3.64	1.90	0.23	3.87	27.73	13.00	29.44	101.02	0.060	Sb-tn
an46	42.64	10.35	0.19	0.03	0.76	0.21	8.12	1.91	12.50	14.00	2.88	9.47	1.20	4.08	27.02	13.00	29.59	102.19	0.294	Sb-tn
an47	42.37	10.31	0.14	0.02	0.92	0.26	8.72	2.06	12.64	13.37	2.76	9.25	1.17	3.93	26.97	13.00	29.57	101.74	0.299	Sb-tn
an48	40.12	10.14	0.14	0.02	1.17	0.34	7.94	1.95	12.45	5.05	1.08	21.76	2.87	3.95	25.95	13.00	29.40	102.12	0.726	As-td
an49	40.34	10.05	0.15	0.02	0.53	0.15	8.21	1.99	12.22	9.20	1.94	15.18	1.97	3.92	26.32	13.00	29.13	99.92	0.504	As-td
an50	43.03	9.92	0.10	0.01	1.38	0.36	7.69	1.72	12.02	19.70	3.85	0.25	0.03	3.88	28.46	13.00	28.90	100.62	0.008	tn
an51	64.37	5.10	0.34	0.02	10.61	0.96	3.36	0.26	6.32	0.00	0.00	0.00	0.00	0.00	25.50	4.00	10.32	104.17		bn

CHM2-39.5(1)

	Cu		Ag		Fe		Zn		total apfu	As		Sb		total apfu	S		total apfu	total wt%	Sb/(As+Sb)	
	wt%	*apfu*	wt%	*apfu*	wt%	*apfu*	wt%	*apfu*		wt%	*apfu*	wt%	*apfu*		wt%	*apfu*				Mineral
an1	38.85	9.89	1.18	0.18	1.82	0.53	7.76	1.92	12.51	6.25	1.35	19.76	2.62	3.97	25.77	13.00	29.48	101.38	0.661	As-td
an2	38.57	10.03	1.36	0.21	2.86	0.85	6.54	1.65	12.74	4.58	1.01	22.26	3.02	4.03	25.22	13.00	29.78	101.39	0.750	As-td
an3	33.73	1.01	0.14	0.00	31.88	1.09	0.06	0.00	2.11	0.00	0.00	0.00	0.00	0.00	33.54	2.00	4.11	99.35		ccp
an4	34.06	1.01	0.19	0.00	31.78	1.07	0.07	0.00	2.09	0.00	0.00	0.00	0.00	0.00	33.98	2.00	4.09	100.07		ccp
an5	35.23	9.33	7.96	1.24	2.03	0.61	6.79	1.75	12.93	5.02	1.13	17.80	2.46	3.59	24.76	13.00	29.52	99.58	0.686	As-td
an6	37.89	9.60	1.22	0.18	1.99	0.57	6.81	1.68	12.04	6.46	1.39	19.80	2.62	4.01	25.88	13.00	29.05	100.05	0.653	As-td
an7	36.51	9.40	4.70	0.71	1.70	0.50	7.39	1.85	12.45	6.27	1.37	17.91	2.41	3.77	25.49	13.00	29.23	99.96	0.638	As-td
an8	33.75	1.01	0.73	0.01	30.32	1.03	0.10	0.00	2.06	0.00	0.00	0.00	0.00	0.00	33.75	2.00	4.06	98.64		ccp
an9	39.48	10.04	0.35	0.05	1.07	0.31	7.84	1.94	12.34	5.27	1.14	21.66	2.87	4.01	25.80	13.00	29.35	101.46	0.717	As-td
an10	39.10	10.11	0.46	0.07	1.23	0.36	8.00	2.01	12.55	5.20	1.14	21.68	2.93	4.07	25.36	13.00	29.62	101.04	0.719	As-td
an11	39.48	10.01	0.61	0.09	0.80	0.23	8.22	2.02	12.35	5.38	1.16	21.40	2.83	3.99	25.89	13.00	29.34	101.78	0.710	As-td
an12	33.86	9.30	10.94	1.77	1.13	0.35	6.67	1.78	13.20	3.32	0.77	19.04	2.73	3.50	23.89	13.00	29.70	98.85	0.779	As-td
an13	38.53	10.02	0.48	0.07	1.99	0.59	7.39	1.87	12.55	2.05	0.45	26.97	3.66	4.11	25.23	13.00	29.66	102.63	0.890	As-td
an14	38.90	9.88	0.31	0.05	0.73	0.21	7.60	1.88	12.01	5.00	1.08	21.66	2.87	3.95	25.82	13.00	28.96	100.02	0.727	As-td
an15	38.98	9.92	0.28	0.04	1.06	0.31	7.59	1.88	12.14	4.93	1.06	21.85	2.90	3.96	25.78	13.00	29.11	100.46	0.732	As-td
an16	38.45	9.83	0.40	0.06	2.10	0.61	7.69	1.91	12.41	4.82	1.04	22.65	3.02	4.07	25.67	13.00	29.47	101.77	0.743	As-td
an17	38.63	9.38	0.60	0.09	1.11	0.31	8.22	1.94	11.71	5.62	1.16	19.67	2.49	3.65	27.03	13.00	28.35	100.88	0.683	As-td
an18	38.29	9.73	0.91	0.14	1.65	0.48	6.92	1.71	12.05	4.97	1.07	22.31	2.96	4.03	25.83	13.00	29.07	100.87	0.734	As-td
an19	39.26	10.00	0.51	0.08	0.98	0.28	7.98	1.98	12.34	4.55	0.98	22.33	2.97	3.95	25.75	13.00	29.29	101.36	0.751	As-td
an20	38.71	9.89	0.90	0.14	1.60	0.46	7.52	1.87	12.36	4.84	1.05	21.77	2.90	3.95	25.67	13.00	29.31	101.00	0.735	As-td
an21	38.57	9.75	0.61	0.09	1.41	0.41	7.87	1.93	12.17	4.59	0.98	22.48	2.97	3.95	25.96	13.00	29.13	101.49	0.751	As-td
an22	38.41	9.70	0.34	0.05	2.82	0.81	7.42	1.82	12.38	6.46	1.38	19.43	2.56	3.94	25.97	13.00	29.33	100.84	0.649	As-td
an23	38.17	9.82	0.86	0.13	1.86	0.54	7.58	1.89	12.39	4.45	0.97	22.47	3.02	3.99	25.49	13.00	29.38	100.87	0.757	As-td
an24	39.74	9.82	0.94	0.14	2.87	0.81	6.56	1.57	12.33	10.30	2.16	14.10	1.82	3.97	26.56	13.00	29.31	101.06	0.457	Sb-tn

an25	39.40	9.76	1.80	0.26	2.99	0.84	6.64	1.60	12.47	9.44	1.98	14.10	1.82	3.81	26.47	13.00	29.28	100.84	0.479	Sb-tn
an26	32.24	9.15	11.58	1.94	3.26	1.05	6.84	1.88	14.02	3.83	0.92	17.60	2.61	3.53	23.12	13.00	30.55	98.47	0.739	As-td
an27	35.64	9.48	0.79	0.12	3.45	1.05	7.11	1.84	12.49	4.62	1.04	20.95	2.91	3.95	24.66	13.00	29.44	97.23	0.736	As-td
an28	41.07	2.83	8.43	0.34	2.09	0.16	0.77	0.05	3.39	7.77	0.45	8.31	0.30	0.75	29.29	4.00	8.14	97.73	0.397	luz
an29	32.71	8.97	11.29	1.82	3.28	1.02	6.22	1.66	13.47	3.27	0.76	16.60	2.37	3.14	23.94	13.00	29.60	97.32	0.757	As-td
an30	44.62	2.87	3.76	0.14	1.81	0.13	0.04	0.00	3.15	14.18	0.77	4.78	0.16	0.93	31.38	4.00	8.08	100.57	0.172	luz
an31	37.13	8.66	1.52	0.21	3.79	1.01	7.76	1.76	11.64	5.35	1.06	19.41	2.36	3.42	28.12	13.00	28.06	103.08	0.691	As-td
an32	37.97	9.53	0.53	0.08	0.65	0.19	7.74	1.89	11.68	5.44	1.16	21.38	2.80	3.96	26.13	13.00	28.64	99.84	0.708	As-td
an33	39.17	9.81	0.51	0.08	2.72	0.78	5.40	1.31	11.98	11.14	2.37	13.53	1.77	4.14	26.19	13.00	29.11	98.66	0.428	Sb-tn
an34	38.78	9.87	0.39	0.06	1.09	0.32	7.35	1.82	12.07	4.23	0.91	22.93	3.05	3.96	25.77	13.00	29.03	100.54	0.769	As-td
an35	38.96	9.80	0.38	0.06	0.59	0.17	8.08	1.97	12.00	4.70	1.00	22.37	2.94	3.94	26.08	13.00	28.94	101.16	0.745	As-td

CHM2-39.5(2)

	Cu		Ag		Fe		Zn		total apfu	As		Sb		total apfu	S		total apfu	total wt%	Sb/(As+Sb)	
	wt%	*apfu*	wt%	*apfu*	wt%	*apfu*	wt%	*apfu*		wt%	*apfu*	wt%	*apfu*		wt%	*apfu*				Mineral
an1	39.67	10.11	0.34	0.05	0.40	0.12	8.23	2.04	12.31	5.74	1.24	20.78	2.76	4.01	25.74	13.00	29.32	100.90	0.690	As-td
an2	39.33	9.84	0.27	0.04	0.97	0.28	8.11	1.97	12.13	6.08	1.29	20.29	2.65	3.94	26.22	13.00	29.06	101.24	0.673	As-td
an3	39.02	9.96	0.33	0.05	0.51	0.15	8.35	2.07	12.23	4.95	1.07	22.61	3.01	4.08	25.70	13.00	29.31	101.49	0.737	As-td
an4	39.41	10.18	0.25	0.04	0.93	0.27	8.07	2.03	12.52	6.25	1.37	20.39	2.75	4.12	25.39	13.00	29.64	100.70	0.668	As-td
an5	39.34	10.18	0.36	0.06	0.47	0.14	8.44	2.12	12.50	4.76	1.05	22.52	3.04	4.09	25.35	13.00	29.59	101.25	0.744	As-td
an6	40.05	10.26	0.34	0.05	0.86	0.25	8.14	2.03	12.59	4.93	1.07	22.03	2.95	4.02	25.60	13.00	29.61	101.94	0.733	As-td
an7	39.45	9.99	0.30	0.04	0.84	0.24	8.05	1.98	12.26	5.74	1.23	20.80	2.75	3.98	25.89	13.00	29.25	101.07	0.690	As-td
an8	39.03	9.97	0.32	0.05	0.76	0.22	8.09	2.01	12.24	4.93	1.07	21.99	2.93	4.00	25.69	13.00	29.24	100.81	0.733	As-td
an9	39.69	9.93	0.25	0.04	1.18	0.34	8.37	2.03	12.33	7.13	1.51	18.39	2.40	3.91	26.23	13.00	29.25	101.25	0.613	As-td
an10	39.61	10.25	0.30	0.05	0.93	0.27	8.32	2.09	12.66	5.05	1.11	22.09	2.98	4.09	25.36	13.00	29.75	101.67	0.729	As-td
an11	40.12	10.23	0.34	0.05	0.71	0.21	8.21	2.03	12.52	5.47	1.18	22.10	2.94	4.12	25.73	13.00	29.64	102.68	0.713	As-td
an12	39.43	10.09	0.30	0.05	0.52	0.15	8.16	2.03	12.32	5.12	1.11	22.14	2.96	4.07	25.63	13.00	29.39	101.31	0.727	As-td
an13	39.96	10.09	0.33	0.05	0.44	0.13	8.01	1.97	12.24	6.29	1.35	19.82	2.61	3.96	25.97	13.00	29.20	100.80	0.660	As-td
an14	39.77	10.26	0.31	0.05	0.57	0.17	8.38	2.10	12.57	6.03	1.32	20.96	2.82	4.14	25.43	13.00	29.71	101.45	0.681	As-td
an15	39.43	10.17	0.32	0.05	0.78	0.23	8.22	2.06	12.51	5.35	1.17	22.10	2.98	4.15	25.43	13.00	29.65	101.62	0.718	As-td
an16	39.63	10.21	0.29	0.04	0.53	0.15	8.48	2.12	12.53	4.82	1.05	22.66	3.05	4.10	25.46	13.00	29.63	101.86	0.743	As-td
an17	39.59	10.25	0.29	0.04	0.71	0.21	8.60	2.16	12.67	5.15	1.13	22.42	3.03	4.16	25.33	13.00	29.83	102.08	0.728	As-td
an18	39.15	10.07	0.31	0.05	1.12	0.33	8.74	2.18	12.63	5.14	1.12	22.24	2.99	4.11	25.51	13.00	29.73	102.20	0.727	As-td
an19	40.30	9.90	0.27	0.04	0.69	0.19	8.92	2.13	12.26	10.35	2.16	14.57	1.87	4.02	26.71	13.00	29.28	101.81	0.464	As-td
an20	40.22	10.08	0.23	0.03	0.36	0.10	8.23	2.00	12.22	7.89	1.68	17.44	2.28	3.96	26.18	13.00	29.18	100.54	0.576	As-td
an21	41.14	10.38	0.19	0.03	0.48	0.14	8.25	2.02	12.57	8.79	1.88	16.64	2.19	4.07	26.00	13.00	29.64	101.49	0.538	As-td
an22	39.85	10.22	0.41	0.06	0.46	0.13	8.36	2.08	12.50	5.16	1.12	22.24	2.98	4.10	25.57	13.00	29.60	102.05	0.726	As-td
an23	39.74	10.29	0.38	0.06	0.45	0.13	8.40	2.11	12.60	5.44	1.20	21.96	2.97	4.17	25.33	13.00	29.76	101.70	0.713	As-td
an24	38.25	10.05	0.36	0.06	0.82	0.24	8.47	2.16	12.51	5.32	1.18	21.47	2.94	4.13	24.97	13.00	29.64	99.66	0.713	As-td
an27	38.84	1.28	3.92	0.08	24.05	0.90	0.06	0.00	2.26	0.00	0.00	0.00	0.00	0.00	30.67	2.00	4.26	97.53		ccp
an28	38.44	1.28	4.45	0.09	23.78	0.90	0.07	0.00	2.27	0.00	0.00	0.00	0.00	0.00	30.25	2.00	4.27	96.99		ccp
an29	33.65	1.01	0.05	0.00	31.69	1.09	0.05	0.00	2.10	0.00	0.00	0.04	0.00	0.00	33.47	2.00	4.10	98.96		ccp
an30	35.66	1.10	1.18	0.02	29.20	1.02	0.07	0.00	2.15	0.00	0.00	0.00	0.00	0.00	32.72	2.00	4.15	98.83		ccp

CHM2-69

	Cu		Ag		Fe		Zn		total apfu	As		Sb		total apfu	S		total apfu	total wt%	Sb/(As+Sb)	
	wt%	*apfu*	wt%	*apfu*	wt%	*apfu*	wt%	*apfu*		wt%	*apfu*	wt%	*apfu*		wt%	*apfu*				Mineral
an1	14.00	0.97	69.52	2.83	1.78	0.14	0.00	0.00	3.93	0.00	0.00	0.00	0.00	0.00	14.62	2.00	5.93	99.92		jalp
an3	40.69	10.20	0.18	0.03	1.22	0.35	8.03	1.96	12.53	7.54	1.60	18.64	2.44	4.04	26.16	13.00	29.58	102.45	0.603	As-td
an4	41.00	10.55	0.31	0.05	0.59	0.17	7.97	1.99	12.77	8.09	1.77	17.26	2.32	4.08	25.49	13.00	29.85	100.71	0.568	As-td
an5	41.05	10.31	0.11	0.02	0.22	0.06	8.60	2.10	12.48	9.06	1.93	16.15	2.12	4.05	26.13	13.00	29.53	101.30	0.523	As-td
an6	41.00	10.31	0.19	0.03	0.15	0.04	8.31	2.03	12.41	7.58	1.62	18.53	2.43	4.05	26.08	13.00	29.46	101.84	0.601	As-td
an7	48.69	3.08	0.18	0.01	0.19	0.01	0.42	0.03	3.12	17.62	0.94	1.26	0.04	0.99	31.93	4.00	8.11	100.30	0.042	enr
an8	37.80	0.73	1.19	0.01	0.11	0.00	34.62	0.65	1.40	0.00	0.00	0.00	0.00	0.00	25.98	1.00	2.40	99.71		sp-cov?
an9	48.77	3.07	0.25	0.01	0.43	0.03	0.09	0.01	3.12	17.35	0.93	1.21	0.04	0.97	32.03	4.00	8.09	100.13	0.041	enr
an10	41.17	10.41	0.20	0.03	0.47	0.14	8.28	2.04	12.61	8.67	1.86	16.85	2.22	4.08	25.93	13.00	29.70	101.57	0.545	As-td
an11	40.06	10.52	0.21	0.03	0.38	0.11	8.28	2.11	12.78	8.11	1.81	18.60	2.55	4.36	24.98	13.00	30.14	100.61	0.585	As-td
an12	41.19	10.69	0.23	0.03	0.75	0.22	7.43	1.87	12.82	8.94	1.97	16.86	2.28	4.25	25.27	13.00	30.07	100.66	0.537	As-td
an13	40.51	10.08	0.22	0.03	0.43	0.12	8.22	1.99	12.22	7.39	1.56	17.74	2.30	3.86	26.36	13.00	29.09	100.87	0.596	As-td
an14	43.69	10.02	0.14	0.02	5.32	1.39	3.10	0.69	12.12	18.86	3.67	1.23	0.15	3.82	28.60	13.00	28.94	100.94	0.039	tn
an15	41.71	10.24	0.34	0.05	3.16	0.88	6.60	1.57	12.74	12.95	2.70	10.30	1.32	4.01	26.73	13.00	29.76	101.79	0.329	Sb-tn
an16	42.92	9.86	0.09	0.01	6.11	1.60	3.34	0.75	12.22	20.10	3.92	0.12	0.01	3.93	28.55	13.00	29.15	101.22	0.004	tn
an17	40.96	9.99	0.12	0.02	3.17	0.88	6.51	1.54	12.43	11.85	2.45	11.79	1.50	3.95	26.90	13.00	29.38	101.29	0.380	Sb-tn
an18	40.15	10.13	0.17	0.02	1.93	0.55	7.48	1.83	12.54	7.27	1.56	19.29	2.54	4.10	26.01	13.00	29.64	102.29	0.620	As-td
an19	40.83	10.52	0.25	0.04	1.62	0.48	7.57	1.89	12.92	6.54	1.43	19.45	2.61	4.04	25.47	13.00	29.96	101.73	0.647	As-td
an20	43.76	10.30	0.10	0.01	4.77	1.28	4.48	1.03	12.62	19.16	3.83	1.60	0.20	4.02	27.86	13.00	29.64	101.73	0.049	tn
an21	43.19	10.04	0.11	0.01	5.36	1.42	3.60	0.81	12.29	18.97	3.74	0.85	0.10	3.84	28.22	13.00	29.13	100.30	0.027	tn
an22	42.08	10.14	0.17	0.02	3.61	0.99	5.89	1.38	12.53	13.16	2.69	9.11	1.14	3.83	27.23	13.00	29.36	101.24	0.299	Sb-tn
an23	42.95	10.11	0.11	0.02	4.39	1.18	4.90	1.12	12.42	19.50	3.89	0.90	0.11	4.00	27.88	13.00	29.42	100.63	0.028	tn
an24	41.07	10.12	0.15	0.02	1.95	0.55	7.70	1.84	12.53	10.83	2.26	13.26	1.70	3.97	26.63	13.00	29.50	101.58	0.430	Sb-tn
an25	41.85	10.29	0.17	0.02	1.25	0.35	7.93	1.89	12.56	11.08	2.31	13.07	1.68	3.99	26.68	13.00	29.55	102.04	0.421	Sb-tn
an26	43.92	10.14	0.13	0.02	4.75	1.25	3.97	0.89	12.29	20.23	3.96	0.07	0.01	3.97	28.42	13.00	29.26	101.49	0.002	tn
an27	41.59	10.33	0.23	0.03	1.48	0.42	7.50	1.81	12.59	10.57	2.23	13.89	1.80	4.03	26.42	13.00	29.61	101.67	0.447	Sb-tn
an28	41.54	10.38	0.14	0.02	2.23	0.64	6.81	1.65	12.69	11.39	2.41	13.84	1.81	4.22	26.25	13.00	29.91	102.20	0.428	Sb-tn
an29	43.51	10.13	0.09	0.01	5.05	1.34	4.11	0.93	12.40	19.84	3.92	0.60	0.07	3.99	28.19	13.00	29.39	101.39	0.018	tn
an30	44.17	10.33	0.15	0.02	4.50	1.20	4.69	1.07	12.62	19.25	3.82	0.44	0.05	3.87	28.04	13.00	29.49	101.23	0.014	tn
an31	40.50	10.00	0.29	0.04	2.55	0.72	6.90	1.65	12.41	10.29	2.15	14.47	1.86	4.02	26.58	13.00	29.43	101.58	0.464	Sb-tn
an32	42.60	10.12	0.20	0.03	3.99	1.08	4.28	0.99	12.22	15.24	3.07	7.35	0.91	3.98	27.61	13.00	29.20	101.26	0.229	Sb-tn
an33	42.39	10.08	0.19	0.03	2.58	0.70	5.98	1.38	12.19	15.38	3.10	6.60	0.82	3.92	27.57	13.00	29.11	100.69	0.209	Sb-tn
an34	38.97	10.13	0.26	0.04	1.32	0.39	6.94	1.75	12.32	3.07	0.68	25.29	3.43	4.11	25.23	13.00	29.42	101.08	0.835	As-td
an35	43.34	10.10	0.21	0.03	6.28	1.67	1.78	0.40	12.20	19.52	3.86	1.41	0.17	4.03	28.15	13.00	29.23	100.68	0.042	tn
an36	42.03	9.85	0.15	0.02	5.08	1.35	2.87	0.65	11.88	18.41	3.66	2.62	0.32	3.98	27.99	13.00	28.86	99.14	0.081	Sb-tn
an37	40.52	10.23	0.23	0.03	1.46	0.42	6.96	1.71	12.39	8.67	1.86	17.38	2.29	4.15	25.99	13.00	29.53	101.21	0.552	As-td
an38	39.59	10.11	0.18	0.03	1.49	0.43	7.15	1.77	12.35	3.09	0.67	25.07	3.34	4.01	25.68	13.00	29.36	102.25	0.833	As-td
an39	41.39	10.10	0.19	0.03	0.75	0.21	8.11	1.92	12.26	9.88	2.04	14.75	1.88	3.92	26.88	13.00	29.18	101.95	0.479	Sb-tn
an40	40.93	10.27	0.13	0.02	0.06	0.02	8.68	2.12	12.42	8.63	1.84	16.29	2.13	3.97	26.14	13.00	29.39	100.84	0.538	As-td
an41	30.81	9.28	42.70	7.58	0.55	0.19	0.11	0.03	17.08	7.02	1.79	1.45	0.23	2.02	18.43	11.00	30.10	101.08	0.113	pearc
an42	37.44	11.46	35.41	6.38	0.46	0.16	0.15	0.04	18.04	6.42	1.66	1.23	0.20	1.86	18.14	11.00	30.90	99.24	0.105	pearc
an43	32.29	9.67	41.33	7.29	0.39	0.13	0.23	0.07	17.15	6.60	1.67	1.54	0.24	1.91	18.54	11.00	30.07	100.91	0.125	pearc
an44	40.69	10.27	0.21	0.03	0.08	0.02	8.57	2.10	12.43	6.54	1.40	20.19	2.66	4.06	25.98	13.00	29.49	102.25	0.655	As-td
an45	41.14	10.32	0.15	0.02	1.19	0.34	7.32	1.79	12.47	7.02	1.49	19.22	2.52	4.01	26.14	13.00	29.48	102.18	0.628	As-td
an46	44.76	10.21	0.13	0.02	6.18	1.60	1.69	0.37	12.20	18.69	3.62	1.14	0.14	3.75	28.76	13.00	28.96	101.36	0.036	tn
an47	42.96	10.08	0.14	0.02	2.88	0.77	5.74	1.31	12.18	17.02	3.39	3.82	0.47	3.86	27.95	13.00	29.04	100.51	0.121	Sb-tn
an48	40.60	10.18	0.12	0.02	0.90	0.26	7.56	1.84	12.29	8.37	1.78	16.90	2.21	3.99	26.17	13.00	29.28	100.62	0.554	As-td
an49	40.89	10.39	0.20	0.03	1.75	0.51	6.97	1.72	12.65	9.37	2.02	16.35	2.17	4.19	25.81	13.00	29.84	101.32	0.518	As-td
an50	43.32	10.11	0.10	0.01	6.01	1.60	2.03	0.46	12.19	18.87	3.74	1.15	0.14	3.88	28.10	13.00	29.06	99.57	0.036	tn

an51	39.14	10.04	0.27	0.04	1.07	0.31	7.24	1.80	12.20	3.60	0.78	24.27	3.25	4.03	25.56	13.00	29.23	101.15	0.806	As-td
an52	39.43	10.36	0.19	0.03	1.85	0.55	6.96	1.78	12.72	3.37	0.75	24.58	3.37	4.12	24.95	13.00	29.85	101.33	0.818	As-td
an53	39.70	10.30	0.16	0.02	0.21	0.06	8.31	2.09	12.47	7.15	1.57	19.45	2.63	4.20	25.29	13.00	29.68	100.26	0.626	As-td
an54	40.69	10.29	0.16	0.02	2.27	0.65	5.97	1.47	12.44	8.21	1.76	17.38	2.29	4.06	25.93	13.00	29.49	100.61	0.566	As-td
an55	40.11	10.29	0.19	0.03	2.44	0.71	5.64	1.41	12.43	7.11	1.55	19.41	2.60	4.15	25.57	13.00	29.58	100.46	0.627	As-td
an56	42.41	10.51	0.24	0.04	4.43	1.25	3.16	0.76	12.56	12.18	2.56	11.22	1.45	4.01	26.47	13.00	29.57	100.11	0.362	Sb-tn
an57	42.31	10.46	0.18	0.03	4.84	1.36	3.02	0.73	12.57	11.74	2.46	12.41	1.60	4.06	26.54	13.00	29.63	101.05	0.394	Sb-tn
an58	40.46	10.27	0.17	0.03	0.19	0.06	8.14	2.01	12.35	6.17	1.33	20.99	2.78	4.11	25.85	13.00	29.46	101.97	0.677	As-td
an59	40.70	10.36	0.16	0.02	0.17	0.05	8.33	2.06	12.50	5.97	1.29	20.98	2.79	4.08	25.76	13.00	29.58	102.07	0.684	As-td
an60	42.93	10.19	0.09	0.01	0.10	0.03	8.88	2.05	12.28	18.26	3.68	2.75	0.34	4.02	27.63	13.00	29.30	100.65	0.085	Sb-tn
an64	42.09	10.28	0.12	0.02	2.65	0.74	5.84	1.39	12.42	12.46	2.58	10.75	1.37	3.95	26.85	13.00	29.38	100.74	0.347	Sb-tn
an65	41.77	10.16	0.13	0.02	5.08	1.41	2.17	0.51	12.10	13.46	2.78	11.08	1.41	4.18	26.96	13.00	29.29	100.66	0.336	Sb-tn
an66	40.82	10.06	0.19	0.03	2.60	0.73	5.80	1.39	12.20	9.41	1.97	15.94	2.05	4.02	26.62	13.00	29.22	101.37	0.510	As-td
an67	40.23	10.03	0.14	0.02	2.17	0.62	6.68	1.62	12.28	9.60	2.03	15.58	2.03	4.06	26.31	13.00	29.34	100.72	0.500	Sb-tn
an68	42.09	10.35	0.18	0.03	3.04	0.85	5.78	1.38	12.61	10.60	2.21	13.60	1.75	3.96	26.67	13.00	29.56	101.96	0.441	Sb-tn
an69	41.02	10.34	0.20	0.03	2.53	0.73	5.69	1.39	12.49	6.88	1.47	19.90	2.62	4.09	26.03	13.00	29.57	102.24	0.640	As-td
an70	42.29	10.39	0.12	0.02	3.78	1.06	4.70	1.12	12.59	12.45	2.59	11.78	1.51	4.11	26.69	13.00	29.70	101.80	0.368	Sb-tn
an71	41.23	10.29	0.14	0.02	2.40	0.68	6.52	1.58	12.58	9.97	2.11	15.40	2.01	4.12	26.28	13.00	29.69	101.94	0.487	Sb-tn
an72	41.81	10.43	0.18	0.03	3.37	0.96	5.07	1.23	12.64	11.08	2.34	13.33	1.74	4.08	26.31	13.00	29.71	101.15	0.426	Sb-tn
an75	40.55	10.09	0.20	0.03	2.31	0.65	6.77	1.64	12.41	8.38	1.77	17.80	2.31	4.08	26.37	13.00	29.49	102.36	0.567	As-td
an76	42.00	10.31	0.17	0.02	2.62	0.73	5.91	1.41	12.47	10.38	2.16	14.18	1.82	3.98	26.73	13.00	29.45	101.99	0.457	Sb-tn
an77	40.10	10.22	0.18	0.03	2.44	0.71	6.09	1.51	12.47	7.40	1.60	18.36	2.44	4.04	25.73	13.00	29.51	100.30	0.604	As-td
an78	41.49	10.51	0.16	0.02	0.11	0.03	8.54	2.10	12.67	6.32	1.36	20.65	2.73	4.09	25.89	13.00	29.76	103.15	0.668	As-td
an79	41.70	10.65	0.22	0.03	2.80	0.82	5.32	1.32	12.82	7.35	1.59	19.63	2.62	4.21	25.68	13.00	30.03	102.70	0.622	As-td
an80	43.60	10.52	0.12	0.02	4.70	1.29	3.55	0.83	12.66	15.10	3.09	7.24	0.91	4.00	27.18	13.00	29.66	101.48	0.228	Sb-tn
an81	40.79	10.22	0.18	0.03	0.68	0.19	8.34	2.03	12.47	6.88	1.46	18.93	2.48	3.94	26.18	13.00	29.41	101.97	0.629	As-td
an82	43.47	10.17	0.14	0.02	4.51	1.20	3.93	0.89	12.28	18.92	3.75	1.40	0.17	3.92	28.05	13.00	29.20	100.41	0.044	tn
an83	40.44	10.25	0.19	0.03	1.06	0.30	7.75	1.91	12.50	6.37	1.37	20.24	2.68	4.05	25.87	13.00	29.54	101.91	0.662	As-td
an84	39.64	10.32	0.27	0.04	1.22	0.36	7.02	1.78	12.50	2.50	0.55	24.44	3.32	3.87	25.20	13.00	29.37	100.29	0.858	As-td
an85	40.86	10.17	0.14	0.02	1.69	0.48	7.44	1.80	12.46	9.80	2.07	15.55	2.02	4.09	26.37	13.00	29.55	101.84	0.494	As-td
an86	40.74	10.22	0.14	0.02	0.34	0.10	8.37	2.04	12.38	7.55	1.61	18.49	2.42	4.03	26.15	13.00	29.40	101.78	0.601	As-td
an87	42.98	10.26	0.12	0.02	0.26	0.07	8.72	2.02	12.37	18.62	3.77	2.33	0.29	4.06	27.47	13.00	29.44	100.49	0.071	Sb-tn
an88	40.75	10.24	0.20	0.03	0.24	0.07	8.23	2.01	12.35	7.22	1.54	19.11	2.51	4.05	26.10	13.00	29.39	101.85	0.620	As-td
an89	42.42	9.96	0.15	0.02	5.78	1.54	2.35	0.54	12.07	19.57	3.90	1.90	0.23	4.13	27.93	13.00	29.20	100.10	0.056	Sb-tn
an90	39.16	10.07	0.25	0.04	0.30	0.09	7.98	1.99	12.18	7.68	1.68	18.31	2.46	4.13	25.52	13.00	29.32	99.21	0.595	As-td
an91	72.94	8.86	0.96	0.07	0.27	0.04	4.20	0.50	9.46	0.00	0.00	0.00	0.00	0.00	20.76	5.00	14.46	99.12		dig?
an92	40.47	10.25	0.14	0.02	0.85	0.25	8.43	2.07	12.59	8.14	1.75	17.82	2.35	4.10	25.91	13.00	29.69	101.74	0.574	As-td
an93	40.48	10.31	0.14	0.02	0.80	0.23	8.22	2.03	12.60	6.61	1.43	20.07	2.67	4.10	25.74	13.00	29.70	102.07	0.651	As-td
an94	39.61	10.16	0.14	0.02	1.21	0.35	7.67	1.91	12.44	6.73	1.46	19.09	2.55	4.02	25.59	13.00	29.46	100.04	0.636	As-td
an95	33.03	11.42	40.32	8.21	0.36	0.14	0.09	0.03	19.80	6.49	1.90	2.74	0.49	2.40	18.97	13.00	35.20	102.00	0.206	pearc
an96	32.82	11.17	41.00	8.22	0.37	0.14	0.09	0.03	19.57	6.67	1.93	2.13	0.38	2.30	19.27	13.00	34.87	102.35	0.164	pearc
an97	48.20	3.03	0.22	0.01	0.96	0.07	0.07	0.00	3.11	19.02	1.01	0.59	0.02	1.03	32.13	4.00	8.14	101.18	0.019	enr
an98	47.57	2.99	0.17	0.01	0.83	0.06	0.09	0.01	3.06	18.94	1.01	0.42	0.01	1.02	32.09	4.00	8.09	100.12	0.014	enr
an99	47.57	3.01	0.22	0.01	1.27	0.09	0.11	0.01	3.12	18.91	1.02	0.37	0.01	1.03	31.88	4.00	8.15	100.34	0.012	enr
an100	48.25	2.99	0.20	0.01	1.57	0.11	0.09	0.01	3.11	18.71	0.98	0.12	0.00	0.99	32.59	4.00	8.10	101.52	0.004	enr
an101	45.32	3.26	11.88	0.50	1.46	0.12	0.81	0.06	3.93	11.92	0.73	0.67	0.03	0.75	28.10	4.00	8.69	100.18	0.034	enr

CHM2-81

	Cu		Ag		Fe		Zn		total apfu	As		Sb		total apfu	S		total apfu	total wt%	Sb/(As+Sb)	
	wt%	*apfu*	wt%	*apfu*	wt%	*apfu*	wt%	*apfu*		wt%	*apfu*	wt%	*apfu*		wt%	*apfu*				Mineral
an1	0.00	0.00	0.00	0.00	0.09	0.00	68.45	1.01	1.01	0.00	0.00	0.01	0.00	0.00	33.17	1.00	2.01	101.72		sp
an2	0.00	0.00	0.00	0.00	0.31	0.01	68.37	1.02	1.03	0.00	0.00	0.00	0.00	0.00	32.85	1.00	2.03	101.54		sp
an3	0.00	0.00	0.00	0.00	0.22	0.00	69.02	1.02	1.02	0.00	0.00	0.00	0.00	0.00	33.33	1.00	2.02	102.56		sp

CHM2-136

	Cu		Ag		Fe		Zn		total apfu	As		Sb		total apfu	S		total apfu	total wt%	Sb/(As+Sb)	
	wt%	*apfu*	wt%	*apfu*	wt%	*apfu*	wt%	*apfu*		wt%	*apfu*	wt%	*apfu*		wt%	*apfu*				Mineral
an1	0.00	0.00	0.00	0.00	0.38	0.01	66.93	0.97	0.98	0.00	0.00	0.01	0.00	0.00	33.84	1.00	1.98	101.15		sp
an2	0.00	0.00	0.00	0.00	0.37	0.01	66.99	0.97	0.98	0.00	0.00	0.02	0.00	0.00	33.77	1.00	1.98	101.14		sp
an3	0.00	0.00	0.00	0.00	0.36	0.01	67.08	0.99	0.99	0.00	0.00	0.00	0.00	0.00	33.33	1.00	1.99	100.77		sp
an4	0.00	0.00	0.00	0.00	0.31	0.01	66.84	0.99	0.99	0.00	0.00	0.05	0.00	0.00	33.19	1.00	1.99	100.39		sp
an5	0.00	0.00	0.00	0.00	0.26	0.00	67.38	0.99	1.00	0.00	0.00	0.00	0.00	0.00	33.33	1.00	2.00	100.97		sp

CHM2-89

	Cu		Ag		Fe		Zn		total apfu	As		Sb		total apfu	S		total apfu	total wt%	Sb/(As+Sb)	
	wt%	*apfu*	wt%	*apfu*	wt%	*apfu*	wt%	*apfu*		wt%	*apfu*	wt%	*apfu*		wt%	*apfu*				Mineral
an1	25.64	7.54	48.14	8.34	1.75	0.59	0.27	0.08	16.55	6.26	1.56	1.10	0.17	1.73	18.87	11.00	29.28	102.03	0.097	pearc
an2	29.89	8.32	40.47	6.63	1.14	0.36	0.43	0.12	15.43	7.49	1.77	1.24	0.18	1.95	19.94	11.00	28.38	100.59	0.092	pearc
an3	33.05	8.39	33.23	4.97	1.09	0.31	0.32	0.08	13.75	8.89	1.91	1.54	0.20	2.12	21.87	11.00	26.87	99.99	0.096	pearc
an4	30.13	8.18	40.78	6.52	1.44	0.44	0.05	0.01	15.17	7.47	1.72	1.41	0.20	1.92	20.44	11.00	28.09	101.72	0.104	pearc
an5	29.43	8.19	41.80	6.85	1.49	0.47	0.01	0.00	15.52	7.55	1.78	1.32	0.19	1.97	19.95	11.00	28.49	101.55	0.097	pearc
an6	27.35	7.97	45.67	7.84	1.89	0.63	0.21	0.06	16.50	5.66	1.40	1.45	0.22	1.62	19.04	11.00	29.12	101.27	0.136	pearc
an9	25.54	7.04	43.23	7.02	2.79	0.87	0.76	0.20	15.14	5.60	1.31	1.28	0.18	1.49	20.14	11.00	27.63	99.33	0.123	pearc
an10	30.53	13.22	44.88	11.45	0.23	0.11	0.17	0.07	24.86	7.90	2.90	2.05	0.46	3.37	12.82	11.00	39.22	98.57	0.137	pearc
an11	32.19	8.27	36.89	5.58	0.35	0.10	0.32	0.08	14.03	9.51	2.07	0.87	0.12	2.19	21.62	11.00	27.22	101.75	0.053	pearc
an12	46.77	2.96	0.09	0.00	0.61	0.04	0.26	0.02	3.03	14.16	0.76	5.92	0.20	0.96	31.86	4.00	7.98	99.65	0.205	luz
an13	47.34	2.91	0.11	0.00	0.38	0.03	0.26	0.02	2.96	17.57	0.92	0.96	0.03	0.95	32.82	4.00	7.90	99.44	0.032	enr
an14	46.37	2.91	0.09	0.00	0.50	0.04	0.34	0.02	2.97	15.33	0.82	3.88	0.13	0.94	32.15	4.00	7.91	98.64	0.135	luz
an15	48.26	3.01	0.27	0.01	0.43	0.03	0.12	0.01	3.05	16.07	0.85	1.89	0.06	0.91	32.40	4.00	7.96	99.43	0.067	enr
an16	47.55	3.07	0.10	0.00	0.25	0.02	0.06	0.00	3.10	12.71	0.70	8.63	0.29	0.99	31.22	4.00	8.09	100.51	0.294	luz
an17	48.13	3.01	0.11	0.00	1.07	0.08	0.09	0.01	3.09	16.58	0.88	2.93	0.10	0.97	32.31	4.00	8.07	101.20	0.098	enr
an18	46.30	2.98	0.12	0.00	0.91	0.07	0.05	0.00	3.06	11.40	0.62	10.34	0.35	0.97	31.34	4.00	8.03	100.46	0.358	luz
an19	48.17	3.07	0.18	0.01	0.81	0.06	0.07	0.00	3.14	16.88	0.91	2.36	0.08	0.99	31.72	4.00	8.12	100.18	0.079	enr
an20	47.84	3.01	0.22	0.01	0.52	0.04	0.09	0.01	3.07	15.48	0.83	4.56	0.15	0.98	32.03	4.00	8.04	100.74	0.153	luz
an21	47.63	3.01	0.19	0.01	0.31	0.02	0.11	0.01	3.05	16.68	0.89	1.08	0.04	0.93	31.91	4.00	7.98	97.91	0.038	enr
an22	46.75	3.01	0.17	0.01	0.46	0.03	0.04	0.00	3.05	14.90	0.81	5.76	0.19	1.01	31.37	4.00	8.06	99.45	0.192	luz
an23	47.74	3.03	0.08	0.00	0.12	0.01	0.11	0.01	3.05	16.84	0.91	3.12	0.10	1.01	31.77	4.00	8.06	99.77	0.102	luz
an24	46.72	2.99	0.12	0.00	0.33	0.02	0.21	0.01	3.03	16.74	0.91	2.04	0.07	0.98	31.58	4.00	8.00	97.75	0.070	enr
an26	28.48	8.09	42.62	7.13	0.11	0.04	1.01	0.28	15.53	7.53	1.81	2.10	0.31	2.13	19.55	11.00	28.66	101.41	0.146	pearc
an27	27.76	7.75	41.22	6.78	0.17	0.05	2.58	0.70	15.29	6.48	1.54	2.06	0.30	1.84	19.87	11.00	28.12	100.14	0.163	pearc
an28	47.96	3.06	0.26	0.01	0.23	0.02	0.18	0.01	3.10	17.26	0.94	1.97	0.07	1.00	31.59	4.00	8.10	99.45	0.066	enr
an29	46.68	3.11	0.19	0.01	0.13	0.01	0.09	0.01	3.13	10.24	0.58	12.55	0.44	1.01	30.34	4.00	8.14	100.22	0.430	luz
an30	48.16	3.02	0.14	0.01	0.77	0.05	0.31	0.02	3.10	17.95	0.95	0.61	0.02	0.97	32.20	4.00	8.07	100.13	0.021	enr

an31	46.60	3.13	0.10	0.00	0.09	0.01	0.21	0.01	3.16	8.61	0.49	14.88	0.52	1.01	30.05	4.00	8.17	100.54	0.515	fm
an32	48.44	3.07	0.18	0.01	0.15	0.01	0.03	0.00	3.09	16.12	0.87	4.09	0.14	1.00	31.84	4.00	8.09	100.84	0.135	luz
an33	44.83	10.97	2.08	0.30	0.36	0.10	7.33	1.74	13.11	15.64	3.25	3.03	0.39	3.63	26.81	13.00	29.74	100.08	0.107	Sb-tn
an34	47.90	3.04	0.21	0.01	0.90	0.07	0.05	0.00	3.11	18.35	0.99	0.95	0.03	1.02	31.83	4.00	8.13	100.19	0.031	enr
an35	47.93	3.03	0.20	0.01	1.28	0.09	0.10	0.01	3.14	16.89	0.91	2.22	0.07	0.98	31.91	4.00	8.12	100.53	0.075	enr
an36	45.64	10.93	1.51	0.21	0.74	0.20	5.66	1.32	12.66	15.46	3.14	2.77	0.35	3.48	27.40	13.00	29.14	99.18	0.099	Sb-tn
an37	47.24	3.00	0.21	0.01	0.92	0.07	0.38	0.02	3.10	17.91	0.97	1.15	0.04	1.00	31.76	4.00	8.10	99.57	0.038	enr
an38	46.31	3.07	0.18	0.01	0.79	0.06	0.04	0.00	3.13	13.84	0.78	7.49	0.26	1.04	30.49	4.00	8.17	99.14	0.250	luz
an39	39.90	10.13	0.36	0.05	0.09	0.02	8.32	2.05	12.26	4.98	1.07	22.00	2.91	3.98	25.85	13.00	29.24	101.49	0.731	As-td
an40	45.10	3.02	0.26	0.01	0.31	0.02	0.18	0.01	3.07	5.54	0.31	19.93	0.70	1.01	30.11	4.00	8.08	101.41	0.689	fm
an41	39.60	10.14	0.46	0.07	1.06	0.31	7.82	1.94	12.46	6.19	1.34	20.55	2.75	4.09	25.62	13.00	29.55	101.29	0.671	As-td
an42	48.26	2.98	0.18	0.01	0.18	0.01	0.20	0.01	3.01	16.13	0.84	3.04	0.10	0.94	32.70	4.00	7.95	100.69	0.104	luz
an45	5.96	2.02	60.46	12.08	0.28	0.11	0.03	0.01	14.21	0.44	0.13	9.57	1.69	1.82	10.42	7.00	23.03	87.15	0.930	benleo?
an46	6.03	2.03	60.67	12.05	0.29	0.11	0.00	0.00	14.19	0.51	0.14	9.55	1.68	1.82	10.48	7.00	23.01	87.52	0.921	benleo?
an47	46.86	2.97	0.13	0.00	1.25	0.09	0.01	0.00	3.07	17.94	0.97	0.65	0.02	0.99	31.80	4.00	8.06	98.64	0.022	enr
an48	13.87	4.54	61.16	11.80	0.93	0.35	0.00	0.00	16.69	5.30	1.47	2.59	0.44	1.91	16.95	11.00	29.60	100.80	0.231	pearc

CHM4-59

	Cu		Ag		Fe		Zn		total apfu	As		Sb		total apfu	S		total apfu	total wt%	Sb/(As+Sb)	
	wt%	*apfu*	wt%	*apfu*	wt%	*apfu*	wt%	*apfu*		wt%	*apfu*	wt%	*apfu*		wt%	*apfu*				Mineral
an1	41.35	10.11	0.17	0.02	1.67	0.46	8.02	1.90	12.50	15.48	3.21	8.15	1.04	4.25	26.84	13.00	29.75	101.66	0.245	Sb-tn
an2	42.01	9.76	0.20	0.03	1.32	0.35	7.28	1.64	11.78	17.68	3.48	3.87	0.47	3.95	28.25	13.00	28.73	100.61	0.119	Sb-tn
an3	41.32	9.89	0.08	0.01	1.45	0.40	8.05	1.87	12.17	18.28	3.71	3.41	0.43	4.14	27.39	13.00	29.31	99.99	0.103	Sb-tn
an4	41.77	9.90	0.06	0.01	1.50	0.41	8.08	1.86	12.17	20.24	4.07	0.45	0.06	4.13	27.68	13.00	29.30	99.79	0.014	tn
an5	40.14	9.83	0.25	0.04	1.54	0.43	8.01	1.91	12.20	13.81	2.87	9.68	1.24	4.11	26.79	13.00	29.31	100.22	0.301	Sb-tn
an6	39.58	9.87	0.35	0.05	0.82	0.23	8.11	1.96	12.11	11.33	2.39	12.18	1.58	3.98	26.32	13.00	29.09	98.69	0.398	Sb-tn
an7	43.55	10.13	0.08	0.01	1.24	0.33	8.25	1.86	12.33	19.68	3.88	0.23	0.03	3.91	28.20	13.00	29.24	101.24	0.007	tn
an9	42.41	9.94	0.09	0.01	0.96	0.25	8.35	1.90	12.10	19.35	3.85	0.39	0.05	3.89	28.00	13.00	29.00	99.55	0.012	tn
an11	42.45	10.19	0.04	0.01	1.13	0.31	8.42	1.96	12.47	20.74	4.22	0.33	0.04	4.26	27.33	13.00	29.73	100.44	0.010	tn
an12	40.78	10.01	0.16	0.02	0.89	0.25	8.29	1.98	12.25	17.93	3.73	3.97	0.51	4.24	26.73	13.00	29.50	98.75	0.120	Sb-tn
an13	40.15	9.66	0.26	0.04	2.01	0.55	7.81	1.83	12.07	14.05	2.87	8.78	1.10	3.97	27.27	13.00	29.04	100.33	0.278	Sb-tn
an15	37.18	9.59	1.64	0.25	1.44	0.42	7.20	1.80	12.06	2.97	0.65	24.92	3.36	4.00	25.43	13.00	29.07	100.77	0.838	As-td
an16	40.66	9.70	0.44	0.06	0.86	0.23	8.17	1.89	11.89	13.02	2.64	9.85	1.23	3.86	27.49	13.00	28.75	100.50	0.318	Sb-tn
an17	37.76	9.72	1.86	0.28	1.16	0.34	7.19	1.80	12.14	3.22	0.70	24.54	3.30	4.00	25.49	13.00	29.13	101.21	0.824	As-td
an18	38.29	9.70	1.46	0.22	1.98	0.57	6.95	1.71	12.19	4.68	1.00	22.12	2.92	3.93	25.90	13.00	29.12	101.37	0.744	As-td
an19	36.89	9.75	2.57	0.40	4.34	1.31	3.99	1.02	12.48	2.79	0.63	25.65	3.54	4.16	24.82	13.00	29.64	101.05	0.850	As-td
an20	38.82	9.57	1.10	0.16	2.54	0.71	5.91	1.42	11.85	9.75	2.04	13.54	1.74	3.78	26.62	13.00	28.63	98.27	0.461	Sb-tn
an21	37.01	10.05	1.19	0.19	0.71	0.22	7.46	1.97	12.43	4.09	0.94	23.87	3.38	4.33	24.15	13.00	29.76	98.48	0.782	As-td
an22	38.06	10.03	0.90	0.14	1.79	0.54	6.67	1.71	12.42	6.44	1.44	20.24	2.78	4.22	24.88	13.00	29.64	98.98	0.659	As-td
an23	45.77	3.05	0.07	0.00	1.13	0.09	0.09	0.01	3.15	9.98	0.56	14.19	0.49	1.06	30.27	4.00	8.21	101.49	0.467	luz
an24	38.83	10.14	1.39	0.21	3.08	0.92	5.98	1.52	12.79	3.21	0.71	24.72	3.37	4.08	25.11	13.00	29.87	102.31	0.826	As-td
an25	48.56	3.03	0.06	0.00	0.92	0.07	0.09	0.01	3.11	17.67	0.94	2.27	0.07	1.01	32.32	4.00	8.11	101.89	0.073	enr
an26	40.45	9.97	0.74	0.11	1.62	0.45	7.95	1.90	12.43	8.65	1.81	16.33	2.10	3.91	26.62	13.00	29.34	102.36	0.537	As-td
an27	40.58	10.07	0.79	0.12	1.38	0.39	7.95	1.92	12.49	8.95	1.88	16.11	2.09	3.97	26.44	13.00	29.46	102.19	0.526	As-td
an28	47.13	3.01	0.07	0.00	0.85	0.06	0.07	0.00	3.08	12.39	0.67	8.12	0.27	0.94	31.63	4.00	8.02	100.27	0.287	luz
an31	41.20	2.68	0.05	0.00	12.29	0.91	0.07	0.00	3.59	8.97	0.49	7.71	0.26	0.76	31.06	4.00	8.35	101.35	0.346	luz
an32	40.48	9.76	0.87	0.12	1.49	0.41	8.02	1.88	12.18	11.11	2.27	12.34	1.55	3.83	27.20	13.00	29.00	101.51	0.406	Sb-tn
an34	45.27	2.84	0.03	0.00	0.90	0.06	0.06	0.00	2.90	14.46	0.77	4.84	0.16	0.93	32.23	4.00	7.83	97.79	0.171	luz
an35	39.20	9.57	0.56	0.08	0.53	0.15	7.98	1.89	11.69	8.74	1.81	16.45	2.10	3.91	26.86	13.00	28.60	100.32	0.537	As-td
an36	37.85	9.74	1.32	0.20	2.28	0.67	5.32	1.33	11.94	2.24	0.49	25.78	3.46	3.95	25.50	13.00	28.89	100.28	0.876	As-td
an37	37.61	9.73	2.09	0.32	4.40	1.30	3.98	1.00	12.34	2.48	0.54	26.14	3.53	4.07	25.36	13.00	29.42	102.07	0.867	As-td
an38	38.53	9.77	1.16	0.17	2.10	0.61	6.78	1.67	12.21	5.05	1.09	22.31	2.95	4.04	25.88	13.00	29.25	101.83	0.731	As-td
an39	47.47	2.94	0.02	0.00	0.96	0.07	0.02	0.00	3.01	17.67	0.93	1.16	0.04	0.97	32.56	4.00	7.98	99.86	0.039	enr
an40	45.30	2.97	0.10	0.00	0.62	0.05	0.02	0.00	3.02	15.46	0.86	5.33	0.18	1.04	30.82	4.00	8.06	97.66	0.175	luz
an41	37.81	9.68	1.32	0.20	0.82	0.24	7.24	1.80	11.92	3.23	0.70	24.32	3.25	3.95	25.63	13.00	28.87	100.37	0.823	As-td
an42	46.69	2.90	0.05	0.00	0.30	0.02	0.08	0.01	2.92	17.11	0.90	2.32	0.08	0.98	32.54	4.00	7.90	99.09	0.077	enr
an43	40.16	9.68	0.57	0.08	0.55	0.15	8.12	1.90	11.81	11.80	2.41	12.14	1.53	3.94	27.21	13.00	28.75	100.54	0.388	Sb-tn

CHM7-23.5

	Cu		Ag		Fe		Zn		total apfu	As		Sb		total apfu	S		total apfu	total wt%	Sb/(As+Sb)	
	wt%	*apfu*	wt%	*apfu*	wt%	*apfu*	wt%	*apfu*		wt%	*apfu*	wt%	*apfu*		wt%	*apfu*				Mineral
an1	41.47	10.34	0.49	0.07	2.78	0.79	7.42	1.80	13.00	12.23	2.59	10.41	1.35	3.94	26.31	13.00	29.94	101.11	0.344	Sb-tn
an2	40.36	10.10	0.35	0.05	2.29	0.65	7.94	1.93	12.74	11.01	2.34	12.18	1.59	3.93	26.20	13.00	29.67	100.34	0.405	Sb-tn
an3	40.79	10.26	0.39	0.06	2.23	0.64	8.13	1.99	12.94	8.90	1.90	15.79	2.07	3.97	26.09	13.00	29.91	102.32	0.522	As-td
an4	47.12	3.15	0.25	0.01	1.09	0.08	0.09	0.01	3.25	12.66	0.72	7.41	0.26	0.98	30.18	4.00	8.23	98.80	0.265	luz
an5	48.58	3.16	0.40	0.02	0.90	0.07	0.03	0.00	3.24	16.90	0.93	1.50	0.05	0.98	31.05	4.00	8.22	99.34	0.052	enr
an6	47.80	3.11	0.35	0.01	1.36	0.10	0.08	0.01	3.23	15.08	0.83	4.34	0.15	0.98	30.98	4.00	8.21	99.99	0.150	luz
an7	48.13	3.08	0.40	0.02	1.63	0.12	0.14	0.01	3.22	17.59	0.95	0.10	0.00	0.96	31.54	4.00	8.18	99.54	0.003	enr
an8	33.77	1.02	0.08	0.00	31.69	1.09	0.02	0.00	2.11	0.00	0.00	0.00	0.00	0.00	33.43	2.00	4.11	98.99		ccp
an9	34.12	1.02	0.08	0.00	31.58	1.07	0.03	0.00	2.09	0.00	0.00	0.00	0.00	0.00	33.80	2.00	4.09	99.62		ccp
an10	34.79	1.04	0.53	0.01	30.53	1.04	0.07	0.00	2.10	0.00	0.00	0.00	0.00	0.00	33.67	2.00	4.10	99.59		ccp
an11	47.18	3.12	0.53	0.02	1.88	0.14	0.10	0.01	3.29	16.90	0.95	1.24	0.04	0.99	30.50	4.00	8.28	98.33	0.043	enr
an12	46.67	3.04	0.43	0.02	1.63	0.12	0.07	0.00	3.19	17.42	0.96	0.87	0.03	0.99	30.94	4.00	8.18	98.02	0.030	enr
an13	38.99	10.19	0.31	0.05	0.78	0.23	8.33	2.11	12.58	7.07	1.57	18.81	2.56	4.13	25.11	13.00	29.71	99.38	0.621	As-td
an14	41.96	10.08	0.70	0.10	3.62	0.99	6.02	1.40	12.58	16.33	3.33	2.99	0.37	3.70	27.30	13.00	29.28	98.92	0.101	Sb-tn
an15	49.86	3.13	0.32	0.01	1.22	0.09	0.03	0.00	3.23	17.57	0.94	0.26	0.01	0.94	32.14	4.00	8.18	101.40	0.009	enr
an16	48.24	3.10	0.32	0.01	0.45	0.03	0.15	0.01	3.15	14.34	0.78	5.58	0.19	0.97	31.42	4.00	8.12	100.51	0.193	luz
an17	47.85	3.06	0.28	0.01	0.91	0.07	0.01	0.00	3.14	16.21	0.88	2.95	0.10	0.98	31.53	4.00	8.12	99.73	0.101	luz
an18	48.72	3.08	0.40	0.02	0.45	0.03	0.15	0.01	3.14	18.02	0.97	0.10	0.00	0.97	31.91	4.00	8.11	99.77	0.003	enr
an19	46.82	3.02	0.06	0.00	1.36	0.10	0.13	0.01	3.13	13.25	0.73	8.35	0.28	1.01	31.25	4.00	8.14	101.22	0.279	luz
an20	45.62	3.02	0.07	0.00	1.64	0.12	0.14	0.01	3.15	9.79	0.55	14.24	0.49	1.04	30.50	4.00	8.20	101.98	0.472	luz
an21	66.04	1.34	0.43	0.01	0.57	0.01	5.00	0.10	1.45	1.45	0.02	0.07	0.00	0.03	24.95	1.00	2.48	98.50		spk
an22	67.72	1.41	0.25	0.00	0.72	0.02	6.37	0.13	1.55	0.00	0.00	0.00	0.00	0.00	24.32	1.00	2.55	99.38		spk
an24	47.28	3.03	0.36	0.01	1.21	0.09	0.19	0.01	3.14	18.01	0.98	0.48	0.02	0.99	31.51	4.00	8.14	99.03	0.016	enr
an25	47.24	3.06	0.26	0.01	0.98	0.07	0.04	0.00	3.14	14.10	0.77	5.87	0.20	0.97	31.19	4.00	8.11	99.69	0.204	luz
an26	47.47	3.05	0.35	0.01	0.99	0.07	0.08	0.00	3.14	16.39	0.89	2.55	0.09	0.98	31.38	4.00	8.12	99.19	0.087	enr
an27	48.02	3.08	0.44	0.02	0.65	0.05	0.15	0.01	3.15	13.98	0.76	6.17	0.21	0.97	31.51	4.00	8.11	100.90	0.213	luz
an28	41.66	10.49	0.28	0.04	0.68	0.20	8.40	2.06	12.79	8.38	1.79	16.87	2.22	4.01	26.05	13.00	29.79	102.32	0.553	As-td
an29	41.10	10.46	0.34	0.05	0.77	0.22	8.46	2.09	12.83	7.64	1.65	18.19	2.42	4.07	25.77	13.00	29.89	102.26	0.594	As-td
an30	48.11	3.06	0.18	0.01	1.67	0.12	0.13	0.01	3.20	18.06	0.97	0.67	0.02	1.00	31.73	4.00	8.19	100.55	0.022	enr
an31	0.76	0.02	0.00	0.00	47.17	1.10	0.03	0.00	1.11	0.00	0.00	0.00	0.00	0.00	49.45	2.00	3.11	97.40		py
an32	47.34	3.02	0.44	0.02	2.25	0.16	0.03	0.00	3.21	16.07	0.87	2.96	0.10	0.97	31.60	4.00	8.17	100.69	0.102	luz
an33	48.00	3.06	0.38	0.01	1.67	0.12	0.02	0.00	3.20	16.49	0.89	2.01	0.07	0.96	31.67	4.00	8.15	100.24	0.070	enr
an34	47.92	3.02	0.47	0.02	2.81	0.20	0.03	0.00	3.24	16.51	0.88	1.49	0.05	0.93	31.99	4.00	8.18	101.22	0.053	enr
an35	34.55	1.04	0.05	0.00	31.44	1.07	0.02	0.00	2.11	0.00	0.00	0.01	0.00	0.00	33.62	2.00	4.11	99.69		ccp
an36	38.59	1.19	4.98	0.09	13.20	0.46	11.29	0.34	2.07	0.00	0.00	0.02	0.00	0.00	32.84	2.00	4.07	100.92		ccp

an37	27.75	1.55	0.16	0.01	14.73	0.94	5.46	0.30	2.79	8.17	0.39	5.90	0.17	0.56	36.09	4.00	7.35	98.25	0.308	luz
an38	48.02	3.03	0.29	0.01	2.22	0.16	0.02	0.00	3.20	17.56	0.94	1.16	0.04	0.98	32.00	4.00	8.18	101.27	0.039	enr
an40	40.27	10.47	0.64	0.10	0.86	0.26	7.49	1.89	12.72	5.43	1.20	20.61	2.80	3.99	25.23	13.00	29.71	100.53	0.700	As-td
an41	40.04	10.24	0.49	0.07	0.96	0.28	7.43	1.85	12.43	5.18	1.12	21.57	2.88	4.00	25.66	13.00	29.43	101.34	0.719	As-td
an42	39.83	10.33	0.58	0.09	0.95	0.28	7.44	1.87	12.57	3.83	0.84	23.30	3.15	4.00	25.30	13.00	29.57	101.22	0.789	As-td
an43	39.58	10.14	0.47	0.07	1.10	0.32	7.45	1.85	12.39	4.13	0.90	23.33	3.12	4.02	25.60	13.00	29.41	101.65	0.776	As-td
an44	40.28	10.08	0.54	0.08	0.52	0.15	8.02	1.95	12.26	6.98	1.48	18.56	2.43	3.91	26.21	13.00	29.17	101.10	0.621	As-td
an45	40.81	10.39	0.53	0.08	0.37	0.11	7.92	1.96	12.54	6.64	1.43	19.13	2.54	3.98	25.76	13.00	29.51	101.15	0.639	As-td
an46	39.71	10.15	0.34	0.05	0.62	0.18	7.80	1.94	12.32	5.48	1.19	21.42	2.86	4.05	25.65	13.00	29.37	101.01	0.706	As-td
an47	42.43	10.17	0.26	0.04	2.72	0.74	5.69	1.33	12.27	15.50	3.15	6.71	0.84	3.99	27.37	13.00	29.27	100.67	0.210	Sb-tn
an48	39.65	10.10	0.45	0.07	1.14	0.33	7.18	1.78	12.28	5.22	1.13	21.51	2.86	3.99	25.75	13.00	29.26	100.90	0.717	As-td
an49	42.08	10.19	0.20	0.03	3.74	1.03	4.39	1.03	12.28	14.82	3.04	7.00	0.88	3.93	27.10	13.00	29.21	99.33	0.225	Sb-tn
an50	40.19	10.24	0.64	0.10	0.54	0.16	7.95	1.97	12.46	8.02	1.73	16.75	2.23	3.96	25.76	13.00	29.41	99.85	0.562	As-td
an51	40.82	10.27	0.31	0.05	1.39	0.40	7.01	1.71	12.43	7.57	1.62	18.43	2.42	4.04	26.06	13.00	29.47	101.58	0.600	As-td
an52	43.50	10.51	0.85	0.12	4.15	1.14	3.63	0.85	12.62	13.70	2.81	6.07	0.76	3.57	27.16	13.00	29.19	99.06	0.214	Sb-tn
an53	41.55	10.44	0.34	0.05	2.51	0.72	5.81	1.42	12.63	9.48	2.02	14.87	1.95	3.97	26.10	13.00	29.60	100.65	0.491	Sb-tn
an54	41.80	10.34	0.35	0.05	1.37	0.39	7.10	1.71	12.48	10.24	2.15	13.74	1.77	3.92	26.52	13.00	29.40	101.11	0.452	Sb-tn
an55	40.36	10.36	0.45	0.07	0.82	0.24	8.02	2.00	12.66	7.54	1.64	17.41	2.33	3.97	25.56	13.00	29.63	100.16	0.587	As-td
an56	41.01	10.11	0.34	0.05	3.11	0.87	5.25	1.26	12.29	10.73	2.24	13.74	1.77	4.01	26.61	13.00	29.30	100.79	0.441	Sb-tn
an57	40.12	10.14	0.33	0.05	1.06	0.30	7.44	1.83	12.32	8.68	1.86	16.49	2.18	4.04	25.95	13.00	29.36	100.06	0.539	As-td
an58	39.56	10.01	0.17	0.03	0.50	0.14	8.06	1.98	12.16	6.87	1.47	19.25	2.54	4.02	25.92	13.00	29.18	100.32	0.633	As-td
an59	4.13	0.07	0.31	0.00	1.83	0.03	62.90	0.97	1.07	0.00	0.00	0.00	0.00	0.00	31.75	1.00	2.07	100.91		sp
an60	0.32	0.01	0.00	0.00	1.65	0.03	67.06	1.01	1.05	0.00	0.00	0.00	0.00	0.00	32.42	1.00	2.05	101.47		sp
an61	1.06	0.02	0.00	0.00	2.15	0.04	66.06	0.98	1.04	0.00	0.00	0.00	0.00	0.00	32.94	1.00	2.04	102.21		sp
an62	4.24	0.07	0.19	0.00	2.73	0.05	61.67	0.94	1.06	0.00	0.00	0.00	0.00	0.00	31.99	1.00	2.06	100.83		sp
an63	39.84	10.26	0.60	0.09	0.85	0.25	7.64	1.91	12.50	4.76	1.04	21.65	2.91	3.95	25.48	13.00	29.45	100.81	0.737	As-td
an64	39.42	10.21	0.46	0.07	0.76	0.22	7.75	1.95	12.45	5.54	1.22	20.91	2.83	4.04	25.34	13.00	29.49	100.18	0.699	As-td
an65	40.16	10.50	0.82	0.13	0.58	0.17	7.43	1.89	12.69	4.23	0.94	21.37	2.92	3.86	25.08	13.00	29.54	99.67	0.756	As-td

Gold

	Au	Ag	Cu	Total		Au	Ag	Cu	Total
	wt%	wt%	wt%	wt%		wt%	wt%	wt%	wt%
an66	76.60	22.56	0.42	99.58	an70	76.78	22.01	0.49	99.28
an67	76.76	22.49	0.48	99.73	an71	76.24	22.57	0.49	99.30
an68	75.64	22.80	0.54	98.98	an72	76.03	22.08	0.50	98.60
an69	76.09	22.19	0.47	98.74	an73	76.42	22.70	0.57	99.70

CHM7-31.4

	Cu		Ag		Fe		Zn		total apfu	As		Sb		total apfu	S		total apfu	total wt%	Sb/(As+Sb)	
	wt%	*apfu*	wt%	*apfu*	wt%	*apfu*	wt%	*apfu*		wt%	*apfu*	wt%	*apfu*		wt%	*apfu*				Mineral
an1	41.46	10.54	0.08	0.01	0.65	0.19	8.39	2.07	12.81	11.63	2.51	14.78	1.96	4.47	25.81	13.00	30.28	102.80	0.439	Sb-tn
an2	41.41	10.62	0.07	0.01	0.90	0.26	8.46	2.11	13.00	8.94	1.95	16.48	2.21	4.15	25.57	13.00	30.16	101.83	0.531	As-td
an3	40.90	10.58	0.06	0.01	0.62	0.18	8.44	2.12	12.89	9.68	2.12	16.50	2.23	4.35	25.35	13.00	30.25	101.54	0.512	As-td
an4	39.76	10.23	0.10	0.02	1.25	0.36	8.20	2.05	12.66	7.81	1.70	17.97	2.41	4.12	25.49	13.00	29.78	100.57	0.586	As-td
an5	39.83	10.25	0.11	0.02	0.78	0.23	8.22	2.06	12.56	8.25	1.80	17.64	2.37	4.17	25.48	13.00	29.73	100.30	0.568	As-td
an6	39.39	10.22	0.10	0.01	0.64	0.19	8.13	2.05	12.47	7.93	1.74	18.43	2.49	4.24	25.29	13.00	29.71	99.91	0.588	As-td
an7	39.84	10.31	0.10	0.02	0.76	0.22	8.15	2.05	12.59	7.49	1.64	18.37	2.48	4.12	25.36	13.00	29.72	100.06	0.601	As-td
an8	39.43	10.17	0.19	0.03	0.76	0.22	8.04	2.01	12.44	7.46	1.63	18.48	2.49	4.12	25.43	13.00	29.56	99.79	0.604	As-td
an9	39.89	10.24	0.08	0.01	0.56	0.16	8.13	2.03	12.45	8.37	1.82	17.60	2.36	4.18	25.54	13.00	29.63	100.16	0.564	As-td
an10	38.92	10.06	0.10	0.01	0.48	0.14	8.05	2.02	12.24	8.20	1.80	17.53	2.36	4.16	25.38	13.00	29.40	98.65	0.568	As-td
an11	39.57	9.99	0.15	0.02	0.53	0.15	8.25	2.02	12.19	9.90	2.12	15.70	2.07	4.19	25.98	13.00	29.38	100.08	0.494	Sb-tn
an12	40.80	10.12	0.05	0.01	0.52	0.15	8.68	2.09	12.37	11.12	2.34	13.31	1.72	4.06	26.44	13.00	29.43	100.91	0.424	Sb-tn
an13	0.79	0.01	0.01	0.00	48.15	1.04	0.12	0.00	1.06	0.00	0.00	0.07	0.00	0.00	53.08	2.00	3.06	102.21		py
an14	40.12	10.09	0.09	0.01	0.48	0.14	8.45	2.06	12.31	8.37	1.79	16.93	2.22	4.01	26.08	13.00	29.32	100.53	0.554	As-td
an15	35.23	1.06	0.02	0.00	31.13	1.07	0.22	0.01	2.14	0.00	0.00	0.08	0.00	0.00	33.43	2.00	4.14	100.10		ccp
an16	40.22	10.40	0.05	0.01	0.46	0.13	8.59	2.16	12.69	8.47	1.86	18.10	2.44	4.30	25.38	13.00	29.99	101.26	0.568	As-td
an17	40.29	10.11	0.11	0.02	0.58	0.17	8.34	2.03	12.33	8.33	1.77	14.58	1.91	3.68	26.14	13.00	29.01	98.36	0.519	As-td
an18	39.67	10.03	0.09	0.01	0.44	0.13	8.27	2.03	12.20	8.24	1.77	16.25	2.14	3.91	25.95	13.00	29.11	98.90	0.548	As-td
an19	35.17	1.03	0.00	0.00	31.75	1.06	0.05	0.00	2.10	0.00	0.00	0.21	0.00	0.00	34.34	2.00	4.10	101.52		ccp
an20	35.34	1.04	0.03	0.00	31.41	1.05	0.00	0.00	2.10	0.00	0.00	0.04	0.00	0.00	34.22	2.00	4.10	101.03		ccp
an21	38.07	10.28	0.30	0.05	2.26	0.69	7.56	1.98	13.01	2.25	0.52	26.98	3.80	4.32	24.29	13.00	30.33	101.70	0.881	As-td
an22	39.64	10.26	0.15	0.02	2.81	0.83	6.98	1.75	12.86	8.12	1.78	18.33	2.48	4.26	25.35	13.00	30.12	101.37	0.582	As-td
an23	38.88	10.28	0.26	0.04	1.35	0.41	7.68	1.97	12.70	4.18	0.94	25.30	3.49	4.43	24.81	13.00	30.13	102.47	0.788	As-td
an24	37.39	9.88	0.21	0.03	2.24	0.67	7.71	1.98	12.57	6.27	1.41	19.24	2.66	4.06	24.81	13.00	29.63	97.88	0.654	As-td
an25	0.26	0.00	0.00	0.00	48.20	1.06	0.03	0.00	1.06	0.00	0.00	0.05	0.00	0.00	52.42	2.00	3.06	100.95		py
an26	40.27	9.79	0.07	0.01	0.33	0.09	8.20	1.94	11.82	12.63	2.60	11.07	1.40	4.01	27.00	13.00	28.83	99.56	0.350	Sb-tn
an27	40.47	10.17	0.17	0.03	0.89	0.26	7.80	1.90	12.35	9.59	2.04	16.15	2.12	4.16	26.10	13.00	29.52	101.17	0.509	As-td
an28	40.91	9.96	0.05	0.01	0.24	0.07	8.36	1.98	12.01	14.17	2.93	9.32	1.18	4.11	26.93	13.00	29.13	99.98	0.288	Sb-tn
an29	38.18	10.11	0.16	0.03	1.53	0.46	7.64	1.97	12.57	2.07	0.46	26.94	3.72	4.19	24.76	13.00	29.76	101.29	0.889	As-td
an30	39.38	9.92	0.07	0.01	0.58	0.17	8.44	2.06	12.16	8.17	1.74	18.18	2.39	4.13	26.04	13.00	29.30	100.84	0.578	As-td
an31	37.67	9.74	0.18	0.03	0.90	0.26	7.58	1.90	11.93	2.96	0.65	24.61	3.32	3.97	25.38	13.00	28.90	99.28	0.836	As-td
an32	39.35	9.95	0.11	0.02	0.62	0.18	8.92	2.19	12.33	6.69	1.43	20.08	2.65	4.08	25.95	13.00	29.41	101.72	0.649	As-td
an33	39.62	9.88	0.12	0.02	1.54	0.44	7.38	1.79	12.13	7.36	1.56	18.76	2.44	4.00	26.29	13.00	29.13	101.07	0.611	As-td
an34	39.48	9.90	0.10	0.01	0.16	0.05	9.49	2.31	12.27	7.15	1.52	19.61	2.57	4.09	26.16	13.00	29.36	102.15	0.628	As-td
an35	39.69	10.13	0.09	0.01	0.84	0.24	8.22	2.04	12.42	8.94	1.93	17.07	2.27	4.21	25.70	13.00	29.63	100.54	0.540	As-td
an36	39.24	10.33	0.19	0.03	1.04	0.31	8.21	2.10	12.77	5.90	1.32	23.45	3.22	4.54	24.92	13.00	30.31	102.95	0.710	As-td
an37	39.82	10.18	0.08	0.01	1.03	0.30	8.07	2.01	12.50	8.35	1.81	17.52	2.34	4.15	25.65	13.00	29.65	100.54	0.563	As-td
an38	39.93	10.05	0.10	0.01	0.88	0.25	8.92	2.18	12.50	7.85	1.67	18.41	2.42	4.09	26.07	13.00	29.59	102.16	0.591	As-td
an39	39.36	10.05	0.09	0.01	0.39	0.11	8.16	2.02	12.20	5.89	1.27	20.52	2.73	4.01	25.69	13.00	29.21	100.10	0.682	As-td
an40	40.34	9.94	0.08	0.01	0.27	0.08	8.78	2.10	12.12	8.89	1.86	16.94	2.18	4.03	26.63	13.00	29.16	101.92	0.540	As-td
an41	38.29	9.97	0.12	0.02	0.97	0.29	8.12	2.05	12.33	7.36	1.63	18.07	2.46	4.08	25.20	13.00	29.41	98.12	0.602	As-td
an42	39.43	10.04	0.05	0.01	1.37	0.40	8.11	2.01	12.44	9.42	2.03	15.65	2.08	4.11	25.77	13.00	29.56	99.79	0.505	As-td
an43	38.64	10.09	0.24	0.04	1.98	0.59	7.99	2.03	12.74	8.10	1.79	18.13	2.47	4.26	25.13	13.00	30.00	100.21	0.579	As-td
an44	35.87	1.13	0.12	0.00	25.35	0.91	0.62	0.02	2.05	0.96	0.03	2.91	0.05	0.07	32.11	2.00	4.13	97.94		ccp
an45	39.05	9.93	0.06	0.01	0.26	0.07	8.40	2.07	12.08	8.02	1.73	17.59	2.33	4.06	25.80	13.00	29.15	99.17	0.574	As-td
an46	39.89	9.98	0.19	0.03	0.12	0.03	8.47	2.06	12.10	7.06	1.50	18.92	2.47	3.97	26.21	13.00	29.07	100.85	0.623	As-td
an47	39.43	10.34	0.26	0.04	0.81	0.24	7.52	1.91	12.53	4.34	0.96	23.62	3.23	4.20	25.02	13.00	29.73	100.99	0.770	As-td
an48	39.51	10.17	0.31	0.05	0.34	0.10	8.24	2.06	12.38	7.07	1.54	19.09	2.56	4.11	25.49	13.00	29.48	100.05	0.624	As-td
an49	42.60	10.20	0.15	0.02	0.35	0.10	9.09	2.11	12.43	18.88	3.83	1.98	0.25	4.08	27.40	13.00	29.51	100.44	0.061	Sb-tn
an50	34.00	1.06	0.05	0.00	30.93	1.10	0.09	0.00	2.17	0.00	0.00	0.00	0.00	0.00	32.25	2.00	4.17	97.31		ccp
an51	40.26	10.52	0.19	0.03	0.27	0.08	8.61	2.19	12.82	13.04	2.89	13.09	1.78	4.67	25.10	13.00	30.49	100.56	0.382	Sb-tn
an52	41.18	10.26	0.20	0.03	0.35	0.10	8.65	2.09	12.48	18.67	3.95	5.22	0.68	4.62	26.33	13.00	30.10	100.59	0.147	Sb-tn
an53	39.77	10.44	0.30	0.05	0.26	0.08	8.50	2.17	12.73	8.86	1.97	17.32	2.37	4.34	24.99	13.00	30.08	100.00	0.546	As-td
an54	39.38	10.08	0.13	0.02	0.19	0.06	9.64	2.40	12.55	6.42	1.39	20.39	2.72	4.12	25.64	13.00	29.66	101.80	0.662	As-td
an55	39.42	9.77	0.25	0.04	5.55	1.56	6.41	1.54	12.91	5.31	1.12	19.95	2.58	3.70	26.48	13.00	29.61	103.38	0.698	As-td
an56	39.71	9.59	0.21	0.03	6.18	1.70	6.50	1.53	12.84	6.97	1.43	15.89	2.00	3.43	27.17	13.00	29.27	102.63	0.584	As-td
an57	40.44	10.21	0.13	0.02	0.81	0.23	9.35	2.29	12.76	8.42	1.80	17.58	2.32	4.12	25.97	13.00	29.88	102.70	0.562	As-td
an58	39.97	10.22	0.10	0.01	0.70	0.20	9.84	2.44	12.88	8.37	1.81	17.79	2.37	4.19	25.66	13.00	30.06	102.42	0.567	As-td
an59	40.00	10.17	0.14	0.02	0.17	0.05	8.76	2.16	12.40	8.96	1.93	16.80	2.23	4.16	25.81	13.00	29.56	100.63	0.536	As-td
an60	39.62	10.27	0.14	0.02	0.13	0.04	8.34	2.10	12.43	8.32	1.83	18.07	2.45	4.27	25.30	13.00	29.71	99.92	0.572	As-td

an61	39.35	10.23	0.22	0.03	0.17	0.05	8.51	2.15	12.46	7.82	1.72	18.99	2.58	4.30	25.24	13.00	29.76	100.30	0.599	As-td
an62	42.09	9.91	0.04	0.01	0.10	0.03	8.85	2.02	11.97	18.15	3.63	2.39	0.29	3.92	27.85	13.00	28.89	99.47	0.075	Sb-tn
an63	40.89	10.59	0.07	0.01	0.08	0.02	8.67	2.18	12.80	8.23	1.81	18.29	2.47	4.28	25.33	13.00	30.08	101.57	0.578	As-td
an64	40.50	10.66	0.09	0.01	0.20	0.06	8.31	2.12	12.85	9.12	2.04	17.79	2.44	4.48	24.93	13.00	30.33	100.93	0.545	As-td
an65	40.13	10.16	0.21	0.03	0.14	0.04	8.93	2.20	12.43	8.12	1.74	17.72	2.34	4.09	25.90	13.00	29.52	101.15	0.573	As-td
an66	40.55	10.30	0.22	0.03	0.38	0.11	8.69	2.14	12.58	9.02	1.94	16.56	2.19	4.14	25.83	13.00	29.72	101.23	0.530	As-td

CHM1B

	Cu		Ag		Fe		Zn		total apfu	As		Sb		total apfu	S		total apfu	total wt%	Sb/(As+Sb)	
	wt%	*apfu*	wt%	*apfu*	wt%	*apfu*	wt%	*apfu*		wt%	*apfu*	wt%	*apfu*		wt%	*apfu*				Mineral
an1	71.11	1.34	0.49	0.01	0.02	0.00	0.04	0.00	1.35	0.00	0.00	0.00	0.00	0.00	26.72	1.00	2.35	98.38		spk
an2	72.37	1.46	1.17	0.01	0.01	0.00	0.05	0.00	1.48	0.00	0.00	0.00	0.00	0.00	24.94	1.00	2.48	98.54		spk
an3	71.20	1.32	0.50	0.01	0.00	0.00	0.05	0.00	1.32	0.00	0.00	0.00	0.00	0.00	27.31	1.00	2.32	99.06		spk
an4	74.57	1.42	0.08	0.00	0.02	0.00	0.05	0.00	1.43	0.00	0.00	0.00	0.00	0.00	26.44	1.00	2.43	101.16		spk
an5	72.65	1.31	0.11	0.00	0.01	0.00	0.01	0.00	1.31	0.00	0.00	0.00	0.00	0.00	28.07	1.00	2.31	100.85		spk
an6	71.24	1.35	0.44	0.00	0.00	0.00	0.06	0.00	1.36	0.00	0.00	0.01	0.00	0.00	26.56	1.00	2.36	98.31		spk
an7	68.98	1.24	0.98	0.01	0.01	0.00	0.07	0.00	1.26	0.00	0.00	0.00	0.00	0.00	27.96	1.00	2.26	98.00		yr
an8	71.18	1.34	0.63	0.01	0.01	0.00	0.05	0.00	1.34	0.00	0.00	0.00	0.00	0.00	26.90	1.00	2.34	98.77		spk
an9	74.42	1.56	0.45	0.01	0.02	0.00	0.06	0.00	1.57	0.00	0.00	0.02	0.00	0.00	24.05	1.00	2.57	99.02		gr
an10	74.50	1.59	0.37	0.00	0.01	0.00	0.06	0.00	1.59	0.00	0.00	0.00	0.00	0.00	23.68	1.00	2.59	98.62		gr

CHM10A

	Cu		Ag		Fe		Zn		total apfu	As		Sb		total apfu	S		total apfu	total wt%	Sb/(As+Sb)	
	wt%	*apfu*	wt%	*apfu*	wt%	*apfu*	wt%	*apfu*		wt%	*apfu*	wt%	*apfu*		wt%	*apfu*				Mineral
an1	39.88	10.35	0.02	0.00	0.38	0.11	8.18	2.06	12.53	6.67	1.47	19.88	2.69	4.16	25.27	13.00	29.69	100.27	0.647	As-td
an2	40.11	10.27	0.02	0.00	0.35	0.10	8.24	2.05	12.42	8.00	1.74	18.37	2.45	4.19	25.63	13.00	29.61	100.71	0.585	As-td
an3	41.65	10.61	0.04	0.01	0.26	0.07	8.26	2.04	12.74	9.85	2.13	15.57	2.07	4.20	25.75	13.00	29.93	101.38	0.493	Sb-tn
an4	40.76	10.58	0.05	0.01	0.34	0.10	8.17	2.06	12.75	5.25	1.16	22.48	3.05	4.20	25.26	13.00	29.96	102.30	0.725	As-td
an5	41.19	10.69	0.03	0.00	0.44	0.13	8.22	2.07	12.89	8.15	1.79	18.17	2.46	4.25	25.28	13.00	30.15	101.47	0.579	As-td
an6	40.16	10.48	0.06	0.01	0.37	0.11	8.43	2.14	12.74	5.41	1.20	22.05	3.00	4.20	25.13	13.00	29.94	101.60	0.715	As-td
an7	44.50	10.74	0.03	0.00	0.93	0.25	7.97	1.87	12.87	21.00	4.30	0.10	0.01	4.31	27.18	13.00	30.18	101.69	0.003	tn
an8	47.70	3.19	0.08	0.00	0.41	0.03	0.17	0.01	3.24	12.26	0.70	12.16	0.42	1.12	30.17	4.00	8.36	102.94	0.379	luz
an9	46.68	3.16	0.03	0.00	0.94	0.07	0.18	0.01	3.25	8.50	0.49	15.07	0.53	1.02	29.78	4.00	8.27	101.17	0.522	fm
an10	48.81	3.21	0.04	0.00	0.28	0.02	0.18	0.01	3.24	15.46	0.86	5.63	0.19	1.06	30.70	4.00	8.30	101.11	0.183	luz
an11	42.63	10.10	0.04	0.01	0.93	0.25	8.23	1.89	12.25	10.26	2.06	12.64	1.56	3.62	27.70	13.00	28.87	102.43	0.431	Sb-tn
an12	39.94	10.25	0.07	0.01	1.04	0.30	8.02	2.00	12.57	5.35	1.17	21.43	2.87	4.04	25.55	13.00	29.61	101.41	0.711	As-td
an13	40.61	10.24	0.03	0.00	0.56	0.16	8.30	2.03	12.44	7.79	1.67	18.28	2.41	4.07	26.00	13.00	29.52	101.56	0.591	As-td
an14	42.98	10.11	0.01	0.00	0.42	0.11	8.78	2.01	12.23	18.18	3.63	1.90	0.23	3.86	27.88	13.00	29.09	100.14	0.060	Sb-tn
an15	40.17	10.18	0.01	0.00	0.29	0.08	8.26	2.03	12.30	6.06	1.30	20.75	2.74	4.05	25.89	13.00	29.34	101.43	0.678	As-td
an16	40.53	10.37	0.04	0.01	0.09	0.03	8.27	2.06	12.45	6.94	1.51	19.78	2.64	4.15	25.65	13.00	29.60	101.29	0.637	As-td
an17	45.06	3.14	0.02	0.00	0.15	0.01	0.15	0.01	3.16	3.29	0.19	23.51	0.86	1.05	28.96	4.00	8.21	101.13	0.815	fm
an18	45.49	3.06	0.06	0.00	1.05	0.08	0.05	0.00	3.14	7.15	0.41	17.40	0.61	1.02	30.05	4.00	8.16	101.24	0.600	fm
an19	47.94	3.06	0.04	0.00	0.40	0.03	0.09	0.01	3.09	15.28	0.83	5.48	0.18	1.01	31.65	4.00	8.10	100.86	0.181	luz
an20	41.32	10.40	0.00	0.00	0.43	0.12	8.56	2.09	12.61	9.43	2.01	15.34	2.01	4.03	26.06	13.00	29.64	101.13	0.500	As-td
an21	40.49	10.89	0.04	0.01	0.51	0.16	8.39	2.19	13.24	7.36	1.68	19.75	2.77	4.45	24.40	13.00	30.69	100.93	0.623	As-td
an22	40.51	10.25	0.03	0.01	0.25	0.07	8.57	2.11	12.43	8.60	1.85	17.36	2.29	4.14	25.94	13.00	29.57	101.26	0.554	As-td
an23	40.11	10.12	0.02	0.00	0.52	0.15	8.13	1.99	12.27	6.51	1.39	19.74	2.60	3.99	25.99	13.00	29.26	101.04	0.651	As-td
an24	47.28	3.08	0.05	0.00	0.27	0.02	0.24	0.01	3.11	11.55	0.64	10.07	0.34	0.98	31.01	4.00	8.09	100.48	0.349	luz
an25	42.09	10.39	0.02	0.00	0.32	0.09	8.47	2.03	12.52	10.87	2.28	13.91	1.79	4.07	26.57	13.00	29.58	102.24	0.441	Sb-tn
an26	47.79	3.04	0.06	0.00	1.63	0.12	0.26	0.02	3.17	14.97	0.81	5.68	0.19	0.99	31.77	4.00	8.17	102.15	0.189	luz
an27	40.91	10.63	0.04	0.01	0.39	0.12	8.23	2.08	12.83	5.75	1.27	21.95	2.98	4.24	25.24	13.00	30.07	102.50	0.702	As-td
an28	46.05	3.07	0.04	0.00	0.88	0.07	0.10	0.01	3.14	9.17	0.52	14.40	0.50	1.02	30.32	4.00	8.16	100.96	0.491	luz
an29	47.96	3.08	0.03	0.00	0.47	0.03	0.17	0.01	3.13	15.23	0.83	5.77	0.19	1.02	31.43	4.00	8.15	101.05	0.189	luz
an30	40.58	10.74	0.02	0.00	0.38	0.11	8.18	2.10	12.96	7.15	1.60	19.88	2.74	4.35	24.79	13.00	30.31	100.99	0.631	As-td
an31	40.96	10.52	0.13	0.02	0.34	0.10	7.84	1.96	12.60	10.42	2.27	15.71	2.11	4.38	25.53	13.00	29.97	100.93	0.481	Sb-tn
an32	40.22	10.39	0.02	0.00	0.41	0.12	8.18	2.05	12.56	6.98	1.53	20.39	2.75	4.28	25.40	13.00	29.84	101.59	0.642	As-td
an33	47.10	3.06	0.06	0.00	0.32	0.02	0.12	0.01	3.10	14.82	0.82	7.35	0.25	1.07	31.03	4.00	8.16	100.80	0.234	luz
an34	38.22	9.82	0.09	0.01	0.44	0.13	7.94	1.98	11.94	8.13	1.77	17.98	2.41	4.18	25.53	13.00	29.13	98.32	0.576	As-td
an35	39.41	9.88	0.06	0.01	0.74	0.21	8.00	1.95	12.05	7.14	1.52	18.96	2.48	4.00	26.17	13.00	29.05	100.48	0.620	As-td
an36	1.12	0.02	0.00	0.00	1.86	0.03	66.81	1.02	1.07	0.00	0.00	0.03	0.00	0.00	32.12	1.00	2.07	101.94		sp
an37	1.42	0.02	0.00	0.00	2.10	0.04	66.24	1.01	1.07	0.00	0.00	0.00	0.00	0.00	32.17	1.00	2.07	101.93		sp
an38	34.66	1.02	0.00	0.00	31.98	1.07	0.00	0.00	2.10	0.00	0.00	0.04	0.00	0.00	34.22	2.00	4.10	100.90		ccp
an39	35.39	1.06	0.00	0.00	32.35	1.10	0.09	0.00	2.16	0.00	0.00	0.01	0.00	0.00	33.79	2.00	4.16	101.64		ccp
an40	49.45	3.07	0.04	0.00	0.56	0.04	0.06	0.00	3.11	15.54	0.82	2.68	0.09	0.90	32.56	4.00	8.01	100.88	0.096	enr

III. BSE images with spots of EPMA analysis

Sample CHM1-59

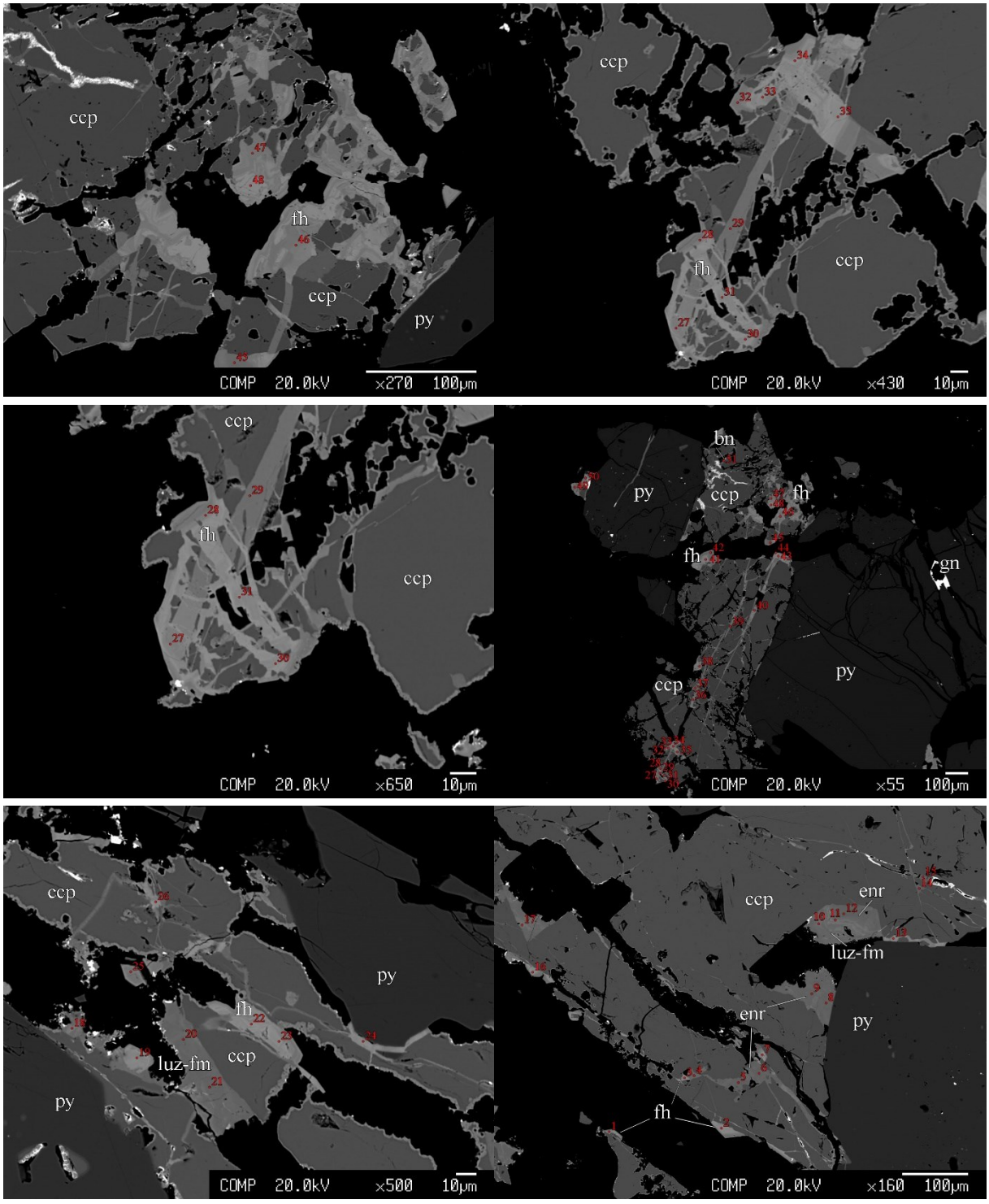

Sample CHM2-39(1)

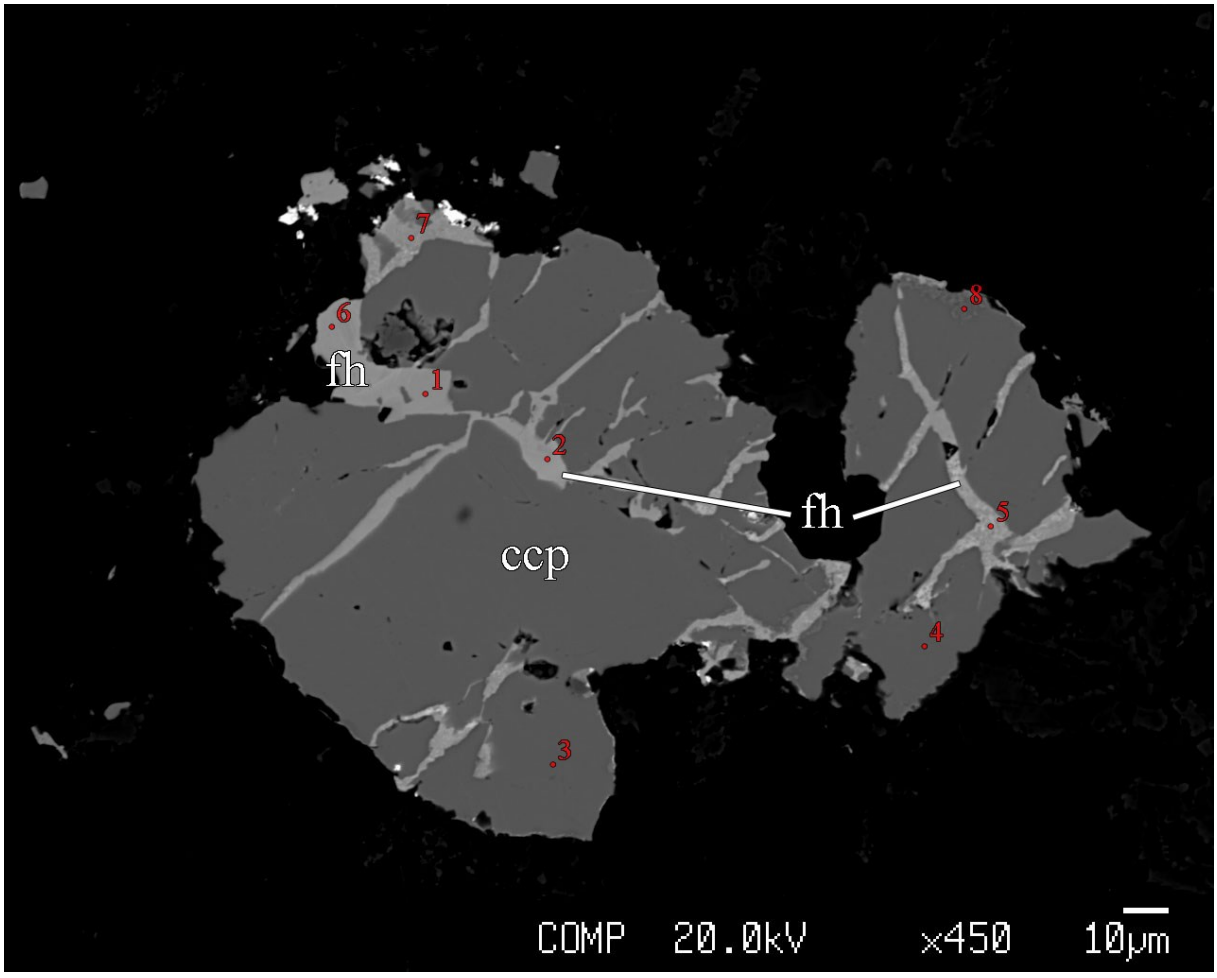

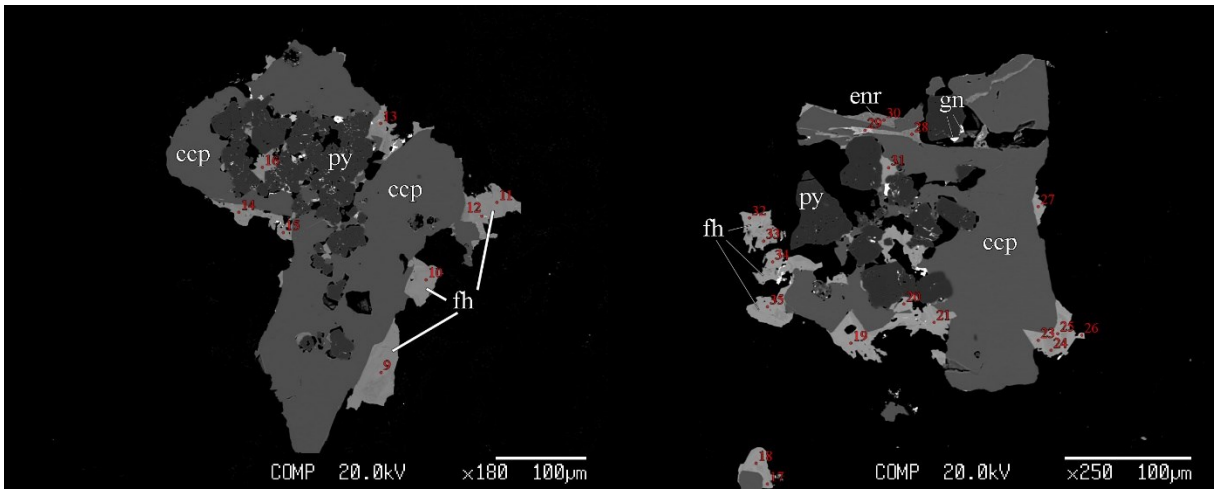

Sample CHM2-39.5(2)

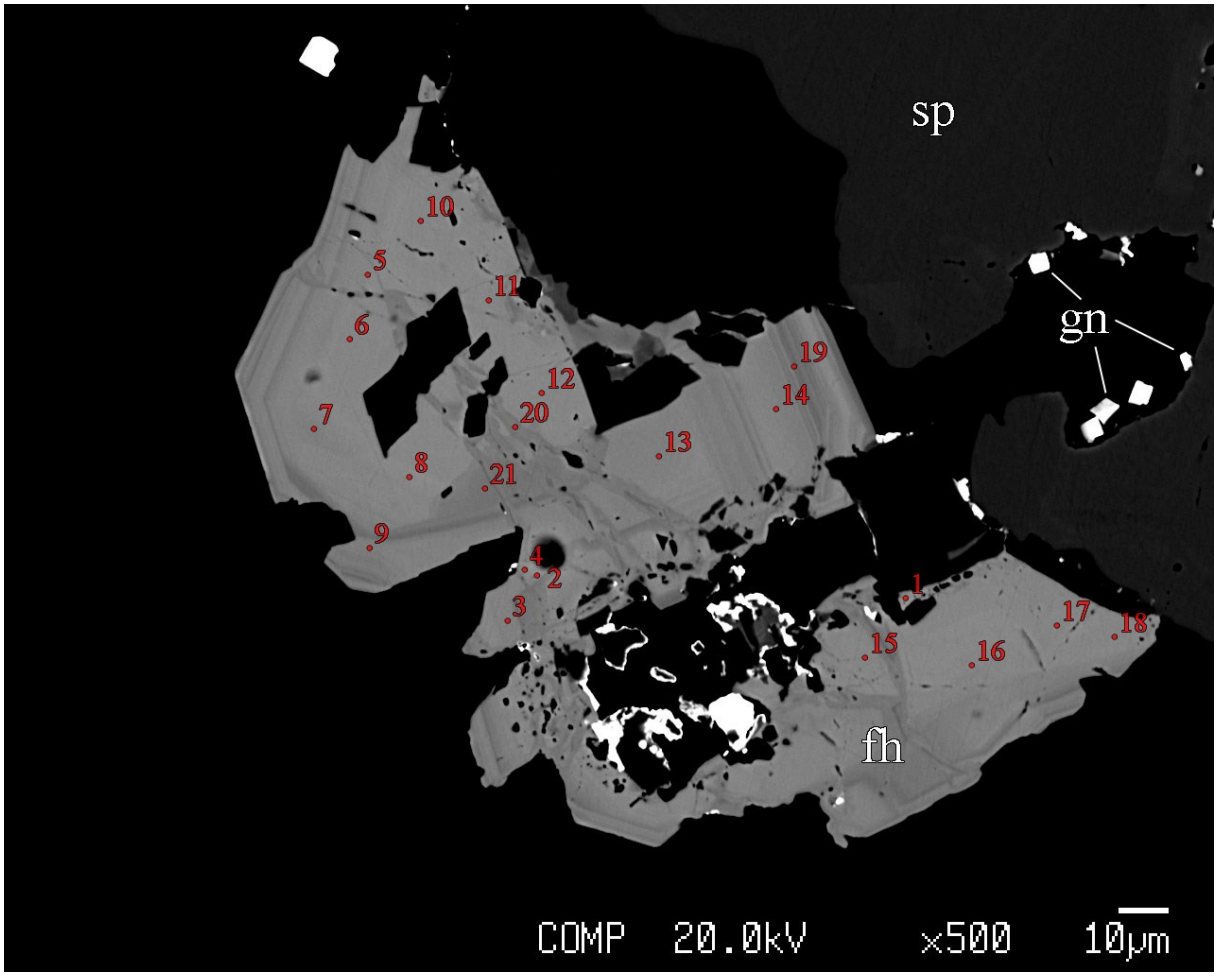

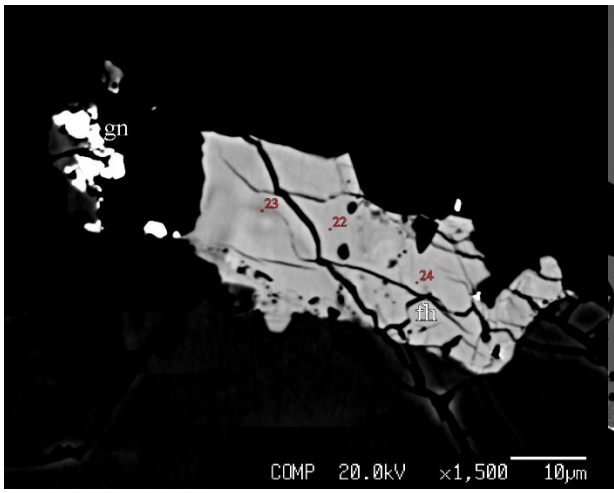

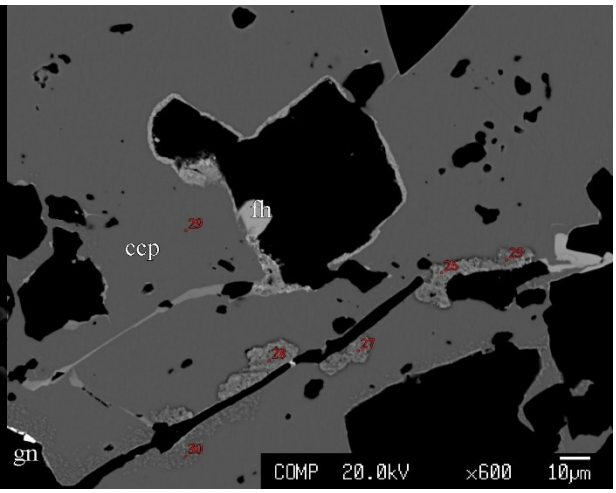

Sample CHM2-69

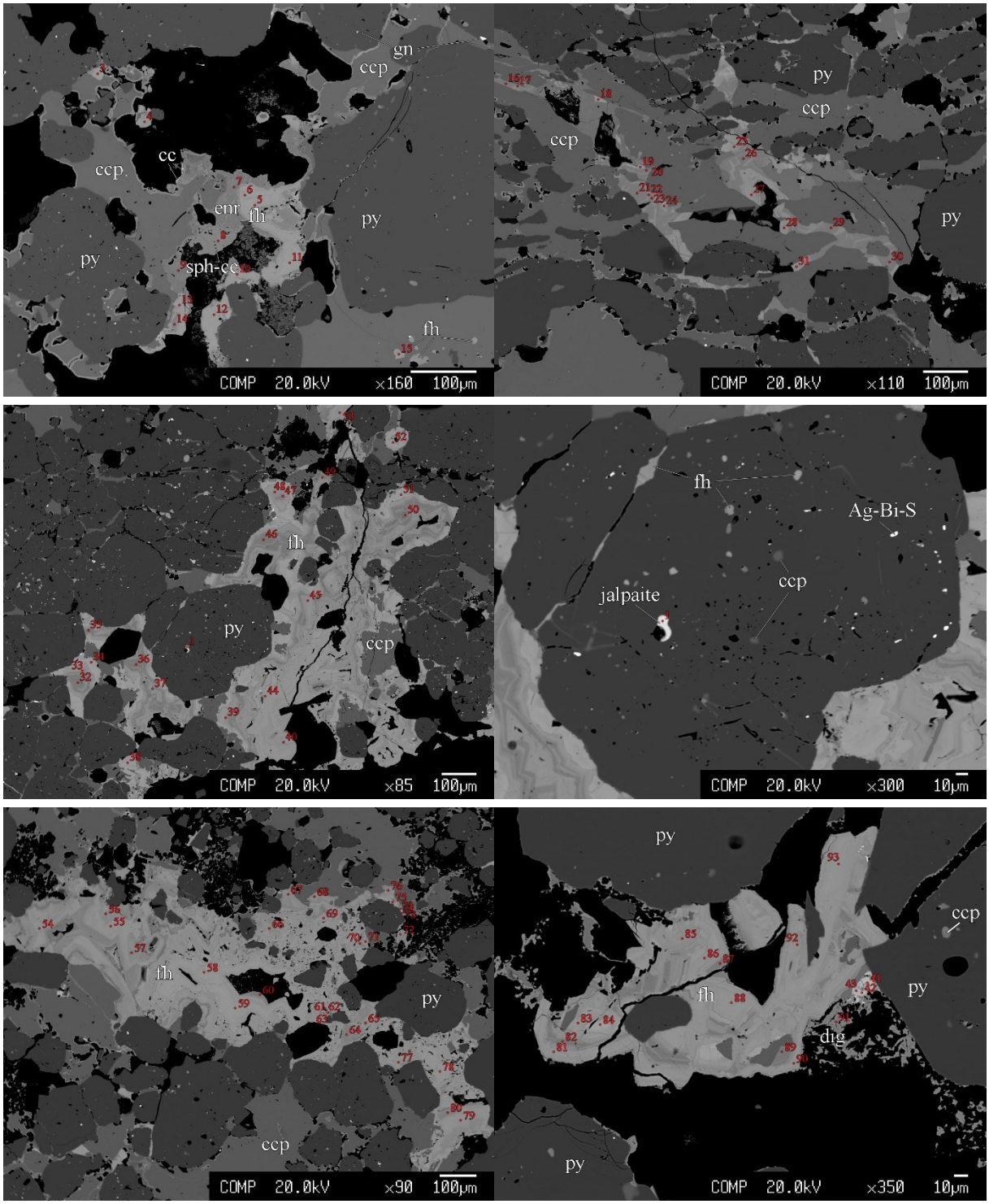

Sample CHM2-81

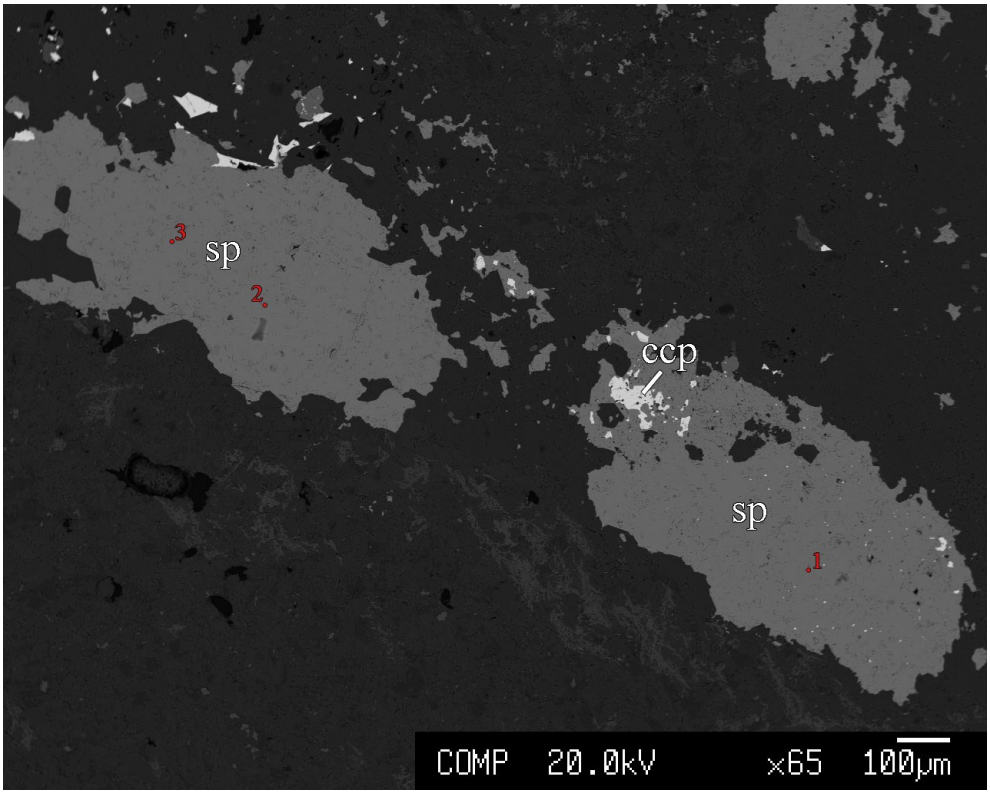

Sample CHM2-136

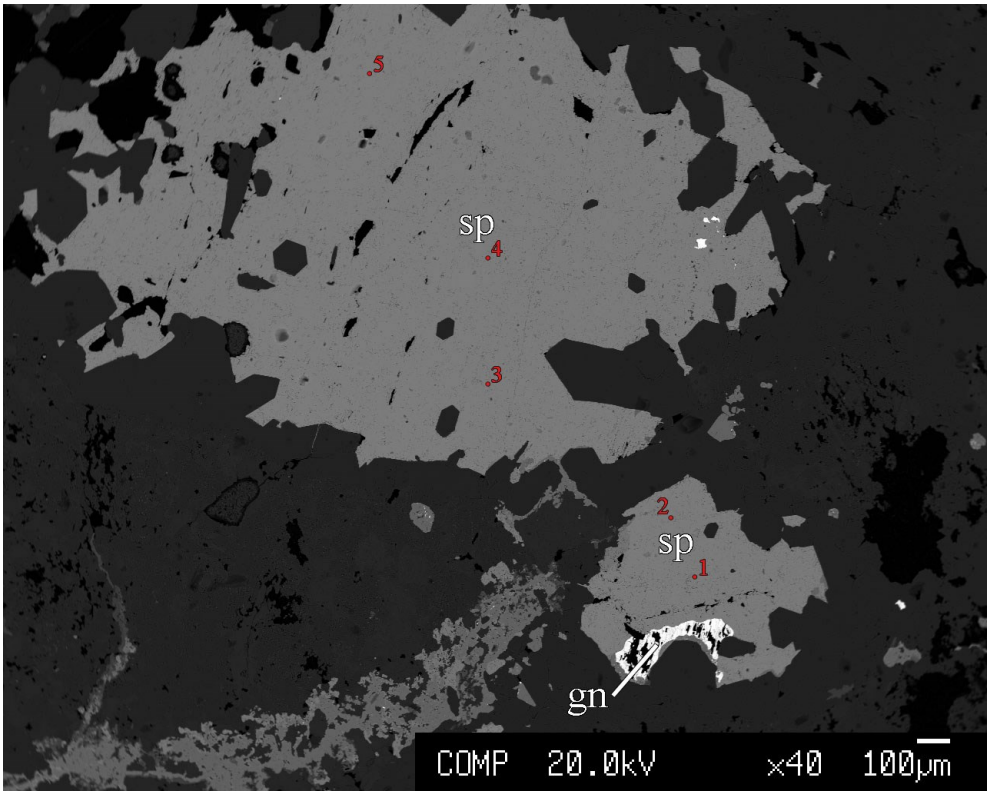

Sample CHM2-89

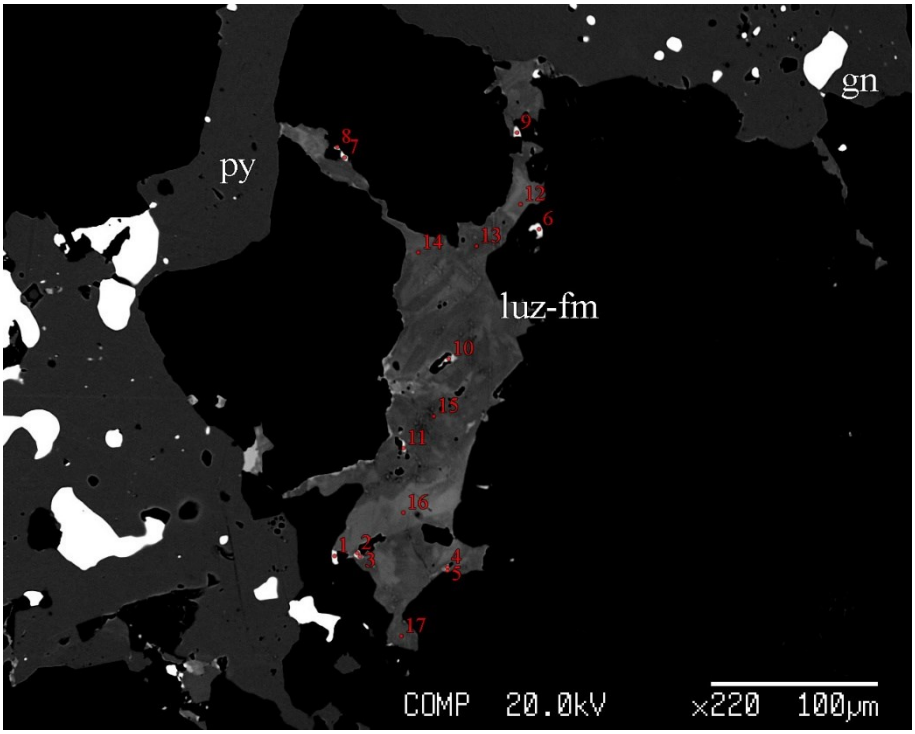

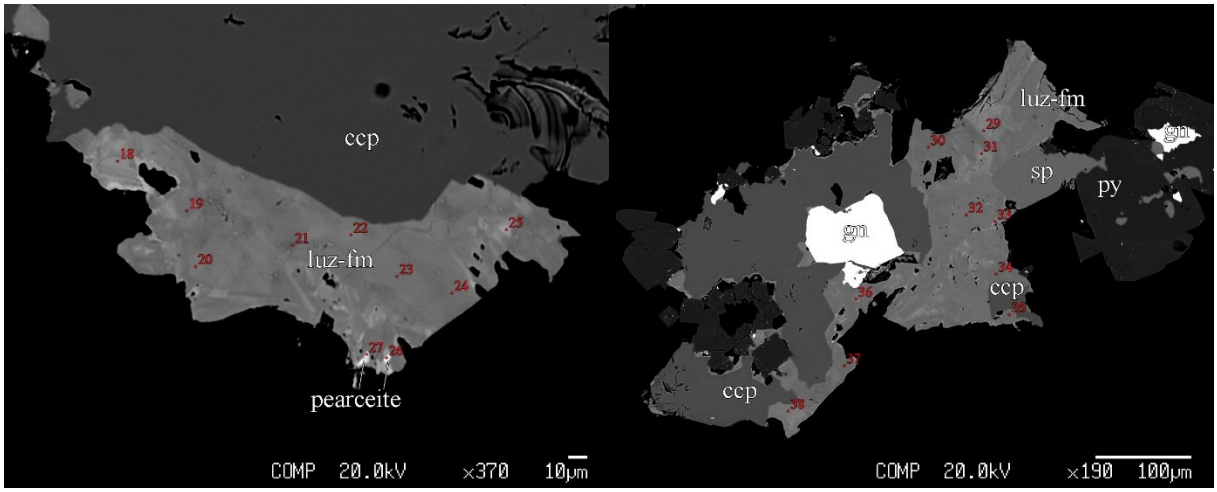

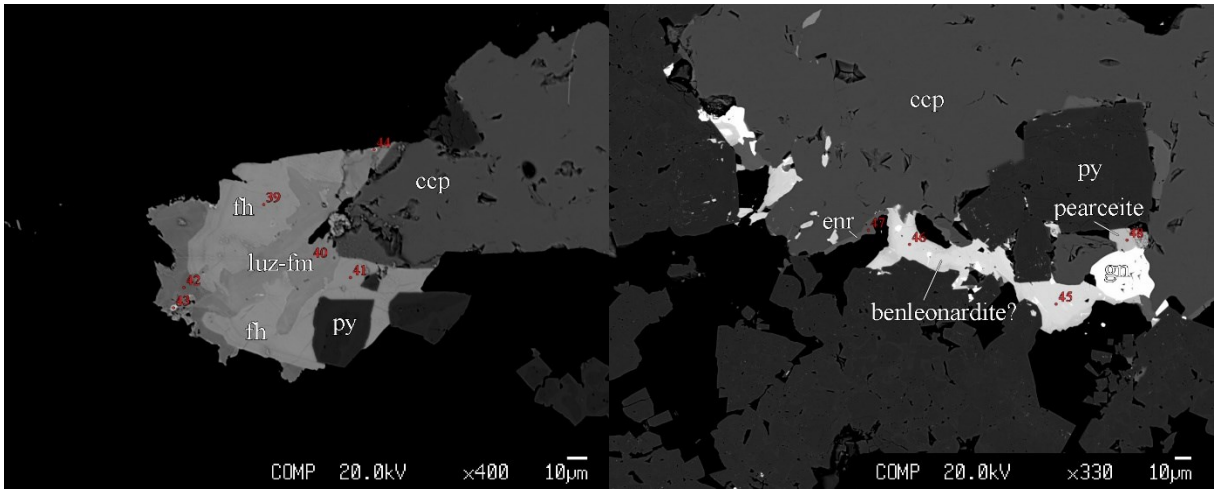

Sample CHM4-59

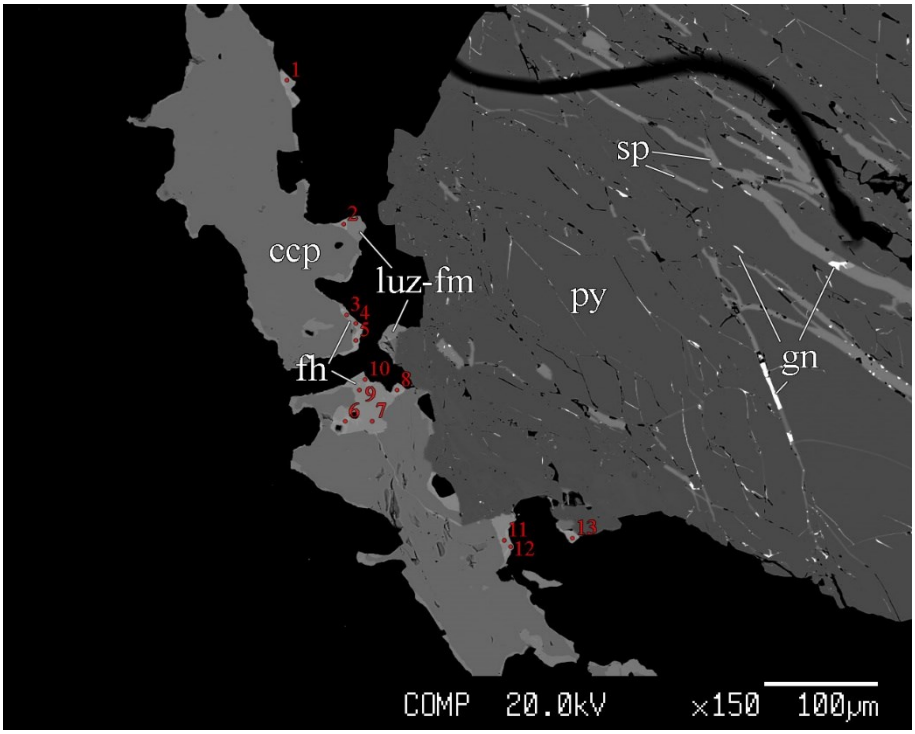

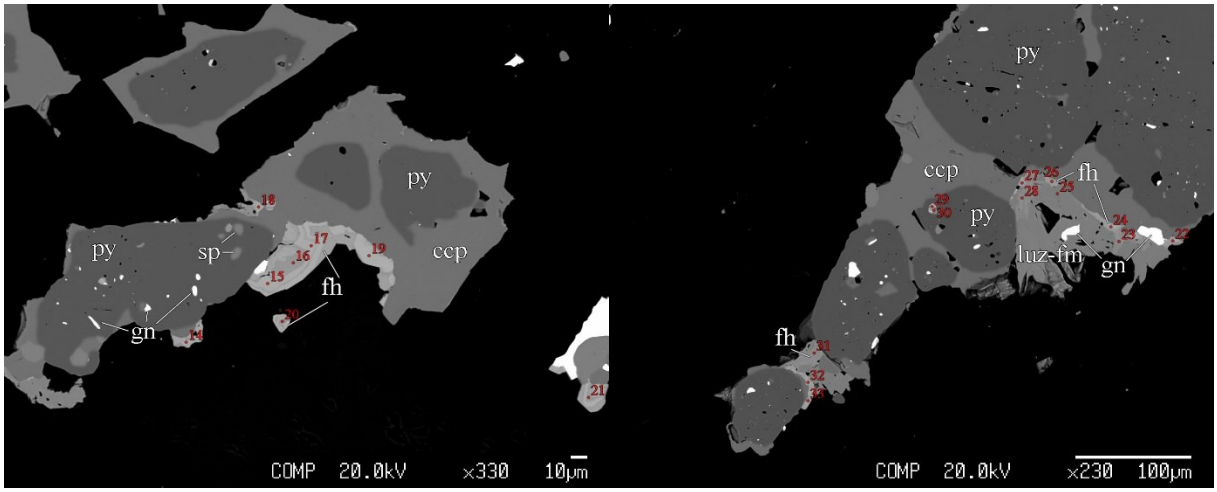

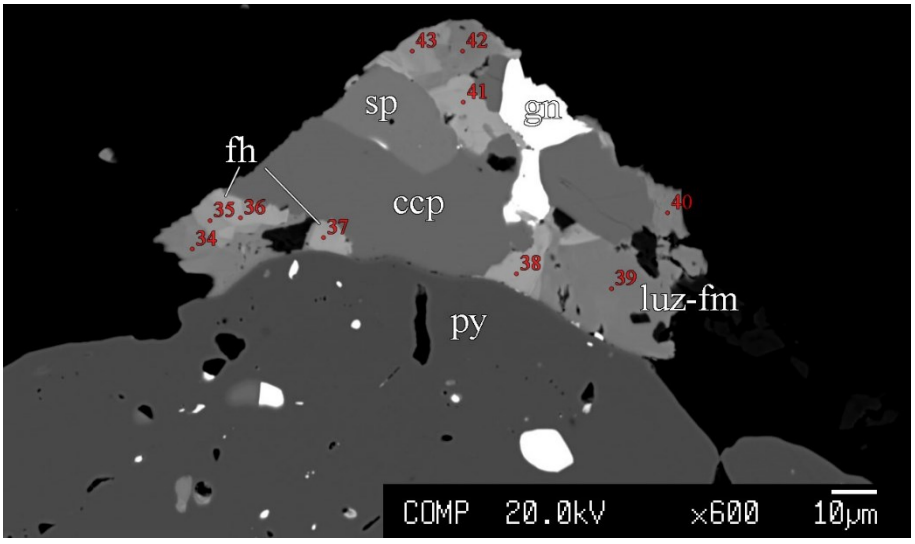

Sample CHM7-23.5

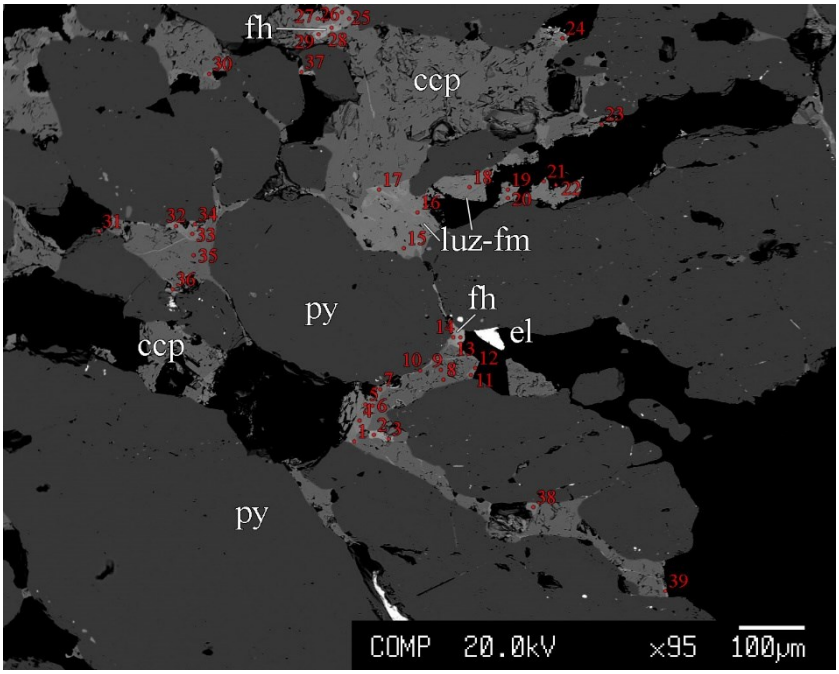

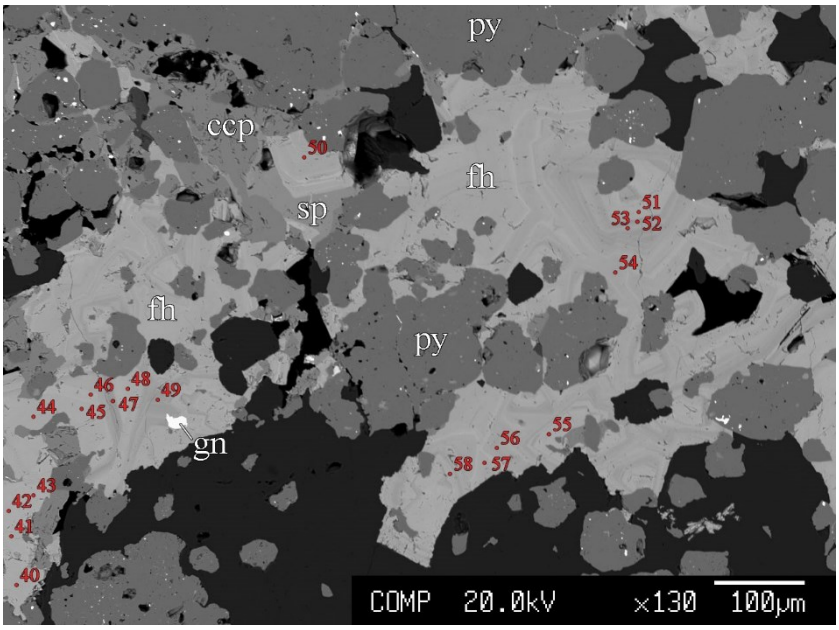

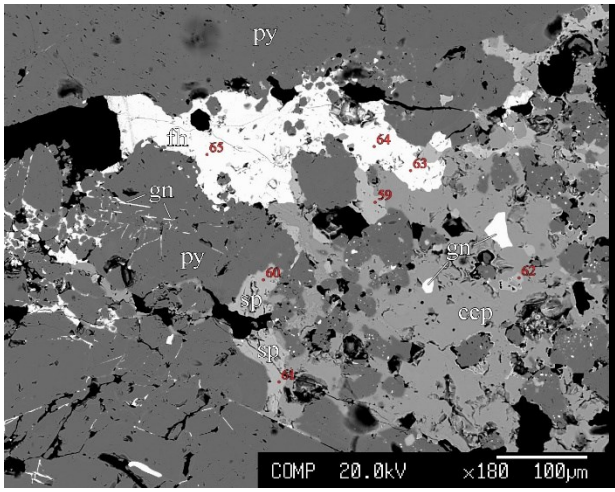

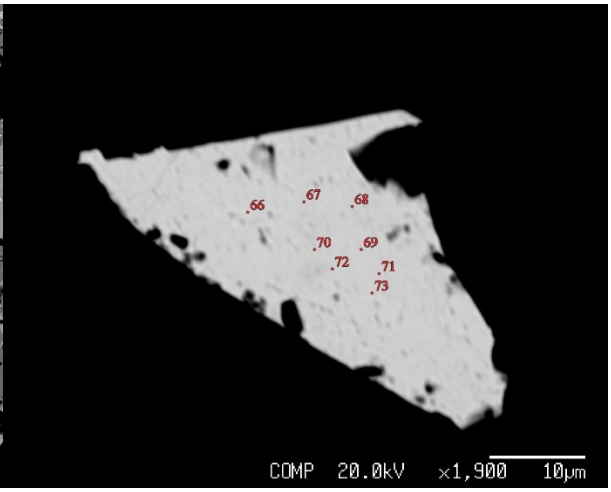

Sample CHM7-31.4

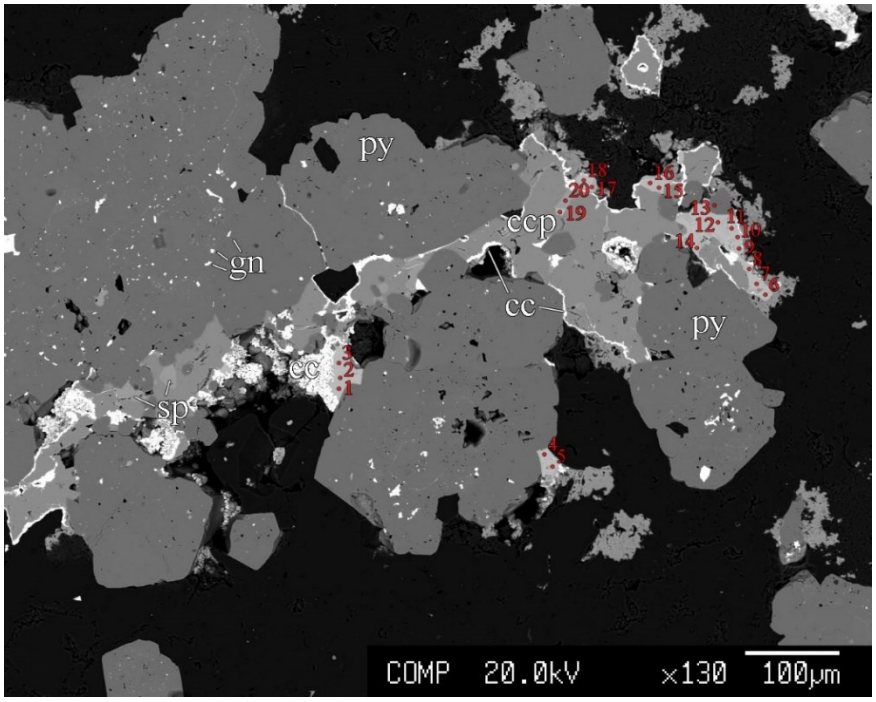

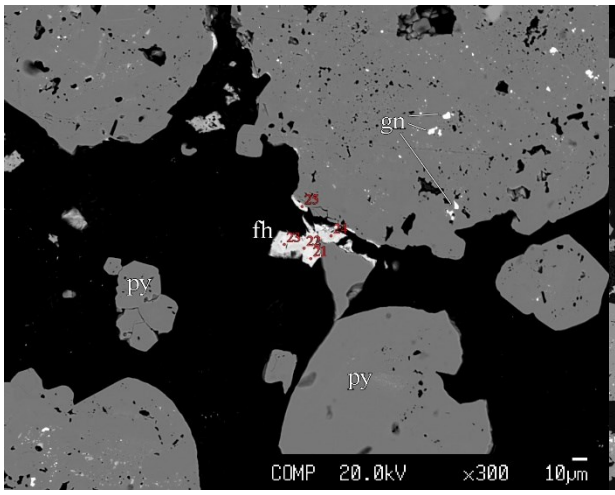

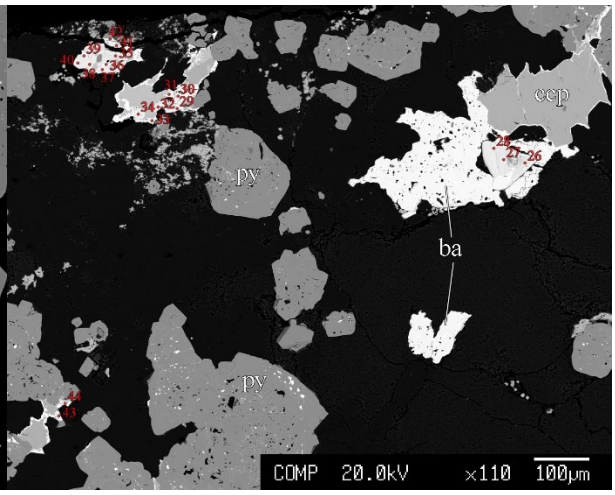

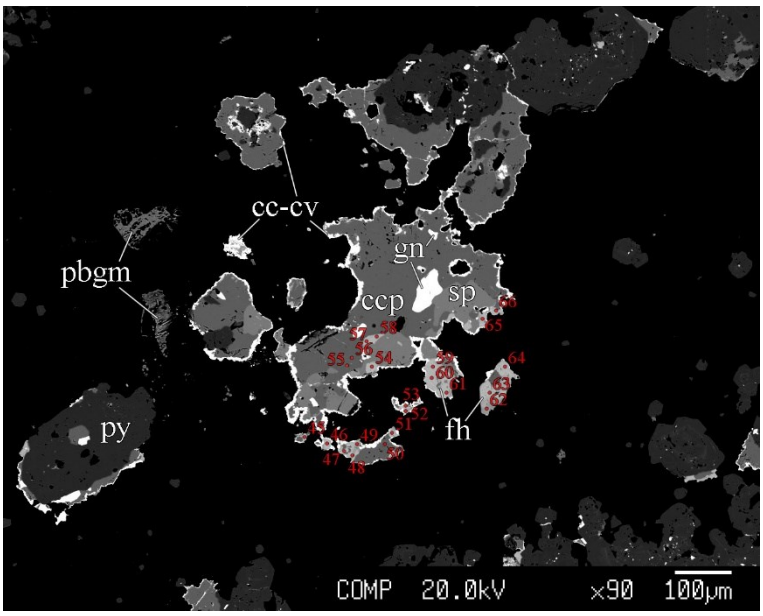

Sample CHM1B

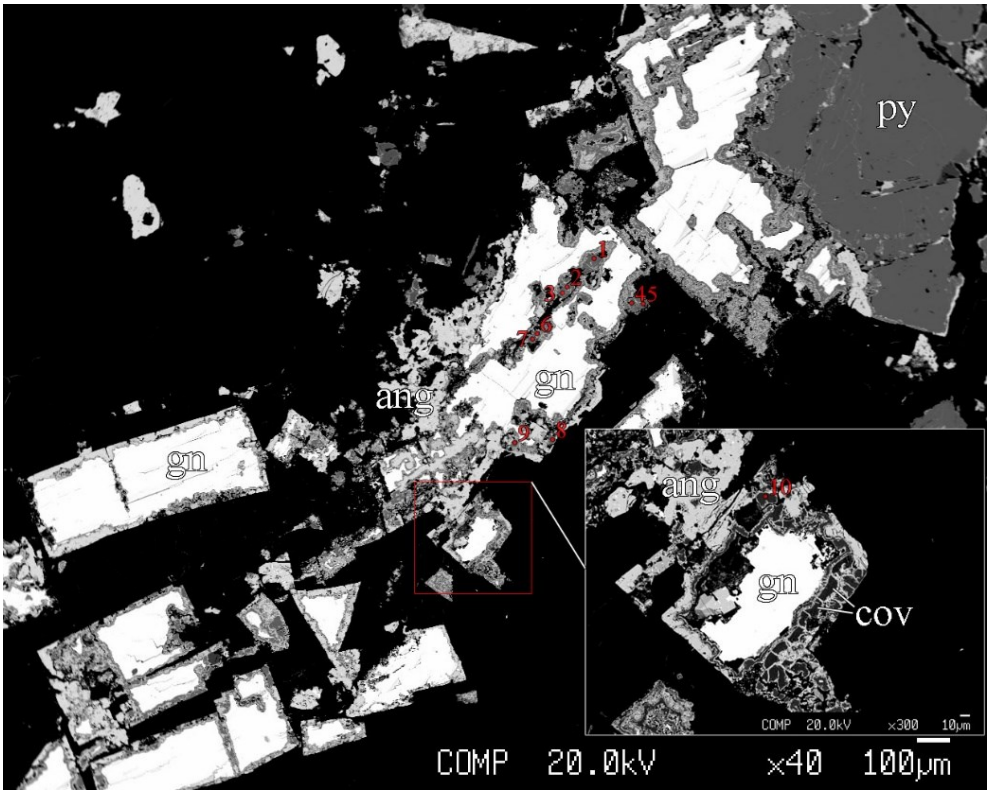

Sample CHM10A